IONIC LIQUIDS: THE IMPORTANCE OF LOCAL STRUCTURES AT MICRO- AND MESOSCALE AND DESCRIPTORS TO TUNE THEM

By

UTKARSH KAPOOR

Bachelor of Engineering (Hons.) in Chemical Engineering
Birla Institute of Technology and Science – Pilani University
Rajasthan, India
2012

Submitted to the Faculty of the
Graduate College of
Oklahoma State University
in partial fulfillment of
the requirements for
the Degree of
DOCTOR OF PHILOSOPHY
December 2018

IONIC LIQUIDS: THE IMPORTANCE OF LOCAL STRUCTURES AT MICRO- AND MESOSCALE AND DESCRIPTORS TO TUNE THEM

Dissertation Approved:

Jindal K. Shah

Dissertation Adviser

Josh D. Ramsey

Ashlee Ford Versypt

Christopher J. Fennell

ACKNOWLEDGMENTS

I would like to sincerely thank my advisor, Dr. Jindal K. Shah, for the guidance, perspective, insight, direction, and feedback he provided during this work. I always enjoyed research meetings with him where we discussed ideas and concepts in-depth. He has been a great mentor and an inspiration since the beginning of my Ph.D. work and has been instrumental in helping me fuel my love and curiosity to learn. I have learned a lot from him, both, professionally as well as personally. I want to extend special thanks to Dr. Christopher J. Fennell and Dr. Ashlee Ford Versypt for their valuable suggestions, exciting discussions and comments, and their willingness to serve on my doctoral committee. I am also grateful to Dr. Josh D. Ramsey for his time and effort to help as my committee member. I would also like to express my gratitude towards Dr. Sundarajan V. Madihally, Dr. Heather Fahlenkamp and Dr. Russell Rhinehart for their immense support and encouragement, that created a significant impact in my graduate life and helped me shape as a leader. I am grateful to all the professors who taught various courses in the department. A special thanks to - Ms. Eileen Nelson, Ms. Shelley Taylor, Ms. Carolyn Sanders, Ms. Shelley Potter, Ms. Paula Kendrick, and Ms. Beth Kelly for their continued assistance.

I am indebted to my parents, Harish Kapoor and Rama Kapoor, my sister, Sakshi Kapoor, and my five-year-old niece, Mayra Khanna, whose unwavering love and support have encouraged me to pursue my interests for my entire academic career. I am truly blessed to have them by my side!

Acknowledgments reflect the views of the author and are not endorsed by committee members or Oklahoma State University.

I have had a wonderful opportunity to form great friendships with many people at Oklahoma State University. I want to mention my colleague and friend Ashwin Kumar with whom I had numerous discussions in and outside the school, at lunches and dinners. I would also like to particularly mention my roommate and friend, Dipen K. Das with whom I have spent some of the most enjoyable as well as difficult moments. I want to thank him for his ingenious and stupid life lessons. I also express thanks to Blake MacNelly, Chuck Han and his family, and Matt Walton and his family for their special friendship, hospitality, and prayers, and for making my stay in the United States memorable and homely. A big thanks to my niece, Taanu (Dr. Vahuka), and my friend Mina Derakshan who have been a constant source of inspiration during the final stages of the work.

A special mention to Dr. Ashwarya Gupta who has been nothing less than my motivation, my biggest strength the entire time and my pillar of support. Thanks Aishi for all those daily phone calls, for trusting me, understanding me, and always being there for me.

Finally, I express sincere thanks to the department for providing me with a wonderful opportunity to carry out Ph.D. work. Last but not least, I acknowledge the funding from the NSF grants (ACI-1339785 and CBET-1706978) and OSU HPCC computing resource with special mention to Jesse Schafer for being patient and considerate dealing the technical issues.

Acknowledgments reflect the views of the author and are not endorsed by committee members or Oklahoma State University.

Name: UTKARSH KAPOOR

Date of Degree: December 2018

Title of Study: IONIC LIQUIDS: THE IMPORTANCE OF LOCAL STRUCTURES AT MICRO- AND MESOSCALE AND DESCRIPTORS TO TUNE THEM

Major Field: CHEMICAL ENGINEERING

Abstract: Ionic liquids (ILs) are novel chemical substances composed entirely of ions. The negligible vapor pressure coupled with the ability to design an IL by judicious choice of cations and anions or their substituent functional groups makes them attractive candidates for replacement of volatile organic compounds used in the chemical industry. According to one estimate, as many as one million ILs could be designed from the available cation-anion combinations. However, trial-and-error based experimentation approach of synthesizing new ILs and measuring properties to identify an IL suitable for a given task is expensive and inefficient. The need for fast and efficient discovery of new materials mandates that we recognize and develop design principles to screen materials without *a priori* knowledge of their properties. This dissertation is primarily directed towards designing ILs for a particular application by understanding molecular interactions, responsible for their macroscopic properties, using molecular simulations approach. The first part of the dissertation focuses on efforts to design or screen binary mixtures of ILs for tuning phase equilibria properties. The results indicate a structure-property correlation, at least qualitatively, between significant differences in molar volume and hydrogen-bond acceptor ability of the anions, that constitute the mixture, and molecular organization of ions within the mixture. This relationship allows us to fundamentally envisage the presence of ideal/non-ideal characteristics, which can further be exploited for better CO_2 absorption, relative to pure IL analogues, making them potential candidates for the application of gas separation processes. The second part of the dissertation focuses on engineering the self-assembly of amphiphilic ILs bearing long-alkyl chains, that exhibit liquid crystal-like behavior relevant for applications such as reaction media, liquid crystalline biosensors, synthesis of nanoparticles, and storage and stabilization of biological materials. For the simultaneous presence of nonpolar moieties on both cation and anion, the morphology at mesoscopic scale changes from sponge-like (less ordered) to layer-like (highly ordered) with an increase in cationic alkyl chain length, provided alkyl chain on the anion is long enough to show nanoscale segregation singlehandedly. Further, for an optimum combination of cationic and anionic chain length nanoscale heterogeneities spanning over multiple length scales are observed; the aggregation behavior of which can be further tuned by the addition of another, less amphiphilic, IL and dilution with organic solvents such as water. Insights obtained from this work suggests that the vital step towards engineering the morphologies at different length scales is the ability to tune the relevant interparticle interactions.

TABLE OF CONTENTS

LIST OF TABLES

Table Page

LIST OF FIGURES

Figure Page

CHAPTER 1

INTRODUCTION

1.1 Ionic Liquids and Their Applications

Liquids solvents are indispensable to chemical processes. Today, solvents are used in a wide range of technologies and applications involved in either making (foods, plastics, pharmaceuticals), processing (energy storage, carbon capture, coatings), or transporting (lubricants, fuels) materials. Much of chemistry revolves around the study of processes where the use of the solvent is convenient and inevitable. The market for solvents is worth billions of dollars and is steadily growing. However, the stock of solvents is finite and has several drawbacks. The usage of solvent from its manufacture to disposal is a highly energy-intensive process. The disadvantages associated with the use of solvents relating to environment or safety issues remain a significant concern. Solvents are often volatile which aggravates problems related to storage, transport, and atmospheric pollution. Moreover, health issues may involve non-aqueous solvents that are toxic if ingested and can bio-accumulate in nature. Against these astounding facts, it is still just not feasible to replace all the solvents. It is undeniable that the majority of reactions will still be conducted in either traditional or chemically modified solvents. However, much of the efforts today are directed to the use of alternative solvents that can help reduce the environmental footprint of the currently used solvents.

In search of better solvents, ionic liquids (ILs) have emerged as alternative candidates. ILs are the solvents comprised of molecular ions that resist solid-phase crystal

formation and exist as a liquid under ambient conditions. They are a unique class of electrolytes that can be designed to be non-volatile, thus, making them greener solvents than many prevalent in industrial practice. In fact, ILs can possess structural features reminiscent of molten salts, ionic crystals, and ionic surfactants that translates to remarkable properties such as high thermal stability, wide electrochemical window, and excellent solvation strength. [1, 2] Such favorable properties have enabled their usage in diversity of applications ranging from energy storage, [3, 4] reaction media, [5,6] battery electrolytes, [7–9] electroplating, [10,11] solar cells, [12–14] to gas separation processes. [15–18]

ILs are special due to the variety of interactions they can participate in. They can interact via weak forces such as van der Waals and dispersion forces, as well as strong forces like Coulombic and anisotropic forces, namely hydrogen or halogen bonding. Depending upon the type of IL, they can also participate in dipole-dipole interactions or electron-pair donor/acceptor interactions. For instance, imidazolium-based ILs can participate in dispersion, electrostatic, hydrogen-bond and π-π or anion-π interactions (Figure 1.1). The number of neat ILs is enormous. Theoretically, more than one billion ILs can be synthesized and exploited for different applications. This makes classification of ILs challenging. Figure 1.2 shows a sample of representative cation and anion chemical structures. [19] The cation is usually organic, while the anion can be both organic or inorganic. A precise modification of the physical, chemical, structural and biological properties of ILs can be achieved by a selective combination of cation, anion or their functional groups [20] making them dubbed as "designer" or "task-specific" solvents. Nonetheless, it is simply not realistic to use an IL and expect an improved outcome, as the use of ILs often deviates from the expected behavior.

Despite such benefits widespread adoption of ILs is yet to occur. Since the dis-

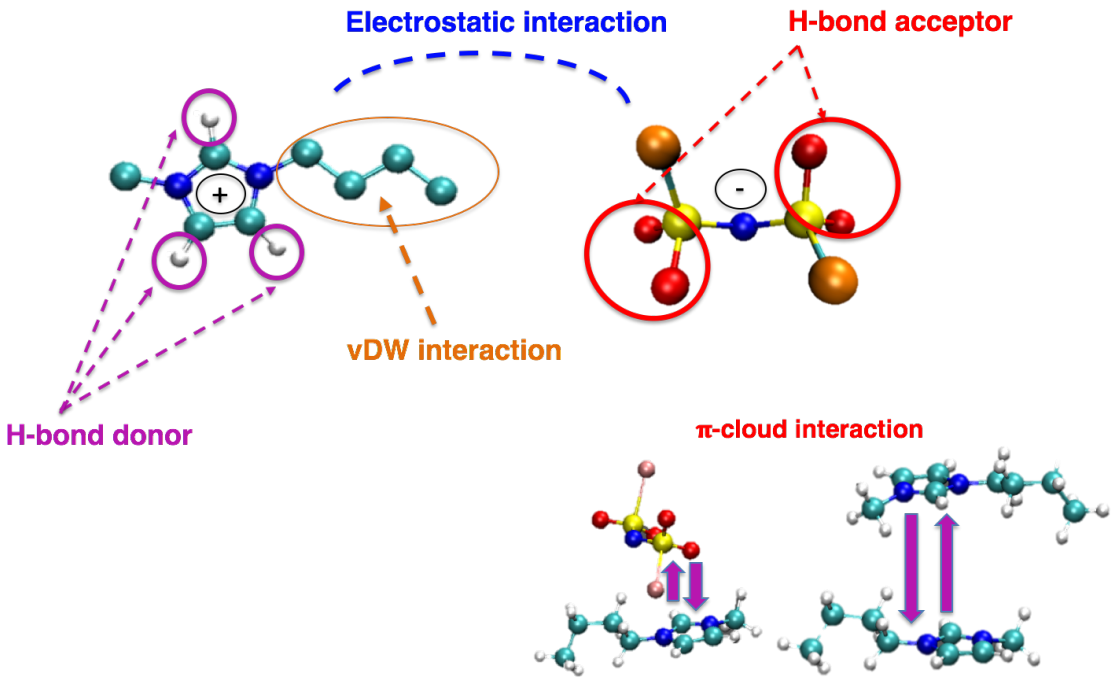

Figure 1.1: Plausible interaction model between imidazolium-based ILs

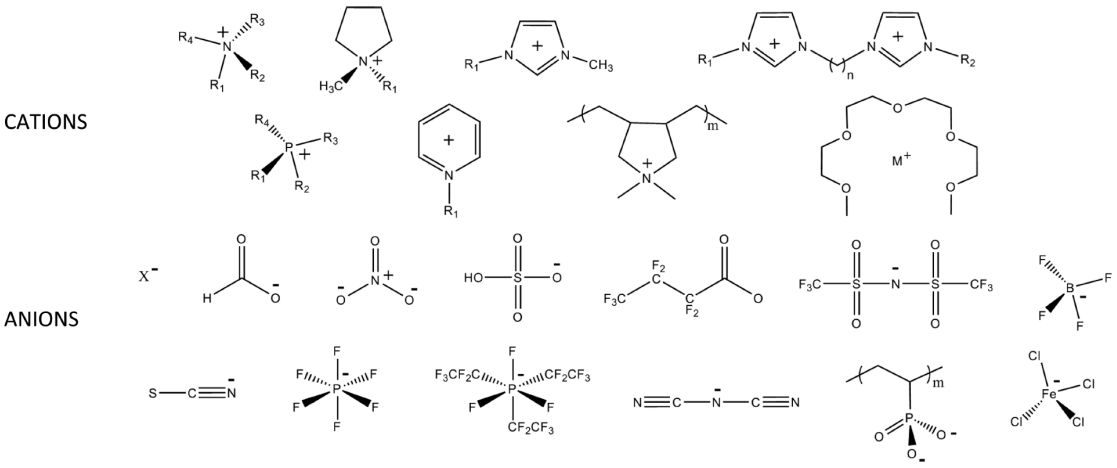

Figure 1.2: Some chemical structures of representative cations and anions used in protic, aprotic, dicationic, polymeric, magnetic, and solvate ILs (taken from Hayes et al. [19]). From left to right, the cations (top row) include: ammonium, pyrrolidinium, 1-methyl-3-alkylimidazolium, 1,3-bis[3-methylimidazolium-1-yl]alkane; (second row) phosphonium, pyridinium, poly(diallyldimethylammonium), metal (M+) tetraglyme. The anions include (third row) halides, formate, nitrate, hydrogen sulfate, heptafluorobutyrate, bis(perfluoromethylsulfonyl)imide, tetrafluoroborate, (bottom row) thiocyanate, hexafluorophosphate, tris (pentafluoroethyl)trifluorophosphate, dicyanamide, poly(phosphonic acid), and tetrachloroferrate.

covery of air- and water-stable ILs in 1992, [21] ILs have been utilized only in a few industrial-scale applications such as BASF's BASIL process that solves a separation problem in the synthesis of alkoxyphenylphosphanes, Chevron's ISOALKY process for alkylation, [22] removal of mercury from natural gas by Petronas, [23] and gas chromatography columns. [24]

The use of ILs is often limited by price (per unit volume) which permits its application to small-scale niche process. For example, 1-ethyl-3-methylimidazolium [C_2mim] bis(trifluoromethylsulfonyl)imide [NTf_2] IL offers great potential for CO_2-capture or gas-separation processes, but a 5 gram-unit bag of this IL costs $845.00 (courtesy Sigma-Aldrich). Furthermore, this fluorinated ion containing IL also raises environmental concerns due to toxicity and poor biodegradability. Whereas usage of cheaper ILs such as [C_2mim] ethyl sulfate [$EtSO_4$], 100 gram-bag costing $137.50, display unfavorable transport properties attributed to high liquid viscosity and may have a presence of impurities like water.

Almost every known physical chemistry technique has been used to investigate ILs, which has sometimes yielded a myriad of conflicting data. Moreover, synthesis of ILs without *a priori* knowledge of the IL properties – the discovery of new materials for a particular application – is a laborious and time-consuming task. Trial-and-error based experimentation is highly expensive and inefficient way of screening potential candidates for the desired application as designing a new material may require complementation of many factors. There is a general lack of fundamental understanding of how these properties of ILs depend on its chemical constitution. There is a need for developing structure-property relationships in ILs. Recognizing this difficulty use of physics-based computational tools that take into account the knowledge of interactions between various moieties in ILs, and may also provide insight where experi-

mentation is limited, are gaining momentum as they can be time- and cost-efficient.

Depending on the length- and time-scales probed in the hierarchy of continuum science, the simulation methodologies can broadly change from quantum mechanical theory – dealing with electronic structure – to atomic/molecular level classical simulations. The focus of this work is to use classical molecular modeling approach to study structures and in-part dynamics of ILs, with the aim of identifying fundamental descriptors for their rational design.

1.2 Scope and Potential Impact of Research

The research objectives for this dissertation concern two broad fields of ILs, whose structures evolve at different length-scales, and can be targeted for different applications.

- Identification of ideal vs. nonideal IL mixtures and assess their potential in the gas separation processes, with particular emphasis on the absorption of CO_2.
- Explore different ways to control the self-assembled structure of long-chain ILs when both the cation and anion possess long-alkyl chains, that find applications in the area of reactions, nanoparticle synthesis, as the pharmaceutical ingredient for drug delivery, for storage of biological materials and as electrolytes for batteries.

The potential impact of the first project is the reduction in the number of experiments or computer simulations needed to identify nonideal IL mixtures, as the qualitative structure-property relationship identified in this study can be used to predict the presence of nonideality and design a large number of binary IL mixtures especially for CO_2 absorption processes.

Further, the molecular-level insights provided in the second project of this dissertation not only adds new literature to the field but also provide hints on the effect modulating the respective polar–nonpolar interparticle strength can have on the overall morphology. The observations made in this study will allow researchers to make a clear judgment on which interaction to target for fine-tuning the self-assembly of an IL in the desired way.

1.3 Outline of the Dissertation

Apart from this introductory chapter that gives a general overview of why we are interested in ILs and outlines the scope of the research presented, this dissertation is organized as follows.

Chapter 2 provides a brief review of the structure and dynamics of ILs with particular emphasis on considerations that need attention.

Chapter 3 gives a general background on statistical thermodynamics and focuses on the theory behind both molecular dynamics (MD) and Monte Carlo (MC) molecular modeling formalisms used in this work. The chapter also provides an in-depth review of existing methods to compute the excess chemical potential via MD simulations. Detailed simulation protocols used to conduct this research work are provided which when followed can help reproduce these results. GitHub link to download all the relevant simulation input files is also provided as part of this dissertation. Also, general introduction to the types of analyses and structural characterization employed in this work is included along with the reference to the tools and utilities that can be utilized to conduct the respective analyses.

Chapter 4 encapsulates a study on imidazolium-based binary ionic liquid mixtures

(BILMs) and their implications on phase equilibria properties. First, thermodynamic properties such as density, molar volumes, and their deviations from the ideal mixing rule and transport properties such as self-diffusion coefficients and ionic conductivities of 13 BILMs are reported, and their concentration dependent trends are discussed. These BILMs showcase the effect of changing anions and cationic alkyl chain length on the properties. Then, two BILMs, specifically one ideal and one nonideal, are chosen from the 13 mixtures and their concentration-dependent liquid structures are elucidated showcasing ion–ion interactions, and the presence of nonideality is rationalized based on the observed structural transitions. The same ideal and nonideal BILMs are then studied for CO_2 absorption, where Henry's constants of CO_2 were assessed as a first step to recognize the suitability of these BILMs for CO_2 solubility. The results of MD simulations in the Henry's law regime with and without CO_2 molecules are discussed to realize the molecular origins of the observed behavior. Further, with the goal of predicting, *a priori*, BILMs as a potential candidate for better CO_2 solubility, a systematic study containing 16 BILMs of fluorinated vs. nonfluorinated anions is discussed. A specific range of correlated parameters, a (qualitative) structure-property relationship, is mentioned that help recognize nonideal BILMs better suited for CO_2 absorption without the need of conducting any experiments or simulations. The last part summarizes the main findings of this chapter with major takeaway points.

Chapter 5 succinctly expresses the essential features of ILs that can self-assemble and have high range order. The overall objective of this chapter is to provide fundamental insight into the self-assembly itself rather than their function. Bi-amphiphilic ILs where there is simultaneous presence of alkyl chains on both the cation and anion are considered. At first, the self-assembled morphology and the nanoscale heterogeneities are discussed for six pure bi-amphiphilic IL systems where cationic alkyl chain length is systematically increased while the length of anionic chains is kept

constant. Structural characterization is done in terms of their morphological connectivity, shapes, aggregate size distribution, and long-range ordering probed via a wide variety of statistical tools. Then, based on the observations made, longest cationic chain containing bi-amphiphilic IL system is chosen for further analysis. The focus is on modulating its morphology. Two BILMs are considered, the molecular insights of the morphological transitions are rationalized using the same statistical tools. The last part of this chapter focused on the aggregation behavior of the same IL in aqueous solutions at very dilute conditions. The study provides molecular-level information on the observed mesoscale micellar aggregates. In the end, the main findings of this chapter with significant takeaway points are summarized.

Finally, Chapter 6 summarizes the work presented in the previous chapters and connect ideas with suggestions for future direction. The supporting information follows in the Appendices, and it provides (i) raw data for the thermophysical properties estimated in this work; and (ii) concentration dependent structures of the binary IL mixture systems discussed in section 4.5.

CHAPTER 2

A REVIEW OF PREVIOUS RESEARCH

2.1 Binary Ionic Liquid Mixtures

Increasing CO_2 emission is a major environmental concern. Although a great deal of effort has been employed for the development of technologies to capture CO_2, the current available industrial scale processes for the absorption of CO_2 pose a series of disadvantages. They are based on aqueous solutions of alkanolamines, and carbonate-based solvents which have energy-intensive high operation costs, corrosion issues and are prone to solvent loss due to evaporation or degradation. [25] In a seminal publication, [15] potential use of IL for gas separations was demonstrated as CO_2 solubility was high over O_2 and N_2. It has been established that for a given cation the CO_2 solubility is anion-dependent, while the cation plays a secondary role unless long alkyl chains are present in the cation. [26] Fluorination of the cation or anion, have also yielded increased physical absorption of CO_2. [17, 27, 28] Currently, ILs with fluorinated ions are expensive and can be toxic. So, one of the key research areas here is to identify ILs that have CO_2 solubility as high as fluorinated containing ILs but does not suffer from the drawbacks they offer.

As mentioned earlier a proper selection of the chemical constituents of ILs can impart the desired properties generating a wealth of ILs, but the limitations of their usage in industrial processes may persist. A brute-force approach is to keep changing the nature of the ion moieties to overcome this challenge, which can be a daunting task if not impossible. Moreover, all newly synthesized ILs would require full physicochem-

ical property characterization. Recognizing this hurdle, mixtures of ILs have been considered as a means to precisely control the desired physicochemical properties of the resulting IL. Coutinho and co-workers showed that the combinatorial approach of different cation and anion does not offer significant changes in the activity coefficient of water. However, if one considers mixtures of just two ILs, the property trends can be precisely tuned. [29, 30] Thus, introducing another degree of freedom in the form of molar compositions of ILs, provides an additional handle over the property trends. The use of mixtures of ILs seems desirable as the properties are fine-tuned based on the already synthesized ILs, reducing the need to synthesize entirely new ILs.

Moreover, some instances have shown that mixtures of ILs can possess properties superior to the pure IL analogues. For example, Stoppa et al. [31] showed enhanced ionic conductivity over the entire composition range for the mixture of 1-ethyl-3-methylimidazolium [C_2mim] dicyanamide $[DCA]_x$ tetrafluoroborate $[BF_4]_{1-x}$, which can be exploited for electrochemical applications. Pinto et al. [32–34] experimentally investigated CO_2 solubilities, in terms of Henry's constants, in binary IL mixtures of $[C_2mim][NTf_2]_x[EtSO_4]_{1-x}$ and $[C_4mim][EtSO_4]$–$[C_2mim][NTf_2]$ at 298.2 K and 1.6 MPa and reported negative deviation from the linear mixing rule, demonstrating that CO_2 solubilities in these IL mixtures may be higher than expected, potentially not only tuning the property behavior but also the IL cost, as nonfluorinated IL is cheaper by almost a factor of 100. Thus, blending such ILs with more economical ones may provide an avenue to overcome some of the disadvantages. However, the question in such a scenario is the extent to which desirable properties of fluorinated ILs are carried over in binary IL mixtures and how these properties vary with the mixture compositions.

Nevertheless, again, it is simply not realistic to mix two ILs and expect an improved

outcome, as even mixtures of ILs have been seen to deviate from the expected behavior. Thus, it is highly desirable to predict if a given binary IL mixture is likely to exhibit ideal, thermophysical as well as phase equilibria, behavior such that the mixture properties can be estimated directly from pure ILs. On the other hand, it is equally important to determine the factors that can dictate the deviation from the expected behavior. At present there is a lack of fundamental knowledge regarding the rules that can be applied to determine *a priori* if a given binary IL mixture will exhibit deviation from the expected ideal behavior.

Previously, ideal mixing behavior has been defined in a variety of ways. A mixture is considered ideal if: (i) ΔH_{mix} is ~ 0 and mixing is entropically driven [35,36]; (ii) the chemical potential of the mixture components is the linear average of the mole fraction dependent pure component chemical potential; [37] (iii) interactions present in the mixture are similar to that found in pure IL analogues. [38] A majority of physicochemical studies suggested close to ideal mixing behaviors, with a few outliers, from a thermodynamic standpoint. [35,38] Changes in the specific preferential interactions have been invoked to account for the small non-ideality. The Kamlet-Taft multi-parameter polarity scale has been employed to characterize specific interactions of the solvation, of specific interest to the work presented in this dissertation is hydrogen bond acceptor ability of anion, β parameter. [39,40] An extensive database of the β parameter is reported by Lungwitz et al. [41,42] and by Welton and co-workers [43]. It has been suggested that the anion size/molar volume and the hydrogen bond acceptor ability of anion, β parameter, plays a major role in solvation. [35,38] Many studies have been reported that correlates β parameter with hydrogen bond energy [44] and ^{1}H NMR chemical shift of C-2 proton, [45,46] linearly. Additionally, tremendous effort has been made to predict β parameter by calculating hydrogen bond interaction energies using COSMO-RS [47] and by computing energy

of formation for a complex between anion and probe molecule HF, [44] to speed up the screening process.

As with pure ILs, the initial research on IL mixtures has primarily focused on their thermodynamic and transport properties and if such ILs can be classified as ideal or nonideal mixtures of the constituent ILs.

2.1.1 Thermophysical Properties

In general, positive excess molar volumes have been observed for binary IL mixtures that contain bis(trifluoromethanesulfonyl)imide $[NTf_2]^-$ as one of the anions. Lopes et al. [48] reported small but positive excess molar volumes for the IL mixtures comprised of the cation 1-n-butyl-3-methylimidazolium,$[C_4mim]^+$ paired with different molar ratios of the anions $[NTf_2]^-$ and tetrafluoroborate $[BF_4]^-$, and IL mixtures of $[C_4mim]^+$ with $[NTf_2]^-$ and hexafluorophosphate $[PF_6]^-$. The nearly ideal behavior of the mixtures led the authors to conclude that, at the molecular level, the interactions in the mixture are probably indistinguishable from those found in the pure ILs. The authors reported similar trends for a number of IL mixtures containing 1-n-decyl-3-methylimidazolium $[C_{10}mim][NTf_2]$ and $[C_nmim][NTf_2]$ (n = 2, 4, 6, and 8) and found that the excess molar volumes were consistently small but positive independent of both temperature and pressure. The magnitude increased with an increase in the difference in the size of the cations. Subtle changes in the structure, due to the aggregation of long alkyl chains, were provided as a possible reason.

Fox et al. reported that for dialkylpyrrolidinium-based $[C_nC_1pyrr][C_mC_1pyrr][NTf_2]$ mixtures the densities followed ideal mixing for all the cases of n and m. [49] Coutinho and co-workers also showed that binary mixtures containing $[C_4mim][NTf_2]$ with eight other anions not differing significantly in their hydrogen bonding strengths formed

nearly ideal mixtures. [50] Other examples include density measurements by Larriba et al. [51] that showed small but positive excess molar volumes for binary IL mixture of $[C_4C_1pyrr][BF_4]$ $[NTf_2]$. Navia et al. [36] also found positive excess molar volumes for $[C_4mim][BF_4][PF_6]$, consistent with Lopes et al. [48], but reported negative excess molar volumes for $[C_nmim][C_6mim][BF_4]$ (n = 2 and 4) and $[C_4mim][BF_4][MeSO_4]$ and suggested packing effects, due to the availability of free space, as a possible explanation for negative values.

The measurements by Stoppa et al. [31] for the binary IL mixtures containing $[C_2mim]$ $[BF_4]$ dicyanamide [DCA] revealed that excess molar volumes were small but positive over the entire composition range. Despite close to ideal behavior for $[C_2mim][BF_4]$ [DCA], the dynamical properties such as conductivity and static permittivity deviated significantly from a simple linear mixing relationship. Strikingly, positive deviation for conductivity, for the entire composition range, was obtained suggesting more independent charge carriers than pure IL counterparts, which can be exploited for electrochemical applications. However, once again, gradual change in the liquid structure between those of the pure ILs was offered as an explanation for the observed mixture properties, however, with no evidence to support the hypothesis.

Similar observations were made by Pinto et al., where the authors investigated the IL mixtures formed from $[C_2mim]$ ethylsulfate $[EtSO_4]$ and $[C_2mim][NTf_2]$ and observed that the excess molar volumes showed positive deviation from ideality over the entire range of compositions with the maximum deviation at a $[C_2mim][NTf_2]$ mole fraction of 0.4. The authors also observed similar results for $[C_4mim][EtSO_4]$ and $[C_2mim][NTf_2]$ mixtures, however, negative deviations in viscosity as high as -60 mPa.s were reported. [32] The viscosities of four series of mixtures reported by Navia et al. [36], failed to follow linear mixing rule. However, it was shown that Grun-

berg and Nissan mixing law gave good quantitative agreement which led authors to conclude ideal mixing for transport properties in these mixtures. This indicates challenges associated in predicting nonidealities in transport properties of IL mixtures based solely on the knowledge of excess thermodynamic properties. The results also point to the fact that the molecular level details for dynamical property trends in IL mixtures are currently not well understood.

Strikingly, IL mixtures containing anions with a substantial difference in hydrogen bond acceptor ability, β parameter, and size/molar volumes of anions have shown nonideal behavior. For instance, Clough et al. [35] reported consistent nonideal behavior in terms of excess molar volumes, viscosity, conductivity and glass transition experiments for anion pair of dimethylphosphate $[Me_2PO_4]^-$ and $[NTf_2]^-$ combined with either $[C_4mim]^+$ or $[C_4C_1pyrr]$ cations, that has very large difference in β strength with $\Delta\beta \sim 0.76$. However, these mixtures have a comparatively small difference in the molar volumes ($\Delta V \sim 41$ cm^3 / mol). Moreover, though the difference in hydrogen bond ability of some anions was moderate ($\Delta\beta \sim 0.4$), small excess molar volumes (nonideality) were observed for the IL mixture series of $[C_4mim]$ methylsulfate $[MeSO_4]$ and $[C_4mim][NTf_2]$, while close to ideal behavior was observed for the mixtures of $[C_4mim]Cl$–$[C_4mim]$ trifluoromethanesulfonate [TFS] and $[C_4mim][MeSO_4]$–$[C_4mim][Me_2PO_4]$. These observations were rationalized via an alternative approach of differences in molar volumes. Large molar volume difference of 61 cm^3 / mol lead to non-ideal behavior in $[C_4mim][MeSO_4]$–$[C_4mim[NTf_2]$ while small differences of 38 and 19 cm^3 / mol in mixtures of $[C_4mim]Cl$–$[C_4mim][TFS]$ and $[C_4mim][MeSO_4]$–$[C_4mim][Me_2PO_4]$ displayed close to ideal behavior. For more examples of the comprehensive collection of binary IL mixtures and their thermophysical properties, interested readers are referred to publications by Chatel et al. [38] and Niedermeyer et al. [37]

Molecular simulations have also been carried out to predict thermodynamic and transport properties of such IL mixtures. Aparicio and Atilhan [52] conducted molecular dynamics (MD) simulations of pyridinium-based IL mixtures varying the composition of anions $[BF_4]^-$ and $[DCA]^-$ paired with 1-n-butyl-3-methylpyridinium $[C_4\text{-3mpyr}]^+$ and another changing the amounts of $[C_4\text{-3mpyr}]^+$ and 1-n-octyl-3-methylpyridinium $[C_8\text{-3mpyr}]^+$ coupled with $[BF_4]^-$. The former system showed negative excess molar volumes ($\sim$ -1 cm^3/mol) while the latter system displayed positive deviation (> 1 cm^3 mol). The observed behaviors were explained in terms of steric hindrance and packing effects. The same authors also suggested the possibility of fine-tuning the interfacial behavior of IL mixtures by varying the ratios of $[C_4\text{mim}]\text{Cl}$ and $[C_4\text{mim}][NTf_2]$ ILs based on MD calculations. [53] Thus, overall, such conflicting conclusions further emphasize that the factors governing the presence of nonideality in IL mixtures are not yet completely understood.

2.1.2 Structural Investigation

MD simulations have played a major role in providing microscopic structural evidence for rationalizing nonideal IL mixtures. The first evidence that the difference in hydrogen bond ability between the anions could modulate the structures in the binary IL mixtures was provided by Payal and Balasubramanian [54]. The authors reported composition dependent radial distribution functions (RDFs), indicative of the organizations of the anions around the cation, for the $[C_4\text{mim}][PF_6]$–$[C_4\text{mim}]\text{Cl}$ system which was attributed to the stronger affinity of Cl^- for the cation; while similar affinity of the anions $[PF_6]^-$ and $[BF_4]^-$ with $[C_4\text{mim}]^+$ yielded negligible dependence of RDFs on the composition of the anions. Since then our understanding of IL fundamentals about chemical structure has reasonably advanced. Much effort has been made to correlate experimental findings with structural transitions. Shimizu et al. [55] also performed MD simulations of equimolar mixtures of the ILs $[C_2\text{mim}][NTf_2]$ and

$[C_6mim][NTf_2]$ and inferred that nearly ideal behavior of the mixtures stems from the absence of cross-interactions between the two cations.

It has now been established that the addition of the second IL could alter the chemical environment around the cation in binary ILs; attested by the fact that the large difference in the nucleophilicity of the anions, for example in $[C_4mim][Me_2PO_4]$–$[C_4mim][NTf_2]$ and $[C_4mim]$Cl–$[C_4mim]$[TFS] (Welton and co-workers [45]), and $[C_2mim]$ acetate [OAC]–$[C_2mim][NTf_2]$ (Rogers and co-workers [46]), resulted in a downfield ^{1}H and ^{13}C-NMR chemical shift of the imidazolium ring protons that varied in a nonlinear fashion with the composition of the anion. The authors explained the behavior by elucidating the local structures of the IL mixtures and showed preferential interactions between the most acidic hydrogen atom in the cation with the strong hydrogen bond accepting anion. While weakly coordinating anions such as $[NTf_2]^-$ were found to organize above and below the plane of the imidazolium ring promoting anion-π interactions and easily disrupting favorable cation π-π interactions established by strongly coordinating anions. Thus, structural rearrangement of anions around the cations, very different from the pure ILs, which was responsible for the appearance of new interactions in the IL mixtures was provided as an explanation. Similar observations have been reported by Kirchner group, where authors studied IL mixtures of $[C_2mim]$Cl and $[C_2mim]$ thiocyanate[SCN] and indicated that cations interact via π-π stacking which is weaker in the case of $[C_2mim][SCN]$. On the other hand, the binary mixtures containing anions with similar hydrogen bond acceptor ability, such as $[C_4mim]$Cl–$[C_4mim][SCN]$ and $[C_4mim][NTf_2]$-$[C_4mim]$[TFS], have shown the chemical shifts of the ring protons vary linearly with molar ratios of the anions, for which preservation of the interactions was provided as an explanation.

However, the ^{1}H-NMR observations, reported above, are in direct contrast with the in-

sight gleaned from the optical Kerr effect (OKE) spectra of the binary IL $[C_5mim]Br$-$[C_5mim][NTf_2]$. Despite the large difference in hydrogen bond basicity, Quitevis and co-workers showed that the OKE spectra of the binary IL could be well described by a linear combination of the neat spectra and proposed that the IL mixtures contained blocks of neat ILs hinting at nanoscale segregation as opposed to local changes around the ions. [56]

Thus, the conflicting conclusions further emphasize that the current understanding regarding the structure of IL mixtures is far from being complete. Although molecular simulation and spectroscopic studies have suggested the possibility of an appearance of novel structures in IL mixtures, it is not entirely clear how different the hydrogen bonding ability of the anions should be so that evolution of nonnative structures may be anticipated. It is essential to identify a structure-property relationship, if any, before a definite conclusion regarding the nonideal behavior of IL mixture could be established. The work presented in Chapter 4 seeks to fulfill this gap and provide some useful insights by tying thermophysical property trends with structural transitions and providing, at least, a qualitative structure-property relationship that can be used to *a priori* predict the presence of novel nonnative structural rearrangement of anions around cations.

2.1.3 Phase Behavior

The Henry's constants are subjective to the types of cations and anions comprising the IL. For imidazolium-based cations, however, it has been speculated that contribution of cation to CO_2 solubility is rather secondary while anions play a primary role in determining CO_2 solubility in ILs. Regarding anions the following trend has been observed for the solubility of CO_2 in ILs for a given cation: nitrate $[NO_3]^-$ < $[SCN]^-$ < methylsulfate $[MeSO_4]^-$ < $[BF_4]^-$ < trifluoromethane-

sulfonate $[TFS]^-$ < trifluoromethylacetate $[TFA]^-$ < $[PF_6]^-$ < $[NTf_2]^-$ < perfluoroheptaneacetate $[C_7F_{15}COO]^-$ < tris(pentafluoroethyl)trifluorophosphate $[eFAP]^-$ < tris(pentafluorobutyl)trifluorophosphate $[bFAP]^-$. [18, 57, 58] CO_2 solubility can favorably be increased by considering fluorination on cation and anion, [59] bromination on anion, [60] cations having branched long alkyl chains or chains containing ether linkages [16, 28] or functional groups such as carbonyl and ester groups, [28] while substitution of most acidic ring hydrogen site with methyl, [16, 28] ether, [61] hydroxyl [28] or alkyne and nitrile group [62] are not favorable for increasing the CO_2 solubility. Further, it is worth mentioning that presence of such gaseous-solutes has a negligible impact on the underlying structure of ILs, which may be in direct contrast to other molecular solvents (liquid) like water or alcohols that have the potential to modulate structure as well as the properties of ILs.

In comparison to the solubility of CO_2 in pure ILs, the studies investigating absorption of CO_2 in the mixture of ILs are fewer. Baltus et al. [63] were the first to report Henry's constants of CO_2 in a mixture of $[C_8mim][NTf_2]$– 1-(3,3,4,4,5,5,6,6,7,7,8,8,8-tridecafluorooctyl)-3-methylimidazolium$[C_8F_{13}mim][NTf_2]$ at ambient conditions. The authors remarked that Henry's constant for the mixture could be calculated using weighted averages, but offered no explanation on the molecular-level processes that leads to the observed behavior. Lei et al. [64] measured the solubility of CO_2 in binary mixtures of $[C_2mim][BF_4]$–$[C_8mim][NTf_2]$ and $[C_4mim][BF_4]$–$[C_8mim][NTf_2]$ with varying proportions and high pressures up to 60 bar and showed physical absorption underscoring the cation and alkyl chain effect. Shiflett and Yokozeki [65] measured the solubility of CO_2 in an equimolar amount of $[C_2mim][OAC]$ and $[C_2mim]$ [TFA] at temperatures of 298.1, 323.1, and 348.1 K and pressures up to 20 bar, showing a combination of chemical and physical absorptions and underscoring the anion effect. The study by Pinto et al. [32–34] investigating CO_2 solubilities in binary IL mix-

tures of [C_2mim][$EtSO_4$]–[C_2mim][NTf_2], [C_4mim][$EtSO_4$]–[C_2mim][NTf_2], ethylpyridinium [C_2py][$EtSO_4$]–[C_2mim][NTf_2] at 298.2 K and 1.6 MPa demonstrated that the CO_2 solubilities in the IL mixtures were higher than those obtained from the linear mixing rule. The authors speculated that the positive excess molar volumes exhibited by these mixtures correspond to an increase in the free volume explaining CO_2 absorption capacity of the mixtures thus hinting at the synergistic effects of mixing two ILs on CO_2 solubility.

In general, in pure ILs, at the same temperature and pressure conditions, solubility of pure gases follows the order: SO_2 (H_2S) > CO_2 ≈ N_2O > C_2H_4 > C_2H_6 > CH_4 > Ar > O_2 > N_2 > CO > H_2. [18] It is really interesting to note that when a gas having higher solubility in ILs is mixed with a gas which possesses lower solubility in ILs, the gas with higher solubility enhances the other gas solubility while its own solubility is reduced. Many experimental studies support this idea. [66–68] For instance, mixed gas solubility of CO_2/H_2 in various ILs namely [C_2mim][NTf_2] [69], [C_4mim][PF_6] [70] and [C_4mim][BF_4] [71] have shown an increase in solubility selectivity of H_2. However, on the contrary, the computational study involving solubility of CO_2/O_2 and SO_2/N_2 in [C_6mim][NTf_2] by Shi and Maginn [72] do not support the argument and speculate that the observed solubility behavior can depend on the operating conditions.

Although the topic of capturing the mixture of CO_2 and CH_4 simultaneously with ILs is of great interest availability of relevant data is scarce especially in binary IL mixtures. Hert et al. [66] concluded that the presence of CO_2 improves the solubility of CH_4 in [C_6mim][NTf_2]. The computational investigation by Budhathoki et al. [73] found slight nonideal behavior of CO_2/CH_4 solubility selectivity and permselectivity in bulk [C_4mim][NTf_2] IL at 333 K; however, the authors suggested that mixed

gas properties can be safely estimated from pure gas data under ideal assumptions. On the other hand, the same authors in another study showed that the permselectivity of CO_2 over CH_4 could be enhanced by using confinement. [74] Noble and co-workers [75] measured the solubility of CO_2, CH_4, and N_2 gases in a mixture of $[C_2mim][BF_4]$–$[C_2mim][NTf_2]$ at 313.2 K. The authors reported that the CO_2/CH_4 and CO_2/N_2 solubility selectivity could be enhanced in $[C_2mim][BF_4]$ IL by using $[C_2mim][NTf_2]$–$[C_2mim][BF_4]$ mixture and that the IL mixture with $[BF_4]$:$[NTf_2]$ molar ratio of 90:10 and 95:5 possessed the highest CO_2/CH_4 and CO_2/N_2 solubility selectivity. The authors suggested that hydrogen bonding in $[C_2mim][BF_4]$ is disrupted by a small amount of $[NTf_2]^-$ enabling $[BF_4]^-$ to interact with CO_2. Further, Marrucho and co-workers [76, 77] showed that the combination of the IL $[C_2mim][NTf_2]$ with anions possessing different chemical nature in a supported IL membrane could be used to obtain an IL mixture with desired physicochemical properties and more importantly such mixtures are at least equal and sometimes more effective than the neat ILs for CO_2/CH_4 and CO_2/N_2 membrane-based separations.

The high carrying capacity of ILs for CO_2 is usually brought about by complexation with the gas. As upon absorption, the viscosity of the IL solution saturated with CO_2 increases dramatically and sometimes leads to the formation of solid products. However, IL mixtures have been designed that decrease the viscosity of the solution complexed with CO_2. [78–80]

All these results are encouraging and indicate attractive possibilities for applications of mixed IL systems in gas separation processes. However, fundamental molecular-level understanding for the observed phase behavior of substances in IL mixtures is, at present, not fully developed. The work presented in this dissertation attempts to fulfill this gap by providing a microscopic picture and identifying fundamental design

principles for enhancing CO_2 capture.

2.2 Self-Assembled Ionic Liquids

ILs containing long alkyl chains are spatially heterogeneous solvents that self-assemble. ILs are now the largest known class of self-assembly media for amphiphiles. [81] However, it is not possible to identify a general set of IL properties due to the structural diversity of the ions. Thus, understanding their structure is key to unraveling their complex behavior.

2.2.1 Structural Investigation

Self-assembled mesoscopic structures of ILs for which either cation or anion having long alkyl chains is responsible for inducing segregated polar-nonpolar domains have been known for more than a decade. The change in the alkyl chain length (an ion substituent) has shown to influence the mesoscale arrangement of polar and nonpolar moieties which can be rationalized by a delicate balance between the amphiphilic character of ions comprising the IL. The first suggestion of the mesoscopic scale IL structure was made by Schröder et al. based on substantial differences between diffusion of neutral and charged species. [82] Of particular interest was the variation of the alkyl chain length on either cation or anion on the morphological properties of ILs.

Considering alkyl chain on the cation, Seddon and co-workers obtained alkyl chain length dependent phase diagrams for the homologous series of 1-n-alkyl-3-methyl imidazolium $[C_n\text{mim}]^+$ cations in combination with the anions hexafluorophosphate $[PF_6]^-$, [83] and tetrafluoroborate $[BF_4]^-$. [84] Experimental investigation by Holbrey and Seddon [84] on $[C_n\text{mim}][BF_4]$ suggested that the ILs are characterized by three structure regimes: (1) short chains ($n < 3$) displaying crystalline behavior; (2) intermediate chains ($3 < n < 10$) with large liquid range and substantial structural

heterogeneity that tends to glassy state on cooling; and (3) large chains ($n > 10$) showing microphase separation of the polar and nonpolar regions. Subsequently, X-ray scattering experiments carried out by Triolo et al. on [$C_n$mim] Cl (n = 3, 4, 6, 8, and 10) and [$C_n$mim][BF_4] (n = 4, 6, and 8) confirmed the presence of nanoscale structural heterogeneity arising due to long alkyl chains in ILs. [85] There have since been a wealth of X-ray [86–94] and Neutron scattering experiments [95–100] confirming the formation of mesoscopic structures. Specifically, a range of different cations (imidazolium, [101–105] pyridinium, pyrrolidinium, [106, 107] piperidinium, triazolium, ammonium, [108, 109] phosphonium [110, 111]) and anions (halides, $[PF_6]^-$, $[BF_4]^-$, nitrate $[NO_3]^-$, chloroaluminate, $[HSO_4]^-$, trifluoromethanesulfonate $[TFS]^-$, thiocyanate $[SCN]^-$, $[NTf_2]^-$) have been examined.

Alternately, in the context of mesoscale structure in ILs with long alkyl chain present in the anion, imidazolium-based ILs with alkylsulfate and alkylsulfonate anions have attracted attention due to their high water solubility [112], low viscosity [113, 114], low melting point [115], low toxicity [112], and good thermal stability [115]. Experimental measurements [86, 112] have established that the IL series [C_2mim][C_nSO_4] (n = 2, 4, 6, 8) is heterogeneously distributed at nanoscale such that the length of the nonpolar domain increases with an increase in the alkyl chain length. Dávilla et al. [116] have also suggested that for a given cation the volume occupied by polar domains is diminished when a symmetric anion such as $[PF_6]^-$ is replaced with octylsulfate that is non-spherical and contains a long alkyl chain.

Molecular simulation studies have equally complemented the experimental studies, if not more. MD simulations on ILs based on the imidazolium, phosphonium, pyrrolidinium, ammonium have converged on the conclusion that the IL structural features are composed of a continuous polar network in which the positive and negative

charges alternate and nonpolar domains that punctuate the polar regions when the alkyl chain length is sufficiently long. The bulk phase structure exists as sponge-like nanostructure, which connect when the alkyl chain length on either the cation or anion is greater than or equal to six -CH2- units long. Below this critical length, the liquid structure is understood to be more homogeneous, but containing globular nonpolar domains. [117] Several of these studies have also demonstrated that the anions possessing heteroatoms have stronger aggregation features as compared to alkyl chain present on the cation. Wang and Voth [118–120] used a coarse-grained computational approach to explore the effect of alkyl chain length on $[C_n\text{mim}][NO_3]$ (n =1, 2, 3, 4, 6, 8). In order to gage the anion effect, Urahata and Ribeiro [121] simulated fluoride F^-, chloride Cl^-, bromide Br^- and $[PF_6]^-$ with the same cation, $[C_n\text{mim}]^+$ (n = 1, 2, 4, 8). Both the papers suggested self-assembled solvent nanostructure and revealed that charged groups (cation-head and anion) were distributed homogeneously in the bulk while alkyl chains were aggregated together heterogeneously. In fact, in the IL series of $[C_n\text{mim}][NO_3]$ Ji et al., using coarse-grained simulations, observed that it is possible to transform a spatially heterogeneous structure to liquid crystal-like bilayered smectic-A phase by increasing the alkyl chain beyond n > 14. [105] By computing the structure factors for the ILs $[C_n\text{mim}][PF_6]$ (n = 2, 4, 6, 8, 10, and 12) from MD simulations, Lopes and Pádua predicted the existence of such nano-segregated polar and nonpolar domains in ILs. Their results also indicated that the nonpolar domain length increases with an increase in the alkyl chain length, 2.1 Å for every -CH2- unit addition. [122] Simulations by Lopes and co-workers [108] showed that bicontinuous nanostructures can also be modulated by changing the cation geometry from imidazolium $[C_n\text{mim}]^+$ to trialkylmethylammonium $[N_{1,n,n,n}]^+$ or tetraalkylphosphonium $[P_{n,n,n,n}]^+$ keeping the anion $[NTf_2]^-$ same for all the systems.

In addition to the presence of a long alkyl chain on either the cation or anion, re-

searchers have attempted to understand the influence of introducing either multiple alkyl chains on imidazolium-based cations or considering mixtures of ILs. For example, Bernardes et al. [123] studied the aggregation behavior of 1,3-dialkylimdiazolum $[C_nC_m\text{im}][NTf_2]$ with $(2 < n < 10)$ and $(2 < m < n)$ homologous series. The authors concluded that the minimum number of carbon atoms (n or m) required in the alkyl chain for the formation of continuous nonpolar domains is six. By comparing the calculated structure factors with those obtained by Shimizu et al., [102] they reported that the pre-peak intensity is governed by the longer side chain when $n \neq m$. In a similar study, Shimizu et al. [103] carried out MD simulations of equimolar mixtures of $[C_n\text{mim}][PF_6]$ and $[C_m\text{mim}][PF_6]$ (with m/n = 3/9, 3/12, 6/9, 6/12) and concluded that nonpolar aggregates percolating the entire system are analogues of pure IL whose alkyl chain is average of the two IL chain lengths present in the IL constituting the mixture. Further, exploring the bulk-phase structure of binary IL mixtures of $[C_2\text{mim}][NTf_2]$-$[C_6\text{mim}][NTf_2]$ by Lopes and co-workers [55] and $[C_6\text{mim}][PF_6]$-$[C_{10}\text{mim}][PF_6]$ by Russina and Triolo [94] suggested dependence of nanostructure on the composition which originates from the difference in the nature and spatial extent of the interactions of heads and tails. Nonetheless, so far, these reports emphasize the influence of alkyl chain on either cation or anion on the mesoscopic structure of ILs.

On the other hand, information regarding the nanoscale heterogeneities resulting from the contributions coming from the presence of alkyl chain length on both the cation and anion simultaneously – bi-amphiphilic ILs – are just beginning to be probed. Usually, such ILs contain alkylsulfates, alkylsufonates and alkanoates groups. Blesic et al. [112,115] studied physicochemical properties of $[C_n\text{mim}]$ alkylsulfonate$[C_nSO_3]$ experimentally, and showed improved viscosity behavior in comparison to other ILs. Shimizu et al. [124] commented, based on preliminary simulation results constructed

on study of Blesic et al. [112, 115], that nonpolar domain morphology remains same irrespective of the source of side chain. Bi-amphiphilic ILs based on alkylsulfate groups are of interest because they can be synthesized in a low-cost halide free manner, [125] have high water solubility and in aqueous solution has the potential to behave like a surfactant, the micellar morphology of which is dependent on the relative hydrophobicity of anion and cation. Very recently, Amith et al. [126] focused on 1-octyl-3-methylimidazolium [C_8mim] octylsulfate [C_8SO_4] using MD simulations and compared its bulk phase structure with the structure at vacuum interface. The authors found that the non-restricted lamellar structure permeates the whole system when an external field, for example vacuum, is applied.

Due to a large number of published articles, these studies are only representative and have been highlighted to provide the breadth and depth of the investigations in the field. A detailed exposition of nanoscale segregation has been dealt with recently in comprehensive reviews by Hayes et al. [19] and Triolo and co-workers. [127] Taken together, the studies demonstrate that the "mixing" of the alkyl chains can lead to interesting nanoscale structure variations that can have a profound effect on the structural properties of these fluids. It is also clear that the studies investigating structuring of ILs when both ions, simultaneously, contributing to the nonpolar domain formation lag behind those performed on probing the influence of alkyl chain present on either of the ions. Our current understanding of these liquids does not provide straightforward speculation for this. This dissertation focuses on alkylsulfate-based ILs with the goal of fundamentally explaining the observed behavior of their self-assembly with detailed molecular simulations and theoretical analyses.

2.2.2 Phase Behavior

With the literature mentioned above, it has been established that long chain ILs possess highly articulated nano-segregated structures of varying polarity: polar and nonpolar. Due to the presence of these domains in a single liquid, ILs are sometimes referred to as "two-in-one" solvents [124] that are capable of dissolving polar, nonpolar and amphiphilic molecular solvents through their association with IL domains of matching polarity. This characteristic finds application in catalytic reactions. Considering biocatalytic reactions, it is well known that enzyme-catalyzed reactions require water molecules to function. In this context, ILs have been shown as an exceptionally suitable medium for such reactions; as amphiphilic nature of ILs allow them to absorb some of the water, while nonpolar region remains hydrophobic thus providing an essential degree of hydration required by the enzyme to remain active. [128] Owing to this amphiphilic nature ILs can provide a one-phase medium for species of varying polarity. For example, biocatalytic synthesis of biodiesel where $[C_{18}mim][NTf_2]$ is not only able to keep the lipase-enzyme active but also provides a one-phase medium dissolving methanol (polar) and triolein (nonpolar fatty acid) simultaneously. After the reaction is complete, the recovery of the IL solvent can be made by simple liquid-liquid extraction. This has shown to increase the reaction efficiency compared to other solvents that result in a two-phase reaction media (one for methanol and one for triolein) leading to a biphasic reaction medium. [129] ILs have also been suggested as extracting agents for aromatics from alkanes, due to their poor alkane solubility. [130–132] However, the usage is sometimes limited by the structural morphology of the IL. Thus, various attempts have been increasingly made to modulate or fine-tune the morphology for the desired application. Unlike gaseous solute, the liquid molecular solvents can have a profound impact on the morphology of the ILs, as explained below.

Alcohols are a class of molecular solvents that are capable of modifying IL prop-

erties. Owing to their amphiphilic nature and ability to act as both hydrogen bond donor and acceptor, alcohols are expected to modify the molecular behavior in ILs in both the domains. For example, an increase in the alkyl chain on imidazolium-based ILs leads to lowering of the upper critical solution temperature for a given alcohol [133,134], which is exactly opposite of the solubility trend for water. [135,136] The topic dealing with the effect of alcohols on the nanostructure of the ILs has been pursued by many researchers, albeit to a less extent. Results from molecular simulations have suggested accumulation of -OH group of alcohols in the polar region of $[C_n\text{mim}]\text{Cl}$ (n = 2, 4, and 6), while the alkyl chain is incorporated in the nonpolar domain. [137, 138] In a concentration-dependent MD study involving $[C_4\text{mim}][BF_4]$ and its mixtures with water, methanol, and ethanol, the authors observed that the structural transitions were qualitatively similar. However, clusters of water molecules are formed at low water concentrations while alcohol molecules were homogeneously distributed. [139] A number of experimental studies have been undertaken to elucidate structural modification (or lack thereof) when alcohols are dissolved in protic ILs. [140, 141]

Mixtures of IL with water find applications in protein crystallization, supercapacitors, and reaction media, [142] as the presence of water in ILs affects many of their properties such as polarity, solvating ability, conductivity, viscosity. However, the impact of water on ILs is dependent on the constituting ions. In this context, IL-water mixtures have been investigated both experimentally [143–148] and using molecular simulation techniques. [149–153] A comprehensive review of computational work dealing with IL-water mixtures is provided by Klein and co-workers. [154] These studies have demonstrated the mesoscopic structure inherent to ILs is preserved at low concentrations of water, and water preferentially interacts with the anion [155–157] and sometimes with the cation. [158] At intermediate concentrations, the continuous

polar network of IL begins to collapse with the appearance of isolated clusters of ILs. [159] At very high concentrations of water, formation of micelles, [160] isolated and dissociated ions pairs may be observed. [161] Recently, it was demonstrated that the temperature can disrupt the IL-water interactions to a greater extent than the water-water interactions in IL mixtures containing low and high water concentrations, respectively. [162] Water-induced structural transitions can have a profound impact on the transport properties such as viscosity and ionic conductivity of the IL-water mixtures providing another avenue for tailoring the properties of ILs. [163–166]

Multiple reports have also focused on the aggregation behavior of bi-amphiphilic ILs in an aqueous medium and have endorsed their application in the field of drug delivery and synthesis of nanoparticles. Mahajan and co-workers have studied the concentration dependence of interaction and morphological aspects in the mixture of chlorpromazine hydrochloride drug with $[C_n\text{mim}][C_8SO_4]$ (n = 4, 6) at neutral pH. [167] The same authors also studied dimerization and solubilization of methylene blue dye in the same ILs. [168] Kumar and co-workers have studied structural changes and stability of cellulose and bovine serum albumin in aqueous solutions of $[C_8\text{mim}][C_{12}SO_4]$. [169,170] Rao et al. [171] have studied synthesis of gold nanoparticles in aqueous solutions of $[C_n\text{mim}][C_mSO_4]$ (n = 4, 6, 8 and m = 8, 12). Triton-100 – a nonionic surfactant commonly used for biological application or household products such as paints and paper – have been extensively examined in aqueous solutions of bi-amphiphilic ILs. A particular study by Thakkar et al. [172] has systematically investigated its interaction with aqueous solutions of $[C_n\text{mim}][C_8SO_4]$ (n = 4, 6, 8, 10) and showed that morphology changes from ellipsoidal micelles to a vesicular structure. Although a myriad of studies has focused on aqueous solutions of such bi-amphiphilic ILs, there is still lack of studies discussing the fundamental reasons behind the observed behavior. Moreover, the information on the bulk phase behavior

of such ILs is also very primitive. Thus, the work in this dissertation focuses on the bulk-phase behavior of several bi-amphiphilic ILs, $[C_n\text{mim}][C_8SO_4]$ (n = 2, 4, 6, 8, 10, 12), and the influence another amphiphilic IL and high concentrations of water have on the aggregation behavior of $[C_{12}\text{mim}][C_8SO_4]$ IL.

CHAPTER 3

THEORY AND METHODOLOGY

This chapter introduces the general theory and methodology for conducting computer simulations and calculating the desired structural and thermophysical properties. The chapter is organized as follows. First, the concepts of statistical thermodynamics are discussed which includes various types of ensembles and the theory regarding its connection with macroscopic properties. Second, a comparison of the different types of force field models available for ILs is made, including the justification for the choice of models used in this work. Third, the importance of both molecular dynamics (MD) and Monte Carlo (MC) simulation techniques are discussed, based on the desirable property of interest, such as the theory and relevant derivations involved in conducting such simulations. A review of existing methods to compute the excess chemical potential via MD simulations is also included. This chapter also touches upon the calculation of several important thermodynamic, structural and transport properties that can be obtained using MD and gas solubility properties using MC methods. Further, a general layout of the simulation protocol is laid out.

3.1 Statistical Thermodynamics: Link between Macroscopic and Microscopic

The re-interpretation of second law of thermodynamics in terms of molecular probability provides the link between classical thermodynamics and statistical mechanics. Ludwig Boltzmann, also known as the father of statistical mechanics, stated that entropy is proportional to logarithm of the number of quantum states. This allows us

to represent a macroscopic system, statistically, by building an ensemble of different configurations with certain constraints such as temperature, volume, and pressure imposed on the system. Though the microscopic quantities for a specific configuration differ, the ensemble average will remain the same giving the macroscopic picture. The objective is to determine the distribution of energy, E, over N identical systems. In other words, the formal definition of entropy by Boltzmann:

$$\mathrm{S} = k_B \times \ln(\mathrm{W}) = k_B \times \ln(\Omega_{NVE}) \tag{3.1}$$

provides a link between microscopic properties in micro-canonical ensemble (NVE) ensemble, an isolated or ideal system; and thermodynamics, where S is the entropy, k_B is the Boltzmann's constant and Ω_{NVE} is the micro-canonical partition function or the density of states (W) representing the multiplicity or the total number of states found in NVE ensemble. The partition function describes the statistical properties of the system in thermal equilibrium. Thermodynamic quantities associated with the system can be expressed in terms of partition functions and its derivatives.

Based on the property of interest, different ensembles can be constructed which depends on the constraints imposed. Common ensembles are (i) micro-canonical ensemble (NVE) where the acronyms represents that number of particles, volume, and energy of the system is kept constant, thus representing an isolated system; (ii) canonical ensemble (NVT) - used for analyzing properties such as energy and pressure of the system; (iii) isothermal-isobaric ensemble (NPT) - used to obtain density/volume, energy, enthalpy of the system; (iv) grand-canonical ensemble (μVT) - used to get pressure vs. number of particles correlation which holds importance in obtaining adsorption isotherms; (v) Gibbs ensemble - to calculate solubility properties and phase equilibria.

Now, average energy E can be defined as $E = \sum \rho_i E_i$; where ρ_i is the probability density distribution and E_i can be expressed in terms of partition functions. Thus, from eq. 3.1 it is clear that our goal is to obtain the probability distribution and partition functions for a given ensemble. In an actual experimental setup, measurable quantities are temperature, pressure, volume. Hence, ensembles such as NVT, NPT are commonly used to represent the system. It can be easily shown that partition function for NVT ensemble is:

$$Q(N,V,T) = \int \exp\left[-\frac{E}{k_B T}\right] \Omega_{NVE} dE = \frac{1}{N!\, h^{3N}} \int \exp\left[-\frac{E(p^N, q^N)}{k_B T}\right] dp^N dq^N \tag{3.2}$$

sum over all states partitioned by energy levels, where h is the Planck's constant, p^N and q^N denotes the momentum and position vectors for the particles in the system, and k_B is the Boltzmann's constant. This equation can be further broken down to show that:

$$Q(N,V,T) = \frac{q^N}{N!\, \Lambda^{3N}} \int \exp\left[-\frac{E(r^N)}{k_B T}\right] dr^N \tag{3.3}$$

where Λ is the thermal de Broglie wavelength of the molecules given by $\sqrt{\frac{h^2}{2\pi m k_B T}}$, computed by integrating over the momentum of the system, q accounts for internal degrees of freedom such as vibrations, nuclear spins, and rotations, E is the configurational energy. From the knowledge of partition function, thermodynamic quantities such as internal energy, Helmholtz energy, and pressure (using Maxwell's transformation) can be computed as:

$$E = k_B T^2 \left(\frac{\partial ln[Q(N,V,T)]}{\partial T}\right)_{V,N} \tag{3.4}$$

$$A = -k_B T ln[Q(N,V,T)] \tag{3.5}$$

$$P = k_B T \left(\frac{\partial ln[Q(N,V,T)]}{\partial V}\right)_{T,N} \tag{3.6}$$

Similarly, for NPT ensemble that constraints temperature and pressure of the system – most suitable for an experiment – it can be shown that the partition function is given by:

$$\Delta(N,P,T) = \frac{q^N P}{N!\,\Lambda^{3N} k_B T} \int \exp\left[-\frac{PV}{k_B T}\right] dV \int \exp\left[-\frac{E(r^N)}{k_B T}\right] dr^N \tag{3.7}$$

which is related to the Gibbs free energy, G, by:

$$G = -k_B T ln[\Delta(N,P,T)] \tag{3.8}$$

3.2 Force Field Models

As shown above, the total energy of the system can be partitioned into the contributions based on position and momentum giving potential and kinetic energy terms. The kinetic energy term is reasonably straightforward, as it depends on momenta and can be computed as $\sum \frac{p^2}{2m}$. However, calculation of potential energy is involved. Although quantum mechanics offers the most accurate description of calculating potential energy based on electronic description; using Born-Oppenheimer's approximation, quantum mechanical interactions can be approximated as bonded and non-bonded energy interactions, thus, providing semi-empirical potentials also known as classical force fields that are computationally less time-consuming.

The intermolecular interactions are represented via dispersion-repulsion interaction in the form of standard Lennard-Jones (LJ) 12-6 potential and the electrostatic interaction calculated from the Coulombic terms, while the intramolecular energy function includes bond stretching, angle bending, and torsions (both proper and improper).

In general, the potential energy model has the following functional form:

$$
\begin{aligned}
E_{tot} &= \sum_{ij}^{\text{bonds}} \frac{k_{r,ij}}{2}(r_{ij} - r_{0,ij})^2 + \sum_{ijk}^{\text{angles}} \frac{k_{\theta,ijk}}{2}(\theta_{ijk} - \theta_{0,ijk})^2 \\
&+ \sum_{ijkl}^{\text{torsions}} \sum_{m=1}^{4} \frac{k_{m,ijkl}}{2}[1 + (-1)^{m+1}\cos(m\phi_{ijkl})] + \\
&+ \sum_{ij}^{\text{nonbonded}} \left\{ 4\epsilon_{ij} \left[\left(\frac{\sigma_{ij}}{r_{ij}}\right)^{12} - \left(\frac{\sigma_{ij}}{r_{ij}}\right)^{6} \right] + \left(\frac{q_i q_j}{r_{ij}}\right) \right\}
\end{aligned}
\tag{3.9}
$$

where $k_{r,ij}$, $k_{\theta,ijk}$, $k_{m,ijkl}$ are the respective force constants, ϵ and σ indicate the LJ energy and size parameters, and q denotes partial charges.

The predictive capability of classical molecular simulation-based methods critically depends on an accurate description of intramolecular and intermolecular interactions in ILs. Towards this end, much effort has been expended to parametrize various classical non-polarizable force field models for estimating thermophysical properties. Notable examples of all-atom force fields for imidazolium-based ILs include those published by Canongia Lopes and Pádua [173–176], Acevedo and co-workers [177–179], Ludwig and co-workers [180, 181] and Maginn and co-workers [182–186]; while Zhiping Liu [187–189] has developed force fields with an united-atom description. The first generation of IL force fields was derived by placing integer charges on the IL ions. Transport properties of ILs obtained with these force fields were found to be lower than the corresponding experimental measurements. In order to remedy this situation, the application of scaled charge models has received increasing attention as a way to account for the polarization in ILs. Adoption of this approach has been demonstrated to considerably improve the agreement between simulation and experimental results for transport properties. For in-depth comparisons, the interested reader is referred to a comprehensive review by Holm and co-workers [190] where various types of force field models are compared that can be used for studying structure

and dynamics of ILs.

In this dissertation, majorly two force field models are used to represent the imidazolium-based ILs, (i) an united-atom force field proposed by Zhiping Liu et al. [188,189]; and (ii) an all-atom model developed by Canongia Lopes-Pádua [175, 176] (CL&P).

In the sections 4.1, 4.2, 4.3, and 4.4 of chapter 4 that discusses thermophysical properties, phase equilibria properties, and their rationalization based on structural properties, the ILs and their mixtures are described by the united-atom force field proposed by Zhiping Liu et al. [188, 189] In this force field, the hydrogens in the imidazolium cation are explicitly modeled while methyl (CH3), methylene (CH2) and trifluoromethyl group (CF3) group are subsumed in the carbon site to which they are bonded, thus, giving an united-atom description whereas the atoms N, S, and O are treated explicitly. The LJ unlike interactions are computed by the Lorentz-Berthelot combining rule such that $\sigma_{ij} = \frac{\sigma_{ii}+\sigma_{jj}}{2}$ and $\epsilon_{ij} = \sqrt{\epsilon_{ii}\epsilon_{jj}}$. The nonbonded interactions for the atoms connected by bonds and angles were excluded while the LJ and electrostatic interactions between the pair of atoms separated by three bonds, the 1-4 nonbonded interactions, are reduced by a factor of 2. The total charge on the cation and anion is ± 0.8, that counters the polarization effect and provides a better estimate of the dynamic properties.

On the other hand, section 4.5 of chapter 4, that discusses *a priori* design of IL mixtures, and chapter 5 that explores self-assembled ILs uses an all-atom classical force field model developed by Canongia Lopes-Pádua (CL&P) [175, 176] to study their micro-structures. This is a well-parameterized and transferable force field model that encompasses homologous series of imidazolium-based cations with arbitrary chain lengths and multiple anions and has been used for over a decade. In this model,

all the atoms are modeled explicitly. In comparison to the Zhiping Liu united atom model, the unlike LJ interactions are computed by the geometric-mean combining rule for both the parameters and the total charge on the cation and anion is ± 1. However, as shown in chapter 4 section 4.5 the structural property trends obtained using any of the two force field models are qualitatively similar. Hence, any of the force field can be equally used to model the physical behavior of the ILs and their mixtures studied in this work.

Additionally, SPC/E [191–193] model was used for water (H_2O) molecules. Parameters for methane (CH_4) were taken from TraPPE [194] while that of carbon dioxide (CO_2) molecules were taken from the works of Shi and Maginn, [195] that is parameterized based on TraPPE force field but includes flexible bonds and angles. All the relevant force field (itp) files can be downloaded from "git clone https://github.com/utk-arsk/Ionic-Liquid.git".

3.3 Molecular Dynamics (MD) Simulations

In molecular dynamics (MD) technique, the natural course of the trajectory of the system, i.e., change in positions and momentum with respect to time, is described by Newton's equations of motion. The equations are given by:

$$F_i = m_i \frac{d^2 r_i}{dt^2} = \frac{1}{m_i} \frac{dp_i}{dt} = -\frac{dE_i}{dr_i} = -\nabla_i [E(r^N)] \tag{3.10}$$

where F_i, p_i, r_i are the force, momentum and position vectors, E is the total energy computed from the definition of the force field model, and m_i is the mass for atom i. First, the initial positions and velocities are defined for the system, and then, these equations of motion are integrated in time to get a new configuration describing the trajectory. One way to accurately update the positions and the velocities is to use

the Verlet-Algorithm. [196] The most time-consuming and expensive step of molecular simulations is the determination of forces, which is calculated by taking the gradient of the energy. That force is then used to compute the accelerations and hence, the positions and velocities by extension.

The equations mentioned above reproduce the NVE ensemble correctly while the ensembles of interest such as NVT and NPT requires some additional implementations to these equations. For NPT, a thermal reservoir and an isobaric controller introduces an external degree of freedom but provide a means for controlling temperature and pressure controls. The Nosé-Hoover thermostat and Parrinello-Rahman barostat are commonly used to control the temperatures and pressures and reproduce NPT ensemble accurately. MD technique offers a trajectory that naturally holds information on the dynamics of the system. This allows the analysis of time-dependent quantities and processes such as transport properties, self-diffusion coefficients and ionic conductivities, that are of great value. At this point, it is worth mentioning that the dynamics of some IL systems are very slow and may require very large simulation timescales, thus, dramatically increasing the computational cost.

Nosé-Hoover Temperature Coupling: The Nosé-Hoover equations of motion are a common way to induce isothermal control. This extended-ensemble approach enables correct reproducibility of NVT simulations by using a chain of thermostats. The need for this additional control rises from the proportional variation of the thermostat momentum with respect to the difference between the instantaneous and set-point kinetic energies. For a particular chain, the Hamiltonian of the system is modified by introducing a thermal reservoir and a friction term that modifies the equations of motion, shown in eq. 3.10, as

$$\frac{d^2 r_i}{dt^2} = \frac{F_i}{m_i} - \frac{p_\xi}{Q}\frac{dr_i}{dt} \tag{3.11}$$

where

$$\frac{dp_\xi}{dt} = (T - T_0) \tag{3.12}$$

suggesting that the force due to friction is proportional to the product of the particle's velocity and the friction parameter. p_ξ is the momentum associated with the friction parameter and Q is the mass parameter of the reservoir given by

$$Q = \frac{\tau_T^2 T_0}{4\pi^2} \tag{3.13}$$

where τ_T and T_0 is supplied as inputs to the simulation. It is interesting to note that the for these Nosé-Hoover equations of motion, total energy is not conserved but rather the Hamiltonian of the system represented as:

$$H = \sum_{i=1}^{N} \frac{p_i}{2m_i} + U(r_1, r_2, \ldots, r_N) + \frac{p_\xi^2}{2Q} + N_f kT\xi \tag{3.14}$$

is conserved where N_f is the total number of degrees of freedom.

Parrinello-Rahman Pressure Coupling: Similar to Nosé-Hoover temperature coupling, the Parrinello-Rahman pressure coupling gives the true NPT ensemble. In addition to Nosé-Hoover modification, Parrinello-Rahman barostat also modifies the equations of motions such that

$$\frac{d^2 r_i}{dt^2} = \frac{F_i}{m_i} - M\frac{dr_i}{dt} \tag{3.15}$$

where M is given by

$$M = \frac{1}{bb'}\left[b\frac{db'}{dt} + b'\frac{db}{dt}\right] \tag{3.16}$$

and b is given by

$$\frac{d^2 b}{dt^2} = \frac{V}{Wb'}(P - P_{ref}) \tag{3.17}$$

V, W, P and P_{ref} are volume of the box, a parameter defining strength of coupling, current pressure and reference pressures, respectively. W is computed by

$$W_{ij} = \frac{3\tau_P^2 L}{4\pi^2 \beta_{ij}} \tag{3.18}$$

where τ_P and β_{ij}, the isothermal compressibility, are supplied as inputs to the simulation.

Please note that both Nosé-Hoover and Parrinello-Rahman approaches produce highly oscillatory relaxation. Thus it is recommended to use weak coupling schemes such as Berendsen to reach the target temperature and pressure, first, and then switch to Nosé-Hoover and Parrinello-Rahman coupling once the system is in equilibrium. Otherwise, due to large oscillations, it will either take a long time to equilibrate, or the simulation may crash.

3.3.1 Simulation Protocols

In this subsection, a complete set of simulation details are described; which can be followed, in general, to reproduce the results of the work reported in this dissertation. Two sets of protocols are reported below as binary IL mixtures, whose structures emerge at short – supramolecular – scale and does not require long time scale simulations as in the case of long-chain ILs whose self-assembled structures evolve at the mesoscopic scale.

Binary Ionic Liquid Mixtures

MD simulations for all the binary IL mixture systems were carried out at a temperature and pressure of 353 K and 1 bar using GROMACS package. [196, 197]. Please note that different versions of GROMACS can give slightly different results, as will be shown in chapter 5. The work presented here used 4.5.5, 5.0.4 and 5.1.5 versions.

Simulations for a total of five intermediate molar ratios (10:90, 25:75, 50:50, 75:25 and 90:10) obtained by varying the concentrations of the respective anions along with pure IL systems were performed. In general, simulations were conducted in a cubic box containing 256 ion pairs for both pure and binary mixture systems, except for 10:90 and 90:10 compositions that had 250 ion pairs, with periodic boundary conditions enforced in three dimensions. The equations of motion were integrated using leapfrog – GROMACS default – integrator that produces trajectories identical to Verlet algorithm.

All the simulations were performed in two steps. First, random initial configurations were generated using PACKMOL [198]. These initial configurations were then subjected to a steepest descent minimization followed by a 2 ns annealing scheme, where the temperature was iteratively raised from 353 K to 553 K linearly in 200 ps followed by canonical (NVT) ensemble equilibration at 553 K for 100 ps and then brought down linearly to the desired temperature of 353 K in the next 200 ps. Each IL system was then simulated in canonical (NVT) ensemble for a duration of 10 ns, followed by isothermal-isobaric (NPT) equilibration run of 20 ns. In the second step, the last configuration obtained from the NPT equilibration run was used as an initial configuration. This configuration was subjected to the same annealing scheme followed by 10 ns of NVT, and 25 ns of NPT equilibration and subsequent NPT production run of 40 ns. The trajectories obtained from the last 20 ns of the production run was used for computing the thermophysical and structural property analyses. In the production run, Nosé-Hoover thermostat with a coupling constant of 0.4 ps and Parrinello-Rahman barostat with 2.0 ps coupling time constant were used to maintain the temperature and pressure. Particle Mesh Ewald (PME) method was used to handle electrostatic interactions while appropriate tail corrections were applied for non-bonded LJ interactions, each with a potential cutoff of 12 Å for Zhiping Liu and

16 Å for CL&P force field. All the simulations were performed with a time step of 2 fs since all the fast vibrating modes comprising hydrogen atoms were constraint; coordinates were saved every 0.4 ps. All the relevant mdp and topology files, to run these calculations, can be downloaded from "git clone https://github.com/utkarsk/Ionic-Liquid.git".

Self-Assembled Ionic Liquids

Bulk Phase: MD simulations for ILs, containing long alkyl chains, that tend to self-assemble were carried out at a temperature of 400 K and pressure of 1 bar using GROMACS package. [196, 197] Again, please note that different versions of GROMACS can give slightly different results, as will be shown in chapter 5. The work presented here used 4.5.5 and 2018 versions. All the molecules were modeled using CL&P force field, and the equations of motion were integrated using leapfrog integrator. Simulations were conducted in a cubic box containing 1000 ion pairs with periodic boundary conditions enforced in three dimensions. The temperature was controlled using Nosé-Hoover thermostat with a coupling constant of 0.4 ps while the pressure was maintained with Parrinello-Rahman barostat for which the coupling time constant was set to 2.0 ps. Appropriate tail corrections were applied for the non-bonded Lennard-Jones interactions while electrostatic interactions were handled using the PME method, each with a potential cutoff of 16 Å. The simulations were performed with a time step of 2 fs since all the fast vibrating modes comprising hydrogen atoms were constraint; coordinates were saved every 1 ps.

Each simulation was performed in four stages. First, low density initial configurations were generated using PACKMOL [198]. These initial configurations were then subjected to steepest descent minimization to remove high energy contacts followed by a 2 ns annealing scheme, where the temperature of the system was iteratively raised

to a temperature 200 K above the desired temperature before bringing it back to the target temperature, linearly at the rate of 1 K/ps. Additional relaxation of the system was achieved by simulating the systems in the NVT ensemble for 10 ns, followed by a isothermal-isobaric (NPT) equilibration run of 20 ns. This cycle was repeated two more times. In the final cycle, the system was subjected to a 10 ns annealing scheme followed by NVT and NPT ensemble equilibration runs of 20 ns and 0.1 μs, respectively. After this, 0.5 μs of NPT ensemble production run was conducted. The trajectories obtained from the final 40-50 ns were used for the structural analysis.

In order to avoid any confusion, please note that the simulation timescales mentioned here are slightly different from the timescales published elsewhere. [199, 200] Although the simulations were extended for longer timescales, the conclusions drawn remain unchanged. The timescales were extended only as a sanity check, to make sure that the IL system was not stuck in any metastable state.

Furthermore, as will be demonstrated in chapter 5 some ILs tend to assemble in a layer-like fashion. One might argue that semi-isotropic pressure coupling should be used, as done in the case of lipid-bilayers. Thus, additionally, some simulations were conducted with semi-isotropic pressure coupling, and results (not shown here) showed that semi-isotropic pressure coupling does not have a significant effect on the structural properties of ILs studied in this work. This is probably because all the simulations were started with random configurations and the layer-like structure was not an inherent part of the initial structure as is in the case of lipid-bilayers.

Binary Mixtures: MD simulations for the mixtures of $[C_{12}mim][C_8SO_4]_x[MeSO_4]_{1-x}$ and $[C_{12}mim]_x[C_1mim]_{1-x}[C_8SO_4]$ IL mixtures were carried out at a temperature of 400 K and pressure of 1 bar. Simulations for a total of five intermediate molar ratios (10:90, 25:75, 50:50, 75:25 and 90:10) obtained by varying the concentrations of the

respective anions along with pure IL systems were performed. In general, simulations were conducted in a cubic box containing 1000 ion pairs for both pure and binary mixture systems. The simulation were equilibrated using the same protocols reported for bulk phase.

Aqueous Media: MD simulations for $[C_{12}mim][C_8SO_4]$ IL at high concentrations of water were carried out at a temperature of 298 K and pressure of 1 bar using GROMACS 2018 package. [196, 197] The IL molecules were modeled using CL&P force field, while the SPC/E model was used for water and the equations of motion were integrated using leapfrog integrator. Simulations were conducted in a cubic box containing a fixed number of water molecules and varying number of IL molecules with periodic boundary conditions enforced in three dimensions. The number of water molecules was fixed at 6250, while the number of IL molecules were varied as 32, 63, 125, 250, 521, and 1042 to get x_{water} (mole fraction of water) of 0.995, 0.99, 0.98, 0.962, 0.923, 0.857. The temperature was controlled using Nosé-Hoover thermostat with a coupling constant of 0.4 ps while the pressure was maintained with Parrinello-Rahman barostat for which the coupling time constant was set to 2.0 ps. Appropriate tail corrections were applied for the non-bonded Lennard-Jones interactions while electrostatic interactions were handled using the PME method, each with a potential cutoff of 16 Å. The simulations were performed with a time step of 1 fs; coordinates were saved every 1 ps.

Each simulation was performed in four stages. First, low density initial configurations were generated using PACKMOL [198]. These initial configurations were then subjected to steepest descent minimization to remove high energy contacts followed by a 2 ns annealing scheme, where the temperature of the system was iteratively raised to a temperature of 498 K and brought back to the target temperature, linearly at the rate of 1 K/ps. Additional relaxation of the system was achieved by simulating

the systems in the NVT ensemble for 10 ns, followed by a isothermal-isobaric (NPT) equilibration run of 20 ns. This cycle was repeated two more times. In the final cycle, the system was subjected to a 2 ns annealing scheme followed by NVT and NPT ensemble equilibration runs of 20 ns and 0.1 μs, respectively. After this, 0.5 μs of NPT ensemble production run was conducted. The trajectories obtained from the final 50 ns were used for the structural analysis.

3.3.2 Henry's Constants Calculation Using MD Simulations

The Henry's constants, $k_{H_{1,2}}$, of a solute in solvent, is defined by

$$k_{H_{1,2}} = \lim_{x_1 \to 0} \frac{f_1}{x_1} \tag{3.19}$$

where f_1 is the fugacity and x_1 is the mole fraction of solute (species 1). The fugacity is related to the excess chemical potential by

$$\mu_1^{ex} = \mu_1(\rho, T) - \mu_1^0(\rho, T) = k_B T ln \frac{f_1}{f_1^0} \tag{3.20}$$

where $\mu_1^0(\rho, T)$ is the ideal gas chemical potential, at a density of ρ taken as a reference. Further, ideal gas fugacity is nothing but pressure given by $\frac{RT}{V}$ where V is the volume of the liquid (V_2). With this eq. 3.20 can be written as

$$\mu_1^{ex} = k_B T ln \left(\frac{x_1 k_{H_{1,2}} V_2}{RT} \right) \tag{3.21}$$

Now, $x_1 = \frac{N_1}{N_1 + N_2}$ (mole fraction). As, Henry's law regime applies in the infinite dilution limit of the solute, it can be safely assumed that $N_1 = 1$ and $N_1 \ll N_2$. Thus, under these conditions, $x_1 V_2$ can be approximated as $\frac{V}{N_2}$ or $\frac{1}{\rho_2}$. With this simplification, the Henry's constants, $k_{H_{1,2}}$, of a solute in solvent, can be computed

using the following relationship:

$$k_{H_{1,2}} = \rho RT \exp\left(\frac{\mu^{ex}}{k_B T}\right) \tag{3.22}$$

where ρ is the molar density of the solvent without the solute dissolved in it, R denotes the gas constant, k_B and T represent Boltzmann constant and temperature respectively, and μ^{ex} is the residual or excess chemical potential: the difference between actual and ideal gas chemical potential. Furthermore, at infinite dilution limit of the solute in solvent, μ^{ex} of solute corresponds to the change in free energy. Thus, determination of the chemical potential using a computer simulation can be considered a special case of computing free energy difference between the two states of the system that differ in the presence of a single molecule.

Methods for Computing Excess Chemical Potential

There are a lot of different methods that can be used to compute the chemical potential in a computer simulation. Free energy difference methods can generally be classified as either equilibrium-based or non-equilibrium based approaches. Equilibrium approaches include thermodynamic integration, [201, 202] Bennett analysis, [203–206] multistage free energy perturbation that contains methods such as umbrella sampling, staged insertions or deletions, [207–209] weighted histogram analysis method (WHAM). [210, 211] All these approaches rely entirely on sampled equilibrium simulations evaluated at discrete stages. Non-equilibrium approaches include methods developed by Jarzynski. [212–214] As all the simulations in this work are equilibrium simulations, a small introduction to equilibrium methodology comparing all the methods is included in the following paragraphs while non-equilibrium methods are beyond the scope of this dissertation. However, importantly, one should note that non-equilibrium methods have the potential to provide free energy difference estimate rapidly but can suffer from significant bias. Other methods, based on Monte Carlo

technique are expanded ensemble method and Widom test-particle insertion method.

We are interested in evaluating free energy difference between two states; one without solute molecule and one with the complete insertion of a single solute molecule in the solvent. As described above, one can write the change in free energy in terms of partition functions of each state. However, the overlap between the two states may be poor, and thus, we devise a thermodynamic path that connects the two states. For this, the interaction of the solute with solvent is coupled linearly using a variable λ, with λ varying from 0 to 1. $\lambda = 0$ refers to ideal gas state while λ=1 defines the fully coupled state.

Equilibrium free energy methods share a commonality of generating equilibrium ensembles at multiple values of the scaling parameter λ. Separate equilibrium simulations at successive values of λ are performed, and then the values of the free energy differences can be estimated by different methods, as shown below. Please note that different methods may yield a different estimate, however, for an adequate amount of λ parameters any method should be able to provide a good estimate. The choice of λ spacing can be much trickier. Reducing the λ spacing points in regions where the slope of the free energy landscape, change in the state of the system defined by the Hamiltonian with respect to λ - $\left(\frac{\partial H}{\partial \lambda}\right)$, is steep is sometimes necessary.

Free energy Perturbation (FEP): In the FEP approach, one performs independent simulations at each λ, then uses exponential averaging to determine the free energy difference between neighboring λ values. [208] These differences are then summed to obtain the total free energy difference. ΔG can be approximated for a path containing n λ-values, including λ=0 and λ=1, using either the forward FEP or

reverse FEP as shown in eqs. 3.23 and 3.24

$$\Delta G = -k_B T \sum_{i=0}^{n-1} ln \left\langle \exp\left[-\frac{E_{\lambda_{i+1}}(x_i) - E_{\lambda_i}(x_i)}{k_B T} \right] \right\rangle_{\lambda_i} \tag{3.23}$$

$$\Delta G = -k_B T \sum_{i=0}^{n-1} ln \left\langle \exp\left[-\frac{E_{\lambda_i}(x_{i+1}) - E_{\lambda_{i+1}}(x_{i+1})}{k_B T} \right] \right\rangle_{\lambda_{i+1}} \tag{3.24}$$

where x is the full set of configurational coordinates. Although, this is is fairly straightforward and provides an exact solution, nowadays this method is not recommended as it has a very poor efficiency. It does not converge quickly and the spacing between λ values may not be small enough to provide sufficient overlap between the configurations spaces corresponding to λ_i or λ_{i+1}.

Thermodynamic Integration (TI): It is probably one of the most common methods for calculating free energy differences, and the easiest to understand. In order to calculate the free energy difference between the two end states I and II, TI makes use of multiple intermediate states as defined by a coupling parameter λ. The state of the system at a given λ is given by the Hamiltonian obtained by combining the Hamiltonians of the end states, H_I and H_{II}. In the simplest form, a linear relationship looks like $H(\lambda) = \lambda\ H_{II} + (1\text{-}\lambda)\ H_I$. The free energy change is then obtained using eq. 3.25:

$$\Delta G = \int_0^1 \left\langle \frac{\partial H(\lambda)}{\partial \lambda} \right\rangle_\lambda d\lambda \tag{3.25}$$

where $\langle \ldots \rangle_\lambda$ indicates ensemble average. Typically, simulations are conducted at discrete λ values, as continuous values of λ (also known as slow-growth method) may suffer from the continuous shift of λ that hinders the system to reach equilibrium and the integral in eq. 3.25 is approximated by numerical integration methods. Most commonly, the simple trapezoidal rule is used. There are, however, many other numerical methods available such as Simpson's rule, [215] cubic spline integration, [216] and Gauss-Legendre method. [215] But, it should be noted that different method may give

different results. Additionally, along with the possibility of inadequate equilibrium sampling at each λ, an error may arise in TI from the fact that only a finite number of values are simulated, and the integral is approximated by a sum. Although TI may be limited by the computational expensiveness due to the requirement of considerable number of λ sampling points, it can provide very accurate free energy estimates. Please note that GROMACS does not offer direct computation of the total free energy change using TI. However, the analysis can be done either using external tools such as "pymbar" script, that can be downloaded from https://SimTK.org/home/pymbar, can compute the required integral directly from the GROMACS dhdl.xvg output file.

Bennett Acceptance Ratio Method (BAR): An alternative approach that works on the same principle for the calculation of free energy differences is the BAR method, proposed by Bennett. [204] Although the original the BAR method might appear different, it is possible to use the same Bennett's method to combine the information normally used for forward and reverse FEPs. In this approach, the free energy difference, δG_i, between successive λ values are computed according to the eq. 3.26

$$\left\langle \left(1+\exp\left[\frac{E_{\lambda_{i+1}}(x_i)-E_{\lambda_i}(x_i)-\delta G_i}{k_BT}\right]\right)^{-1}\right\rangle_{\lambda_i} = \left\langle \left(1+\exp\left[\frac{E_{\lambda_{i+1}}(x_{i+1})-E_{\lambda_i}(x_{i+1})+\delta G_i}{k_BT}\right]\right)^{-1}\right\rangle_{\lambda_{i+1}} \tag{3.26}$$

and the total free energy difference is calculated by taking the sum, $\Delta G = \sum_{i=0}^{n-1} \delta G_i$. [204] Previous studies [203,216] have shown that BAR method is the most efficient, in comparison to TI or FEP methods, and gives accurate estimates even with a low number of samples. This method is implemented as a module in GROMACS newer versions as gmx bar utility, which makes the total free energy change available readily.

Adaptive Integration Method: The adaptive integration method is very similar to the TI method and seeks to estimate the same integral. However, in addition to the fixed-λ equilibrium sampling, it also generates equilibrium ensembles for the set of λ values using the Metropolis Monte Carlo method. The sampling of λ is done by attempting Monte Carlo moves that changes the value of λ during the simulation and is accepted based on the following criteria:

$$acc(\lambda_{old} \rightarrow \lambda_{new}) = min\left(1, \exp\left[-\frac{(E_{\lambda_{new}} - E_{\lambda_{old}})}{k_B T}\right] \times \exp\left[\frac{(\delta\hat{G}(\lambda_{new}) - \delta\hat{G}(\lambda_{old}))}{k_B T}\right]\right) \tag{3.27}$$

where $\delta\hat{G}(\lambda_i)$ is the current running free energy estimate that is obtained by approximating the integral. [217]

$$\delta\hat{G}(\lambda_i) = \int_{\lambda=0}^{\lambda_i} \left\langle \frac{\partial E(\lambda)}{\partial \lambda} \right\rangle_{\lambda} d\lambda \tag{3.28}$$

In MD, this is achieved by propagating the system at a fixed λ, using Langevin dynamics. This method has an associated advantage over TI as it assists in sampling at other λ values due to frequent Monte Carlo λ moves unlike TI where only one single starting configuration is passed between λ values. Furthermore, implementation of Langevin dynamics integrator in GROMACS provides an additional advantage. We can keep track of the convergence of ΔG and can merely run long simulations to make sure uniformity across all the values of λ.

Simulation Protocols

In work described in sections 4.3 and 4.4 of this dissertation, the suitability of binary IL mixtures for absorption of CO_2 and CH_4 was assessed in terms of Henry's constants. Langevin dynamics integrator was used to integrate the equations of motion and perform equilibrium sampling. BAR method has been employed to compute excess chemical potential, due to its high accuracy, using gmx bar utility of GROMACS

5.0.4. For coupling both van der Waal and coulombic interactions, an equidistant spacing of 0.05 was used to linearly vary λ from 0 (ideal gas state) to 1 (fully coupled state). This gave 40 state-points; first 20 λ parameters were used to scale van der Waal interaction from 0 to 1 and the other 20 points for scaling the electrostatic interactions from 0 to 1 while the van der Waal interactions were at full interaction strength, thus, providing a fully couple state at the last λ.

For such free energy calculations, a softcore potential [218] was also used. A softcore potential modifies the LJ potential to allow the overlap of the van der Waal spheres of the adjacent atoms. Given the 12-6 LJ potential (shown in eq. 3.9), the softcore potential couples the potential between the two end states linearly as:

$$E_{LJ}^{SC}(r) = \lambda E_{LJ}(r_{II}) + (1-\lambda)E_{LJ}(r_I) \tag{3.29}$$

with r_I and r_{II} given as $(\alpha\sigma_I^6\lambda + r^6)^{\frac{1}{6}}$ and $(\alpha\sigma_{II}^6(1-\lambda) + r^6)^{\frac{1}{6}}$ where E_{LJ} denote the 12-6 LJ potential for states I and II, α is the soft-core parameter, σ is the radius of interaction, and r_I and r_{II} are the distances of an arbitrary atom pair in the respective states. In this work, $\alpha = 0.5$ and $\sigma = 0.3$ are used as parameters for the softcore potential.

All the analyses were done at a temperature and pressure of 353 K and 1 bar using GROMACS 5.0.4 [196, 197]. The initial configurations were generated using PACKMOL [198] by inserting 1 molecule of solute with 256 (or 250 for 10:90 and 90:10 compositions) ion pairs for an IL in a cubic box with periodic boundary conditions. The box sizes obtained as part of the study presented in section 4.2 were used as the first estimate. The initial configurations were subjected to steepest descent minimization followed by a 2 ns annealing scheme where the temperature of the whole system was iteratively changed from 353 K to 553 K. Following, each system was

then equilibrated in canonical (NVT) and isothermal-isobaric (NPT) ensembles for 10 ns each, followed by a subsequent production run of 20 ns in the NPT ensemble. The temperature and pressure were controlled using Nose-Hoover thermostat and Parrinello-Rahman barostat respectively, with coupling time constants of $\tau_T = 0.4$ ps and $\tau_P = 2.0$ ps. With a potential cutoff of 12 Å, appropriate tail corrections were applied for non-bonded LJ interactions while electrostatic interactions were handled using the Particle Mesh Ewald (PME) method. Three independent simulation trials were conducted to determine the statistical uncertainties at each value of λ.

3.3.3 Analyses of Thermophysical Properties

In this work, the thermophysical properties are calculated for 13 binary IL mixtures (see section 4.1). Each mixture is characterized in terms of thermodynamic properties such as densities and molar volumes. Dynamic/Transport properties such as self-diffusion coefficients and ionic conductivities of the mixtures are also evaluated.

Liquid Density and Molar Volumes

These properties are readily available from MD simulations. To analyze the departure of these properties from ideal/linear mixing behavior, excess properties, especially excess molar volumes, are calculated using eq. 3.30

$$M^{ex} = M_{mix} - \sum_i x_i M_i \tag{3.30}$$

where M is the property of interest and x is the mole fraction. The comparison of the predicted values with the available experimental and simulation data for pure ILs are made. The statistical uncertainties for the predicted values are computed by running three independent MD trials, whereas for the experimental data the error bars are included where ever possible.

Self-diffusion Coefficients

The self-diffusion coefficients D are calculated by tracking the mean square displacement (MSD) of individual molecules and using Einstein's relation given by eq. 3.31

$$D = \frac{1}{6} \lim_{t \to \infty} \frac{d}{dt} \left\langle \sum_{i=1}^{N} [\vec{r}_i(t) - \vec{r}_i(0)]^2 \right\rangle \tag{3.31}$$

where $\langle \ldots \rangle$ indicates averages obtained over the number of particles (N) of a given species and time (t); $\vec{r}_i(t)$ is the position vector of the center-of-mass (COM) of a molecule. The MSD data collected over the 20 ns MD trajectories are linearly fit over 4–10 ns to obtain ionic self-diffusion coefficients. gmx msd utility of GROMACS was used to compute the MSD's. The predicted values for the ion moieties in pure ILs are compared with the experimentally available data. Please note that experimental data may not have error bars, because of the extrapolation of data based on the average parameters reported for Vogel-Fulcher-Tamman (VFT) (Arrhenius behavior) equations. [219] Further, in this work, the self-diffusion coefficients were not corrected for finite-system size effect, as viscosity was not one of the property that was looked at.

Ionic Conductivities

Ionic conductivity data is vital to understand the interactions in IL and their mixture systems, which is dependent on the strength of correlated ion movement. As mentioned earlier, the ion-ion interactions can be modulated due to steric or packing effects. Therefore in the presence of more than two ions, as in case of binary IL mixtures, a stronger correlation between two species can potentially make the other species more mobile thereby increasing the contribution to the overall conductivity.

Ionic conductivity is calculated using two different formalisms: Einstein's relation

(eq. 3.32) where the term inside the $\langle \ldots \rangle$ is plotted as a function of the simulation time, and a least-square linear fit is performed between 0-1 ns [184, 220]; the second approach involved using the Nernst-Einstein (NE) equation (eq. 3.33) in which the conductivities are computed from the self-diffusion coefficients of the individual ions. Eq. 3.32 accounts for the correlated ion motion while the latter does not, assuming that the diffusion of each species contributes to the total ionic conductivity of the system independent of the presence of the other ions. The presence of such ion correlations result in a deviation from the ionic conductivities computed from the NE relation, as has been pointed out earlier [221–224].

$$\sigma = \frac{1}{6k_BVT} \lim_{t\to\infty} \frac{d}{dt} \left\langle \sum_{i=1}^{N} \sum_{j=1}^{N} q_i q_j [\vec{r}_i(t) - \vec{r}_i(0)].[\vec{r}_j(t) - \vec{r}_j(0)] \right\rangle \tag{3.32}$$

$$\sigma_{NE} = \frac{N_{pair}}{Vk_BT} \left(q_+^2 D_+ + q_-^2 [x_1 D_{1-} + x_2 D_{2-}] \right) \tag{3.33}$$

The ratio, $Y = \left(\frac{\sigma}{\sigma_{NE}}\right)$, termed as "ionicity" is also computed to quantify the fraction of the ions available for charge transport.

Since no external utility is available, to the best of my knowledge, to compute the ionic conductivities using Einstein's relation, a fortran90 code was written in-house for the same.

3.3.4 Analyses of Structural Properties

As pointed out earlier, the primary goal of this dissertation is directed towards identifying structural features and transitions of imidazolium-based ILs, and its implications for their usage in a particular application. Although for all the IL presented in this dissertation an in-depth structural characterization has been attempted, the structural analyses probed is highly dependent on the type of ILs of interest. In other words, a different type of structural analyses is conducted for the two categories of ILs under

investigation. For binary IL mixtures the departure of the thermophysical property trends from the ideal mixing behavior is rationalized mainly by computing composition dependent radial distribution functions (RDFs), coordination numbers, spatial distribution functions (SDFs), and angular distribution functions (ADFs) that helps observe the structural transitions. While for long-chain ILs that can self-assemble, due to the presence of high ordered system with structuring evolving at mesoscopic scale, apart from RDFs the basic structural features were probed in the form of structure factors. The heterogeneity was judged by computing the heterogeneity order parameter, while the orientational order was accounted by calculating the nematic order parameters. Further, the connectivity of phases of varying polarity was quantified using Voronoi-tesselation based domain analysis and aggregate size distributions. All these analyses taken together helped reveal the structural origin of the nanoscale heterogeneity and the favorable interactions responsible for such structures that can be tuned to modulate the morphology.

The following subsections provides small introduction to the analyses and the utilities that can be used to compute them.

Radial Distribution Functions

The radial distribution functions (RDFs) also termed as pair correlation function is the measure of local structuring in a system. It describes how density changes as a function of distance from the reference molecule. In other words, it is the measure of the probability of finding a molecule at a particular distance, seen radially outward, from a reference particle relative to the uniform density of the observed particle. Thus, by definition, RDF is given by:

$$g(r) = \frac{\rho(r)}{\rho_{bulk}} = \frac{V}{N^2} \left\langle \sum_i \sum_{j \neq i} \delta(r - r_{ij}) \right\rangle \tag{3.34}$$

At short distances, RDF values larger than 1 depict that finding a particle within that distance is more probable than it should on average. For larger distances, g(r) should tend to 1. Although RDF appears simple, it is of seminal importance. The Kirkwood-Buff solution theory [225], shows that RDF can provide information on macroscopic properties. In one of the following subsections, it will also be shown that information of g(r) can be used to measure the presence of heterogeneity and can be transformed to obtain structure factors that can directly be compared to the diffraction spectra of the system. This enables the validation of performed simulations.

All the RDFs reported in this dissertation were computed using the tools implemented in TRAVIS [226, 227] software. Nonetheless, there are various other packages that can be used to compute g(r) such as VMD [228] and STRFACT [102]. In fact, gmx rdf utility is readily available in GROMACS as well. A tutorial on computing the RDFs using TRAVIS was written as a part of this dissertation and can be downloaded from "git clone https://utkarshkapoor@bitbucket.org/utkarshkapoor/tutorials.git".

Coordination Numbers

The number integrals or the coordination numbers were obtained as the integral of g(r):

$$N_c = 4\pi\rho_b \int_0^{R_{min}} r^2 g(r) dr \tag{3.35}$$

where N_c is the number of particles with the first solvation shell (from 0 to R_{min}, the first minimum of the g(r)) and ρ_b is the bulk density. This allows us to determine the number of neighbors around a central atom. As shown in this dissertation, ILs considered in this work has coordination number greater than 1, that suggests that structure of the ILs, to the very least, is supramolecular – a molecule interacting with more than a molecule – in nature.

Spatial Distribution Functions

Like RDFs, spatial distribution functions (SDFs) also show the probability of finding a particle at a particular position around a fixed reference system. SDFs are nothing but a three-dimensional enhancement to RDFs. However, a slightly different arrangement of the reference molecule is required. For setting up the reference, three atoms from the reference molecule are chosen: which are respectively placed at the origin, positive x-axis and x-y plane (with positive y values). This enables the averaging of probabilities of the observed molecule in space around the reference molecule.

Once, all the points are placed in three dimensions, it is visualized by drawing iso-surfaces on the data. Iso-surfaces are the surfaces that pass through an area with the same probability. It is analogous to contour plots in topographic maps. Thus, the particle density is specified along the iso-surface. In general, as in the case of RDFs that have peaks higher than 1, SDFs are usually instructive when the iso-surface or particle density is chosen a few times the uniform density. In this work, 1.5 to 2.5 times the bulk density is chosen for the visualization of all the SDFs. It is also worth mentioning that SDFs only provide a qualitative picture of the pair correlation functions and one should take proper care when comparing SDFs as the inference may depend on the iso-surface value used. Thus, it is highly recommended to maintain consistency and use SDFs as a visual aid.

All the SDFs reported in this dissertation were computed using the tools implemented in TRAVIS [226,227] software and were rendered using VMD [228]. There are various other packages that can be used to compute SDFs such as STRFACT [102]. In fact, gmx spatial utility is readily available in GROMACS as well. A tutorial on computing the SDFs using TRAVIS was written as a part of this dissertation and can be downloaded from "git clone https://utkarshkapoor@bitbucket.org/utkarshkapoor/tutori-

als.git".

Angular Distribution Functions

As RDFs are histograms over distances, angular distribution functions (ADFs) are histograms over a certain angle. Both RDFs and ADFs taken together provides a quantitative metric to the qualitative representation depicted by SDFs. Another way (not used in this dissertation) is to consider combined distribution functions that simultaneously provide information on the distance as well as the angle of the observed molecule and may directly complement the SDFs.

As will be shown in the results, all the RDFs and SDFs points to the fact that maximum structural transitions were observed only within the first solvation shell. Hence, all the ADFs reported in this dissertation were computed with an additional constraint such that angular changes only within the first solvation shell neighbors were considered for better comparisons. Again, all the ADFs were computed using TRAVIS [226, 227] software.

Structure Factors

The structure factors, $S(q)$, were calculated using eq. 3.36;

$$S_{ij}(q) = \frac{\rho_o x_i x_j f_i(q) f_j(q) \int_0^R 4\pi r^2 \left[g_{ij}(r) - 1\right] \frac{\sin(qr)}{qr} \left(\frac{\sin\left(\frac{\pi r}{R}\right)}{\frac{\pi r}{R}}\right) dr}{\left[\sum_i x_i f_i(q)\right]^2} \tag{3.36}$$

where $S_{ij}(q)$ is the partial structure factor obtained from the Fourier transform of the radial distribution function, $g_{ij}(r)$, between the atoms of type i and j, ρ_o is the average atomic number density, x_i is the atomic fraction of i, q is the scattering vector, and $f_i(q)$ is the X-ray atomic form factor for the atomtype i taken from the International Tables for Crystallography. [229] R represents the cutoff distance defined for

calculating g_{ij}(r). A Lorch type window function, $\left(\frac{\sin(\frac{\pi r}{R})}{\frac{\pi r}{R}}\right)$, is also used to attenuate the effect of using finite cutoff in calculating the radial distribution function between the atoms types i and j. [230] Half of the simulation box length, R, was used as the cutoff distance for these calculations.

Experimentally, $S(q)$ is determined from the coherent X-ray diffraction scattering intensity, $I_{coh}(q)$, using eq. 3.37

$$S_{ij}(q) = \frac{I_{coh}(q) - \sum_i x_i f_i^2(q)}{\left[\sum_i x_i f_i(q)\right]^2} \tag{3.37}$$

Although the intensity scale of $S(q)$ obtained from MD simulations and experimental diffraction data may differ, the trends along each plot can still be directly compared. On similar lines, if one uses coherent bound neutron scattering lengths, available in the International Tables for Crystallography Vol. C [229], the structure factors from simulations can be compared with experimentally obtained neutron diffraction patterns. Such structure factors can be computed from MD trajectories using STRFACT [102] software package.

To learn about the specific liquid motifs that give rise to the different features in $S(q)$, eq. 3.37 was conveniently partitioned into various subcomponents, also known as partial structure factors. Various types of partitioning are possible that give rise to features dependent on the wavenumber, q. First, to the study the low-q phenomena, $S(q)$ can be partitioned into the contributions from polar-polar, polar-nonpolar and nonpolar-nonpolar interactions that do not regard for the nature of charges present on the ion moieties. Second, to study the short-range (large-q) order, that arises due to charge alternation and intermolecular-intramolecular interactions of the ions, $S(q)$ can be partitioned into cation-cation, cation-anion, and anion-anion or in other words

positive-positive, positive-negative and negative-positive type contributions.

The structure factors were computed using TRAVIS [226,231] software after including the Lorch type function in the source code.

Nematic and Heterogeneity Order Parameter

The degree of orientational order can be characterized using nematic order parameter, which can be computed through traceless and symmetric Maier-Suape [232, 233] second rank ordering tensor (eq. 3.38)

$$Q_{\alpha\beta} = \frac{1}{N_m} \sum_{i=1}^{N_m} \left(\frac{3}{2} \hat{u}_{i\alpha} \hat{u}_{i\beta} - \frac{1}{2} \delta_{\alpha\beta} \right) \tag{3.38}$$

where α and β are the Cartesian indices, $\hat{u}$ is the unit vector associated with each molecule along its molecular axis, N_m is the number of molecules, δ is the Kronecker delta function. The nematic director (preferred orientation direction) and the order parameter are associated with the eigenvectors of the diagonalized $Q_{\alpha\beta}$. The order-parameter takes values between 0 for randomly oriented to 1 for perfectly aligned molecules. The significance of such orientational correlations have also been observed for the broad class of liquid crystals where the usual order-parameter range is 0.3–0.8. [232, 234]. It is also interesting to note that the nematic order-parameter can be measured using X-ray or neutron scattering techniques by coupling the orientational and positional orders of the scattering moieties. [235] Furthermore, this approach can be considered as an alternative to the director obtained using second Legendre polynomial definition along a particular direction which has proved useful for analyzing self-assembly of ILs in the past studies. [105, 126, 236, 237] The orientational order-parameters were obtained using MDTraj [238] package.

In order to dissect the presence of spatially heterogeneous domains, heterogeneity

order parameters (HOPs) were also computed. For a given pair of atomic sites, the average HOP is defined as:

$$\hat{h} = \frac{1}{N_S} \sum_{i}^{N_S} \sum_{j}^{N_S} \exp(-r_{ij}^2/2\sigma^2) \tag{3.39}$$

where r_{ij} is the distance between the sites; N_S is the total number of sites of interest and $\sigma = \mathrm{L}/(N_S)^{1/3}$ with box length L. Previous studies [105, 118–120, 239] have shown that the HOP order parameter is a useful metric for quantifying structural heterogeneity in a system. Furthermore, eq. 3.40 can be written as:

$$\hat{h} = \frac{1}{N} \sum_{r} \sum_{i} \sum_{j \neq i} \delta(r - r_{ij}) \exp(-r_{ij}^2/2\sigma^2) \tag{3.40}$$

which can be further transformed to eq. 3.41, given eq. 3.34, suggesting its connection to the RDF.

$$\hat{h} = \frac{1}{\rho} \sum_{r} g(r) \exp(-r_{ij}^2/2\sigma^2) \tag{3.41}$$

This connection was first demonstrated by Deng et al. [240]. Since, no external utility is available to compute the heterogeneity order parameter, to the best of my knowledge, a fortran90 code was written in-house for the same.

Domain Analysis

The connectivity of the nano-segregated spatially heterogeneous domains of varying polarity was examined using a Voronoi tessellation technique based domain analysis. The concept and the implementation of this technique has been described by Brehm et al. [227]. Adjacent Voronoi cells that shares a face and belong to a given subunit forms a domain. In this analysis, Voronoi sites are located on each of the atoms. The van der Waals radius of each of the sites is then used as input to demarcate Voronoi cell boundaries according to the radical Voronoi tessellation. [241] Individual

Voronoi cells can also be combined to represent a larger domain for a given collection of atoms. For this analysis, the IL system was partitioned into different subunits of varying polarity: polar and non-polar. The polar domain is usually comprised of the cation-heads and anion-heads while the non-polar subunits are represented by the uncharged alkyl chain.

The first output of average "domain count" sheds light the continuity of the subunits. Further insight into the morphology of the domains, is deduced in the form of a rich diversity of shapes adopted by such domains. For this, the isoperimetric quotient, Q^{peri}, given by eq. 3.42 was computed.

$$Q^{\text{peri}} = \left(\frac{r_{\text{sphere}}(V)}{r_{\text{sphere}}(A)} \right)^6 = 36\pi \frac{V^2}{A^3} \tag{3.42}$$

In this equation, V and A denote the volume and area of a given domain respectively while $r_{\text{sphere}}(V)$ and $r_{\text{sphere}}(A)$ represents the radius of a sphere with volume V and radius of the sphere with are A. By this definition, the shape parameter assumes a value of 1 for a perfectly spherical shape while any deviations from sphericity lead to the values lower than 1. [227].

Also analyzed are the average number of neighbors with which a given site shares at least one common Voronoi face. Therefore, this analyses, as a whole, provides information on domain connectivity, the shape of the aggregated domain and the average number of neighbors, thus allowing to identify the origin for the change in the morphology quantifiably.

This analyses was conducted using the tools implemented in TRAVIS [226, 227] software. Other packages such as voro++ [242] may also be looked at to perform a similar aggregate analysis.

Aggregate Size Distribution

The connectivity and size of the polar and nonpolar domain formed only by terminal carbon atoms of the long-chain bearing ions were further probed by computing probability distribution $P(n_a)$ of observing the aggregate size of n_a for each of the IL. For this, two molecules were considered a part of the same aggregate if they are found within the first coordination shell of each other, defined by the minimum of the respective RDFs. By definition, the maximum number of molecules in an aggregate cannot exceed the size of each system. This analysis complements the above-mentioned domain analysis and provides information on the varying sizes of the aggregates. This was performed using AGGREGATES. [243]

3.4 Monte Carlo (MC) Simulations

The simulations performed using Monte Carlo (MC) methods are stochastic. In order to implement a MC method, generation of random states of the system that satisfies a given probability distribution, ρ is required. Efficient sampling of a given probability distribution is essential to reproduce the ensemble correctly. Time-dependent quantities cannot be determined through the use of these stochastic algorithms. Thus, there is no momentum contribution available in MC simulations which is in contrast to MD simulations. In other words, MC simulations cannot be used to compute transport/dynamic properties. The progression of the configurations towards equilibrium or averaging is achieved by constructing a Markov chain that meets the following requirements: (i) the outcome of each random trial is exclusively dependent on the preceding move and (ii) each trial belongs to a finite set of outcomes, known as state space.

The transition probability, denoted by $\pi(old \rightarrow new)$, to move the system from old to new configuration typically follows the seminal Metropolis importance sampling

formalism [244]. In this, the equilibrium of the system is maintained employing a conditional transition probability that satisfies microscopic reversibility

$$\rho_{old}\pi(old \rightarrow new) = \rho_{new}\pi(new \rightarrow old) \tag{3.43}$$

which states that in equilibrium the average number of accepted moves from *old* state to the *new* state are precisely balanced by the number of moves in reverse direction. Further, this transition probability is comprised of two terms such as

$$\pi(old \rightarrow new) = \alpha(old \rightarrow new) \times acc(old \rightarrow new) \tag{3.44}$$

where $\alpha(old \rightarrow new)$ represents the attempt probability to go from *old* to a *new* state while $acc(old \rightarrow new)$ denotes the probability of accepting that stochastic move. This acceptance probability follows the Metropolis criteria [244] and is given by

$$acc(old \rightarrow new) = min\left(1, \frac{\alpha(new \rightarrow old)\rho_{new}}{\alpha(old \rightarrow new)\rho_{old}}\right) \tag{3.45}$$

Eq. 3.45 is the initial point from which acceptance rules are derived for various moves employed in the MC method, for correctly reproducing a particular ensemble.

3.4.1 Gibbs Ensemble

As mentioned above, as a first step, gas solubilities in terms of Henry's constants were computed in the IL mixtures using BAR approach in MD. However, Henry's law regime only offer a picture at the saturation limit and low-pressure regions and assumes a linear solubility relationship which is regarded as ideal solubility when considering gas separation processes. Usually, such linear relationship is not satisfied at high pressures. For ILs, as will also be shown in this dissertation, at high pressures a strong curvature instead of linear increase has been observed both computationally

as well as experimentally. [73] Because of the difficulties associated with experimental gas absorption measurements, predictions of absorption isotherms is vital. In this work, the solubility of pure gas CO_2 and CH_4, and their binary mixtures in a nonideal binary IL mixture is evaluated.

For such calculations, in this work, Gibbs ensemble Monte Carlo (GEMC) simulation methodology is employed to determine phase coexistence and compute pure as well as binary gas absorption isotherms through computer simulations. The Gibbs ensemble is essentially a combination of NVT, NPT, and μVT ensembles. In order to observe phase equilibrium, thermodynamics demands equality of temperature, pressure and chemical potential of each component. Thus, Gibbs ensemble offers the advantage of using only one simulation to deduce phase equilibria. Phase equilibria of pure fluids can be carried out in the Gibbs ensemble with a constant number of molecules (N), volume (V) and temperature (T). However, in the case of mixtures, the Gibbs phase rule dictates that an additional intensive variable, usually the pressure (P), is required to specify the system requiring GEMC-NPT simulations completely. Since, in this work, we will look at the phase equilibria of gases such as CO_2 and CH_4 in an IL mixture; this can be regarded as phase equilibria of a mixture of fluids. Hence, GEMC-NPT simulations are employed in this dissertation.

In the GEMC-NPT method, the system is comprised of two boxes A and B denoting the two phases that are equilibrated to the same pressure, temperature and the chemical potential of the species for which phase equilibria are to be determined. While the temperature and pressure are specified, the chemical potentials are not. Molecules are exchanged between the two boxes under the constraint that the total number of molecules ($N = N_A + N_B$) is constant. The probability of a particular

configuration *old* of the system is given by

$$\rho_{old} \propto \exp\left[-\frac{(U^A_{old}+U^B_{old})}{k_BT} - P\frac{(V^A_{old}+V^B_{old})}{k_BT} + N^A_{old}ln(V^A_{old}) + N^B_{old}ln(V^B_{old})\right] \quad (3.46)$$

where k_B is the Boltzmann's constant and T is the temperature and U represents the internal energy of a given box and is computed by the force field expression provided in eq. 3.9

During the course of a GEMC-NPT simulation, a number of Monte Carlo moves designed to ensure equilibration of temperature, pressure and chemical potentials are performed. Thermal equilibration is attained by translation of molecules (e.g., IL, CO_2 and CH_4), rotation of molecules about the center-of-mass (COM) of the molecules, and conformational changes of dihedral angles of molecules (IL). The probability of accepting a thermal move, e.g. going from a particular configuration *old* to *new* in box A, is dependent on the change in the energy of the system and is given by

$$acc(old \rightarrow new) = min\left(1, \exp\left[-\frac{(U^A_{new}-U^A_{old})}{k_BT}\right]\right) \quad (3.47)$$

Pressure of the two boxes is maintained by individually making random volume changes, ΔV, with a uniform probability in the user defined interval $[-\Delta V_{max}, \Delta V_{max}]$. The acceptance rule for the move, e.g. for box A, is given by

$$acc(old \rightarrow new) = min\left(1, \exp\left[-\frac{(U^A_{new}-U^A_{old})}{k_BT} - P\frac{(V^A_{new}-V^A_{old})}{k_BT} + Nln\left(\frac{V^A_{new}}{V^A_{old}}\right)\right]\right) \quad (3.48)$$

As the vapor pressure of ILs considered here is extremely low, the box representing the vapor phase will not contain any IL molecules and no molecular swaps are required for ILs. While chemical potentials of CO_2 and CH_4 will be enforced by exchanging molecules between the two boxes. For transfer of gas molecules from one box to the

other (from A to B), the acceptance rule is

$$acc(old \rightarrow new) = min\left(1, \left(\frac{P^{bias}_{old\rightarrow new}}{P^{bias}_{new\rightarrow old}}\right)\left(\frac{V^B}{V^A}\right)\exp\left[-\frac{(U^A_{new} - U^A_{old})}{k_BT} - \frac{(U^B_{new} - U^B_{old})}{k_BT}\right]\right) \tag{3.49}$$

where $P^{bias}_{old\rightarrow new}$ denotes the probability of attempting such a biased move taking the system from an *old* state to a *new* state, configurational bias strategies [245], as it is difficult to insert or delete molecules in the dense IL phase.

All these calculations of pure and mixed gas absorption in IL mixture are carried out using an open source Monte Carlo code, CASSANDRA. [245, 246]

3.4.2 Simulation Protocols

IL mixtures containing the cation 1-n-butyl-3-methylimidazolium $[C_4mim]^+$, and anions chloride Cl^- and bis(trifluoromethanesulfonyl)imide $[NTf_2]^-$ were modeled using an united-atom (UA) classical force field developed by Zhiping Liu. [187–189] This is same as the force field model used for examining the structure and dynamics of the same binary IL mixtures and the calculation of Henry's constants for CO_2 in these mixtures using BAR approach in MD simulations (sections 4.1, 4.2 and 4.3). The force field parameters for carbon dioxide (CO_2) and methane (CH_4) molecules were obtained from Shi and Maginn [195] and TraPPE [194] respectively.

The absorption isotherms of CO_2 and CH_4 and their mixtures in binary IL mixture system of $[C_4mim]\ Cl_x\ [NTf_2]_{1-x}$ (x = 0.0, 0.10, 0.25, 0.5, 0.75, 0.90, 1.0) were computed in GEMC_NPT simulations using CASSANDRA package. [245, 246] Pure gas solubilities were calculated at pressures ranging from 1 to 100 bar, while CO_2 and CH_4 mixed gas solubilities were computed at 100 bar pressure with the CO_2/CH_4 mole ratio of 05:95 and 15:85 in the gas phase. All the simulations were performed

at a temperature of 353 K, to ensure liquid phase of ILs used in this work and be consistent with all the work presented in this dissertation. In general, a system size 256 ion pairs of ILs was used for all the compositions, except $x = 0.10$ and $x = 0.90$ for which 250 ion pairs were simulated. For pure gas solubilities, the liquid phase was represented by randomly placing the IL molecules in a cubic box; the initial dimensions of which are obtained from MD study data while the gas phase contains 500 molecules of either CO_2 or CH_4 molecules. This was done using the in-built Cassandra code that uses a configurational bias methodology. [245] Though the size system size of IL used for mixed gas solubilities remained the same, number of CO_2/CH_4 molecules were varied as 100/1900 and 150/850 to represent 05:95 and 15:85 molar ratios in the gas phase.

In order to achieve the thermal equilibration CASSANDRA package is equipped by translation, rotation, and fragment regrowth moves in which the center-of-mass (COM) of a molecule translated, rotated randomly about x, y or z-direction and regrown by altering the conformation of the fragments, which are generated using fragment-based sampling approach. [245] The probability of performing the above mentioned moves was set equally to 30 % for all the simulations. Volume fluctuation moves were attempted with a frequency of 0.5 % independently for liquid and gas phase boxes. Due to the nonvolatile nature of the ILs, only gas molecules were exchanged between the two phases to enforce chemical potential equality. Such an exchange was attempted on an average frequency of 9.5 %. The LJ and electrostatic interactions were truncated at 12 Å distance, consistent with the force field model. All the simulated were equilibrated for 25 million Monte Carlo (M MC) steps, followed by subsequent production runs of 50 M MC steps. Final 10 M MC steps were used to compute averages. Standard deviations were calculated by conducting three independent trials using different initial configurations along with different random

seeds to generate the Markov Chains.

3.4.3 Solubility Selectivity

Again, taking a linear fit to the solubility data as pressure tends to zero allows us to evaluate Henry's constants. Comparison of these Henry's constants with the values predicted using MD simulations will complement each other and help us determine the accuracies and reliabilities of the property trends. It is important to mention that Henry's constant values are dependent on the range of data used for linear fit due to the curvature at high pressures. In this study, for CO_2, the linear fit was taken by selecting the range of data points from P = 0 bar to the pressure where x_{CO_2} is at least 0.1 whereas for CH_4 due to very low solubility, linear fits from P = 0 up to P = 50 bar were taken to calculate Henry's constants. This range is justified as the experimental value of 541 bar for the CH_4 in pure $[C_4mim][NTf_2]$ was computed by taking a linear fit of the data ranging between 15.9 to 50 bar [247] which shows maximum CH_4 solubility among all the IL studied in this work.

Because of the difficulties associated with experimental measurements of binary gas absorption isotherms, ideal solubility selectivity is usually employed to assess the capability of a solvent for gas separation. However, usually the gas separation conditions are not ideal especially when high pressures are involved, and the presence of one species may influence the solubility behavior of another species contributing to the nonideality of the system. Thus, ideal solubility selectivity computed above provides a starting point for evaluating the potential of a given IL mixture for separating gaseous mixtures. The ideal solubility selectivities can be determined by taking the ratio of Henry's constants, as shown in eq. 3.50

$$\beta^{S,H}_{CO_2/CH_4} = \left(\frac{k_{H,CO_2}}{k_{H,CH_4}}\right) \tag{3.50}$$

Furthermore, in order to determine the extent of non-ideal behavior expected when binary mixtures of CO_2 and CH_4 are absorbed at high pressures in binary ILs, binary gas absorption isotherms were computed at a total pressure of 100 bar and T = 353 K. As mentioned above, two gas phase CO_2/CH_4 molar are investigated 15:85, and 5:95 to ascertain the effects of high and low concentrations of CO_2 on the separation potential of the mixture of ILs. Then, solubility selectivities were computed directly from the liquid and gas phase compositions of the corresponding components obtained from the GEMC-NPT simulations using the eq. 3.51

$$\beta^{S}_{CO_2/CH_4} = \left(\frac{x_{CO_2}/y_{CO_2}}{x_{CH_4}/y_{CH_4}} \right)_{P,T} \tag{3.51}$$

where x and y are the mole fractions in liquid and gas phase, respectively, which was then compared with ideal solubility selectivities in order to adequately account for any non-ideal trends observed in mixed gas absorption isotherms.

CHAPTER 4

DESIGNING BINARY IONIC LIQUID MIXTURES FOR BETTER CO_2 ABSORPTION

As mentioned earlier, ionic liquids (ILs) have emerged as potentially environmentally benign chemicals essentially due to their negligible vapor pressure and unique physicochemical properties. By judiciously selecting the cation, anion or functional groups on the ions desired physical, chemical and biological properties can be imparted to ILs. The vast majority of the experimental and modeling work to date has focused on such a combinatorial approach. Although such an approach can potentially be exploited to generate as many as a million ILs, a continuing challenge that remains is that many ILs display unfavorable transport properties which limit their use in industrial processes. Furthermore, identifying a suitable IL to meet the specification for a given process is a daunting task as synthesizing a large number of ILs and measuring relevant properties, experimentally, is extremely time-consuming and challenging. More importantly, the registry of a new IL can be a cumbersome process. Thus, one clever way of modifying and perhaps tuning the desirable properties is to consider the mixtures of already synthesized ILs. According to Plechkova and Seddon, [248] more than 1 billion mixture combinations of ILs can be exploited for task-specific applications. In fact, it has been shown that mixing two ILs not only provide a means to precisely control the desired physicochemical properties but can potentially possess properties superior to pure IL counterparts. [31] Thus, it is highly desirable to predict if a given binary IL mixture is likely to exhibit ideal behavior such that the mixture properties can be estimated from those of pure ILs. Alternately, it is also important

to estimate if IL mixtures will possess molecular interactions that are different from pure ILs, the behavior which can potentially be exploited to obtain properties that are superior to the pure IL properties. The central hypothesis of the work presented in this chapter is that mixing of ILs differing widely in their hydrogen bonding capability and molar volumes leads to non-native molecular interactions/structures that are not found in the parent ILs, and additionally, these non-native structures lead to solubility behavior that is a non-linear function of the IL composition.

The present chapter strives to determine fundamental design rules to *a priori* predict if the properties of binary IL mixtures can be estimated based on pure IL analogues or not, by rationalizing molecular interactions based on the microscopic structures. Further, the implication of nonideal IL behavior on the phase equilibria properties, with gaseous solutes, is also examined.

Rather than chronologically presenting the topics, they are arranged to form a series where the later topics apply and extend the findings of the former topics. I believe that this organization is more instructive and provides a cohesive progression of the research efforts. In the first part of the chapter, thermophysical properties of the ILs and their mixtures predicted from molecular simulations are reported. Since the experimental data for the IL mixtures studied in this work is scarce, in general, the calculated values of the thermodynamic and transport properties such as molar volumes, densities, self-diffusion coefficients, and ionic conductivities are compared against the experimental data only for pure ILs. While values for binary mixtures of ILs are discussed with special emphasis on the overall composition-dependent trends: linear (ideal) vs. non-linear (nonideal). This is followed by the rationalization of these thermophysical property trends on the observed structural changes, i.e., structurally what changes in the liquid that gives rise to linear/non-linear property trend. Elu-

cidation of local structures is done by computing center-of-mass radial distribution functions (RDFs), angular distribution functions (ADFs), and spatial distribution functions (SDFs). The deviation from ideality and its origin is explained based on structural changes that occur as the composition of the IL mixture is changed. The second part of the chapter focuses on the implications of the nonideal behavior of IL mixtures on CO_2 absorption; calculating solubilities in terms of Henry's constants using Bennett Acceptance Ratio (BAR) approach and accounting the property trends via local structure properties. Moreover, pressure dependent absorption isotherms predicted using the Gibbs Ensemble Monte Carlo (GEMC) technique with a small discussion on the exploitation of nonideal IL mixtures for better separation of mixed gases is also included. The last part of this chapter scrutinizes the initial hypothesis of expecting nonideal behavior and provides a potential (qualitative) structure-property relationship which can be extrapolated to foretell nonideality in IL mixtures.

4.1 Thermophysical Properties of Imidazolium-based Binary Ionic Liquid Mixtures

MD simulations (using GROMACS 4.5.5) were employed to predict thermodynamic and transport properties – density, molar volumes, self-diffusion coefficients, and ionic conductivities – for 13 binary IL mixture systems as a function of mole fractions of the constituent ILs, at 353 K and 1 bar, using an united-atom force field as described in section 3.3.1.

The first group of IL mixtures investigated here showcase the *anion effect* where the cation 1-n-butyl-3-methylimidazolium $[C_4mim]^+$ is paired with different combinations of anions, namely chloride Cl^-, acetate $[OAC]^-$, methylsulfate $[MeSO_4]^-$, trifluoromethylacetate $[TFA]^-$, trifluoromethanesulfonate $[TFS]^-$, and bis (trifluoromethanesulfonyl)imide $[NTf_2]^-$. For ILs, the Kamlet-Taft parameter [39, 40] – β –

is generally used to characterize the hydrogen bond basicity. The usefulness of the β parameter has been shown in the works of Lungwitz and Spange, [41, 42] where the authors determined the β values for the ILs, based on $[C_4mim]^+$ combined with different anions, and found an excellent correlation between ^1H NMR chemical shift of C-2 proton of imidazolium cation and β values. For the anions considered in this work, the hydrogen bond basicity decreased in the order $Cl^- > [OAC]^- > [MeSO_4]^- > [TFA]^- > [TFS]^- > [NTf_2]^-$ with β values of 0.95, 0.85, 0.75, 0.74, 0.57 and 0.42 respectively. Henceforth, these IL mixtures are referred as (1) $[C_4mim]\ Cl_x\ [OAC]_{1-x}$, (2) $[C_4mim]\ Cl_x\ [MeSO_4]_{1-x}$ (3) $[C_4mim]\ Cl_x\ [TFA]_{1-x}$, (4) $[C_4mim]\ Cl_x\ [TFS]_{1-x}$, (5) $C_4mim]\ Cl_x\ [NTf_2]_{1-x}$, (6) $[C_4mim]\ [OAC]_x\ [TFA]_{1-x}$, and (7) $[C_4mim]\ [OAC]_x\ [TFS]_{1-x}$.

The second group of IL mixtures were derived from the mixtures of Cl^-–$[MeSO_4]^-$ and Cl^-–$[NTf_2]^-$ paired with the cations: 1-ethyl-3-methylimidazolium $[C_2mim]^+$, 1-n-hexyl-3-methylimidazolium $[C_6mim]^+$, and 1-n-octyl-3-methylimidazolium $[C_8mim]^+$ exhibiting the *alkyl chain effect*. In the following, these ILs are abbreviated as (8) $[C_2mim]\ Cl_x\ [MeSO_4]_{1-x}$, (9) $[C_6mim]\ Cl_x\ [MeSO_4]_{1-x}$, (10) $[C_8mim]\ Cl_x\ [MeSO_4]_{1-x}$, (11) $[C_2mim]\ Cl_x\ [NTf_2]_{1-x}$, (12) $[C_6mim]\ Cl_x\ [NTf_2]_{1-x}$, and (13) $[C_8mim]\ Cl_x\ [NTf_2]_{1-x}$.

These anion combinations were chosen based on the differences in their hydrogen bonding ability with the cation and size/molar volumes of pure ILs. [38,249] This work is part of two different journal articles and was published in 2016 [250] and 2018 [251]. The objective was to determine the influence of the difference in hydrogen bonding ability of the anions and size/molar volume on the thermophysical properties of the mixtures. Figure 4.1 summarizes the objective of this section pictorially. Please note that molecular structures are united-atom as per the employed force field.

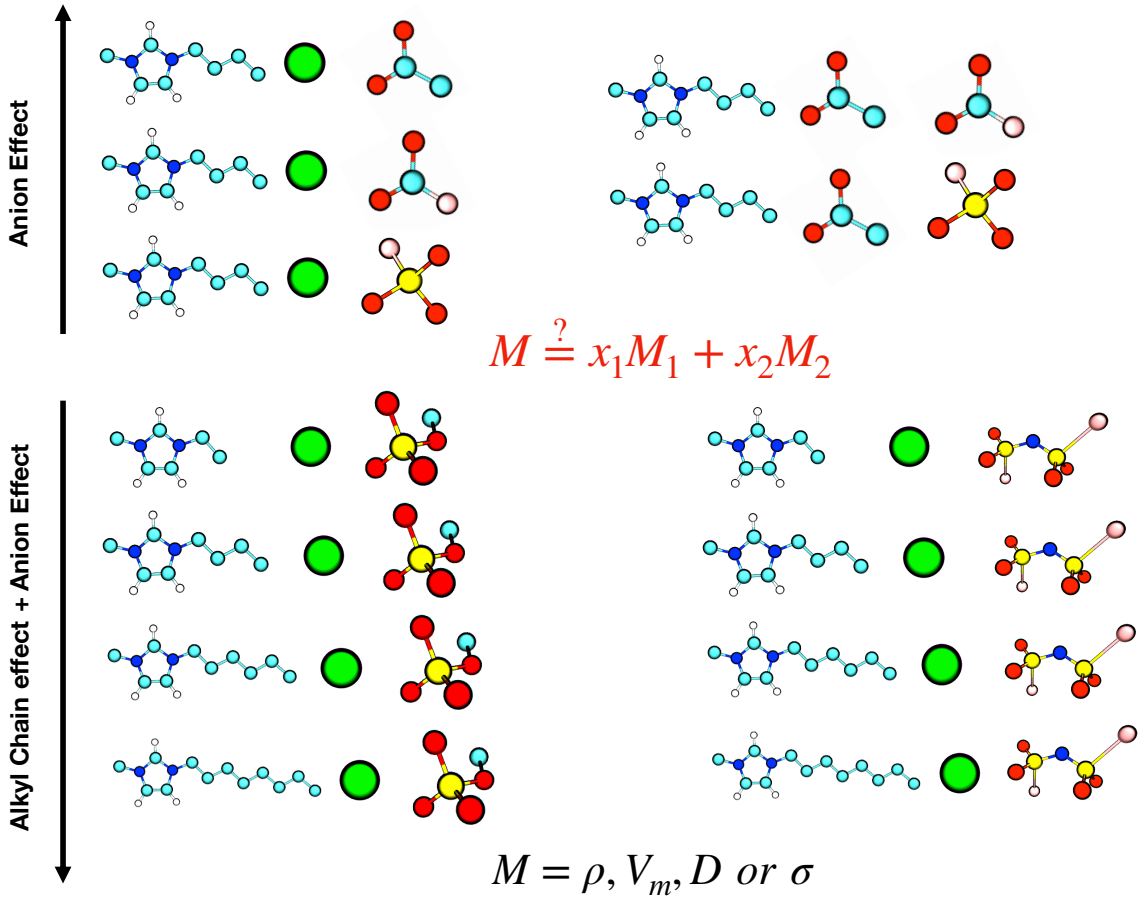

Figure 4.1: List of imidazolium-based binary IL mixtures for which thermophysical properties are predicted

Additionally, all the numerical data are included as part of the Appendix A.

4.1.1 Liquid Densities

The predicted densities for pure ILs in the first group: [C_4mim] Cl (1.055 g/cm^3), [C_4mim] [OAC] (1.027 g/cm^3), [C_4mim] [$MeSO_4$] (1.205 g/cm^3), [C_4mim] [TFA] (1.181 g/cm^3), [C_4mim] [TFS] (1.281 g/cm^3) and [C_4mim] [NTf_2] (1.391 g/cm^3), and second group: [C_2mim] [NTf_2] (1.474 g/cm^3), [C_6mim] [NTf_2] (1.326 g/cm^3) and [C_8mim] [NTf_2] (1.274 g/cm^3) at 353 K are in very good agreement, deviation less than 0.5 %, with the predicted densities published by Cao and co-workers [188, 189] – from where the force field parameters were obtained. In fact, the experimental densities reported for [C_4mim] [$MeSO_4$] [252], [C_4mim] [TFA] [253], [C_4mim] [TFS] [254],

[C_4mim] [NTf_2] [254], [C_6mim] Cl [255], [C_8mim] Cl [255], [C_2mim] [NTf_2] [256], [C_6mim] [NTf_2] [257], and [C_8mim] [NTf_2] [258] are 1.175 (at 353 K), 1.17 (at 348 K), 1.254 (at 353 K), 1.014 (at 343 K), 1.385 (at 353 K), 0.983 (at 343 K), 1.464 (at 353 K), 1.323 (at 353 K), 1.285 (at 343 K), respectively, and the deviations are less than 1 % between the values predicted from simulations and the experimental data.

Figure 4.2 (a) shows the *anion effect* for a series of imidazolium-based IL mix-

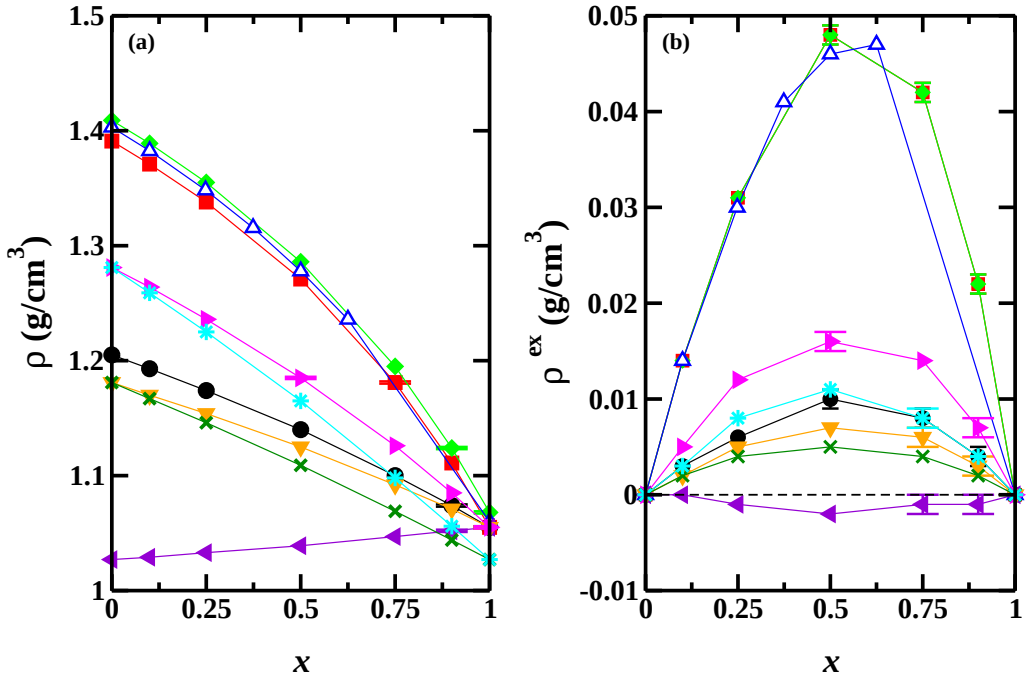

Figure 4.2: (a) Variation of liquid densities for as the function of anion molar composition and (b) Deviation of liquid densities from mole fraction averaged densities at 353 K and 1 bar, for IL mixtures that share a common cation and have different anions, showcasing *anion effect*; [C_4mim] Cl_x [$MeSO_4$]$_{1-x}$ •, [C_4mim] Cl_x [NTf_2]$_{1-x}$ ■, [C_4mim] Cl_x [NTf_2]$_{1-x}$, this work, at 333 K ♦, [C_4mim] Cl_x [NTf_2]$_{1-x}$, by Brennecke [259], at 333 K △, [C_4mim] Cl_x [OAC]$_{1-x}$ ◄, [C_4mim] Cl_x [TFA]$_{1-x}$ ▼, [C_4mim] Cl_x [TFS]$_{1-x}$ ►, [C_4mim] [OAC]$_x$ [TFA]$_{1-x}$ ×, [C_4mim] [OAC]$_x$ [TFS]$_{1-x}$ ∗. Standard deviations were calculated from three independent MD trials for all mixture compositions. Solid lines are just guide to the eye.

tures with the common cation [C_4mim]$^+$. The pure IL density increases in the order

$[OAC]^- < Cl^- < [TFA]^- < [MeSO_4]^- < [TFS]^- < [NTf_2]^-$ and is expected based on the increase in the molecular weight of the anion with the exception of $[OAC]^-$ and Cl^-. This discrepancy is probably due to efficient molecular packing in the case of $[C_4mim]$ Cl as Cl^- is spherical. The variation of liquid densities as a function of molar compositions for all the binary IL mixture systems is smooth and lies between the densities of the pure ILs. For all the systems, except $[C_4mim]$ Cl_x $[OAC]_{1-x}$, a positive curvature from the mole fraction averaged densities can be discerned with maximum positive curvature from the mole fraction averaged densities, is noticeable for the $[C_4mim]$ Cl_x $[NTf_2]_{1-x}$ systems. The deviations from the linear mixing rule ($\rho^{\text{ex}} = \rho_{mix} - \sum_i x_i \rho_i$) have been quantified in Figure 4.2 (b). This indicates that a gradual transition in the molecular structures can be anticipated due to packing effects. It is also worth mentioning that such mole fraction dependent density variation is independent of the temperature. The density variation for the $[C_4mim]$ $Cl_x[NTf_2]_{1-x}$ system exhibits non-linear dependence on Cl^- mole fraction at 333 K which is consistent with the density trends measured by Brennecke and co-workers [259] at 333 K. Further, the non-linear density variation for $[C_4mim]$ Cl_x $[TFS]_{1-x}$ was also presented in the study by Matthews et al. [45] using an all-atom force field model.

The densities for the $[C_nmim]$ Cl_x $[MeSO_4]_{1-x}$ and $[C_nmim]$ Cl_x $[NTf_2]_{1-x}$ mixture systems are presented in Figure 4.3 (a) for $n = 2$, 4, 6, and 8. As expected, the density decreases with an increase in the cationic alkyl chain length for a given anion combination. The non-linear behavior is noticeable for the $[C_nmim]$ Cl_x $[NTf_2]_{1-x}$ systems in comparison to that for the analogous system containing Cl^- and $[MeSO_4]^-$. The deviations from the linear mixing rule are also included in Figure 4.3 (b). It is important to mention that for $n \geq 6$ aggregation of alkyl chains start to dominate which influences the cation-anion intermolecular interactions, as nonpolar domains are accommodated in the polar domains. It appears that the curvature becomes less

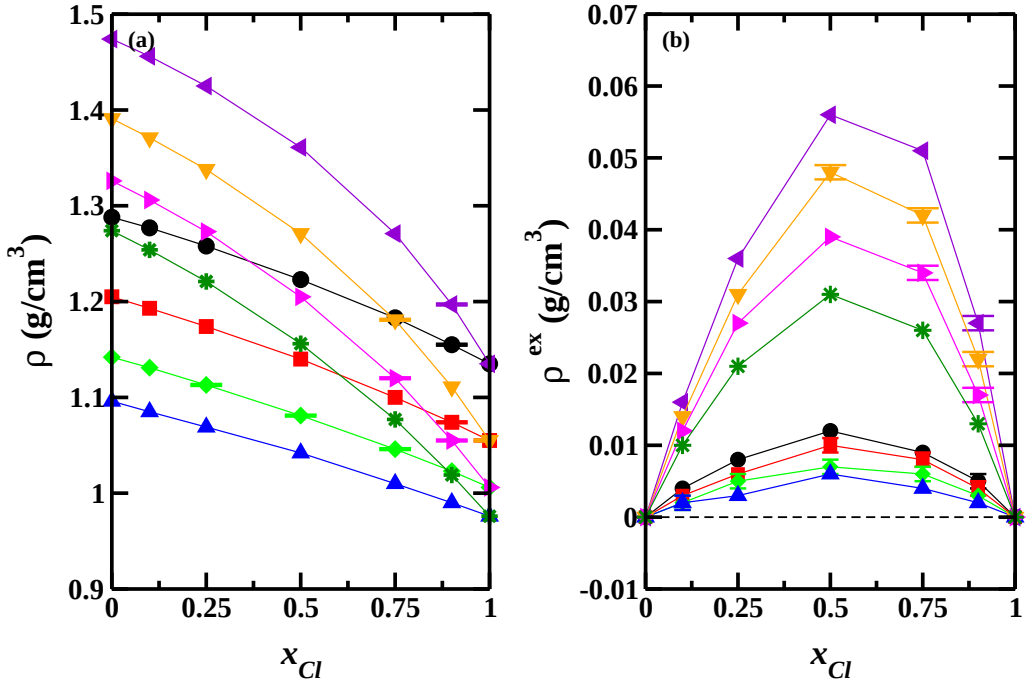

Figure 4.3: (a) Variation of liquid densities for as the function of anion molar composition and (b) Deviation of liquid densities from mole fraction averaged densities at 353 K and 1 bar, for IL mixtures that have a common cation, *but varies systematically in alkyl chain length*, and different anions; for [C_2mim] Cl_x [$MeSO_4$]$_{1-x}$ ●, [C_4mim] Cl_x [$MeSO_4$]$_{1-x}$ ■, [C_6mim] Cl_x [$MeSO_4$]$_{1-x}$ ♦, [C_8mim] Cl_x [$MeSO_4$]$_{1-x}$ ▲, [C_2mim] Cl_x [NTf_2]$_{1-x}$ ◀, [C_4mim] Cl_x [NTf_2]$_{1-x}$ ▼, [C_6mim] Cl_x [NTf_2]$_{1-x}$ ▶, [C_8mim] Cl_x [NTf_2]$_{1-x}$ ∗. Standard deviations were calculated from three independent MD trials for all mixture compositions. Solid lines are just guide to the eye.

pronounced with an increase in the alkyl chain length, suggesting that as alkyl chain aggregation increases the anion-effect is undermined.

4.1.2 Molar Volumes

Figure 4.4 (a) shows the variation of molar volumes, for the binary IL mixture systems containing the same cation and different anion combinations, as a function of mole fraction at 353 K. Concerning the pure IL volumes, it is clear that anion size plays a vital role in determining the molar volumes. For example, larger size of $[NTf_2]^-$ is reflected in the molar volumes. Further, substitution of methyl (-CH_3) for trifluo-

romethane (-CF_3) group leads to an increase in the molar volume ([C_4mim][OAC] vs. [C_4mim][TFA]).

The variation of molar volume with compositions appears close to linear, suggesting

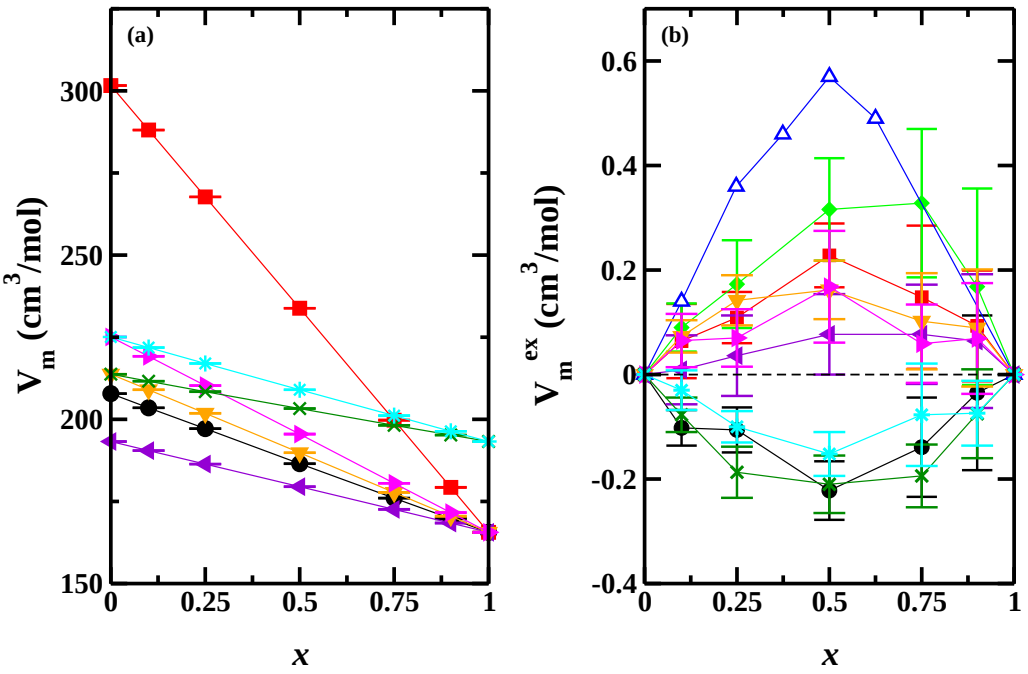

Figure 4.4: (a) Variation of molar volumes for as the function of anion molar composition and (b) Deviation of molar volumes from mole fraction averaged densities at 353 K and 1 bar, for IL mixtures that share a common cation and have different anions, showcasing *anion effect*; [C_4mim] Cl$_x$ [$MeSO_4$]$_{1-x}$ ●, [C_4mim] Cl$_x$ [NTf_2]$_{1-x}$ ■, [C_4mim] Cl$_x$ [NTf_2]$_{1-x}$, this work, at 333 K ♦, [C_4mim] Cl$_x$ [NTf_2]$_{1-x}$, by Brennecke [259], at 333 K △, [C_4mim] Cl$_x$ [OAC]$_{1-x}$ ◄ , [C_4mim] Cl$_x$ [TFA]$_{1-x}$ ▼, [C_4mim] Cl$_x$ [TFS]$_{1-x}$ ►, [C_4mim] [OAC]$_x$ [TFA]$_{1-x}$ ×, [C_4mim] [OAC]$_x$ [TFS]$_{1-x}$ ∗. Standard deviations were calculated from three independent MD trials for all mixture compositions. Solid lines are just guide to the eye.

almost ideal mixing behavior for these IL mixtures. In fact, the excess molar volumes computed for these mixtures, using eq. 4.1, show that the deviation from the linear mixing rule, average V_m^{ex} values, is rather small and is subjected to large statistical uncertainty as they are calculated from the difference in relatively large pure IL molar

volumes.

$$V_m^{\text{ex}} = V_{mix} - \sum_i x_i V_i = \frac{(MW)_{\text{mix}}}{\rho_{\text{mix}}} - \sum_i x_i \frac{(MW)_i}{\rho_i} \tag{4.1}$$

As can be visualized from Figure 4.4 (b), a given binary IL mixture consistently shows either positive ([C_4mim] Cl_x [NTf_2]$_{1-x}$, [C_4mim] Cl_x [TFS]$_{1-x}$, [C_4mim] Cl_x [TFA]$_{1-x}$), close to zero ([C_4mim] Cl_x [OAC]$_{1-x}$), or negative ([C_4mim] Cl_x [$MeSO_4$]$_{1-x}$, [C_4mim] [OAC]$_x$ [TFS]$_{1-x}$, [C_4mim] [OAC]$_x$ [TFA]$_{1-x}$) excess molar volumes. Negative or close to zero excess molar volumes are an indication that the molecular packing observed in the pure IL system is preserved in the mixture systems, which can arise due to similarity in size (e.g., $[OAC]^-$ and $[TFA]^-$, $[OAC]^-$ and $[TFS]^-$) or similarity in interactions between the cation and anions forming mixtures (for example, Cl^- and $[MeSO_4]^-$, and Cl^- and $[OAC]^-$). On the other hand, positive excess molar volumes suggest that the mixture systems are characterized by a less efficient packing than that exists in the pure IL systems, due to size asymmetry or difference in hydrogen bonding strength of the anions with cations. This is the case for all the mixtures involving Cl^- and fluorinated anions ($[TFA]^-$, $[TFS]^-$, and $[NTf_2]^-$). Furthermore, Brennecke and co-workers [259] measured the excess molar volumes for the system of [C_4mim]Cl_x[NTf_2]$_{1-x}$ at 333 K and 1 bar condition and reported that the mixing of the two ILs leads to molar volumes higher than those calculated based on an ideal mixing model. This is in accordance with the molecular simulation predictions, the data also included in Figure 4.4 (b). It is worth noting that no standard errors were reported for the experimental data. Although the experimental measurements of excess molar volumes are consistently higher than those predicted from the MD simulation, given the difficulty associated with calculating excess molar volumes such *a priori* predictions of the sign and magnitude of the excess molar volumes are quite remarkable.

Similarly, Figures 4.5 (a) and (b) show molar volume variation and its devia-

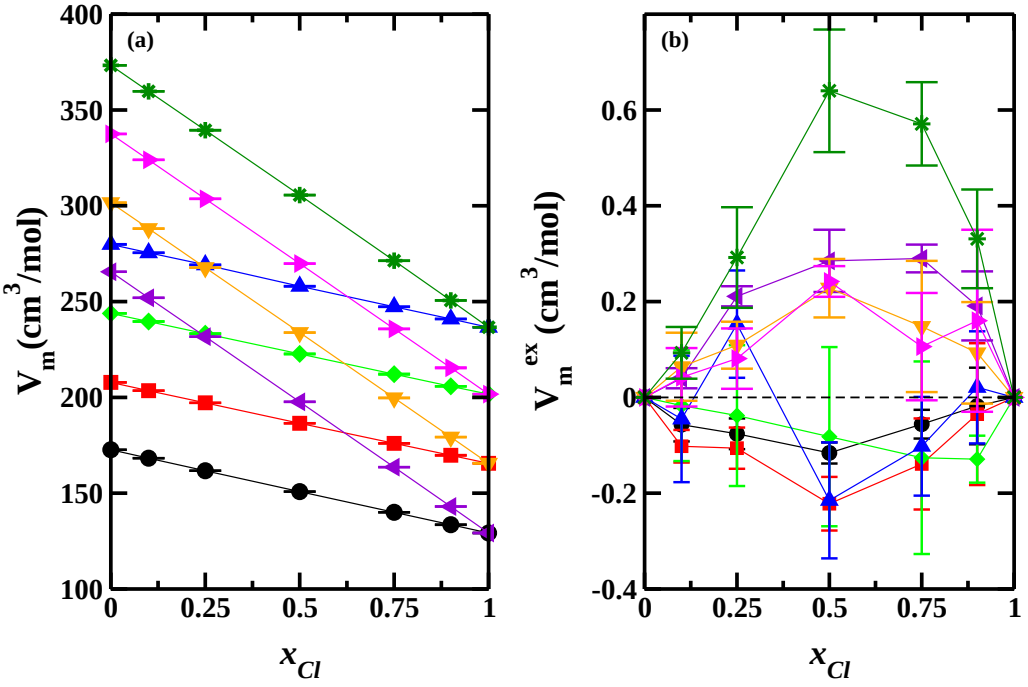

Figure 4.5: (a) Variation of molar volumes for as the function of anion molar composition and (b) Deviation of molar volumes from mole fraction averaged densities at 353 K and 1 bar, for IL mixtures that have a common cation, *but varies systematically in alkyl chain length*, and different anions; for $[C_2mim]$ Cl_x $[MeSO_4]_{1-x}$ ●, $[C_4mim]$ Cl_x $[MeSO_4]_{1-x}$ ■, $[C_6mim]$ Cl_x $[MeSO_4]_{1-x}$ ♦, $[C_8mim]$ Cl_x $[MeSO_4]_{1-x}$ ▲, $[C_2mim]$ Cl_x $[NTf_2]_{1-x}$ ◀ , $[C_4mim]$ Cl_x $[NTf_2]_{1-x}$ ▼, $[C_6mim]$ Cl_x $[NTf_2]_{1-x}$ ▶, $[C_8mim]$ Cl_x $[NTf_2]_{1-x}$ ∗. Standard deviations were calculated from three independent MD trials for all mixture compositions. Solid lines are just guide to the eye.

tion from the linear mixing rule for the the systems of $[C_nmim]Cl_x[MeSO_4]_{1-x}$ and $[C_nmim]Cl_x[NTf_2]_{1-x}$ with $n = 2, 4, 6, 8$. It is interesting to note that the sign of the deviation is independent of the alkyl chain length ($[C_nmim]Cl_x[MeSO_4]_{1-x}$ shows negative or close to zero while $[C_nmim]Cl_x[NTf_2]_{1-x}$ shows positive excess molar volumes with the maximum at equimolar composition). However, the magnitude increases with the increase in the alkyl chain length suggesting that an increase in alkyl chain aggregation interactions aids the formation of local free volume. Moreover, IL mixtures that contain $[NTf_2]^-$ anion tend to exhibit positive deviation for the excess

molar volumes such as those found for [C_4mim] tetrafluoroborate $[BF_4]_x[NTf_2]_{1-x}$ (+0.28 cm^3/mol at equimolar composition), [C_2mim] ethylsulfate $[EtSO_4]_x[NTf_2]_{1-x}$ (+0.76 cm^3/mol at equimolar composition). [38] Smith and co-workers [260] have also reported that the IL mixture of [C_4mim] Cl_x $[NTf_2]_{1-x}$ shows positive deviation from ideality, with a maximum of $\sim$ +0.7 cm^3/mol at equimolar composition.

4.1.3 Self-diffusion Coefficients

Table 4.1 provides a comparison of the self-diffusion coefficients of cations and anions predicted for pure ILs with the literature at 353 K. The self-diffusion coefficients obtained in this work for [C_4mim] Cl, [C_4mim] [$MeSO_4$], [C_4mim] [NTf_2], [C_4mim] [TFS], [C_4mim] [TFA], [C_4mim] [OAC], [C_2mim] [NTf_2], [C_6mim] [NTf_2] and [C_8mim] [NTf_2] are in good agreement with previous molecular simulation and experimental studies. Small differences between the self-diffusion coefficients obtained in this work and those reported in the simulation studies are probably due to the use of different simulation protocols. [189] For [C_4mim] [NTf_2], with respect to the experimentally measured diffusion coefficients, it can be easily discerned that the values predicted by Maginn and co-workers [184] (cation: 4.3 and anion: 2.7) using a non-polarizable force field with integer ($\pm$ 1) charges are nearly of $(1/4)^{th}$ order, while substantial improvement in the agreement is observed when force fields use non-integer charges ($\pm$ 0.8) to account for the polarization effect, values reported in this work and by Zhong et al. [189]

A number of other observations can also be made from this comparison. The self-diffusion coefficient for the cation, especially for $[C_2mim]^+$ and $[C_4mim]^+$, in a given IL is higher than that for the anion. This behavior has been observed in other studies [184, 189, 219, 262] as well and has been shown to be directly linked to the preferential translation motion of the cation along the directions of the imidazolium-

Table 4.1: Self-diffusion coefficients, D, (10^{-7} cm^2/sec) of ions for pure ILs, obtained from simulations in this work and compared with literature at 353 K.

Ionic Liquid	This Work		Zhong et al. [188, 189]		Experiment [219, 261]	
	Cation	Anion	Cation	Anion	Cation	Anion
[C_4mim][TFS]	9.0 ± 0.1	6.0 ± 0.4	7.8	6	10	9
[C_4mim][TFA]	19.5 ± 0.4	16.7 ± 0.3	19.8	17.2	12	11
[C_4mim][OAC]	4.5 ± 0.3	4.1 ± 0.4	3.5^a	3.2^a	–	–
[C_2mim][NTf_2]	17.3 ± 0.1	10.0 ± 0.3	18.5	10.2	22	14
[C_4mim][NTf_2]	13.4 ± 0.5	8.9 ± 0.9	10.8	7.8	15	13
[C_6mim][NTf_2]	9.7 ± 1.2	7.6 ± 0.5	6.9	6.2	12	11
[C_8mim][NTf_2]	6.1 ± 0.3	6.1 ± 0.8	4	4	9	8.8
[C_2mim][$MeSO_4$]	5.1 ± 0.2	2.4 ± 0.2	–	–	–	–
[C_4mim][$MeSO_4$]	3.0 ± 0.2	1.9 ± 0.2	1.4^a	0.9^a	–	–
[C_6mim][$MeSO_4$]	1.6 ± 0.1	1.3 ± 0.1	–	–	–	–
[C_8mim][$MeSO_4$]	0.9 ± 0.1	0.9 ± 0.1	–	–	–	–
[C_2mim]Cl	3.0 ± 0.2	2.0 ± 0.1	–	–	–	–
[C_4mim]Cl	1.3 ± 0.2	1.0 ± 0.1	0.4	–	1.8	–
[C_6mim]Cl	0.5 ± 0.1	0.4 ± 0.1	–	–	–	–
[C_8mim]Cl	0.4 ± 0.1	0.3 ± 0.2	–	–	–	–

[a]D at 343 K

Note: There are no error bars on the data obtained from the literature, as diffusion coefficients at the temperature of interest, in general, were computed using the average parameter values reported for Vogel-Fulcher-Tamman (VFT) equation fitted for diffusivity.

ring plane and the alkyl chain, while the motion normal to the ring plane is highly restricted. [184, 263, 264]. For the [C_4mim] Cl and [C_4mim] [OAC] ILs, the cation and anion self-diffusion coefficient are very similar, which is consistent with strong interactions between the cation and anion in these ILs. For the given cation ($[C_4mim]^+$), the anion self-diffusion coefficients are ranked in the order: $Cl^- < [MeSO_4]^- < [OAC]^- < [TFS]^- < [NTf_2]^- < [TFA]^-$ and is in agreement with the decreasing trend in viscosity derived by Gardas and Coutinho [265] using a group contribution method, except for $[TFA]^-$. The over-prediction of diffusion of $[TFA]^-$ is due to the molecular model adopted for this work [189] where the authors observed similar behavior. Further, the cation self-diffusion coefficients are found to decrease with the increase in the cationic alkyl chain length irrespective of the anions ($[NTf_2]^-$, Cl^-, $[MeSO_4]^-$]), which can

be attributed to increasing alkyl chain aggregation interactions for $[C_6mim]^+$ and $[C_8mim]^+$. [85,122,266,267] It is also worth pointing out that the cation self-diffusion coefficients for $[C_6mim]^+$ and $[C_8mim]^+$ become comparable to those of the anions with which they are paired.

Figures 4.6 (a) - (f) present the self-diffusion coefficients for cations and anions in the respective binary IL mixtures as a function of molar composition at 353 K for all the systems except [C_4mim] Cl_x $[MeSO_4]_{1-x}$ and [C_4mim] Cl_x $[NTf_2]_{1-x}$ which are discussed separately below. For all the binary IL mixtures, the self-diffusion coefficients of the ions are bracketed by those found for the pure ILs. Similar to the pure IL systems, the self-diffusion coefficients for the cation is higher than those of the anions for the entire composition range. It is very interesting to note that for binary IL systems yielding positive excess molar volumes, the self-diffusion coefficients drop rapidly with the increase in the concentration of strongly coordinating anion up to equimolar concentration beyond which the decrease in self-diffusion coefficients is more gradual, suggesting a non-linear deviation from ideal behavior. On the contrary, the self-diffusion coefficients show weak dependence with the change in concentration for the systems for which small negative or close to zero excess molar volumes are predicted.

In order to provide deeper insights about linear vs. non-linear dependence, [C_4mim] Cl_x $[MeSO_4]_{1-x}$ and [C_4mim] Cl_x $[NTf_2]_{1-x}$ systems are chosen for the extended discussion. Figures 4.7 illustrates the self-diffusion coefficients of the ions as a function of the Cl^- composition at 353 K. For both the systems, the self-diffusion coefficients were found to decrease with the increase in Cl^- concentration. Self-diffusion coefficients of the ions in the [C_4mim] Cl_x $[MeSO_4]_{1-x}$ mixtures decreased linearly with the Cl^- concentrations while those for the [C_4mim] Cl_x $[NTf_2]_{1-x}$ system dropped

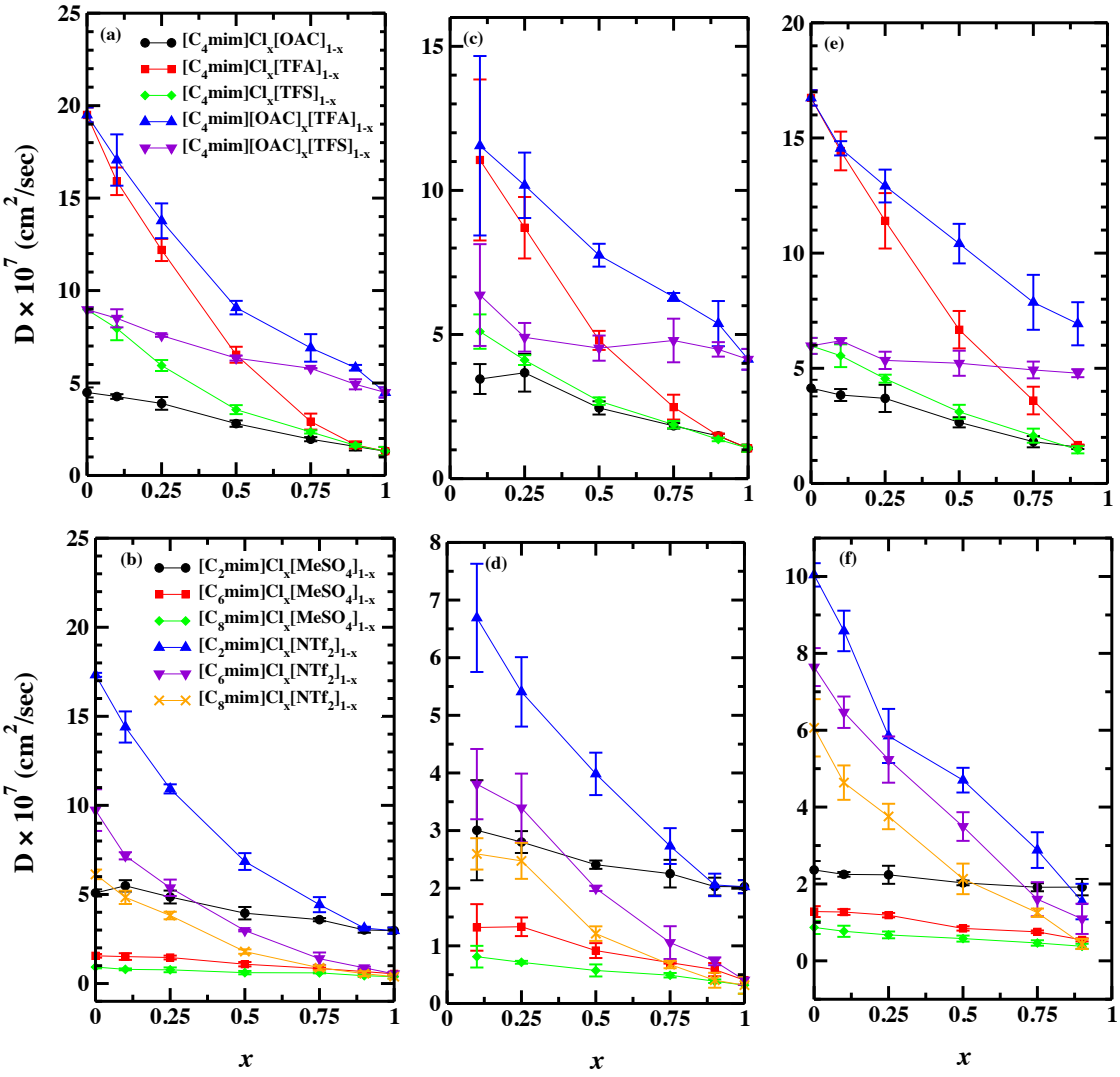

Figure 4.6: Self-diffusion coefficients for cations in (a) and (b); anion1 in (c) and (d); and anion2 in (e) and (f) for the mixture systems of [C_4mim] Cl_x $[OAC]_{1-x}$, [C_4mim] Cl_x $[TFA]_{1-x}$, [C_4mim] Cl_x $[TFS]_{1-x}$, [C_4mim] $[OAC]_x$ $[TFA]_{1-x}$, [C_4mim] $[OAC]_x$ $[TFS]_{1-x}$, [C_2mim] Cl_x $[MeSO_4]_{1-x}$, [C_6mim]$Cl_x[MeSO_4]_{1-x}$, [C_8mim]$Cl_x[MeSO_4]_{1-x}$, [C_2mim]$Cl_x[NTf_2]_{1-x}$, [C_6mim] Cl_x $[NTf_2]_{1-x}$, and [C_8mim] Cl_x $[NTf_2]_{1-x}$ as a function of composition at 353 K. Standard deviations were calculated from three independent trials for all mixture compositions. Note that the continuous lines joining data points are only guide to the eye. Also, [C_4mim] Cl_x $[OAC]_{1-x}$ is designated as [Cation] $[Anion1]_x$ $[Anion2]_{1-x}$

rapidly – in a non-linear fashion – with increase in the Cl^- concentrations at least up to 0.75 mole fraction beyond which the decrease in the self-diffusion coefficients was gradual. A closer inspection of the cation self-diffusion coefficients reveals that only a small amount of Cl^- is capable of reducing the self-diffusion of $[C_4mim]^+$ to half of its original value in $[C_4mim][NTf_2]$. This can further be visualized by considering

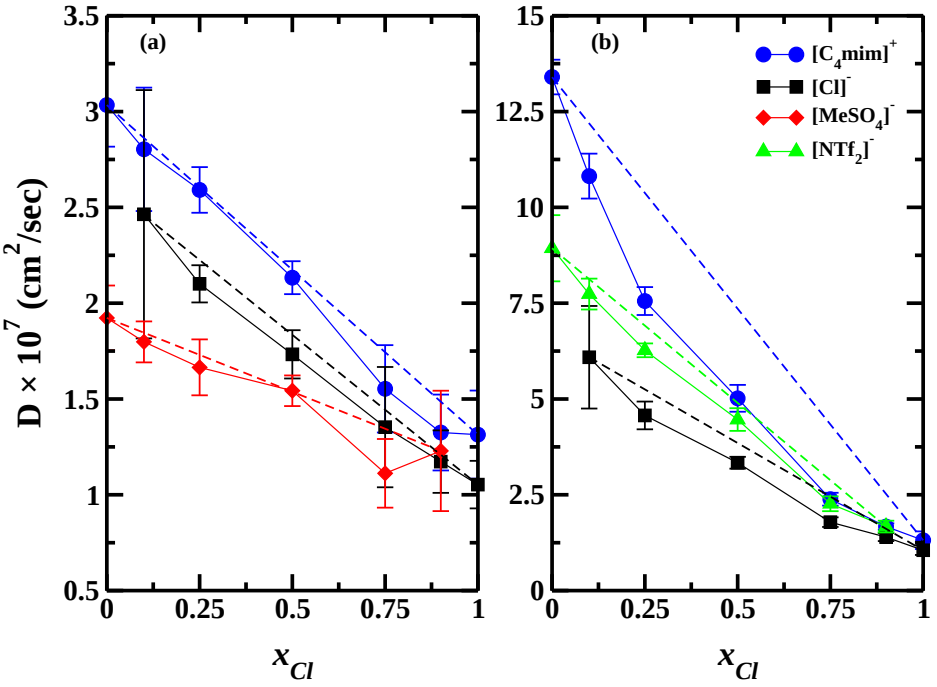

Figure 4.7: Variation of self-diffusion coefficients of cations and anions as the function of anion molar composition for (a) $[C_4mim]\ Cl_x\ [MeSO_4]_{1-x}$ and (b) $[C_4mim]\ Cl_x\ [NTf_2]_{1-x}$ mixture systems. Standard deviations were calculated from three independent MD trials for all mixture compositions. Continuous lines are only guide to the eye, while dotted lines represent linear weighted average (ideal mixing).

the dotted line shown in Figures 4.7 that display the ideal prediction of self-diffusion coefficients of the ions. It is clear that for $[C_4mim]\ Cl_x\ [MeSO_4]_{1-x}$ mixtures the self-diffusion coefficients of ions, at any particular mixture composition, can be estimated entirely based on the self-diffusion coefficients of ions in the pure IL analogues, by taking a mole fraction weighted average. On the other hand, self-diffusion coefficients

of ions in $[C_4mim]\ Cl_x\ [NTf_2]_{1-x}$ system deviates from linear mixing rule for the entire composition range, suggesting the presence of nonideality.

It is interesting to see that the self-diffusion coefficients of the ions in $[C_4mim]Cl_x\ [MeSO_4]_{1-x}$ system follow the order: $[C_4mim]^+ > Cl^- > [MeSO_4]^-$ up to Cl^- mole ratio of 50 mol %. Beyond this composition, the self-diffusion coefficient of the ions is merely superimposable especially taking into account statistical uncertainties. However, the self-diffusion coefficient of $[MeSO_4]^-$ is higher than that of Cl^- in the respective pure ILs, but when the mixture system is considered Cl^- exhibits self-diffusion coefficients that are either higher or nearly equal to those of $[MeSO_4]^-$ for the entire composition range. Since the interaction strengths between either $[C_4mim]^+$-Cl^- or $[C_4mim]^+$-$[MeSO_4]^-$ are not very different slower diffusion of $[MeSO_4]^-$ than Cl^- is probably related its larger size. In addition, the negative excess molar volumes also contribute to a decrease in the self-diffusion coefficients. On the contrary, the order of the anion self-diffusion coefficients in $[C_4mim]Cl_x[NTf_2]_{1-x}$ system is reversed such that it is higher for the bulkier $[NTf_2]^-$ in comparison to the smaller Cl^- anion. As will be shown in the following subsections, the higher self-diffusion coefficient of $[NTf_2]^-$ is probably due to re-organization of $[NTf_2]^-$ from a stronger, in-plane, direct interaction position to a weaker anion-π interaction above and below the cation imidazolium-ring, allowing cation, $[C_4mim]^+$, and anion, $[NTf_2]^-$, to diffuse together which is reflected in their respective self-diffusion coefficients beyond 50 mol % of Cl^-.

4.1.4 Ionic Conductivities

Ionic conductivities were calculated using two different formalisms: Einstein's relation (eq. 3.32) and the Nernst-Einstein (NE) equation (eq. 3.33). As mentioned earlier, eq. 3.32 accounts for the correlated ion motion while the latter assumes that diffusion

of each species contributes to the total ionic conductivity of the system independent of the presence of the other ions. The presence of ion correlations results in the deviation from the ionic conductivities computed from the NE relation, which has been pointed out by many earlier studies. [221–224]

Similar to self-diffusion coefficients Figures 4.8 (a) - (d) display ionic conductivities determined from eq. 3.32 and eq. 3.33 for the entire composition range for all the mixture systems except [C_4mim] Cl_x $[MeSO_4]_{1-x}$ and [C_4mim] Cl_x $[NTf_2]_{1-x}$ which are discussed below separately for deeper insights. The trends followed by ionic conductivity computed using NE relation are the same as that obtained by Einstein's relation. Some general features for the pure IL systems are: (i) for the given cation ($[C_4mim]^+$), the ionic conductivity decreases in the order [C_4mim] $[NTf_2]$ > [C_4mim] [TFA] > [C_4mim] $[MeSO_4]$ > [C_4mim] [TFS] > [C_4mim] [OAC] > [C_4mim] Cl. The higher ionic conductivity for [C_4mim][TFA] than that of [C_4mim][TFS] is opposite to the experimental observation at room temperature, [219] which is possibly related to the fact that even the self-diffusion coefficients are overpredicted for the molecular model adopted in this work for [C_4mim][TFA]; (ii) similar to the self-diffusion coefficients, the ionic conductivities also decreases with longer alkyl chains on the imidazolium-based cations. [219, 268]

A closer look suggests that the ionic conductivity values for the binary IL systems fall within those for the parent ILs with the exception of 10:90 and 25:75 compositions of [C_4mim] $[OAC]_x$ $[TFA]_{1-x}$ and 90:10 mixture of [C_4mim] Cl_x $[OAC]_{1-x}$. Such behavior can potentially be exploited for electrochemical applications. It is also interesting to note that ionic conductivity for the IL system [C_2mim] Cl_x $[MeSO_4]_{1-x}$ exhibits a weak dependence on the molar composition, suggesting that the ionic correlations remain nearly identical as a result of simple ion exchange.

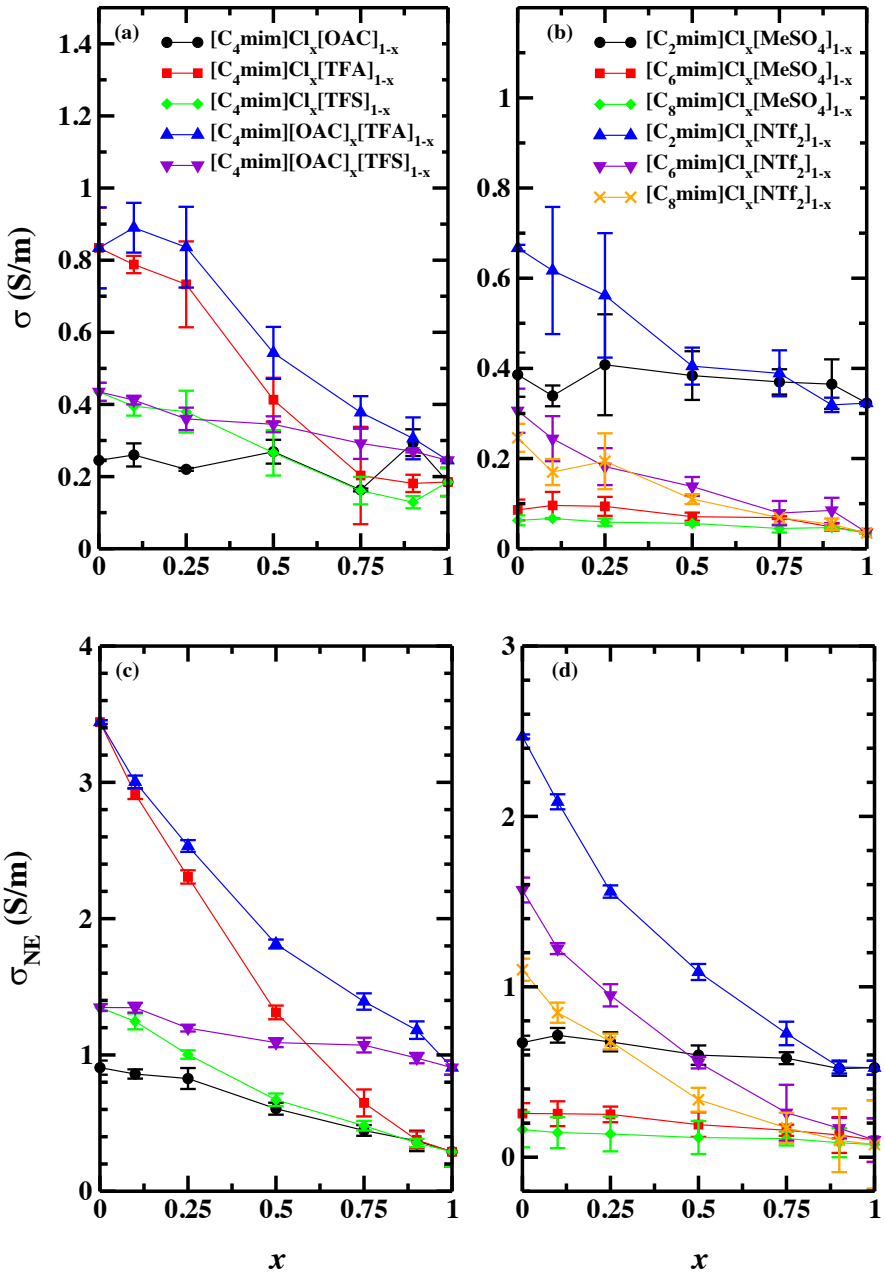

Figure 4.8: Ionic conductivity for common cation $[C_4mim]^+$ paired with different anions namely Cl^-–$[OAC]^-$, Cl^-–$[TFA]^-$, Cl^-–$[TFS]^-$, $[OAC]^-$–$[TFA]^-$, and $[OAC]^-$–$[TFS]^-$; and cations $[C_2mim]^+$, $[C_6mim]^+$, and $[C_8mim]^+$ coupled with different anions Cl^-–$[MeSO_4]^-$ and Cl^-–$[NTF_2]^-$ computed using the Einstein relation (a) and (b) and Nernst-Einstein (NE) relation (c) and (d) as a function of composition at 353 K. Standard deviations were calculated from three independent trials for all mixture compositions. Note that the continuous lines joining data points are only guide to the eye.

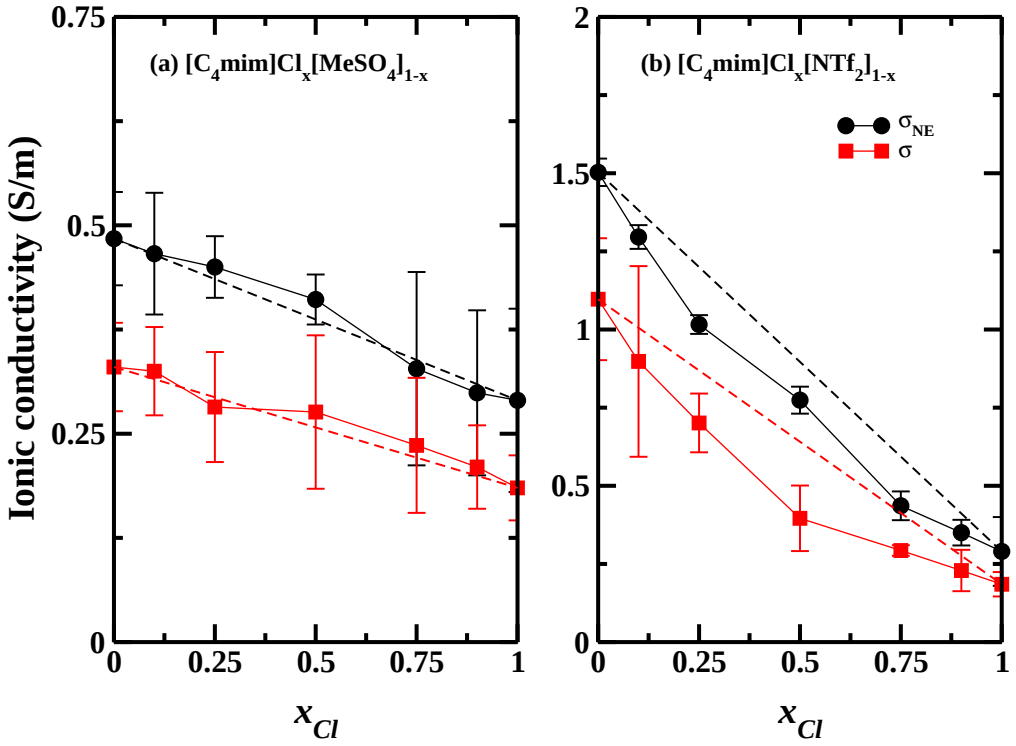

Figure 4.9: Variation of ionic conductivities, calculated using both Einsteins's and Nernst-Einstein's relation, as the function of anion molar composition for (a) [C_4mim] Cl_x $[MeSO_4]_{1-x}$ and (b) [C_4mim] Cl_x $[NTf_2]_{1-x}$ mixture systems. Standard deviations were calculated from three independent MD trials for all mixture compositions. Continuous lines are only guide to the eye, while dotted lines represent linear weighted average (ideal mixing).

Figures 4.9 depicts the ionic conductivities computed from the NE (eq. 3.33) and the Einstein (eq. 3.32) relations for both [C_4mim] Cl_x $[MeSO_4]_{1-x}$ and [C_4mim] Cl_x $[NTf_2]_{1-x}$ mixture systems at 353 K. Similar to self-diffusion coefficient data, ionic conductivities, using both the formalisms, for [C_4mim] Cl_x $[MeSO_4]_{1-x}$ mixtures decreased linearly with the Cl^- concentrations and can be estimated entirely based on the pure IL analogues, by taking a mole fraction weighted average. On the other hand, for [C_4mim] Cl_x $[NTf_2]_{1-x}$ system ionic conductivities reduces in a non-linear fashion and deviates from linear mixing rule for the entire composition range, hinting

nonideality.

Apparently, for all the mixture systems, the calculated NE conductivities are higher

Table 4.2: The degree of correlated motion, given by $Y = \left(\frac{\sigma}{\sigma_{\mathrm{NE}}}\right)$, for pure ILs studied in this work, at 353 K

Ionic Liquid	Predicted Y
$[C_4mim][TFS]$	0.32
$[C_4mim][TFA]$	0.24
$[C_4mim][OAC]$	0.32
$[C_2mim][NTf_2]$	0.27
$[C_4mim][NTf_2]$	0.73
$[C_6mim][NTf_2]$	0.20
$[C_8mim][NTf_2]$	0.22
$[C_2mim][MeSO_4]$	0.57
$[C_4mim][MeSO_4]$	0.68
$[C_6mim][MeSO_4]$	0.34
$[C_8mim][MeSO_4]$	0.39
$[C_2mim]Cl$	0.62
$[C_4mim]Cl$	0.64
$[C_6mim]Cl$	0.36
$[C_8mim]Cl$	0.47

than those obtained from the Einstein's relation implying the presence of correlated ionic motions. The degree of correlated motion can be gauged by computing "ionicity", the ratio $Y = \left(\frac{\sigma}{\sigma_{\mathrm{NE}}}\right)$, which provides a measure of the fraction of ions available for charge transport. When $Y = 0$ the ionic motion is said to be completely correlated such that there is no net transport of charge. On the other hand, ions can be considered to be fully dissociated and move independent of the other ions when $Y = 1$. The values of Y for pure ILs are reported in Table 4.2 which shows that Y span over the range from 0.2 to 0.75, suggesting that the considered ILs and their mixtures show a range of ionic character. The ionicity values of 0.32 and 0.58 calculated for $[C_4mim][TFS]$ and $[C_2mim][MeSO_4]$, respectively are in reasonable agreement with those experimentally derived by Husson and co-workers. [268] Similar Y values have been reported for other pure ILs. [184, 269, 270] Further, our results predict that the

ionicity decreases with an increase in the alkyl chain length on the cation, in agreement with experiments. [219, 268] Strikingly, the IL mixtures that show higher ionic conductivity than that of the constituent ILs are also characterized by higher ionicity values in comparison to the parent ILs. All the composition dependent data is included in Appendix A.

4.2 Molecular Origins of Non-ideality in Binary Ionic Liquid Mixtures: Thermophysical Property Trends Rationalized on Structural Transitions

In this section, the focus is on the microstructures of two binary IL mixture systems, one containing the cation 1-n-butyl-3-methylimidazolium, $[C_4mim]^+$, paired with the anions Cl^- and methylsulfate $[MeSO_4]^-$ ($[C_4mim]Cl_x[MeSO_4]_{1-x}$) while the other is composed of $[C_4mim]^+$ in combination with Cl^- and bis (trifluoromethanesulfonyl)imide $[NTf_2]^-$ ($C_4mim]Cl_x$ $[NTf_2]_{1-x}$) that will provide understanding on what changes in the structure giving rise to linear vs. non-linear thermophysical property trends. The chemical structure representation is shown in Figure 4.10.

As described in section 4.1, [C_4mim] Cl_x $[MeSO_4]_{1-x}$ shows near-ideal or linear mixing behavior while [C_4mim] Cl_x $[NTf_2]_{1-x}$ display non-linear thermophysical property trends. For the [C_4mim] Cl_x $[MeSO_4]_{1-x}$ system, both the anions Cl^- and $[MeSO_4]^-$ possess very strong and similar hydrogen bonding capability with the cation. On the other hand, $[NTf_2]^-$ having a large size and very weak hydrogen bonding affinity towards cation presents Cl^- and $[NTf_2]^-$ anions at the two extremes of the hydrogen bonding scale. The hydrogen bond basicity decreases in the order $Cl^- > [MeSO_4]^- > [NTf_2]^-$ with β values of 0.95, 0.75 and 0.42 respectively. [41, 42]

As will be shown in the following subsections, the difference in the strength of hy-

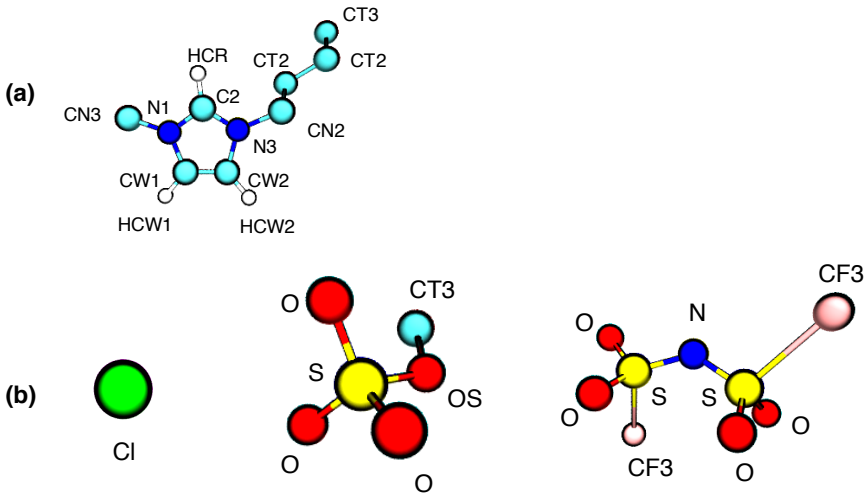

Figure 4.10: Chemical structure schematic and atom numbering used in this work (a) $[C_4mim]^+$ (b) Cl^-, $[MeSO_4]^-$ and $[NTf_2]^-$ respectively.

drogen bonding and size/molar volume of the anions lead to dramatic changes in the organizations of the ions, in comparison to the pure IL structure, and thus, accounts for the nonideal thermophysical property behavior.

Liquid Structures:

4.2.1 Spatial Distribution Functions

Figures 4.11 illustrates organization of anions (Cl^-, $[MeSO_4]^-$ or $[NTf_2]^-$) around the given cation ($[[C_4]mim]^+$) as a function of Cl^- concentration through spatial distribution functions (SDFs) for both the $[C_4mim]$ Cl_x $[MeSO_4]_{1-x}$ and $[C_4mim]$ Cl_x $[NTf_2]_{1-x}$ mixture systems at 353 K. The local spatial (isosurface) densities are plotted such that the anion density is 2.5 times the corresponding bulk density. For pure ILs, the general features of these SDFs include: (i) interactions of the anions with the imidazolium-ring at acidic hydrogen sites; (ii) the anions tend to occupy both in-plane and on-top positions. Further, the extension of the isosurface in the vicinity of the ring hydrogen atoms above and below the ring implies that a given anion is likely to mediate interactions between two cation rings. Additionally, such behavior

is indicative of the ability of the anion to participate in anion-π interactions. It is also interesting to note that, for both the mixtures, Cl^- anion is able to interact with the methyl group (CN3) while the site is unavailable to the bulkier anions $[MeSO_4]^-$ and $[NTf_2]^-$.

For $[C_4mim]Cl_x[MeSO_4]_{1-x}$ system, the SDFs for Cl^- and $[MeSO_4]^-$ display similar

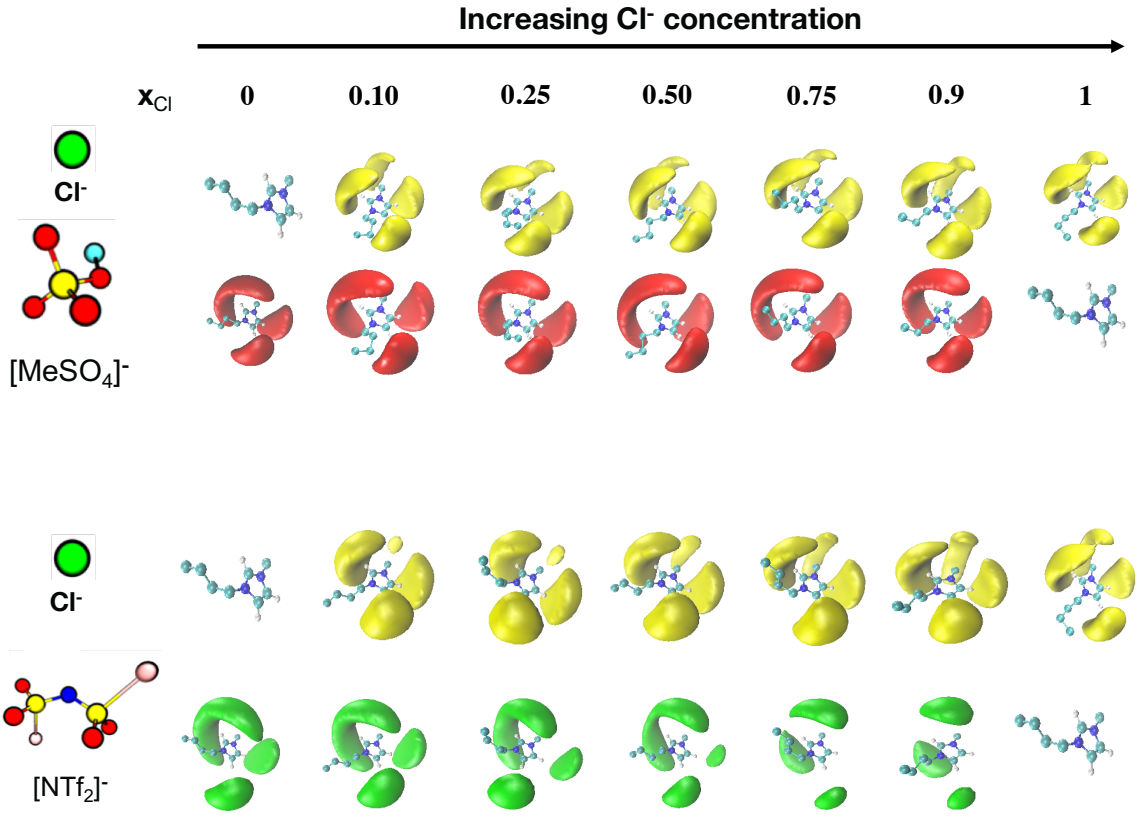

Figure 4.11: Spatial distribution functions (SDFs), of anions around the cations as the function of anion molar composition for (a) $[C_4mim]$ Cl_x $[MeSO_4]_{1-x}$ and (b) $[C_4mim]$ Cl_x $[NTf_2]_{1-x}$ mixture systems. Isosurface density is 2.5 times the bulk density. Color coding: Cl^- in yellow and $[MeSO_4]^-$ in red and $[NTf_2]^-$ in green. Atoms: C in cyan, N in blue, and H in white.

distributions of density around the ring hydrogen atoms throughout the entire composition range, which is not surprising given that there is only a marginal difference in their basicity, suggesting very weak dependence of change in the cation-anion interactions. In other words, the molecular interactions in the pure ILs are preserved

even in the mixture, referred to as "native interactions" in this dissertation, such that the mixture properties can be estimated from those of pure ILs, in line with the observations made in the thermophysical properties for this system. Furthermore, the enrichment of Cl^- around the CN3 carbon in addition to the ring hydrogen atoms even at the lowest Cl^- concentrations points to the fact that as Cl^- is added to the system it can favorably bind to the CN3 site, which remains inaccessible to $[MeSO_4]^-$. This also suggests that Cl^- gets accommodated within the existing ionic framework and, hence, probably explains the negative excess molar volume.

Unlike the $[C_4mim]Cl_x[MeSO_4]_{1-x}$ system, a rich diversity of structural transitions occurs in the $[C_4mim]Cl_x[NTf_2]_{1-x}$ system as the Cl^- concentration is varied. For the lowest Cl^- concentration examined in this work (10 mol%), the enhancement in Cl^- density around the CN3 site is relatively minor when compared to that in the $[C_4mim]Cl_x[MeSO_4]_{1-x}$ system implying that Cl^- primarily displaces $[NTf_2]^-$ from the ring binding sites. As the concentration of Cl^- further increases (50 mol%), there is a noticeable decrease in the $[NTf_2]^-$ concentration around the most acidic site (HCR). Moreover, $[NTf_2]^-$ appears to have been nearly eliminated from interacting with another hydrogen bonding site, pointing away from the butyl chain (HCW1). At this concentration, Cl^- density increases around the CN3 primarily due to an expected increase in the competition among the Cl^- occupying the most favorable binding sites. At the highest Cl^- content (90 mol%) in the mixture, $[NTf_2]^-$ completely loses its ability to access the ring hydrogen sites and the only significant interactions with the cation are established above or below the plane of the ring. This indicates the emergence of different molecular interactions that are not present in the pure ILs, referred to as "non-native interactions" in this dissertation, that can help explain the non-linear thermophysical property trends.

4.2.2 Radial Distribution Functions

The center-of-mass (COM) based radial distribution functions (RDFs) – a 2D representation of SDFs – elucidating cation-anion and cation-cation interactions are shown in Figures 4.12 (a)-(f) for both the $[C_4mim]Cl_x[MeSO_4]_{1-x}$ and $[C_4mim]Cl_x[NTf_2]_{1-x}$ mixture systems at 353 K. First, considering cation-anion COM-based RDFs for $[C_4mim]Cl_x[MeSO_4]_{1-x}$, Figures 4.12 (a) and (b), it is clearly evident that the peak intensity within the first coordination shell is greater than 1, which indicates an enhanced localization of both the anions around the cation. The RDFs reveal that the peak intensity for the $[C_4mim]$-Cl is higher than that of the $[C_4mim]$-$[MeSO_4]$ implying that Cl^- is more structured around the cation and is consistent with the fact that Cl^- is a stronger hydrogen bond acceptor than $[MeSO_4]^-$. Secondly, consistent with the extended SDFs above and below the imidazolium ring-plane, a smaller second peak suggests that anions are able to mediate interactions between two neighboring cations. Further, the bulkier nature of the $[MeSO_4]^-$ anion with respect to the Cl^- anion is apparent from the fact that the first coordination shell – the distance of RDF minimum after the first peak – appears at a distance farther than that of Cl^-. Also, the first peak appears at a distance of $\sim$4.1 Å for the $[C_4mim]$-Cl RDFs while it develops at $\sim$4.6 Å for the $[MeSO_4]^-$ anions which can be expected given that Cl^- has a stronger affinity for the cation. This happens irrespective of the change in mixture composition. On top of that, the intensity of the first peak in both the RDFs shows a weak dependence on the anion concentration suggesting that the cation-anion interactions remain largely unperturbed due to the dilution of one anion relative to the other. In other words, similarities of a given pair of cation-anion, for example $[C_4mim]$-Cl, RDF can be explained by a simple exchange of Cl^- with the $[MeSO_4]^-$, as Cl^- is depleted in the system.

The fact that $[NTf_2]^-$ is larger and weakly coordinating than both $[MeSO_4]^-$ and

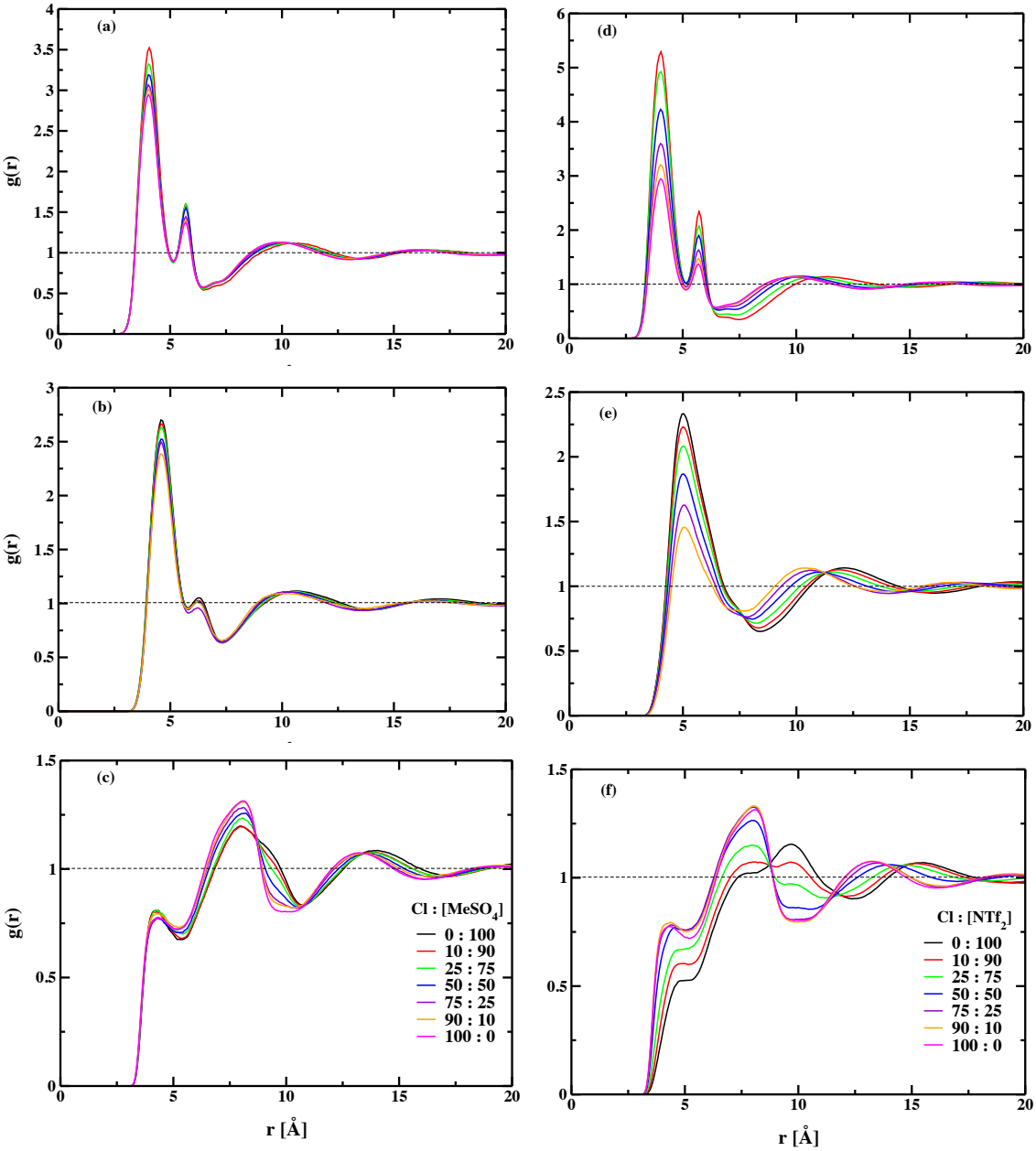

Figure 4.12: Radial distribution functions (RDFs) with varying Cl^- ion concentration between (a) cation-Cl and (b) cation-$[MeSO_4]$, based on center-of-mass (COM), and (c) cation-cation, based on center-of-ring (COR), in the $[C_4mim]Cl_x[MeSO_4]_{1-x}$ system; (d) cation-Cl and (e) cation-$[NTf_2]$, based on center-of-mass (COM), and (f) cation-cation, based on center-of-ring (COR) in the $[C_4mim]Cl_x[NTf_2]_{1-x}$.

Cl^- is apparent from the Figure 4.12 (e) which shows a significant increase in the first coordination shell radius and the first peak displaced to ∼5 Å. However, unlike $[C_4mim]Cl_x[MeSO_4]_{1-x}$ system, remarkable differences in the intensities of the first peak are observed with varying compositions such that, for both the RDFs, intensities increase as the mole fraction of Cl^- decreases. These differences are more pronounced for the $[C_4mim]$-Cl RDFs than $[C_4mim]$-$[NTf_2]$ RDFs. Additionally, $[C_4mim]$-$[NTf_2]$ RDFs indicate that the first coordination shell around the cation becomes more compact with increasing Cl^- content in the system. Better organization of the Cl^- anion is primarily due to increase in the number density of Cl^- while relatively more structured first solvation shell for $[NTf_2]^-$ is principally due to its conformational flexibility (see Figure 4.13) that allows dramatic rearrangement of $[NTf_2]^-$ at high Cl^- concentrations.

In contrast to the direct hydrogen bonding and electrostatic interactions between

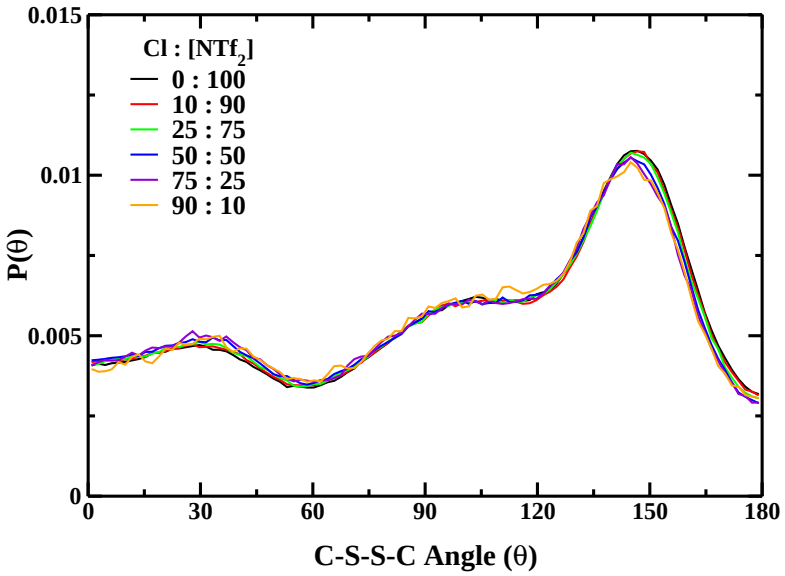

Figure 4.13: Distribution of pseudo-dihedral (C-S-S-C) of $[NTf_2]^-$ – showing conformational flexibility of the anion – as a function of mixture composition for $[C_4mim]Cl_x[NTf_2]_{1-x}$ system.

cations and anions, imidazolium cation-cation interactions usually involve π-π stacking. [45, 271] Strikingly, the analyses presented so far point to the possibility that the direct cation-cation interactions may be partly replaced by the anion-mediated interactions. It has been suggested earlier that that presence of a pre-peak at $\sim$4 Å for center-of-ring (COR) based cation-cation ([C_4mim]-[C_4mim]) RDF can be taken as an indication of the π-π stacking. [45] Figure 4.12 (c) and (f) reports the COR-based cation-cation RDFs for both the mixture systems. For [C_4mim] Cl_x $[MeSO_4]_{1-x}$ presence of pre-peak at $\sim$4 Å over the entire range of compositions indicating that π-π stacking is prevalent in these mixtures. Additionally, the position and intensity of the pre-peak bear weak concentration dependence suggesting that the π-π stacking between the cations are preserved at all the concentrations although the distance between the cation rings is slightly increased as the proportion of $[MeSO_4]^-$ increases (evident from the shift of the RDF minimum distance). However, the first peak intensity and the first solvation shell minimum are concentration dependent. The origin of the shift is related to preferable anion-π stacking as the relative amount of $[MeSO_4]^-$ increases, seen as extended SDF isosurfaces above and below the ring. For [C_4mim] Cl_x $[NTf_2]_{1-x}$ system, the COR-based cation-cation RDFs show that the pre-peak shoulder becomes less prominent and shifts to larger distances with decreasing Cl^- which is an indication of progressive disruption of the π-π stacking. Further, with an increase in the $[NTf_2]^-$ concentration, the first solvation shell expands considerably, and the corresponding primary peak in the RDFs is displaced from $\sim$7 Å to $\sim$10 Å. As concluded from SDFs, due to the bulkier size of $[NTf_2]^-$, $[NTf_2]^-$ anion occupies the position above and below the imidazolium ring and is able to shield the cation-cation interaction disrupting π-π stacking interactions, yet allowing the formation of anion-π interactions. This shielding increases the distance between two cations and perhaps explain small but positive excess molar volumes.

It is also worth mentioning that these RDFs show cation-anion interactions at a distance of ∼4 Å which is not a true representative of the formation of hydrogen bonds. Though the results are not included in this dissertation, the presence of hydrogen bonds (published elsewhere [250]) can be discerned by computing RDFs between acidic hydrogens present on the imidazolium ring (cation) and Cl^-, and oxygen atoms of either $[MeSO_4]^-$ or $[NTf_2]^-$, which display a first RDF peak at a distance of ∼2 Å suggesting formation of hydrogen bonds. However, it is noteworthy that the concentration dependence trend of such RDFs is strikingly similar to COM-based RDFs. Thus, in this dissertation, only COM-based RDFs will be discussed for this

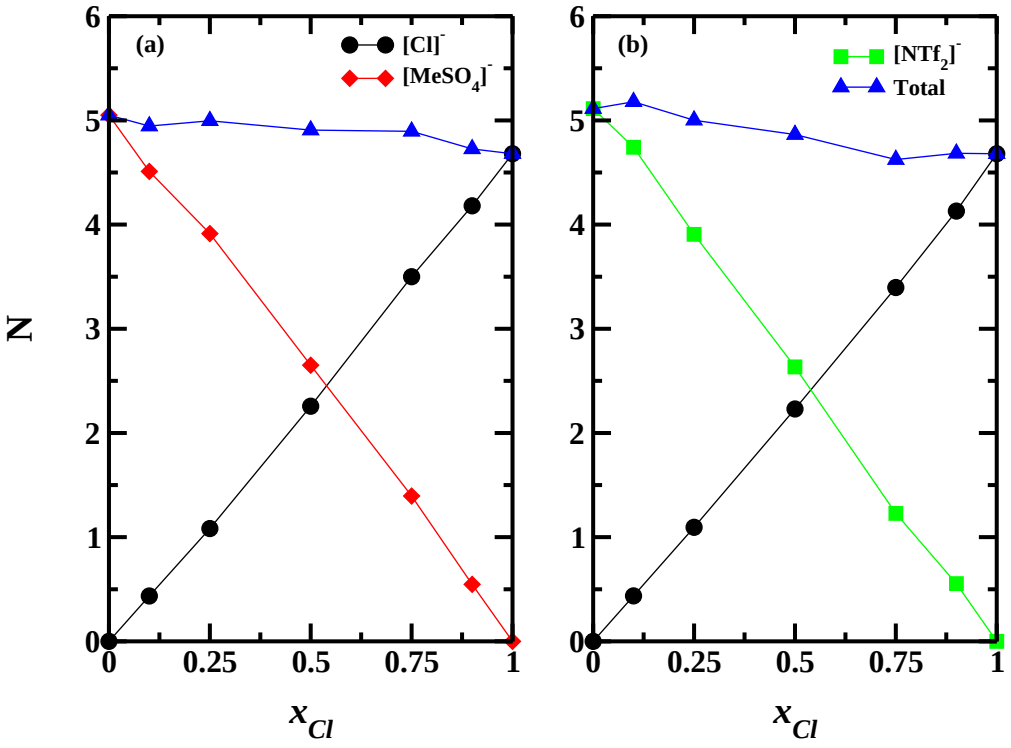

Figure 4.14: Average coordination numbers of anions Cl^-, $[MeSO_4]^-$ and $[NTf_2]^-$ with respect to a given $[C_4mim]^+$ within the first solvation shell, defined by the respective RDF minimum, for both the mixture systems of $[C_4mim]\ Cl_x\ [MeSO_4]_{1-x}$ and $[C_4mim]\ Cl_x\ [NTf_2]_{1-x}$ respectively.

and the following sections, as the primary goal is to investigate the composition de-

pendence of cation-anion interactions.

The overall coordination numbers, shown in Figures 4.14 demonstrate that the first coordination shell of the cation is occupied by ∼5 anions over the entire composition range for both the mixture systems, suggesting that these mixtures are "supramolecular" in nature forming structures that are connected via hydrogen bond networks. Further, it can be easily seen that the composition dependent trends for both the mixture systems are very similar. This suggests that although the overall the coordination of anion with cation is not marked different there are subtle re-arrangements of the anions around the cation that leads to nonideal property behavior.

4.2.3 Angular Distribution Functions

To further scrutinize the subtle re-arrangement of the anions around the cation, the relative orientational distribution in the form of angular distribution functions (ADFs), for the anions around the cation in the respective first coordination shell are computed. The coordinate system for these calculations is fixed at the center of the imidazolium ring and is sketched in the inset of Figure 4.15. The ADFs are computed for the angles designated as θ and and ϕ; the polar angle θ is the angle between the ring normal and the vector connecting the COM of an anion and COR, while the azimuthal angle ϕ is defined with respect to the vector joining the COR to the nitrogen bonded to the first carbon atom in the butyl chain.

For $[C_4mim]Cl_x[MeSO_4]_{1-x}$ mixture system, polar-angle ADFs suggest that the Cl^- locates in the plane of the positively charged imidazolium ring at all the concentrations, the probability of which is the greatest at the lowest Cl^- concentration. The in-plane locations of Cl^- enable direct hydrogen bonding interaction to be established between the anion and the ring hydrogens. In addition, azimuthal-angle ADFs

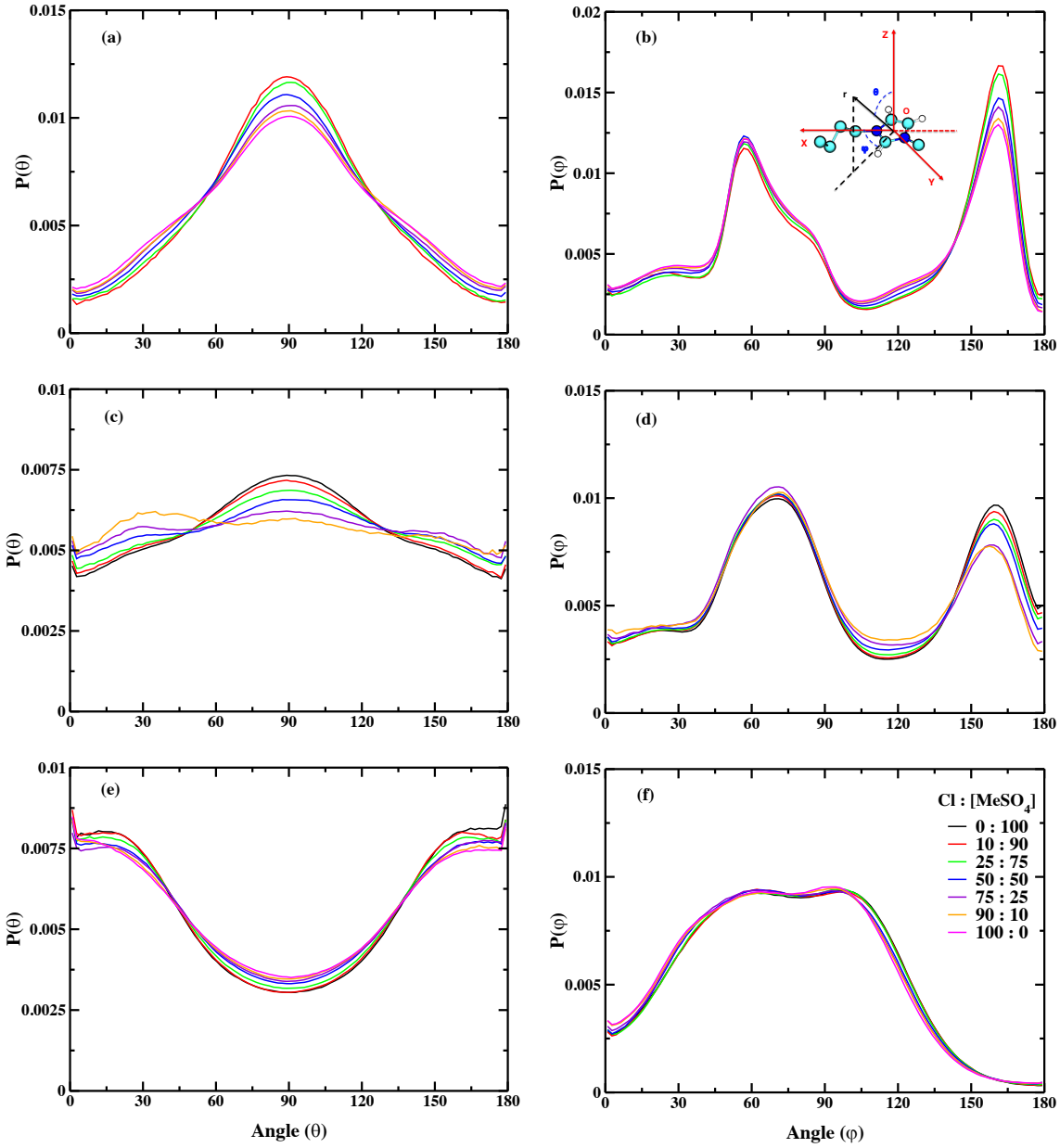

Figure 4.15: Angular distribution functions (ADFs) of COM of anions Cl^-, $[MeSO_4]^-$ and cation around a given $[C_4mim]^+$ within the first solvation shell, defined by the respective RDF minimum, for mixture system of $[C_4mim]$ Cl_x $[MeSO_4]_{1-x}$ are shown in (a) - (b); (c) - (d); and (e) - (f) respectively, while the coordinate system defining a particular angle is shown as an inset in (b).

show that the maximum probability of finding a Cl^- anion is between 60-90° – which again points to the in-plane location of Cl^- – and 150-180° which locates Cl^- near the CN3 methyl position. As expected, there is a weak concentration dependence of in-plane Cl^- anions. However, noticeable changes in the 150-180° regions are visible, which is not directly apparent in SDFs suggesting subtle re-organization even in the $[C_4mim]Cl_x[MeSO_4]_{1-x}$ system. Further, the lowest probability of azimuthal-angle ADFs for 0-30° suggests that Cl^- anion is not able to approach the cation from the butyl-chain side, which is also consistent with the SDFs. Similarly, for $[MeSO_4]^-$ anion the polar-angle ADFs suggests that as the Cl^- concentration is increased the in-plane location of $[MeSO_4]^-$ anion is slightly reduced, occupying positions above and below the ring-plane, evident from the increase in propensity around 0-60° and 120-180° regions, while the azimuthal angle ADFs mimics that of Cl^- anion. This corroborates the inferences drawn from RDFs and SDFs that the interactions are preserved and can be explained on the basis of a simple exchange of Cl^- with the $[MeSO_4]^-$ as Cl^- is depleted in the system. Also, the ADFs showed in Figure 4.15 (e) and (f) and Figure 4.17 (a) suggests that π–π interactions are not disrupted for this mixture system.

Likewise, for $[C_4mim]Cl_x[NTf_2]_{1-x}$ systems the polar-angle and azimuthal-angle ADFs of Cl^- around cation are qualitatively similar to those obtained for the $[C_4mim]Cl_x[MeSO_4]_{1-x}$ system, but perhaps with stronger concentration dependence. Very different behavior is observed for position of $[NTf_2]^-$ anions. Although the polar-angle ADFs suggests that $[NTf_2]^-$ is displaced from equatorial position to the position above and below the cation-ring, the azimuthal-angle ADFs shows that the interaction position of $[NTf_2]^-$ is very different from Cl^- anion and the location is highly dependent on the mixture composition. The $[NTf_2]^-$ conformers in or near the plane of the imidazolium ring produce a broad peak which advocates the presence

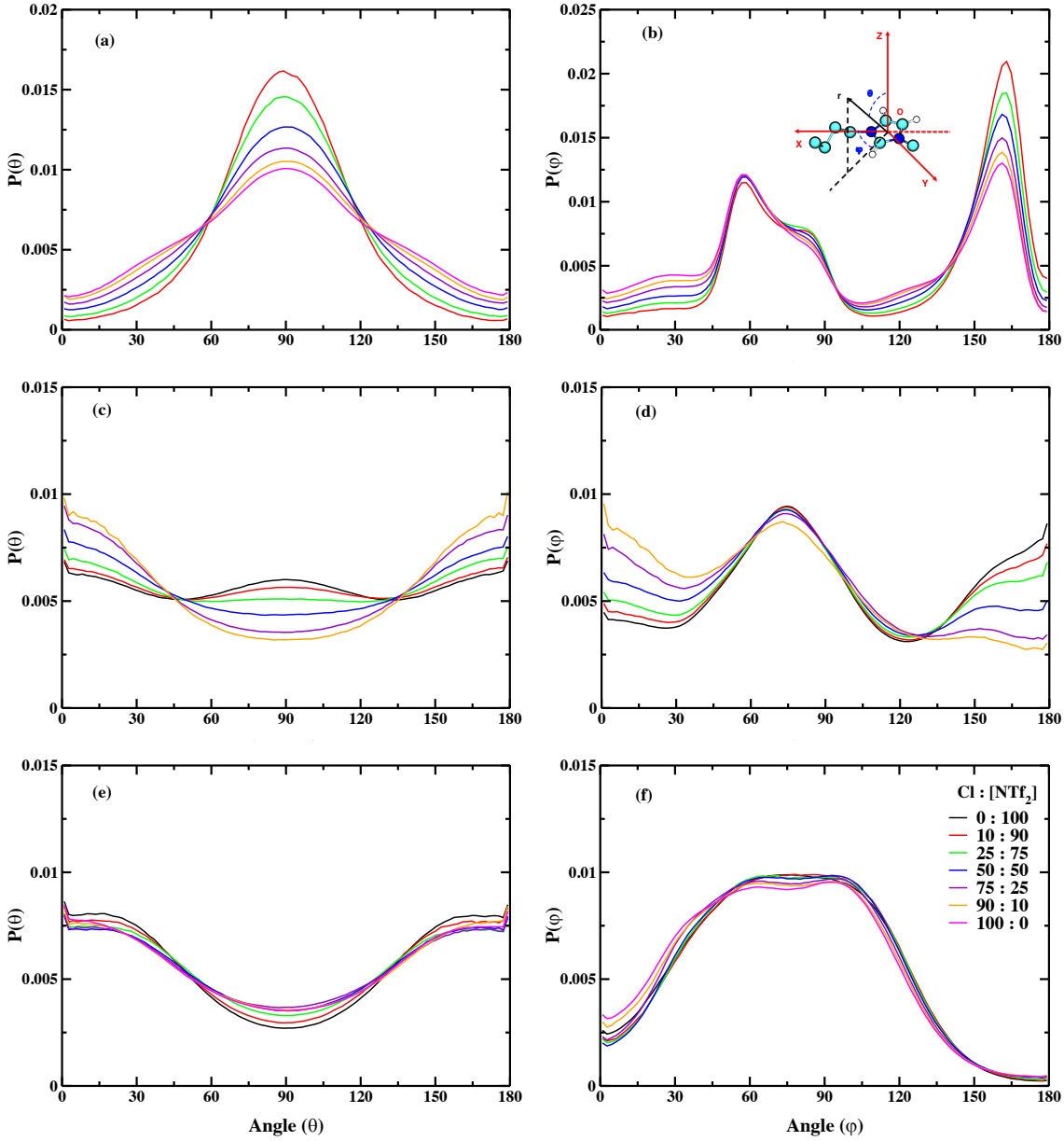

Figure 4.16: Angular distribution functions (ADFs) of COM of anions Cl^-, $[NTf_2]^-$ and cation around a given $[C_4mim]^+$ within the first solvation shell, defined by the respective RDF minimum, for mixture system of $[C_4mim]$ Cl_x $[NTf_2]_{1-x}$ are shown in (a) - (b); (c) - (d); and (e) - (f) respectively, while the coordinate system defining a particular angle is shown as an inset in (b).

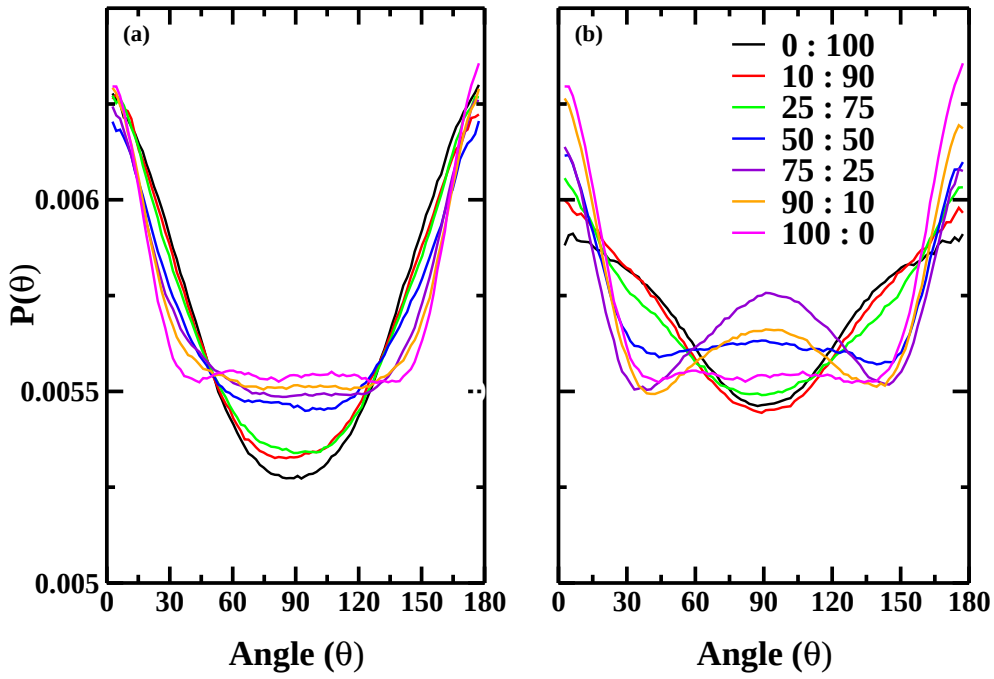

Figure 4.17: Angular distribution functions (ADFs) of COR of cations around a given $[C_4mim]^+$ within the first solvation shell, defined by the respective RDF minimum, for (a) $[C_4mim]$ Cl_x $[MeSO_4]_{1-x}$ and (b) $[C_4mim]$ Cl_x $[NTf_2]_{1-x}$ mixture systems.

of favorable $[NTf_2]^-$ mediated anion-π interactions and the its high conformational flexibility. It can also be realized that with the increase in Cl^- concentration, $[NTf_2]^-$ is depleted from the CN3 methyl position and tries to occupy a position towards the butyl chain. This is consistent with the observation made in SDFs that at 75 mole % of Cl^- $[NTf_2]^-$ loses its ability to interact with the ring-hydrogen that points away from the butyl chain. Furthermore, ADFs showed in Figure 4.17 (b) suggests that cation-cation interaction is changed with the change in the molar composition of the mixture system.

The above analyses provide a convincing argument that for the $[C_4mim]Cl_x[MeSO_4]_{1-x}$ system the cation-cation and cation-anion interactions in the pure IL are retained to

a large extent in the IL mixtures as well. Replacement of $[MeSO_4]^-$ by Cl^- thus does not incur an energetic penalty. In fact, it was shown that Cl^- could establish additional stabilizing interactions with the methyl group of the cation. On the other hand, for the $[C_4mim]$ Cl_x $[NTf_2]_{1-x}$ system, the presence of $[NTf_2]^-$ disrupts the favorable π-π interactions by significantly increasing the distance between cations and promoting the formation of anion-π interaction due to its size and weak coordinating behavior. The non-linear thermophysical property trends obtained for this system indicates that the loss in cation-cation interactions is not compensated by hydrogen bonding interactions between the cation and anion. Thus, it can be reasoned that significant differences in the strength of hydrogen bonding and size/molar volume of the anions lead to dramatic changes in the organizations of the ions in comparison to the pure IL structure and, thus, accounts for the non-ideal thermophysical property behavior.

4.3 Implications of Non-Ideal Binary Ionic Liquid Mixture on CO_2 Phase Equilibria

Based on the analyses provided in section 4.2 $[C_4mim]Cl_x[MeSO_4]_{1-x}$ is designated as an ideal mixture, as the underlying structures of the mixtures are similar to that of pure IL analogues, whereas $[C_4mim]Cl_x[NTf_2]_{1-x}$ system is nonideal as it shows structures non-native to the pure IL counterparts.

In a recent study, Hiraga et al. [272] demonstrated that CO_2 solubilities in the $[C_4mim]Cl$-$[C_4mim][NTf_2]$ system are higher than ideal mixing predictions. As the $[C_4mim]Cl$-$[C_4mim][NTf_2]$ system has been shown to display a nonideal behavior in terms of CO_2 solubility, we hypothesized that the existence of non-native IL structures are responsible for this solubility trend. In order to test the hypothesis, CO_2 solubility in terms of the Henry's constant as a function of the IL composition was

determined at 353 K. MD simulations (using GROMACS 5.0.4) were conducted to compute Henry's constants using BAR [204] approach, as described in section 3.3.2.

Results indicate that the Henry's constant for CO_2 follows a highly non-linear trend with respect to the increasing concentration of Cl^- in the [C_4mim] Cl_x $[NTf_2]_{1-x}$ system while it is almost independent of the anion composition for the [C_4mim] Cl_x $[MeSO_4]_{1-x}$ system. The deviation from the linearity was then correlated with structural features of the binary IL systems in the presence of CO_2 by conducting MD simulations at 10 bar, in Henry's law regime. Structural analyses point to an enhanced CO_2-$[NTf_2]^-$ association as $[NTf_2]^-$ anion is displaced from the equatorial plane of the imidazolium ring to occupy positions above and below the cation-ring. This re-arrangement also weakens the cation π-π interactions resulting in the formation of increased local free volume, thus, aiding CO_2 accommodation. On the contrary, as expected, such structural transitions are absent in the [C_4mim] Cl_x $[MeSO_4]_{1-x}$ mixture system. Therefore, binary IL mixture systems containing a cation paired with different anions differing significantly in hydrogen bond acceptor ability and size possesses non-native (nonideal) structures that can potentially possess superior CO_2 phase equilibria properties. This work was published in 2018. [273]

4.3.1 Henry's Constants

The values predicted for Henry's constants of CO_2 (k_{H,CO_2}) in pure ILs of [C_4mim]Cl, [C_4mim][$MeSO_4$], and [C_4mim][NTf_2] are 179.2 ± 0.0 bar, 181.0 ± 8.1 bar, and 73.4 ± 2.3 bar, respectively. The statistical uncertainties are reported from the values obtained by conducting three independent MD trials. For [C_4mim][NTf_2] and [C_4mim][$MeSO_4$] ILs, the values in very good agreement with the experimental values, 67.1 bar [274] and 184.4 ± 2.5 bar [275] respectively. The calculated k_{H,CO_2} for [C_4mim]Cl is approximately four times lower than the experimentally reported value

of 228.9, [276] which is probably related to its high viscosity that makes the measurement of CO_2 solubility difficult. It is evident that these values of CO_2 solubility in these ILs follows the order $Cl^- \sim [MeSO_4]^- < [NTf_2]^-$, for a given cation, which is consistent with the Kamlet-Taft parameter, β, values. [41, 42]

Figures 4.18 (a) and (b) show k_{H,CO_2} as a function of anion composition for the binary IL mixture systems, $[C_4mim]Cl_x[MeSO_4]_{1-x}$ and $[C_4mim]\ Cl_x\ [NTf_2]_{1-x}$, respectively, at 353 K. For both the mixture systems, the k_{H,CO_2} values are bracketed by those found for the pure ILs. $[C_4mim]\ Cl_x\ [MeSO_4]_{1-x}$ system displays ideal mixing

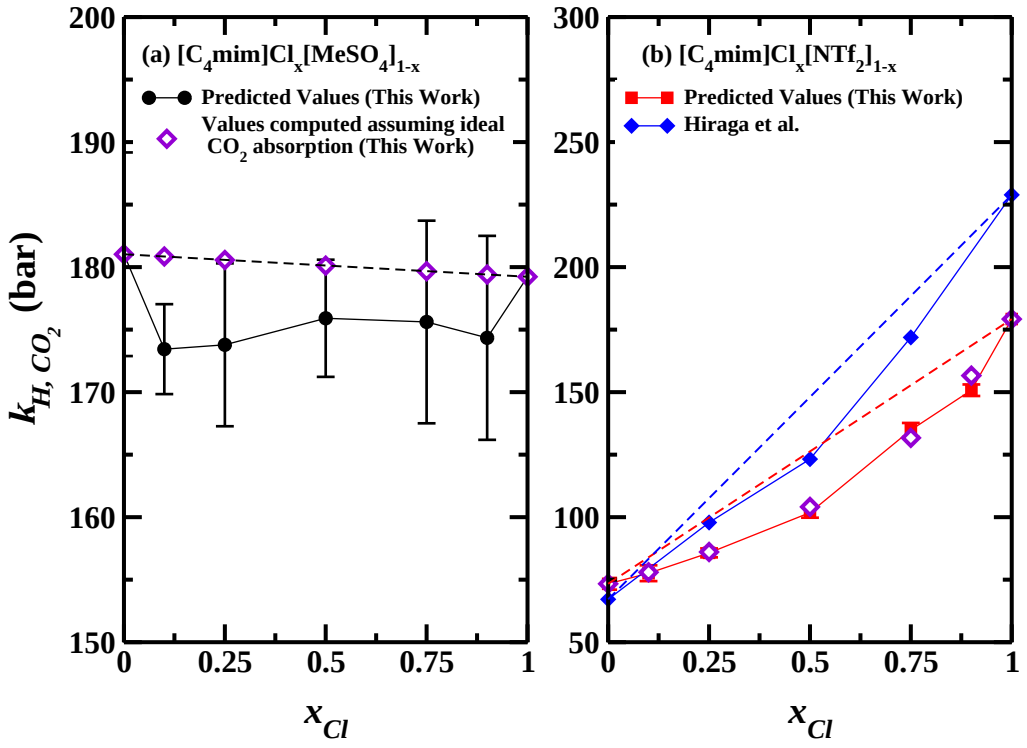

Figure 4.18: Henry's constants, k_H, of CO_2 as a function of Cl^- composition in binary IL mixture of (a) $[C_4mim]\ Cl_x\ [MeSO_4]_{1-x}$ and (b) $[C_4mim]\ Cl_x\ [NTf_2]_{1-x}$ at 353 K. Please not that the dashed line is shown for reference for linear mixing average while the continuous lines joining data points are only guide to the eye. The standard deviations were calculated from three independent molecular dynamics (MD) trials for all the mixture compositions.

behavior for CO_2 solubilities in terms of Henry's constants; as k_{H,CO_2} can be predicted using a linear mixing rule. On the contrary, for $[C_4mim]Cl_x[NTf_2]_{1-x}$ system Henry's constants in the binary IL system follow a highly non-linear curvature. Henry's constant at all the mixture compositions are lower than that expected on the basis of linear mixing rule, which, in general, implies higher CO_2 solubilities in this binary IL mixture. In fact, the experimental measurements of the Henry's constant, by Hiraga et al. [272], also demonstrate a non-linear dependence on the anion concentration and are lower than those obtained assuming a linear mixing rule.

However, in this work we derive an expression, included in Appendix B, which shows that apparently, the values of Henry's constants for mixtures can still be estimated solely on the basis of information of Henry's constant in pure ILs; if mole fraction weighted harmonic mean of their Henry's constants is considered instead of arithmetic mean. The overlap of the values predicted from the simulations and those determined using the harmonic mixing rule for $[C_4mim]\ Cl_x\ [NTf_2]_{1-x}$ system clearly corroborates this. Although such expression may have been known earlier, Chen and co-workers [18] suggested similar lever rule for predicting the mole fraction (solubility) of CO_2 in mixtures based on individual ILs constituting the mixture, it has never been shown that it can be used for approximating Henry's constants. It should be noted that, the values calculated using the harmonic mean approach are identical to the values predicted using linear mixing rule for $[C_4mim]\ Cl_x\ [MeSO_4]_{1-x}$ system since the values Henry's constants for pure $[C_4mim]$ Cl and $[C_4mim]$ $[MeSO_4]$ ILs are very similar. Thus, it can be inferred that in Henry's law regime CO_2 absorption still follows ideal mixing rule. This is also corroborated by the absorption isotherms as will be discussed in section 4.4.

To advocate this viewpoint, Henry's constants for the binary mixtures of $[C_2mim][NTf_2]$

- $[C_2mim][EtSO_4]$, $[C_2mim][NTf_2]$ - $[C_4mim][EtSO_4]$, and $[C_2mim][NTf_2]$ - $[C_2py][EtSO_4]$ were calculated using mole fraction weighted harmonic mean of Henry's constants of pure ILs, based on the actual experimental measurements of Henry's constants reported by Pinto et al. [32–34], the results of which are included in Figure 4.19. It is evident that these Henry's constants can be approximated using harmonic mixing rule. Thus, it is believed that Henry's constants for the mixture will always exhibit an "apparent" non-ideal behavior when compared to a linear mixing rule in cases where Henry's constants for the pure ILs are significantly different.

At this point, it is worth mentioning that although Henry's constants can be estimated solely based on pure ILs data, the molecular level picture of the non-linear behavior is entirely different. All the experimental studies that have suggested enhanced solubility in the binary IL system, based on the negative deviation from the linear mixing rule, have offered the explanation that the enhancement in the solubility of CO_2 for the mixture is caused by a combination of energetic and volume (entropic) effects due to mixing. However, in the following subsections, it will be rationalized that molecular-level structural organization of both the anions which results in struc-

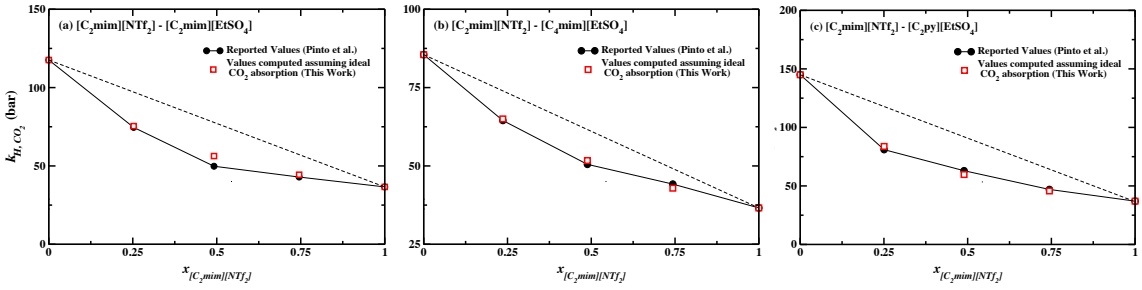

Figure 4.19: Comparison of Henry's constants, k_H, of CO_2 between the values reported by Pinto et al. [32–34] and the values computed using mole fraction weighted average harmonic mean of the pure IL components, assuming ideal CO_2 absorption, as a function of $[C_2mim][NTf_2]$ composition in binary IL mixtures of (a) $[C_2mim][NTf_2]$-$[C_2mim][EtSO_4]$, (b) $[C_2mim][NTf_2]$-$[C_4mim][EtSO_4]$, and (c) $[C_2mim][NTf_2]$-$[C_2py][EtSO_4]$. Please note that solid symbols are literature values, open symbols are harmonic mean computed values and dashed line is linear average.

tural features that are absent in the pure ILs, non-native interactions, enables an enhanced interaction between CO_2 molecules and fluorinated anions ($[NTf_2]^-$). In addition, such re-arrangement slightly shields cation-cation interaction allowing local free volume to increase that perhaps also aids in better CO_2 accommodation. For the following discussion in this section, $[C_4mim]^+$ will be referred to as the cation.

4.3.2 Distribution of CO_2 in IL Mixtures

Spatial Distribution Functions: Figure 4.20 depicts relative positions of CO_2 molecules around an anion for both $[C_4mim]Cl_x[MeSO_4]_{1-x}$ and $[C_4mim]Cl_x[NTf_2]_{1-x}$ mixture systems in the form of SDFs. These SDFs were generated at the isosurface densities two times the corresponding bulk density, which is in-part chosen based on the first RDF peaks (see below). It is clear that the molecular level picture is entirely different. For $[C_4mim]Cl_x[MeSO_4]_{1-x}$ mixture system (top panel) it appears that CO_2 is likely to lie in regions in-plane of the three equivalent oxygen atoms of $[MeSO_4]^-$ with two distinct high-density regions: (i) along the sulfur-oxygen vector; (ii) along the bisector of the oxygen-sulfur-oxygen bond angle. The small difference in intensities is indicative of the strong directional interaction of CO_2 with oxygen atoms of $[MeSO_4]^-$. The comparison of these SDFs along the entire composition range suggests that the structural diversity or transition in these SDFs is almost non-existent at all the concentrations except at the mole ratio of 75:25 at which the high-density regions disappear. At this point, it is unclear why such behavior is observed only at this particular composition, since, two additional independent simulations were able to reproduce the same features. This behavior can be expected after visualizing the respective RDFs, where the peaks intensity reduces considerably for x_{Cl}=0.75 as opposed to other concentrations and the isosurface density where this SDF is visualized is slightly higher than the peak maximum. It is worth mentioning that computing the SDF at a lower isosurface density (1.7 times the bulk density), not shown here, re-

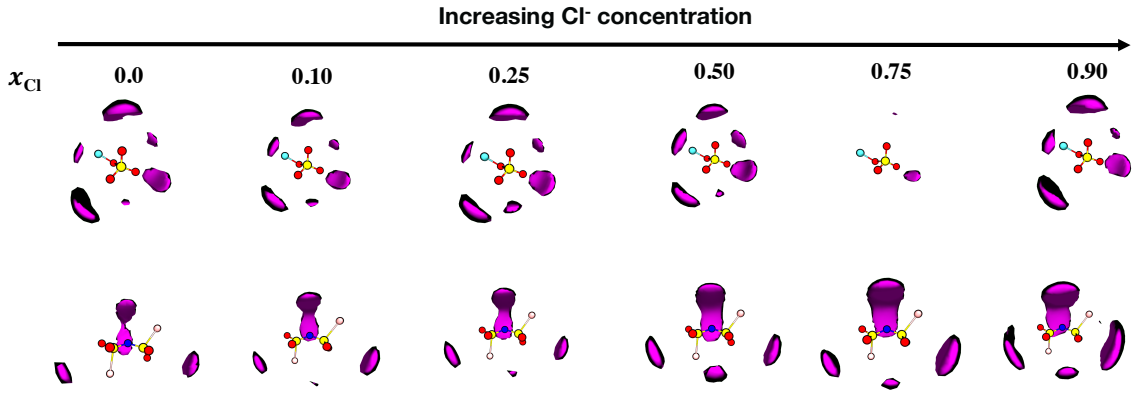

Figure 4.20: Spatial distribution functions (SDFs) of CO_2 molecules around the $[MeSO_4]^-$ (top panel) and $[NTf_2]^-$ (bottom panel) anions. Isosurface density is 2.0 times the bulk density. The top row, x_{Cl}, represents the Cl^- concentration. Color coding: CO_2 in purple. Atoms: S yellow, O red and CT3 cyan, N blue and CF3 orange.

stores the most likely positions CO_2 is expected to occupy. Furthermore, interestingly, small changes in the SDFs are discernible for the areas occupied along the bisector of the two equivalent oxygen atoms which may be attributed to minute fluctuations seen in the RDF peaks but is not significant enough to change the interaction of CO_2 with $[MeSO_4]^-$ anion, as will be shown below.

For $[C_4mim]Cl_x[NTf_2]_{1-x}$ mixtures the structural transitions are readily discernible, unlike $[C_4mim]Cl_x[MeSO_4]_{1-x}$ system. For the pure $[C_4mim][NTf_2]$ system, the CO_2 molecules coordinate with $[NTf_2]^-$ at three sites that appear to arise due to the synergistic interaction of CO_2 with both trifluoromethane (-CF3) group and four equivalent oxygen atoms. However, as will be shown below, the interaction of CO_2 with $[NTf_2]^-$ is major defined by (-CF3) group. Even for the lowest Cl^- concentration (x_{Cl}=0.10), a slight enhancement in the CO_2 densities (middle region and the area towards the right, when compared with pure $[C_4mim][NTf_2]$ system) is visible along with an additional site. Moreover, as the concentration of Cl^- is further increased, there is a noticeable intensification around all the four sites. This signifies that addition of Cl^-,

which displaces $[NTf_2]^-$ from the ring binding sites (see section 4.2), enhances the interaction of CO_2 with the weakly coordinating anion $[NTf_2]^-$.

Radial Distribution Functions: In order to provide a quantitative picture as opposed to SDFs, the association of CO_2 with different moieties is shown in the form of center-of-mass (COM)-based RDFs for both the mixture systems is illustrated in Figure 4.21. For cation-CO_2 RDFs the first peak intensity is only slightly greater than 1 and shows a nearly homogeneous distribution of CO_2 in the second coordination sphere and thereafter, which reinforce lower affinity of cation for CO_2 in comparison to the anion. In fact, the peak position shows a weak dependence on the molar composition of anions, suggesting that cation-CO_2 interactions are largely unperturbed irrespective of the anion identity.

However, as expected, a strong localization of CO_2 around the anions is observed as indicated by the first peak height exceeding the value of 1. This demonstrates that the interaction of CO_2 with anions is dominant and supports previous investigations speculations. [18] Further, the trend observed for the change in RDF with the change in anion, intensity as well the location, is consistent with the hydrogen bond acceptor ability of $Cl^- > [MeSO_4]^- > [NTf_2]^-$ anions, [41, 42] The difference in the molecular size and shape of the anions is further reflected in the shape of the first coordination shell. The RDFs between CO_2 and spherically symmetric Cl^- results in a narrower distribution of CO_2 distances in the first coordination shell for both the mixture systems. The bulky $[MeSO_4]^-$ anion due to the presence of multiple coordinating sites lead to a more expanded first solvation shell of CO_2 around them. Nonetheless, as all the oxygen atoms of $[MeSO_4]^-$ are equivalent, the interaction of CO_2 results in a single first peak. On the other hand, $[NTf_2]^-$ anion not only has more expanded solvation shell, but a distinguishing feature of the RDF between the COMs of $[NTf_2]^-$ and CO_2 from the other RDFs is the appearance of a split peak, signifying the fact

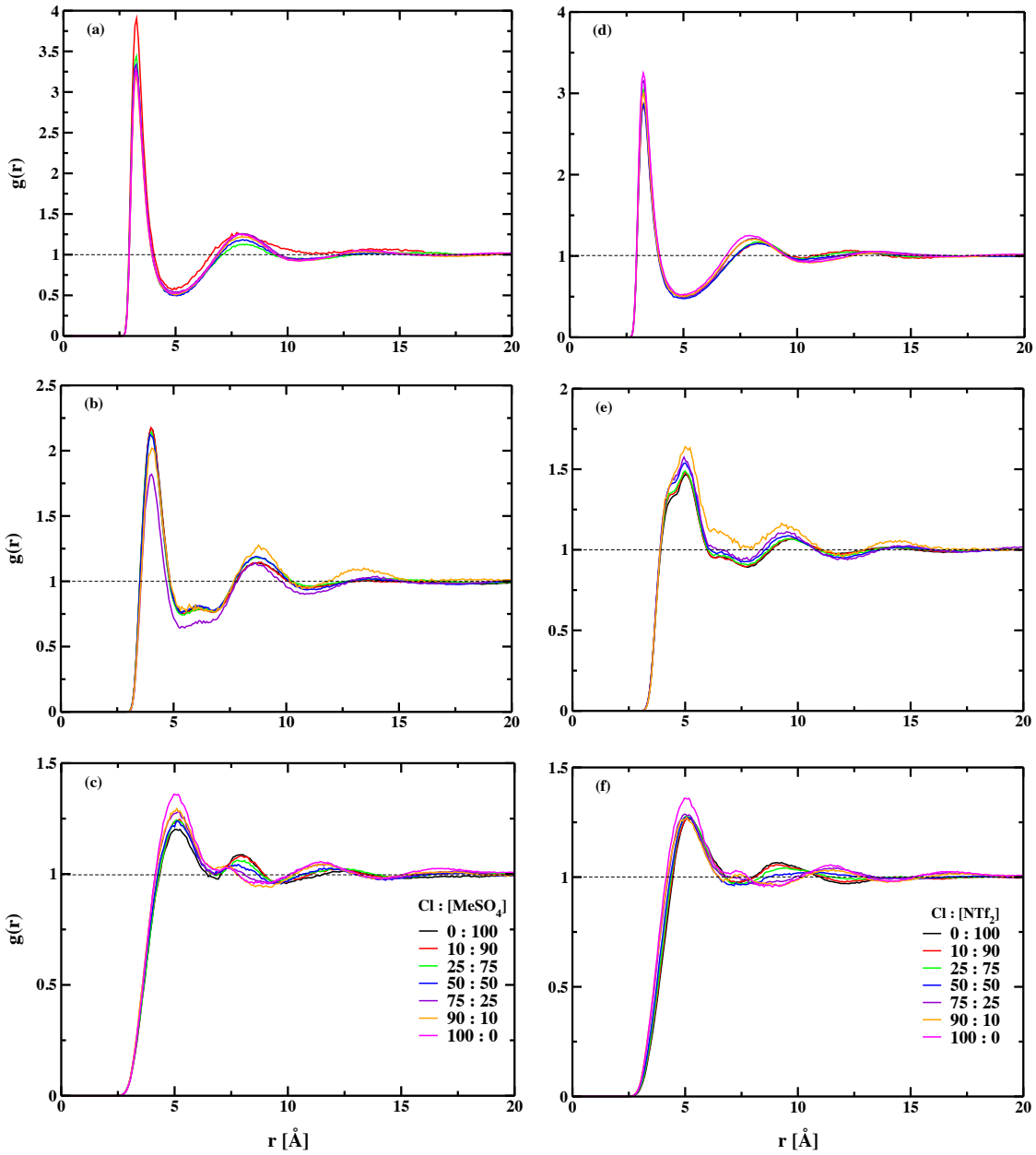

Figure 4.21: Center-of-mass (COM) based radial distribution functions (RDFs) between CO_2 molecules and (a) Cl^- (b) $[MeSO_4]^-$ (c) $[C_4mim]^+$ in $[C_4mim]Cl_x[MeSO_4]_{1-x}$. Similarly (d), (e), and (f) represents RDFs between CO_2 and Cl^-, $[NTf_2]^-$ and $[C_4mim]^+$ in $[C_4mim]Cl_x[NTf_2]_{1-x}$ at 353 K with varying Cl^- composition.

that interaction of CO_2 with $[NTf_2]^-$ occurs via multiple binding sites unlike with Cl^- or $[MeSO_4]^-$.

From the direct comparison of all the CO_2-anion RDFs, it is clear that the first peak intensity in all the CO_2-anion RDFs bears a weak dependence on the anion concentration, pointing to the CO_2-anion association that is independent of the dilution of one anion with respect to the other; which is not in line with the observations made in CO_2-$[NTf_2]^-$ SDFs. This suggests that visualization of RDFs or SDFs, alone, is not enough to provide the whole picture of the interactions present in the system. Given that the RDF value is obtained as the ratio of the local number density to that of the bulk density and the CO_2 bulk density changes considerably over different IL mixtures, the weak concentration dependence of CO_2-anion RDFs provide clues that the coordination of CO_2 molecules must be altered to a significant extent in order to maintain a similar association, as shown by SDFs.

Coordination Numbers: Figure 4.22 presents the composition dependence of coordination numbers, in the respective first solvation shells, of CO_2 with respect to the COM and specific sites of the anions in both the binary IL mixture systems. In $[C_4mim]Cl_x[MeSO_4]_{1-x}$ system, the coordination numbers of CO_2 with both Cl^- and $[MeSO_4]^-$ anion has very weak concentration dependence. In fact, the coordination number are nearly constant $\sim$1.75 for Cl^- and $\sim$2 for $[MeSO_4]^-$. Further, as expected, the trend for the number of CO_2 molecules around the oxygen atoms in these systems mirrors that obtained for the COM of the anion as these are the primary association sites for CO_2.

A very different picture emerges for the CO_2 distribution in the $[C_4mim]Cl_x[NTf_2]_{1-x}$ system. Strikingly, although, the number of CO_2 molecules found in the first coordination shell around a Cl^- anion only increases steadily from 1 at the lowest Cl^-

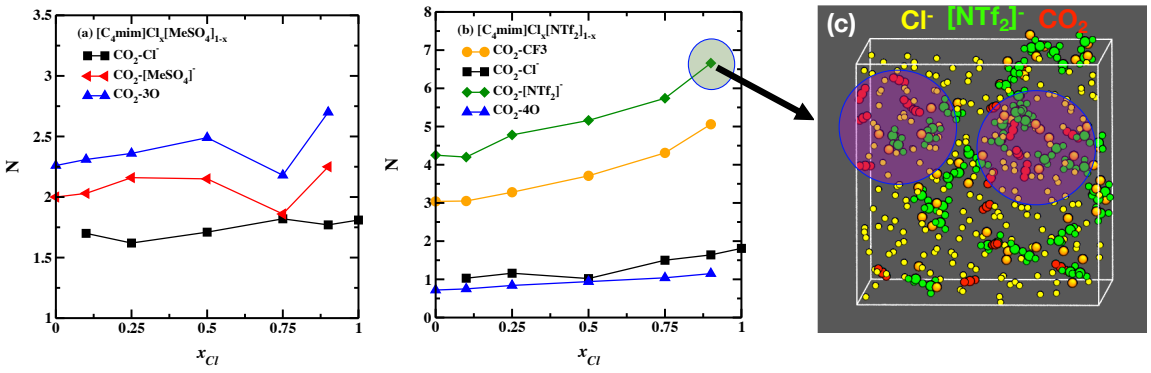

Figure 4.22: Average number of CO_2 molecules around both anions (a) Cl^- and $[MeSO_4]^-$; and (b) Cl^- and $[NTf_2]^-$ in the first coordination shell of an anion as a function of mixture composition at 353 K; (c) represents a simulation snapshot for Cl:$[NTf_2]$ :: 90:10 system showing isolation of $[NTf_2]^-$ anion and its enhanced coordination with CO_2. Note that the radius of first solvation shell is determined from the respective CO_2-anion RDFs.

concentration to approximately 2; the coordination number of CO_2 with $[NTf_2]^-$ increases from 4 to ∼7 with the increase in the Cl^- concentration. In support, a static configuration snapshot (from MD trajectory) show casing isolation of $[NTf_2]^-$ anions and coordination with more than 6 CO_2 molecules is included for the mixture system of $x_{Cl} = 0.9$. Since, both the RDFs and SDFs point to the bidentate modality of the $[NTf_2]^-$ anion, it is important to trace back the origin of such a dramatic change in the coordination number. Based on respective the RDFs (not shown here), coordination number around the oxygen atoms as well as -CF3 groups are computed. As can be noted from Figure 4.22(b), the number of CO_2 molecules around the -CF3 group mirrors that of COM of $[NTf_2]^-$ anions and increases from 3 to 5 as Cl^- is added to the system. However, only one CO_2 molecule is observed to interact with the oxygen atom at any composition, clearly suggesting that the increase in the average number of CO_2 molecules around $[NTf_2]^-$ can be rationalized in terms of enhanced interaction with (-CF3) group or fluorine atoms.

4.3.3 Changes in the Underlying Structure of Ionic Liquids Due to the Presence of CO_2

In order to determine the influence of CO_2 absorption on the microstructure of IL system the potential change in cation-anion and cation-cation coordination numbers, for the $[C_4mim]Cl_x[NTf_2]_{1-x}$ mixture system with and without CO_2 molecules, are reported in Figure 4.23. Due to the complete overlap, it is evident that the cation-anion

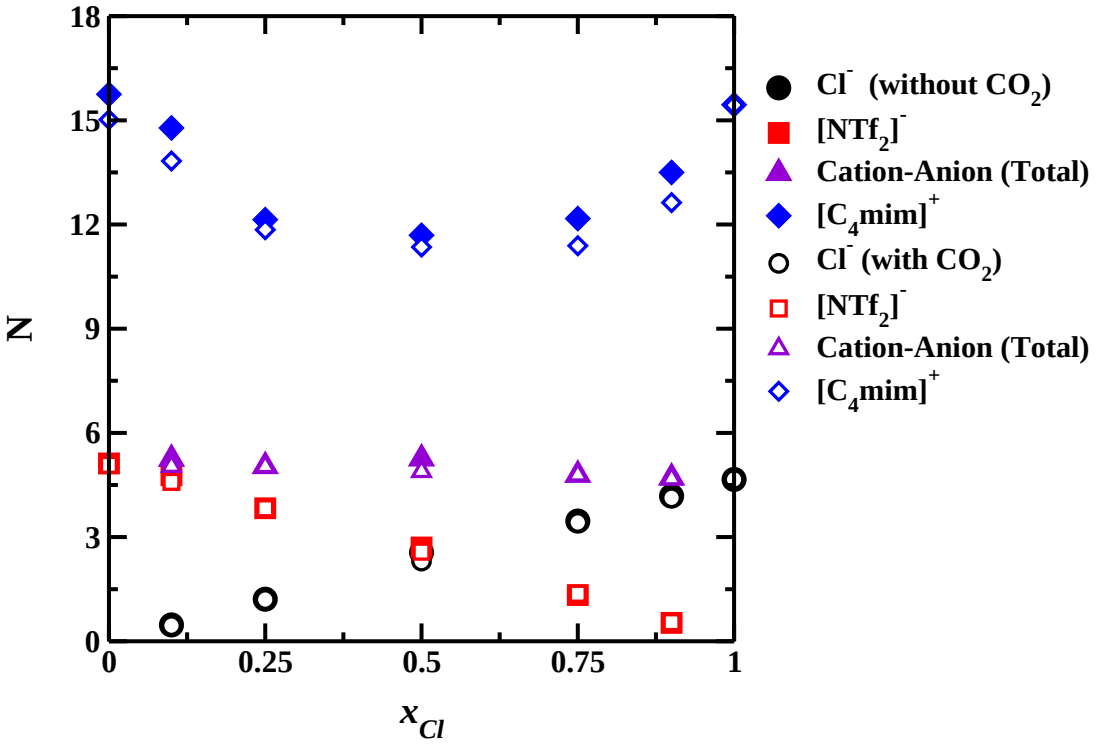

Figure 4.23: Cation-cation and cation-anion coordination numbers for $[C_4mim]Cl_x[NTf_2]_{1-x}$ mixture systems, with and without CO_2 saturation at 353 K and 10 bar. Please note that filled symbols are for the systems without CO_2 molecules while unfilled symbols are with CO_2 molecules.

(individual and total) coordination numbers for IL mixtures with and without CO_2 saturation are almost identical, suggesting that distribution of anions around cation do not deviate. However, a small but noticeable reduction in the coordination number

of cation with respect to another cation can be detected in the presence of CO_2. This suggests that the presence of CO_2 slightly shields the interaction between two cations.

To further scrutinize the change in the cation-cation coordination numbers the relative orientational distribution in the form of ADFs, with vectors sweeping both polar and azimuthal angles (see inset of Figure 4.24), for the cations, anions and the CO_2 molecule around the cation in the respective first solvation shell are computed. For better comparison the ADFs with and without CO_2 molecules in IL mixture systems are plotted together; solid-line with CO_2 while dotted-line without CO_2 molecules. The ADFs reported in Figures 4.24 (a)-(f) shows that the presence of CO_2 molecules does not influence the distribution of strongly interacting Cl^- anion. However, subtle rearrangements in the relative orientations of the bulkier, weakly-coordinating, $[NTf_2]^-$ anion are noticeable, especially in the 0-30° and 150-180° regions. Further, CO_2 molecules are preferentially located above or below the imidazolium ring and associate from the cationic tail site ($\phi \sim$ 0-60°), which is not easily accessible for the cation-anion interaction. The weak association of CO_2 with cation and occupancy of CO_2 above and below the ring-plane is in agreement with previous studies. [277, 278] Thus, the molecular picture in these systems is that, the need for positioning of CO_2 molecules and large-size anion above and below the cation results in a partial shielding of the cation-cation interactions causing a slight reduction in cation-cation coordination numbers. Since the coordination numbers do not change significantly, it may be inferred that there is subtle re-organization of cations that causes re-arrangement of the available free volume which in-turn aids the accommodation of CO_2 molecules. Furthermore, similar angular preferences of the CO_2 and $[NTf_2]^-$ is responsible for the CO_2-anion interactions and can explain the increasing coordination number of CO_2 around $[NTf_2]^-$ as Cl^- concentration increases. Based on the angular preferences exhibited by the weakly coordinating $[NTf_2]^-$, we surmise that empty spaces

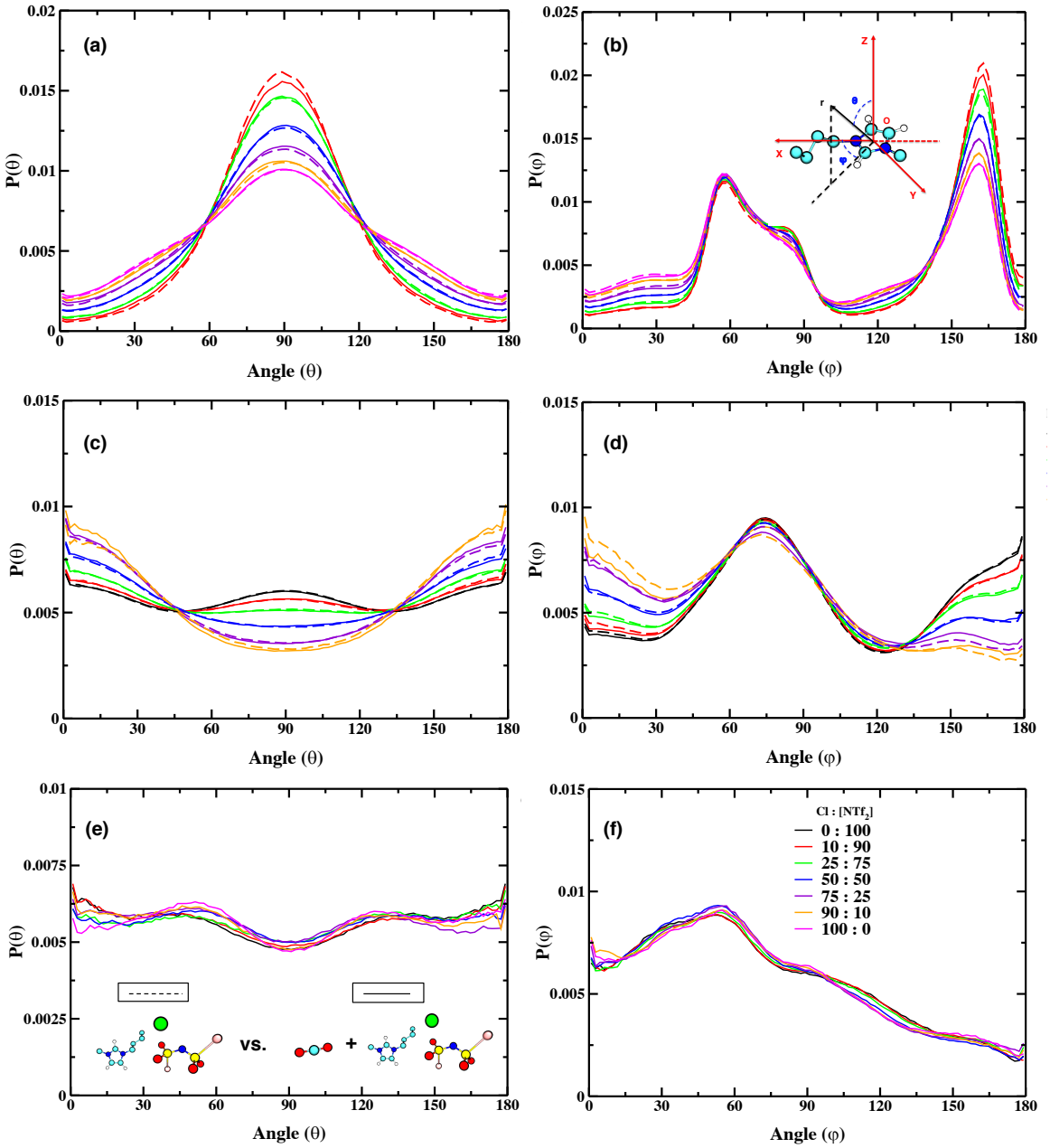

Figure 4.24: Angular distribution functions (ADFs) of Cl^-, $[NTf_2]^-$ anions and CO_2 molecules around $[C_4mim]^+$ within the first solvation shell, defined by the respective RDF minimum, for mixture system of $[C_4mim]Cl_x$ $[NTf_2]_{1-x}$ are shown in (a) - (b); (c) - (d); and (e) - (f) respectively. For direct comparison ADFs with and without CO_2 molecules in IL mixture systems are plotted together; solid-line with CO_2 while dotted-line without CO_2 molecules.

are generated around $[NTf_2]^-$. The appearance of an entirely new high density region in the SDF of CO_2 around $[NTf_2]^-$ is most likely due to this phenomena.

As an aside, the juxtaposition of the coordination numbers and the ADFs of the system without CO_2 saturation with those reported in Figures 4.14 and 4.16 included in section 4.2 indicates that the structures of binary IL mixtures undergo minimal changes with the increase in pressure, consistent with the incompressible nature of these systems. Furthermore, it is worth mentioning that subtle angular re-organization of the anions around cations due to change in the molar composition of Cl^- happens even for the IL mixture systems without CO_2 molecules. Thus, re-organization of ion moieties leading to re-arrangement of free molar volume can be considered an inherent property of this binary IL mixture, which likely leads to an increase in the free volume (observed as positive excess molar volumes) in which CO_2 molecules can be inserted.

Please note that in this subsection the analyses for $[C_4mim]Cl_x[MeSO_4]_{1-x}$ is not included. The interested reader is referred to the published work. [273] The invariance of all the RDFs and SDFs (see above), and ADFs and coordination numbers along the entire composition range, showed that the distribution of all the molecules around the cation is quite similar. This helps provide a rationale for the weak dependence of CO_2 Henry's constants on the anion composition.

Hence, from the results presented in this section, it is possible to provide a molecular reasoning of the apparent ideal solubility behavior in the binary IL mixture of $[C_4mim]Cl_x\ [NTf_2]_{1-x}$. The previous section demonstrated that a binary mixture of ILs containing a common cation and anions with a significant difference in hydrogen bond acceptor ability and sizes undergo structural transitions as the anion composition is

varied and molecular structures non-native to the neat IL analogues are produced. These non-native structures are characterized by the occupancy of the stronger coordinating anion in the plane of the imidazolium ring, while the weakly associating anion is displaced to the regions above and below the plane. The repositioning of the anions also causes small but perceptible changes in the angular arrangement of the weakly coordinating anion, possibly increasing the number or the volume of the voids between the cation and $[NTf_2]^-$. Further, re-organization of the anions around the cation occurs in the presence of CO_2 which expands the unoccupied volume and leads to CO_2 taking positions above and below the imidazolium ring plane, thus, enhancing the interaction of CO_2 with $[NTf_2]^-$. The lack of such structural features in $[C_4mim]Cl_x[MeSO_4]_{1-x}$ mixture system implies that the CO_2 dissolution mechanism does not differ from that observed for the pure IL systems leading to the ideal behavior.

4.4 Better Separation of Mixture of Gases Using Non-Ideal Binary Ionic Liquid Mixtures

It is a well-known fact that gases, in reality, exists as mixtures. Owing to the amphiphilic nature, ILs can have variable solubility character. It has been well established that a given IL has a high solubility for polar species such as CO_2 while solubility of nonpolar species such as alkanes, CH_4, is rather poor. This difference in ability has been employed for gas separation purposes. [15, 27, 75, 279–281] Although the topic of capturing the mixture of CO_2 and CH_4 simultaneously with ILs is of great interest, availability of the relevant data is scarce. We believe that, as with thermophysical properties, IL mixtures can offer control over precisely tuning the gas solubilities.

Based on the analyses so far, it is clear that the presence of non-native structures in $[C_4mim]Cl_x[NTf_2]_{1-x}$ mixture system allows an enhanced interaction between CO_2

and anion, which can be termed beneficial for better solubility. However, even though Henry's constant show non-linear behavior theoretical Henry's constants for CO_2 in this binary IL mixture can still be predicted solely on the basis of pure IL data under the assumption that the absorption of CO_2 is ideal. In other words, in low-pressure regime, a nonideal IL mixture possess solubility property that is apparently ideal. In Henry's law regime, a linear relationship between solubility and pressure is assumed, which does not seem to be followed for any pure IL or mixtures of IL at higher pressures. Thus solubilities, if estimated based on Henry's law, will be overpredicted at higher pressures, as it has been shown that as pressure is increased the solubility reaches a plateau suggesting no further increase in solubility with increase in pressure. Since ILs are incompressible, it is tempting to infer that such non-native structures will persist even at higher pressures and this nonideal IL mixture can potentially be employed for an efficient separation of gaseous mixtures.

Therefore, in this section, solubilities of pure gases CO_2 and CH_4, and their mixtures, with CO_2:CH_4 gas phase mole ratios of 05:95 and 15:85, in binary IL mixture of $[C_4mim]Cl_x[NTf_2]_{1-x}$ at 353 K and pressures ranging from 0 - 100 bar computed using Gibbs Ensemble Monte Carlo (GEMC) simulations, described in section 3.4, are presented. The predicted data was used to evaluate solubility selectivities and the respective Henry's constants. Furthermore, a comparison of Henry's constants obtained using both the absorption isotherms and BAR technique employed in MD simulations (section 3.3.2) is included to enforce the reliability of the trends reported.

It will be shown that for both CO_2 and CH_4, at low-pressure range, prediction of the solubilities along the entire IL mixture composition range can be safely made using linear mixing rule. However, as the pressure is increased nonideal solubility behavior is observed; solubilities are consistently higher for the mixtures of up to

25 % of [C_4mim][NTf_2] in [C_4mim]Cl. These IL mixtures have shown to possess local structures non-native to pure IL counterparts, *vide supra*, which allows enhanced solute-anion interaction. This nonideal solubility behavior is better perceived for CO_2 than CH_4, for the pressure range studied in this work, due to poor solubility of CH_4 in these ILs. Further, CO_2/CH_4 solubility selectivities are found to be lower than the ideal mixing rule estimation for both the CO_2:CH_4 gas phase mole ratio of 05:95 and 15:85. The non-linear behavior is more pronounced for the mole ratio of 05:95. However, solubility selectivities for the mole ratio of 15:85 are not very different from the ideal solubility selectivity, which indicates that the solubility selectivity in a given IL mixture can be safely estimated from pure gas solubility data of that IL mixture. On the other hand, improved solubility selectivities are observed for the CO_2:CH_4 gas phase mole ratio of 05:95, for the mixtures of up to 25 % of [C_4mim][NTf_2] in [C_4mim]Cl. This improvement shows that the presence of non-native structures in IL mixtures can potentially enhance CO_2 selectivity due to the increase in CO_2-anion association.

4.4.1 Pure Gas Absorption Isotherms

Figure 4.25 (a) and (b) shows the calculated CH_4 and CO_2 solubilities, traditional mole fraction vs. pressure solubility trends, in binary IL mixture of [C_4mim]Cl_x $[NTf_2]_{1-x}$ at pressures ranging from 1-100 bar and temperature of 353 K as a function of anion composition. Mole fraction presented on the y-axis is computed by taking the ratio of moles of CH_4 or CO_2 absorbed in the liquid phase and sum of the total moles of IL and gas. A comparison of the computed solubilities in pure IL system of [C_4mim][NTf_2] with the available experimental data, for the same pressure range, is included in order to postulate the reliability of these trends. To my knowledge, solubilities of CH_4 in the pure IL system of [C_4mim]Cl has not been studied for the same pressure range. Please note that for experimental data the original report

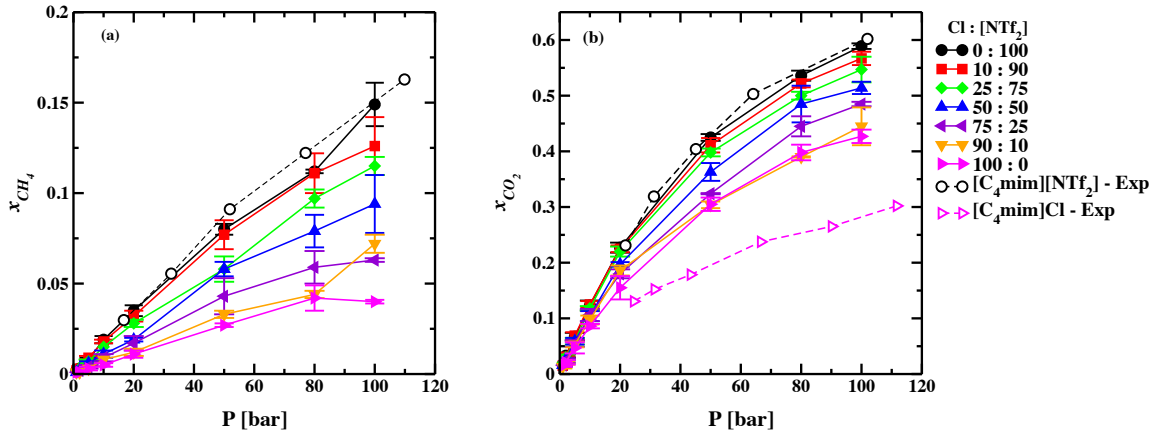

Figure 4.25: Solubilities of (a) CH_4, (b) CO_2 in binary IL mixture of $[C_4mim]Cl_x[NTf_2]_{1-x}$ computed at 1, 2, 5, 10, 20, 50, 80, 100 bar and 353 K. Please note that the comparison of calculated solubilities in pure ILs $[C_4mim][NTf_2]$ and $[C_4mim]Cl$ at 353 K and the available literature values (Jang et al. [282] for $[C_4mim]Cl$ and Carvalho et al. [283] for $[C_4mim][NTf_2]$ - CO_2; and Raeissi et al. [247] for $[C_4mim][NTf_2]$ - CH_4) only for the same pressure range and temperature conditions are done, otherwise to the best of our knowledge literature data for mixture systems at same operating conditions are unavailable.

contains uncertainties in pressure rather than mole fraction. So, for clarity, only average values of mole fraction vs. pressure values are included here with no error bars.

It is evident that the computed solubilities of CH_4 in this work agrees well with the literature values published by Raeissi et al. [247] for pure $[C_4mim][NTf_2]$ IL, for the entire pressure range. Further, the absorption isotherm assumes a linear curvature even up to P = 50 bar. Moreover, this linear relationship seems to hold for pure $[C_4mim]Cl$ as well, along with all the binary IL mixtures studied in this work. Direct comparison of the values suggests that the absorption of CH_4 in ILs such as $[C_4mim][NTf_2]$, $[C_4mim]Cl$ or their mixtures is rather poor.

Similarly, for CO_2, it is clear that the solubility values computed in this work, at 353 K, for $[C_4mim][NTf_2]$ agree very well with the experimental [283] results, even at high pressures where it is known that sampling for convergence becomes challeng-

ing [73]. However, unlike CH_4, the absorption of CO_2 in pure $[C_4mim][NTf_2]$ IL does not follow a linear trajectory as the pressure is increased. Cross-comparison of the CO_2 vs. CH_4 solubilities demonstrates that CO_2 is more soluble than CH_4. This behavior is consistent with the previous investigations. As far as CO_2 solubilities in pure $[C_4mim]Cl$ IL is concerned, high-pressure solubility values reported by Jang et al. [282] and Hiraga et al. [272] shows that the solubility trend up to 100 bar pressure is almost linear, while, unexpectedly, solubility trend predicted, in this work, for pure $[C_4mim]Cl$ IL follows a non-linear curvature. But, it is worth mentioning that though the solubilities for $[C_4mim]Cl$ IL are consistently overpredicted for almost the entire pressure range; the number of CO_2 molecules absorbed is consistent from each of the three completely independent trials, as suggested by very small standard deviations. Furthermore, the remarkable consistency between Henry's constants predicted via both GEMC and BAR method, as shown in the following subsection, suggests that the overall trends are reliable. The overprediction of solubility values is just an artifact of the force field model employed or is attributable to the high viscosity of $[C_4mim]Cl$ which makes the sampling convergence challenging.

Using the traditional absorption isotherms, the effect of nonideal IL mixture does not become readily available. In order to provide more profound insights, the same absorption isotherms are resketched to depict mole fraction dependence of the solubilities at a given pressure, as shown in Figure 4.26 (a) and (b), where the ideal mixing prediction is depicted as a dotted line for every pressure.

For CO_2, it is evident that at low-pressure range ($P < 10$ bar) the CO_2 solubilities are weakly dependent on the molar compositions of IL and can be safely estimated using the linear mixing rule. As the pressure is increased, a slight deviation from the ideal mixing behavior becomes prevalent. For $P = 20$ bar, the CO_2 solubility in

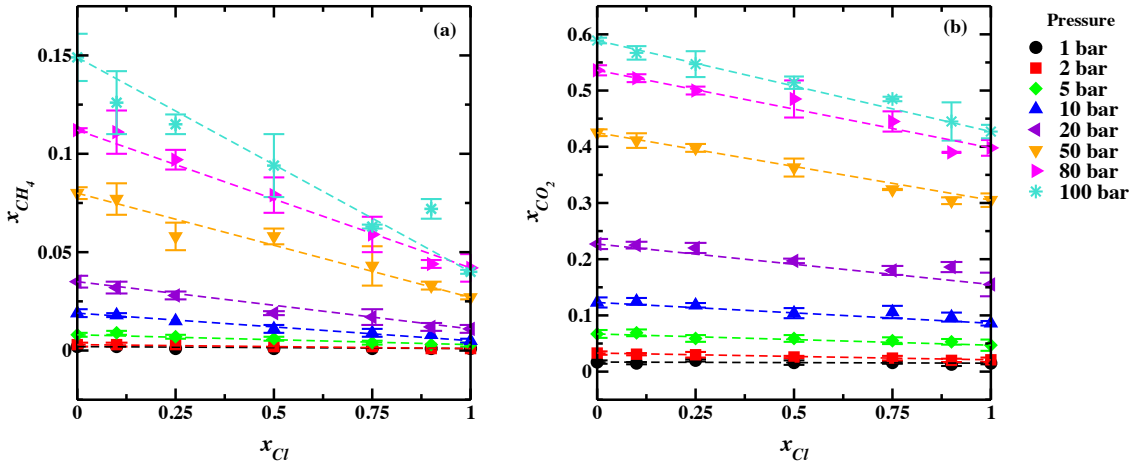

Figure 4.26: (a) CH_4 and (b) CO_2 solubilities in binary IL mixture of $[C_4mim]Cl_x[NTf_2]_{1-x}$ as a function of molar composition computed at 353 K and pressure 1, 2, 5, 10, 20, 50, 80, 100 bar. Standard deviations were calculated from three independent trials for all mixture compositions. Note that the continuous lines joining data points are only guide to the eye while dotted lines represent linear mixing rule.

excess to ideal behavior is predicted for the entire composition range. Nevertheless, in general, as the pressure is increased up to 100 bar the CO_2 solubility do not follow ideal mixing behavior and is more apparent for $x_{Cl} > 0.5$. This is remarkable and is in line with the fact that $[C_4mim]Cl_x[NTf_2]_{1-x}$ IL mixture show nonideal structures at these compositions. As shown in previous sections, as $x_{Cl} > 0.5$, $[NTf_2]^-$ anion occupies only top and bottom position with respect to the cation, $[C_4mim]^+$, and loses its ability to hydrogen bond with the cation along the vector of the most acidic imidazolium-ring hydrogen, a structure different from pure IL analogue, which then allows an enhanced interaction between CO_2 and $[NTf_2]^-$ giving rise to excess CO_2 solubilities in terms of Henry's constants. Thus, it is plausible to infer that nonideality present in the binary IL mixture of $[C_4mim]Cl_x[NTf_2]_{1-x}$ can be used to induce nonideal CO_2 solubility in high pressure systems and the deviation from ideal mixing behavior is more likely in systems with a higher concentration of strongly coordinating ions.

Unlike CO_2 solubility, as mentioned earlier, the absorption of CH_4 in ILs such as $[C_4mim][NTf_2]$, $[C_4mim]Cl$ or their mixtures is rather poor. Nevertheless, some trends are apparent. At low pressures ($P \leq 20$ bar) the solubility of CH_4 in binary IL mixture of $[C_4mim]Cl_x[NTf_2]_{1-x}$ display ideal behavior. As the pressure is increased some deviation in the solubility can be perceived, however, due to very low solubility, it becomes challenging to discern the concentration of IL mixture that has potential to offer nonideal CH_4 solubility. It is only at $P = 100$ bar that nonideal solubility of CH_4 becomes evident. We believe that further increase in the pressure will perhaps provide a better judgment of the nonideal solubility.

Henry's Constants: Henry's constants can be obtained from the traditional absorption isotherms by taking a linear fit as pressure tends to zero. However, as the isotherms have a non-linear curvature, it is important to mention that Henry's constant values are dependent on the range of data used for linear fit due to the curvature at high pressures. In this study, due to a reasonable CO_2 solubility, a linear fit is taken by selecting the range of data points from $P = 0$ bar to the pressure where x_{CO_2} is at least 0.1. On the contrary, due to very low CH_4 solubility, linear fits from $P = 0$ up to $P = 50$ bar are taken to calculate Henry's constants. This range is justified as the experimental value of 541 bar for the CH_4 in pure $[C_4mim][NTf_2]$ was computed by taking a linear fit of the data ranging between 15.9 to 50 bar [247] which shows maximum CH_4 solubility among all the ILs considered in this study.

The comparison of Henry's constants calculated using both GEMC and BAR techniques are reported in Figures 4.27 for both the gases. For CO_2, it is evident that both the techniques give very similar results for $x_{Cl} \leq 0.5$. However, as the Cl^- ion concentration is increased further, due to higher solubility predicted in this study, Henry's constants by GEMC are under-predicted. Nonetheless, the trend suggesting nonideal excess CO_2 solubility is reasonably reproduced. Therefore, the trends ob-

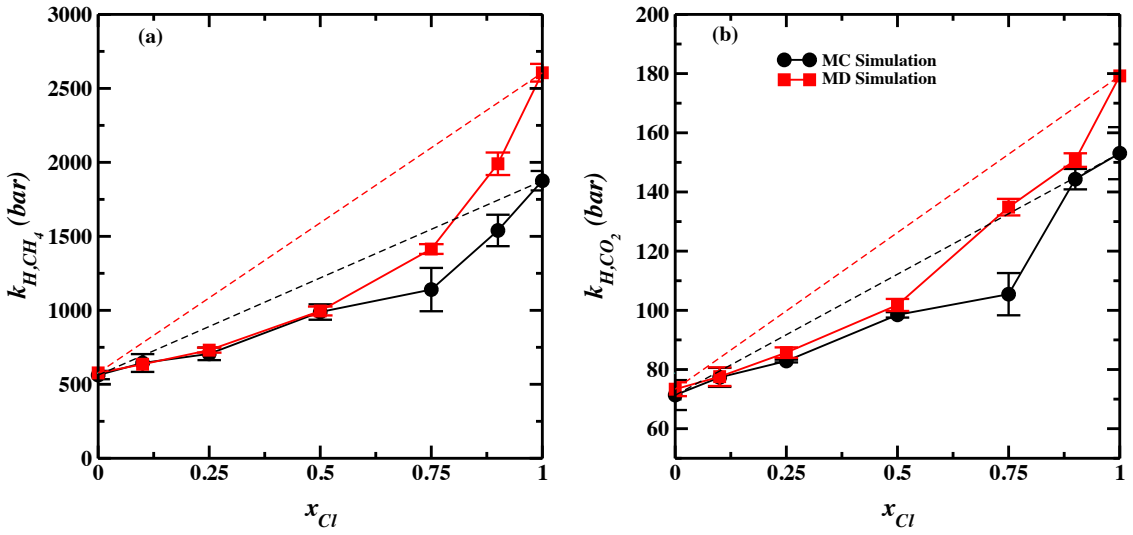

Figure 4.27: (a) CH_4 and (b) CO_2 comparison of Henry's constants calculated using MC simulations and that computed using BAR technique employed in MD simulations for the mixture system of $[C_4mim]Cl_x[NTf_2]_{1-x}$. Standard deviations were calculated from three independent trials for all mixture compositions. Note that the continuous lines joining data points are only guide to the eye while dotted lines represent linear mixing rule.

tained in this work can be presumed accurate. Similar results are obtained for CH_4. The comparison of Henry's constants calculated using both techniques deviates for $x_{Cl} \geq 0.5$. However, the nonlinear trend is well reproduced. Further, Henry's constants less than ideal mixing rule hints that excess CH_4 solubilities can be expected for the entire composition range. Thus, an observation similar to CO_2 absorption, it can be inferred that IL mixtures possessing a higher concentration of strongly associating ions as opposed to weakly coordinating ions can be considered as potential candidates to explore better solubility options for CH_4 absorption than pure IL analogues, but probably requires very higher pressures for that to take into effect.

4.4.2 CO_2/CH_4 Mixture Solubility

A natural gas sweetening process, typically, contains up to 10 % CO_2 with a high operating pressure. Therefore, solubilities of CO_2/CH_4 gas mixtures in the binary IL mixture of $[C_4mim]Cl_x[NTf_2]_{1-x}$ at 353 K and a total pressure of 100 bar, with

CO_2:CH_4 gas phase mole ratio of 05:95 and 15:85 were calculated. The objective was to discern if nonideality in the IL mixture can help improve the selectivity of one solute over other in the mixture.

Figures 4.28 show the comparison of liquid phase composition of the solute in the mixture at a given partial pressure with respect to solute composition from the pure gas isotherm at a total pressure equal to partial pressure, i.e., assuming independent absorption of gases. For pure [C_4mim][NTf_2] IL, the amount of CO_2 absorbed, for both the CO_2:CH_4 mole ratios of 05:95 and 15:85, is slightly lower than observed in the pure CO_2 system at the same CO_2 partial pressure. On the contrary, the amount of CH_4 absorbed is slightly greater than the pure CH_4 system. Additionally, it is important to mention that as the mole ratio of CO_2:CH_4 is increased, the difference between mixed gas absorption with respect to pure systems is significantly reduced. These trends for pure [C_4mim][NTf_2] IL system are consistent with the previous studies. [73, 284, 285] Similar observations are made for pure [C_4mim]Cl IL except for CH_4 solubility in mixed gas components at the CO_2:CH_4 mole ratio of 15:85, which overlaps the pure CH_4 system.

As shown in Figure 4.28 (a), for the CO_2:CH_4 mole ratio of 05:95, the gas mixture solubilities for both CO_2 and CH_4 show moderately excess absorptions, unlike pure system solubilities of CO_2 and CH_4 which shows ideal dependence on the molar compositions of IL. However, direct comparison of CO_2 solubilities in both pure and mixed gas systems suggest that the presence of Cl^- ion retards the CO_2 absorption, which becomes apparent at $x_{Cl} \geq 0.75$, while CH_4 solubilities are not affected as suggested by excess CH_4 absorption across the entire composition range. Thus, for the CO_2:CH_4 mole ratio of 05:95 it can be inferred that CO_2 improves the solubility of CH_4 while its own solubility is reduced, an observation consistent with previous

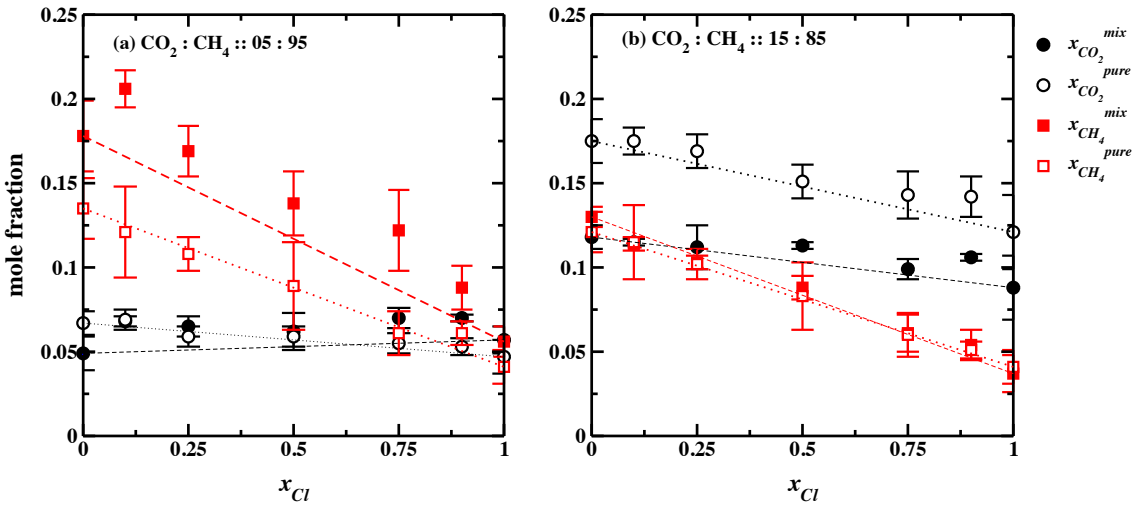

Figure 4.28: CO_2/CH_4 gas mixture solubility in binary IL mixture of $[C_4mim]$ Cl_x $[NTf_2]_{1-x}$ as a function of molar composition computed at 353 K and total pressure of 100 bar compared with pure gas solubilities at the same partial pressures for CO_2 and CH_4, respectively, (a) for the mixture ratio of CO_2/CH_4 :: 05/95; and (b) for the mixture ratio of CO_2/CH_4 :: 15/85. Standard deviations were calculated from three independent trials for all mixture compositions. Note that the dotted lines represent the linear mixing rule.

studies. [73, 74]

In contrast, for the CO_2:CH_4 mole ratio of 15:85, it is clear from Figure 4.28 (b) that gas mixture solubilities can be predicted using the ideal linear mixing rule for all the binary IL mixtures studied in this work. It is also interesting to note that solubilities of CH_4 in both pure and mixed gas systems overlap for all the IL mixtures while the amount of CO_2 absorbed is lower than the pure CO_2 system for the entire composition range. This means that at this CO_2:CH_4 mole ratio, with a slight introduction of Cl^- ion, CO_2 is not able to facilitate absorption of CH_4 while CH_4 still deteriorates the CO_2 solubilities. This may be due to the change in preferential interactions between the ions comprising the IL mixture.

Therefore, the addition of small amount of $[C_4mim][NTf_2]$ in $[C_4mim]Cl$ (10 - 25

%) may result in an improved gas separation for the CO_2:CH_4 gas phase mole ratio of 05:95. This is consistent with the fact that improved pure gas solubilities were also observed for the similar concentration range at higher pressures. Hence, the presence of nonideal structures in these IL mixtures help modulate the solute-anion interaction and thus improve the solubility.

4.4.3 Solubility Selectivity

In order to adequately account for the trends observed in mixed gas absorption isotherms, solubility selectivities were computed using two different methods (see section 3.4.3 for more details). Eq. 3.51 was used to calculate solubility selectivity directly from the liquid and gas phase compositions of the corresponding components obtained from the GEMC simulations, while the ideal solubility selectivities were determined by taking the ratio of Henry's constants, for a specific IL mixture, as shown in eq. 3.50.

Figure 4.29 displays the comparison of solubility selectivities obtained for both the CO_2:CH_4 mole ratio of 05:95 and 15:85 with ideal solubility selectivity computed using GEMC and BAR technique. It is evident that ideal solubility selectivities ($\beta^{S,H}_{CO_2/CH_4}$) obtained for the binary IL mixture of $[C_4mim]Cl_x[NTf_2]_{1-x}$ at 353 K using both the methods are in excellent agreement. Predictions suggest that selectivity in pure $[C_4mim][NTf_2]$ IL is less than that in $[C_4mim]Cl$. This can be attributed to the fact that the difference in Henry's constants of CO_2 and CH_4 in $[C_4mim][NTf_2]$ IL, computed using both the methods respectively, is less significant than that in $[C_4mim]Cl$. Further, the ideal solubility selectivity of $\sim$7.88 for pure IL $[C_4mim][NTf_2]$ is comparable to the value published by Ramdin et al. [284] at the same temperature condition.

For $[C_4mim][NTf_2]$ IL, both the CO_2:CH_4 mole ratio of 05:95 and 15:85 mixture sol-

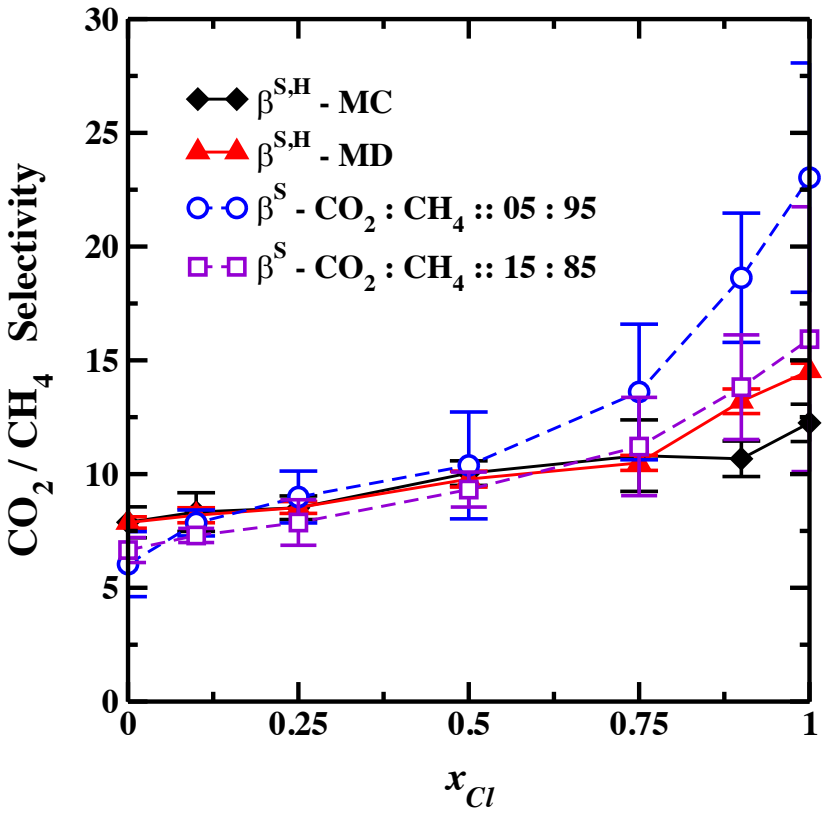

Figure 4.29: Comparison of CO_2/CH_4 gas mixture solubility selectivities ($\beta^{S}_{CO_2/CH_4}$), with CO_2:CH_4 gas phase mole ratios of 05:95 and 15:85, in binary IL mixture of $[C_4mim]Cl_x[NTf_2]_{1-x}$ as a function of molar composition computed at 353 K and total pressure of 100 bar with ideal solubility selectivities ($\beta^{S,H}_{CO_2/CH_4}$) computed using the ratio of Henry's law constants using both GEMC and BAR techniques. Standard deviations were calculated from three independent trials for all mixture compositions. Note that the lines joining data points are only guide to the eye.

ubility selectivity ($\beta^{S}_{CO_2/CH_4}$) is lower than the ideal solubility selectivity ($\beta^{S,H}_{CO_2/CH_4}$) with larger deviation for the mole ratio of 05:95. Similar observation has been reported by Budhathoki et al. for the CO_2:CH_4 mole ratio of 04:96 [73], 05:95 [74] and 16:84 [73] at 333 K. On the other hand, for pure IL system of $[C_4mim]Cl$ the mixture solubility selectivity with CO_2:CH_4 mole ratio of 05:95 is significantly higher than ideal solubility selectivity even including the standard deviations, while CO_2:CH_4 mole ratio of 15:85 shows solubility selectivity can be estimated using pure gas solubility data. In fact, for the entire composition range of IL mixtures the ideal assumption

for the prediction of solubility selectivity in CO_2:CH_4 mole ratio of 15:85 seems to be valid even though the solubility selectivities changes in a non-linear fashion with the change in Cl^- ion concentration. It is also noteworthy that the deviation of mixture solubility selectivities $\beta^S_{CO_2/CH_4}$ from the ideal mixing rule increases as the ratio of CO_2:CH_4 decreases. It can be discerned that for the CO_2:CH_4 mole ratio of 05:95, a slight introduction of [C_4mim][NTf_2] in [C_4mim]Cl (up to 25 %) improves the gas separation performance, while for higher concentrations of [C_4mim][NTf_2] solubility selectivity can be safely estimated using pure gas-IL data.

A similar observation has been reported previously for enhancement in solubility selectivity of CO_2 over both CH_4 and N_2 by adding 5-10% of [C_2mim][NTf_2] in [C_2mim][BF_4]. [75] The authors rationalized the observation by suggesting lowering of the molar volume and slight disruption of the hydrogen bond network of pure [C_2mim][BF_4] IL. The observations made in this study in-part supports the idea and provide further insight that the disruption of preferential hydrogen bonding network which embarks the possibility of nonideal structures, structures non-native to pure IL analogues, not only helps improve the pure gas solubilities but can also enhance the solubility selectivity of the mixed gases.

4.5 A Step Towards *a priori* Design of Non-ideal Binary Ionic Liquid Mixtures

Previous sections of this chapter have shown that binary IL mixtures that contains a common cation paired with different anions, where the anions differ significantly in their hydrogen bonding ability with the cation and size/molar volumes, can posses (i) thermophysical properties that depart from the ideal mixing behavior, and (ii) gas solubilities that are also a non-linear function, with the potential of being superior to the pure IL analogues. These non-linear trends are found to be the implication of

the composition dependent structural transitions observed for these mixtures. The distribution of the ion moieties, cation-anion as well as cation-cation, is different from that found in the neat ILs, i.e., the so-called non-native structures emerge. The main focus was only one binary IL mixture of $[C_4mim]\ Cl_x\ [NTf_2]_{1-x}$.

Now, such an extensive characterization of every new binary IL mixture is nearly impossible. Thus, identification of nonideal IL mixtures through fundamental physical principles is of the essence. Due to the prevalence of a synergistic effect of differences in both size / molar volume and anion hydrogen bond acceptor ability, β parameter, this section attempts to determine a correlation between the two, a structure-property relationship (at least qualitatively), to *a priori* predict nonideal behavior of binary IL mixtures which can further be used to predict the presence of nonideal effects on the CO_2 absorption as well.

With that in mind, anions – fluorinated (expensive but less viscous and high CO_2 absorption capability) vs. nonfluorinated (cheaper but viscous and low-to-moderate CO_2 absorption capability) – with a wide-ranging size/molar volumes as well as hydrogen bond ability are considered. MD simulations (using GROMACS 5.1.5) are employed to predict the structural properties for a total of 16 binary IL mixture systems containing common cation 1-n-butyl-3-methylimidazolium $[C_4mim]^+$ and mixtures of fluorinated (trifluoromethylacetate $[TFA]^-$, trifluoromethanesulfonate $[TFS]^-$, bis (trifluoromethanesulfonyl)imide $[NTf_2]^-$, and tris (pentafluoroethyl)trifluorophosphate $[eFAP]^-$) vs. non-fluorinated (chloride Cl^-, acetate $[OAC]^-$, methylsulfate $[MeSO_4]^-$, and dimethyl phosphate $[Me_2PO_4]^-$) anions (Figure 4.30). The β parameter for all the anions is taken from the works of Lungwitz et al. [41, 42] except for $[Me_2PO_4]^-$ and $[eFAP]^-$, where the β parameters were predicted using a correlation between the β parameter and calculated hydrogen bond energies suggested by Claudio et al. [249].

The molar volumes are the simulation predicted values obtained in this work. It is a well-known fact that solvatochromic Kamlet-Taft polarity scale parameters depend on the dye used to probe the measurement. Lungwitz et al. [41, 42] and Welton and co-workers [43] are the two research groups that have determined and reported a substantial database of the β parameters for pure ILs. Since both the research groups use different dyes, the absolute values of solvatochromic parameters are different, and thus, discretion is advised for choosing the β parameter values. However, the overall cation-anion pair tendencies, strong vs. weak coordination, observed for the plethora of ions pairs by both the research groups are similar.

All the molecules were modeled using CL&P [175,176] force field except for $[Me_2PO_4]^-$ anion, the parameters of which were taken from OPLS-AA [286] force field. These parameters have been shown to work well when combined with CL&P parameters. [45, 287, 288] In this work anticipation of nonideality is rationalized based only on local structure properties, as we believe that although the prediction results for the thermophysical properties of IL mixtures can depend on the choice of force field model, the essential local structure features required to differentiate nonideal vs. ideal mixtures remains independent of the model. In support, the preferential ion interactions elucidated in terms of RDFs for the binary IL mixture of $[C_4mim]Cl_x[NTf_2]_{1-x}$ using an all-atom model (CL&P) vs. united atom model (Zhiping Liu – used in previous sections) are included in Figure 4.31. It is evident that the conclusions drawn from the composition dependent trends are invariant, irrespective of the force field model. In fact, previous structural investigation by Matthews et al. [45], using an all-atom model, for $[C_4mim]\ Cl_x\ [NTf_2]_{1-x}$ have reported similar observations.

Figure 4.32 displays a plausible correlation between the respective differences between the pure IL volumes and hydrogen bond acceptor ability of the anions for all

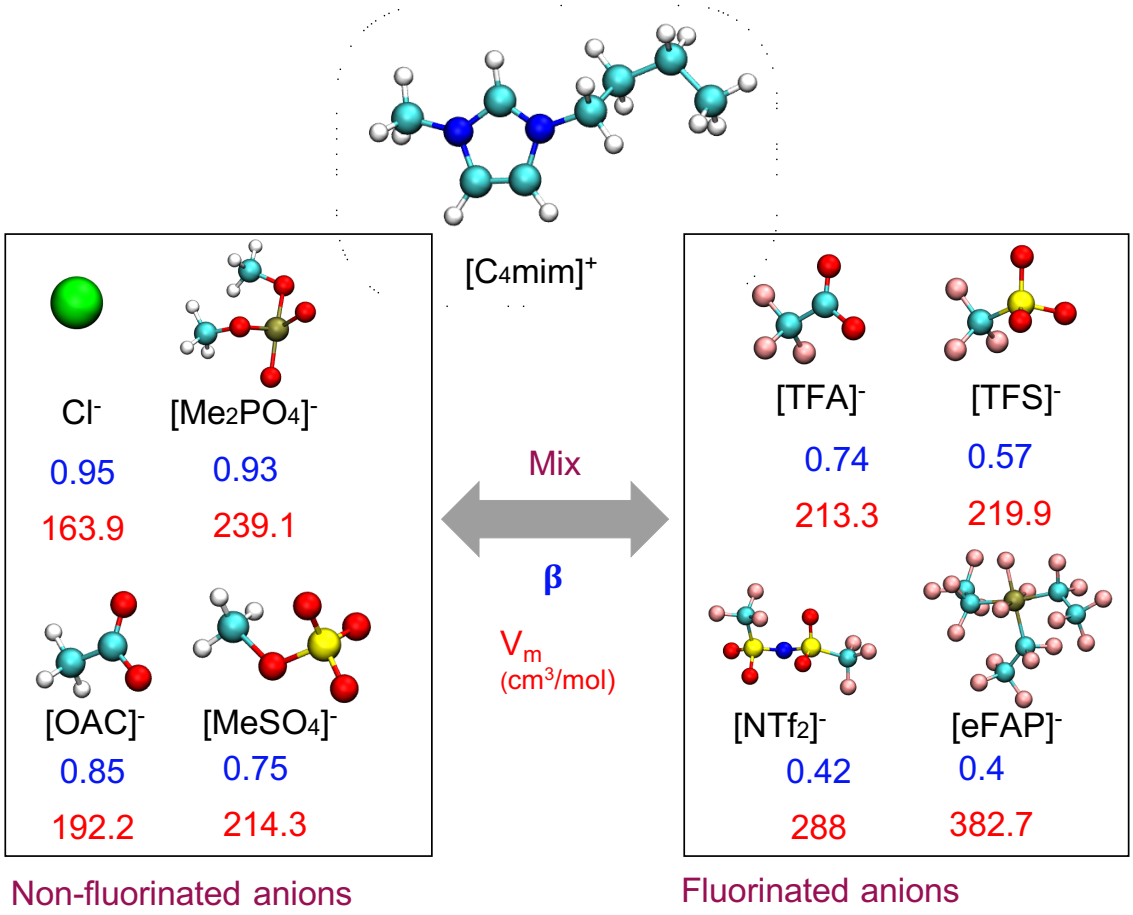

Figure 4.30: Molecular structure of the ILs under study. The β parameters are taken from the works of Lungwitz et al. [41, 42] whereas molar volumes are the simulation predicted values obtained in this work.

the 16 IL mixtures (Figure 4.30) considered in this study. Full structural characterization in the form of SDFs is included in Appendix C for all these mixtures. The nomenclature that will be used is [Cation] [Strongly Coordinating Anion]$_x$ [Weakly Coordinating Anion]$_{1-x}$. Apart from the 16 binary IL mixtures, additional mixture systems of [C_4mim] [BF_4]$_x$ [NTf_2]$_{1-x}$, [C_4mim] [PF_6]$_x$ [NTf_2]$_{1-x}$ and [C_4mim] [DCA]$_x$ [NTf_2]$_{1-x}$ are considered and are shown as open symbols, to have a better understanding in the top-left region.

In this work, the largest difference in the pure IL molar volumes and hydrogen bond ability of anions was encountered for [C_4mim]Cl$_x$[eFAP]$_{1-x}$ ($\Delta V \sim 218.7$ cm^3 /

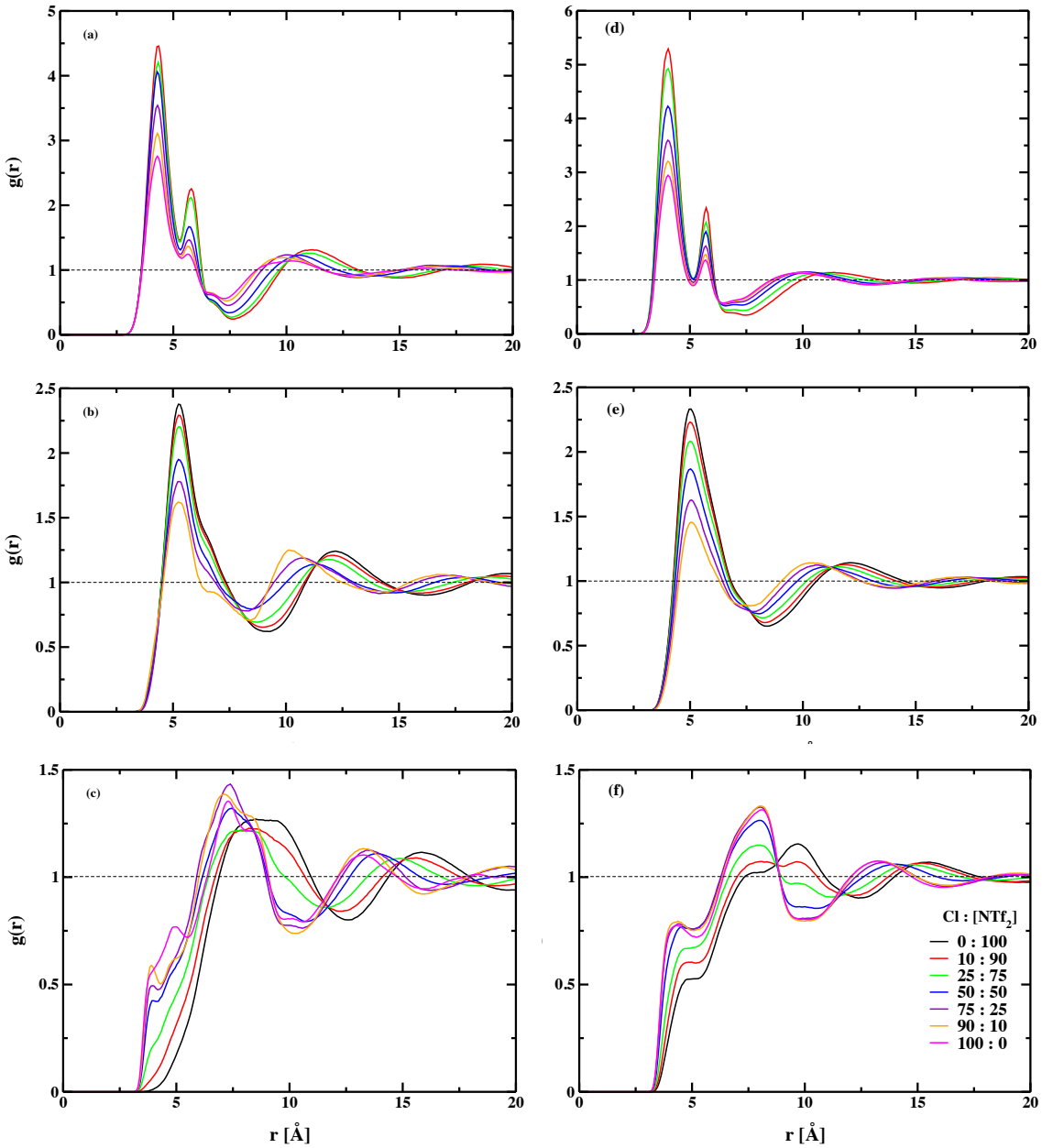

Figure 4.31: Comparison of radial distribution functions (RDFs) with varying Cl^- ion concentration between (i) cation-Cl - (a) AA and (d) UA; (ii) cation-[NTf_2] - (b) AA and (e) UA , based on center-of-mass (COM), and (iii) cation-cation - (c) AA and (f) UA, based on center-of-ring (COR), in the $[C_4mim]Cl_x[NTf_2]_{1-x}$ mixture system using an all-atom (AA) vs. united-atom (UA) force field model.

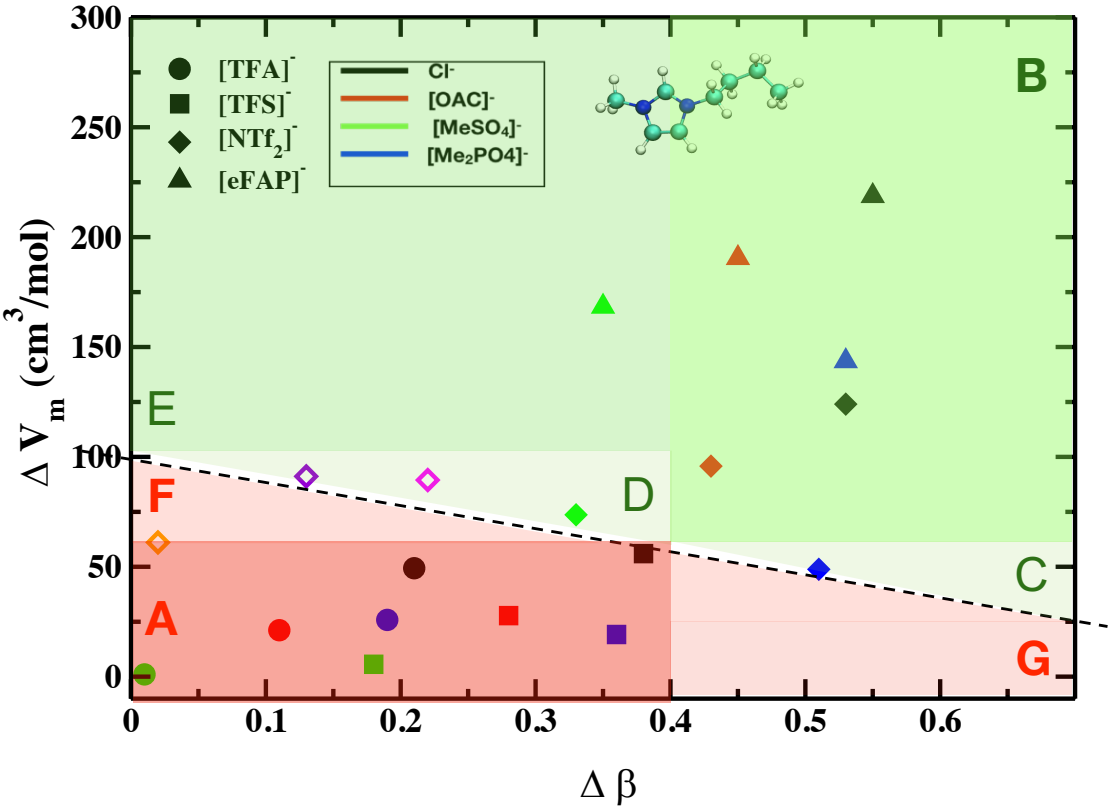

Figure 4.32: A qualitative correlation between differences in hydrogen bond acceptor ability and size/molar volume of anions that leads to nonideality in binary IL mixtures. 16 IL mixtures (Figure 4.30) shown as solid symbols while three additional mixture systems of $[C_4mim][BF_4]$-$[C_4mim][NTf_2]$, $[C_4mim][PF_6]$-$[C_4mim][NTf_2]$ and $[C_4mim][DCA]$-$[C_4mim][NTf_2]$ shown as open symbols.

mol and $\Delta\beta \sim 0.55$). This mixture shows nonideal behavior in the form of non-native structures (see Appendix C). These molecular structures are qualitatively comparable to the structures observed in the IL mixture of $[C_4mim]Cl_x$ $[NTf_2]_{1-x}$, discussed in the previous sections. However, it appears that the concentrations at which the weakly coordinating anion loses its ability to interact with HCR and HCW1 positions and disruption of π-π interaction depend, at least qualitatively, on the differences in molar volume and β values. On the contrary, the lowest differences of $\Delta\beta \sim 0.01$ and $\Delta V \sim 1$ cm^3 / mol recorded for $[C_4mim][MeSO_4]_x$ $[TFA]_{1-x}$ mixture displays ideal mixing throughout the entire composition range. Similar results have been observed

for $[C_4mim][MeSO_4]_x$ $[TFS]_{1-x}$ that does not have significant differences in both molar volume and hydrogen bond acceptor ability of the anions.

Considering the mixtures of $[C_4mim][OAC]_x$ $[TFA]_{1-x}$, $[C_4mim][OAC]_x$ $[TFS]_{1-x}$, $[C_4mim][Me_2PO_4]_x$ $[TFA]_{1-x}$, and $[C_4mim][Me_2PO_4]_x$ $[TFS]_{1-x}$, where ΔV ranges only between $\sim$ 20-30 cm^3 / mol and $\Delta\beta$ changes three folds from 0.11 to 0.36 respectively, close-to-ideal mixing behavior is observed suggesting that even moderately high $\Delta\beta$ may not be a sufficient condition for nonideality. However, there are some essential features worth discussing. Although native structures are anticipated for the mixtures mentioned above for the entire composition range, the direct association of weakly coordinating fluorinated anions, $[TFA]^-$ and $[TFS]^-$, at HCR position is weak, as shown in SDFs of pure IL systems (see Appendix C). In fact, small introduction of strongly associating anions (even 10 mol %) nearly eliminates the HCR-anion interaction, forcing the fluorinated anion to occupy positions above and below. This observation is advocated by the respective cation-anion ADFs. Therefore, some non-ideal outliers may be expected. For instance, in section 4.1 it was observed that IL mixture of $[C_4mim]$ $[OAC]_x$ $[TFA]_{1-x}$ can potentially have ionic conductivity higher than the pure IL counterparts for the mixture compositions of $x_{[OAC]} = 10$ % and 25 %, although it possesses ideal mixing behavior for the other thermophysical properties. Nonetheless, as can be observed from cation-cation SDFs or RDFs, the cation-cation distances do not change due to an already greater distance between the rings arising due to poorly stabilized π-π interaction. In addition, subtle re-organization of anions do not affect the relative arrangement of the cations throughout the mixture composition-range thereby displaying an ideal behavior. Thus, we speculate that mixtures such as $[C_4mim]$ $[Me_2PO_4]_x$ $[TFA]_{1-x}$, and $[C_4mim]$ $[Me_2PO_4]_x$ $[TFS]_{1-x}$ with moderately high $\Delta\beta$ values, although can be assumed to display ideal behavior, has potential to enhance a specific physicochemical property plausibly but the con-

centration dependence may not be significant.

Previously, Clough et al. [35] has experimentally shown that mixture of $[C_4mim]$ Cl_x $[TFS]_{1-x}$ displays an ideal behavior whereas $[C_4mim]$ $[Me_2PO_4]_x$ $[NTf_2]_{1-x}$ mixtures are nonideal, consistently over a broad spectrum of physicochemical properties such as molar volume, glass transition, viscosity and conductivity. This was further investigated by Matthews et al. [45], both experimentally and computationally, and similar conclusions were reached which were justified based on the structural reorganizations of the constituent ions, specifically increase in cation-cation distances and poor stabilization of π-π interaction. The results obtained in this study are consistent with similar insights. In fact, all the SDFs, RDFs and ADFs reported in this study can be directly compared with the structures reported by Matthews et al. [45], as same force field models are used in both the studies. It is interesting to see that for both the mixtures ΔV is ~ 50 cm^3 / mol, consistent with Clough et al. [35], whereas $\Delta\beta$ value changes from 0.38 to 0.55 that changes the mixing behavior from ideal to nonideal behavior respectively. This indicates that at this ΔV limit, increasing the difference between the hydrogen bond accepting ability of the anions can lead to nonideal mixing behavior. Contrastingly, $\Delta\beta$ value < 0.4 maintains ideal behavior. For example, $[C_4mim]$ Cl_x $[TFA]_{1-x}$ mixture shows ideal behavior, as suggested by structures although all the structural characteristics are essentially similar to $[C_4mim]$ Cl_x $[TFS]_{1-x}$. It is also worth mentioning that as the molar volume difference is large, RDFs appear to have a strong dependence on the anion concentration, but since cation-cation interactions are not substantially affected to increase the cation-cation distances the relative change is not considered drastic enough to have non-native structures, thus showing close-to-ideal behavior.

Similarly, considering binary IL mixtures of $[C_4mim][Me_2PO_4]_x[TFS]_{1-x}$ and $[C_4mim]$

$[MeSO_4]_x[eFAP]_{1-x}$ that has nearly same $\Delta\beta$ of 0.35 and 0.36 respectively, while molar volumes are different by almost nine folds, ~ 19 cm^3 / mol vs. ~ 169 cm^3 / mol respectively has strikingly dissimilar features. As observed for the IL mixtures of $[C_4mim]$ $[MeSO_4]_x$ $[TFA]_{1-x}$ and $[C_4mim]$ $[MeSO_4]_x$ $[TFS]_{1-x}$, mentioned above, both RDFs and ADFs clearly exhibits a very weak dependence on the anionic composition. In addition, cation-cation interactions seem to remain unaltered thus suggesting that the IL mixture of $[C_4mim][Me_2PO_4]_x[TFS]_{1-x}$ is close to ideal. Nonetheless, few distinct characteristics are simple to point out. First, the SDFs indicate that the interaction of anion with CN3 position mainly depends on the size of the anion; smaller size anion is able to approach CN3 position irrespective of the hydrogen bond accepting strength. This observation is unlike any other mixture system studied in this work where $[TFS]^-$ interacts with CN3 position even at its lowest concentration while it remains inaccessible to $[Me_2PO_4]^-$ anion. Second, although visual inspection of SDFs show that at the highest $[Me_2PO_4]^-$ concentration (90 %) $[TFS]^-$ direct association at HCR position appears to be eliminated; ADFs suggests that probability of in-plane configuration is higher than the probability of $[TFS]^-$ localizing above and below the ring-plane. Thus, demonstrating that the structures are similar to pure IL counterparts or in other words will display close-to-ideal behavior.

On the other hand, $[C_4mim]$ $[MeSO_4]_x$ $[eFAP]_{1-x}$ clearly show non-native (nonideal) structures. This is probably attributable to the packing effects, as smaller size anion will tend to occupy strongly coordinating positions. Therefore, very significant differences in anion size can lead to packing effects thus leading to nonideal behavior. We speculate that this inference can also be extended for IL mixtures where the anions do not form hydrogen bonds with the cation, for example, pyridinium-based ILs.

Furthermore, IL mixtures of $[C_4mim]$ $[Me_2PO_4]_x$ $[NTf_2]_{1-x}$, $[C_4mim]$ Cl_x $[NTf_2]_{1-x}$

and $[C_4mim]$ $[Me_2PO_4]_x$ $[eFAP]_{1-x}$ that have similar $\Delta\beta > 0.5$ and have monotonically increasing ΔV also display a nonideal behavior, with structures comparable to $[C_4mim]Cl_x$ $[eFAP]_{1-x}$ IL mixture. In fact, the previous structural investigation by Matthews et al. [45], using an all-atom model, for $[C_4mim]$ $[Me_2PO_4]_x[NTf_2]_{1-x}$ and $[C_4mim]$ Cl_x $[NTf_2]_{1-x}$ has reported similar observations. Additionally, IL mixtures of $[C_4mim]$ $[OAC]_x[NTf_2]_{1-x}$ and $[C_4mim]$ $[OAC]_x[eFAP]_{1-x}$ also display non-native structures, which can be expected based on the differences in the molar volumes of the anions.

Thus, based on all the observations and insights presented above, we speculate that Figure 4.32 can be divided into multiple regions to anticipate the presence of ideal vs. nonideal structures in binary ILs mixtures. The division is not only marked by the dotted-line but also by colors – green (for nonideal) and red (for ideal structures) – with varying intensities giving seven quadrants (A-G). At this point, it is imperative to mention that the definition of "non-native" structures includes different distribution of both anions and cations around a given cation. As shown below, differences only in the distribution of the anions around the cation may not be a sufficient condition to get a nonideal behavior.

Quadrants "A" and "B", shown in dark shades of red and green, are the regions where we surmise a definite presence of native and non-native structures, respectively. Quantitatively, if $\Delta V > 60$ cm^3 / mol and $\Delta\beta > 0.4$, simultaneously, IL mixtures will portray non-native structures or nonideal mixing behavior, and oppositely, ideal mixing behavior is anticipated for the simultaneous $\Delta V < 60$ cm^3 / mol and $\Delta\beta < 0.4$.

However, this measurement fails to address two major quadrants of this diagram – the top left corner and the bottom right corner. Quadrants "C", "D" and "E" also

tend to show non-native structures. The extent of nonideality (features of non-native structural transition) is slightly less pronounced as compared to the IL mixtures considered in "B", thus shown in light green color. However, the reliability of this demarcation is achieved by making comparisons with the literature.

As mentioned above, Clough et al. [35] reported consistent nonideal behavior in terms of excess molar volumes, viscosity, conductivity and glass transition experiments for anion pair of $[Me_2PO_4]^-$ and $[NTf_2]^-$ combined with either $[C_4mim]^+$ or 1-n-butyl-methylpyrrolidinium $[C_4C_1pyrr]$ cations. This corresponds to the same IL mixture ($[C_4mim]$ $[Me_2PO_4]_x$ $[NTf_2]_{1-x}$) in quadrant "C" suggesting that although the difference in molar volume is smaller than 60 cm^3 / mol, a $\Delta\beta$ significantly higher than 0.4 can still lead to nonideal behavior. The same authors also showed that if the difference in hydrogen bond ability of some anions was moderate, small excess molar volumes (nonideality) were still observed for the IL mixture series of $[C_4mim]$ $[MeSO_4]$ and $[C_4mim]$ $[NTf_2]$. The authors rationalized the observations based on the large differences in molar volumes. The observation made in this work is consistent, as the IL mixture of $[C_4mim]$ $[MeSO_4]_x[NTf_2]_{1-x}$ display non-native structures.

On the other hand, Clough et al. [35] suggested close to ideal behavior for the mixture of $[C_4mim]$ Cl_x $[TFS]_{1-x}$. We believe, this mixture system is very unique. It is on the verge of ideal vs. nonideal and helps define the boundary. The visualization of structural features (see Appendix C) can tempt to infer that this IL mixture will display nonideal behavior based on the fact that distribution of $[TFS]^-$ anion around the cation changes with the change in composition. Whereas, it should be noted that the cation-cation interactions are not marked different from the neat ILs, possibly rationalizing its close to ideal behavior. Thus, we believe that this is a classic example showcasing that arrangement of all the ion moieties should change in order to display

nonideality.

Apart from the 16 binary IL mixtures considered, additional mixture systems of $[C_4mim]\ [BF_4]_x\ [NTf_2]_{1-x}$, $[C_4mim]\ [PF_6]_x\ [NTf_2]_{1-x}$ and $[C_4mim]\ [DCA]_x\ [NTf_2]_{1-x}$ were considered, shown as open symbols in Figure 4.32, to have a better understanding in the top-left region. Out of these three, mixtures containing $[BF_4]$-$[NTf_2]$ and $[DCA]$-$[NTf_2]$ anion combinations displayed nonideality (non-native structures) while $[PF_6]$-$[NTf_2]$ possess close-to-ideal behavior. This is further corroborated by the literature. For instance, Lopes et al. [48] reported that mixture of $[C_4mim]\ [BF_4]_x[NTf_2]_{1-x}$ possess high deviations in terms of excess molar volumes while $[C_4mim][PF_6]_x[NTf_2]_{1-x}$ possess close to ideal behavior. In fact, Larriba et al. [51] showed that same anions, $[BF_4]^-$ and $[NTf_2]^-$, when paired with a common cation of $[C_4py]^+$ display highly non-ideal behavior with large deviations in the thermophysical properties such as molar volumes and viscosities across the entire composition range. This type of comparison is justified as differences in the anion molar volumes must remain preserved. Similarly, although no data for $[C_4mim]\ [DCA]_x\ [NTf_2]_{1-x}$ is available for direct comparison, indirect comparisons can be made with the works of MacFarlane and co-workers [4]. The authors were able to show that mixture of $[C_3pyr]\ [DCA]_x\ [NTf_2]_{1-x}$ displays strong deviations from the ideal mixing rule for the thermophysical properties. Thus, allowing us to identify two different quadrants, namely "D" and "F". Since, the mixture of $[C_4mim][DCA]_x[NTf_2]_{1-x}$, with $\Delta\beta$ as low as 0.13, is able to display nonideal behavior due to large differences in molar volume, we believe it is safe to assume that quadrant "E" with a further increase in differences in molar volumes the IL mixtures will keep possessing nonideal behavior, thus, characterizing the top-left region.

As far as boundaries of quadrant "C" and "G" are concerned, at this point, it is still unclear where are the exact boundaries. However, based on the observations

made, we can at least say that if the difference in the hydrogen bond ability of anions is significantly large smaller differences in molar volume can still give nonideal mixtures and vice-versa. This is shown as a dotted line with a negative slope.

Since all the analyses and comparisons done in this section were conducted to help predict, *a priori*, the presence of non-native (nonideal) structures in IL mixtures, in an effort to identify potential candidates for enhanced CO_2 solubility; it becomes necessary to discuss CO_2 solubilities in some of the IL mixtures that are classified as nonideal. Figure 4.33 shows preliminary results (only one calculation) of

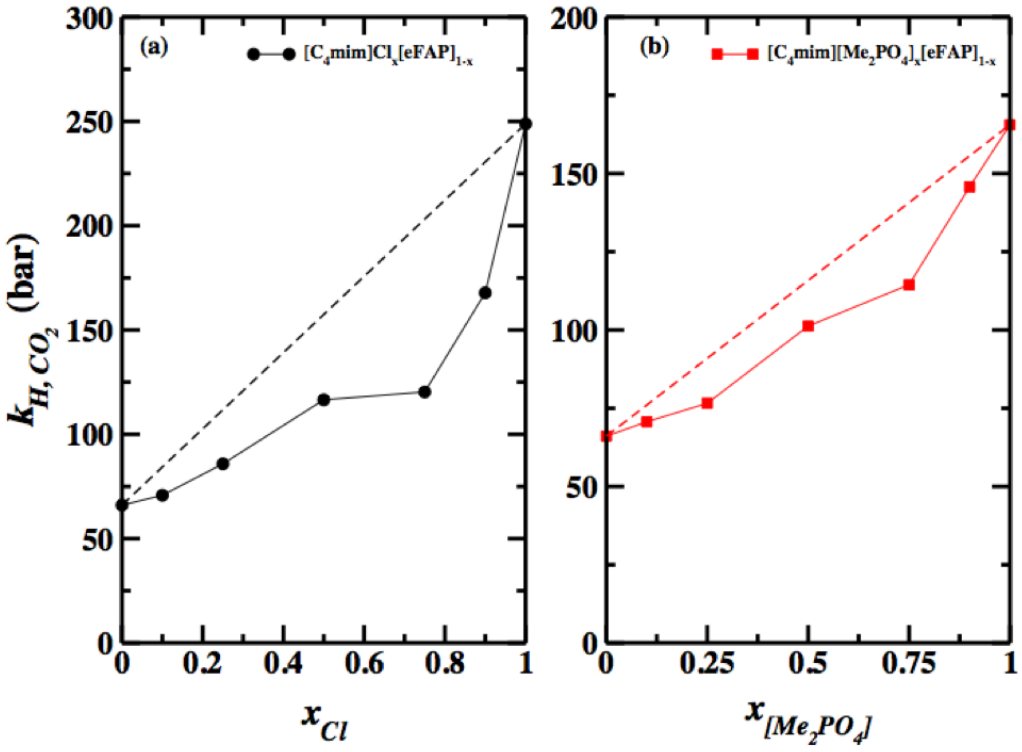

Figure 4.33: Henry's constants, k_H, of CO_2 as a function of composition of strongly coordinating anion in binary IL mixture of (a) [C_4mim] Cl_x [eFAP]$_{1-x}$ and (b) [C_4mim] [Me_2PO_4]$_x$ [eFAP]$_{1-x}$ at 353 K. Please not that the dashed line is shown for reference for linear mixing average while the continuous lines joining data points are only guide to the eye. This is only preliminary calculation and the standard deviations were not calculated.

Henry's constants of CO_2 in binary IL mixtures of $[C_4mim][Me_2PO_4]_x[eFAP]_{1-x}$ and $[C_4mim]Cl_x[eFAP]_{1-x}$. As speculated and expected, both the mixtures display highly nonlinear Henry's constants in comparison to the ideal mixing behavior.

As shown in the previous sections, it is the presence of non-native structures that allows large weakly coordinating anion to occupy positions above and below the ring, that makes fluorine atoms available thus, leading to an enhanced interaction between CO_2 and the weakly coordinating fluorinated anion; along with re-organization of free molar volume that aids the CO_2 accommodation. Such behavior leads to a nonlinear behavior in Henry's constants. Therefore, if one chooses an IL mixture such that the two anions comprising the mixture differ significantly in both molar volume and hydrogen bond acceptor ability, the CO_2 solubility can be fine-tuned and essentially be enhanced.

4.6 Summary

To summarize:

- Mixing of ILs differing substantially in their hydrogen bonding capability and molar volumes leads to non-native molecular structures that are not found in the neat ILs.
- Non-native structures are definitely expected if $\Delta\beta > 0.4$ and $\Delta V > 60$ cm^3/mol simultaneously.
- These non-native structures lead to thermophysical property behavior and gas solubility behavior that is a non-linear function of the IL composition.
- Gas solubility has better chances to be enhanced, in comparison to neat ILs, at higher pressures.

The summary is also presented pictorially in Figure 4.34.

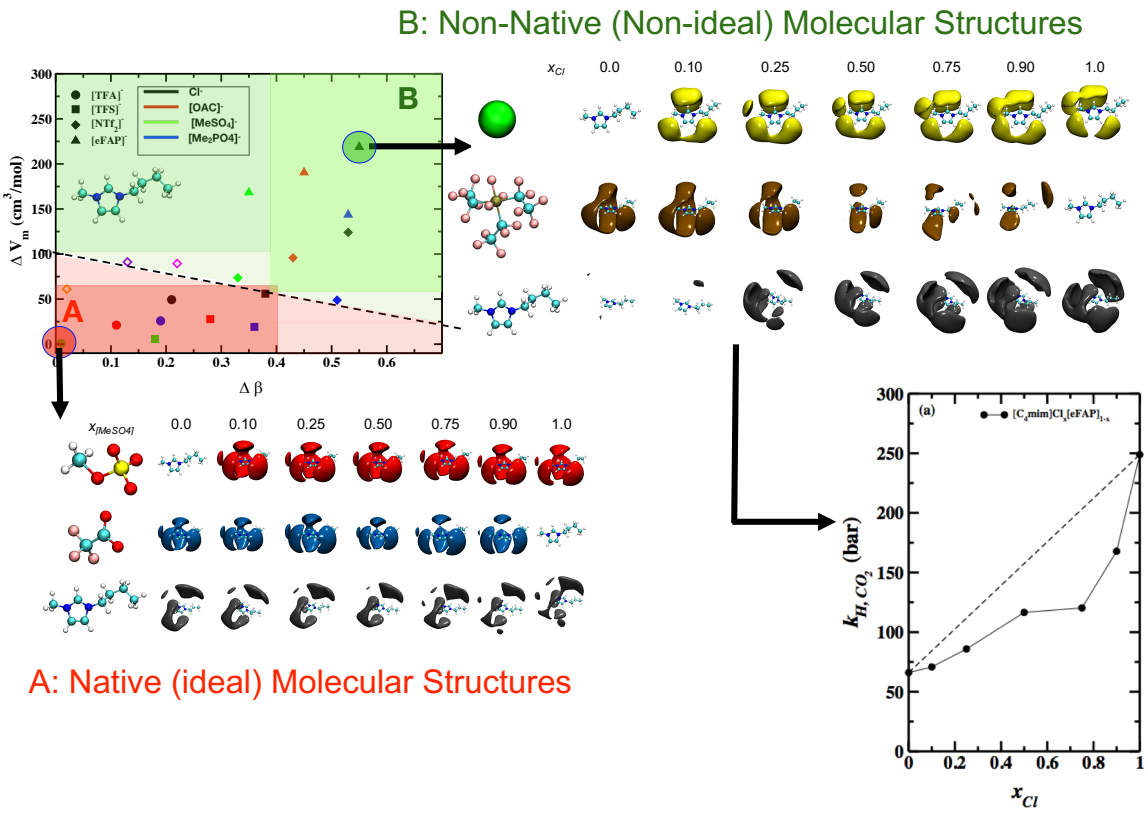

Figure 4.34: Main findings of Chapter 4

CHAPTER 5

UNDERSTANDING THE SELF-ASSEMBLY OF LONG-CHAIN IONIC LIQUIDS HAVING BOTH THE CATIONIC AND ANIONIC TAILS

Unlike binary ionic liquid (IL) mixtures, discussed in chapter 4, the focus here is to fundamentally understand the self-assembly of long-chain ILs, rather than their function. This chapter considers unique bi-amphiphilic ILs, in which alkyl chain present on both the cation and anion contribute simultaneously in defining the non-polar domain, and provide information regarding their self-assembled morphology and nanoscale heterogeneities.

The first part of this chapter deals with six different pure bi-amphiphilic ILs where alkyl chain on the cation is increased evenly from 2 to 12 while the anionic chain length is kept constant at 8 – $[C_n\text{mim}][C_8SO_4]$. The morphologies and structural features of shorter cationic chains, $n = 2$ and 4, are compared with the literature, as experimental studies for them are available; while for $n = 6$, 8, 10, 12 no experimental studies, to our knowledge, are available. Thus, for these ILs, new molecular level insights are provided. The mesoscale morphology is characterized by computing site-specific radial distribution functions, structure factors, and orientational order parameters. Additional insights are provided by judiciously partitioning the IL domains into polar and nonpolar subunits and probing their connectivity and shape using Voronoi tessellation based domain analysis and reporting changes in the distribution of their aggregate sizes.

Due to the uniqueness of the morphology and structural features displayed by [C_{12}mim] [C_8SO_4] IL, the later sections of the chapter focuses on modulating its self-assembly. Dissolution in another IL is employed as a strategy to control/modulate the structures. Two binary IL mixtures are considered. The concentration dependence of the morphological transitions is rationalized based on the various analyses mentioned above. On the related topic, another example of binary IL mixture, [C_8mim][BF_4]-[C_2mim][BF_4], is included to demonstrate the implications of fine-tuning the morphologies at mesoscale at physicochemical property behavior. Further, aqueous solution of [C_8mim][$C_{12}SO_4$] IL, where length of cationic and anionic chains are swapped compared to the system studied in this work, has been known to form vesicle-like structure at very dilute water concentration, experimentally, which can potentially be exploited for various applications such as mixed micellar surfactant systems, protein-stabilizer in detergent industries or solvents for synthesis of nanoparticles. Although the studies had rationalized the thermodynamics based on scattering measurements, they failed to provide a fundamental molecular-level picture regarding the structural transitions. Thus, the last part of this chapter focuses on studying the aggregation behavior of [C_{12}mim] [C_8SO_4] IL in aqueous media, at very dilute conditions, with the objective of characterizing the morphological changes. A spontaneous formation of a unilamellar vesicle-like structure is observed at the highest water concentration. A concentration range spanning small clusters of ILs and continuous water network to small clusters of water and percolation of the bicontinuous IL phase is recognized and structurally characterized.

5.1 Alkyl Chain Dependence of Morphological Transitions in 1-n-Alkyl-3-methylimidazolium Octylsulfate Ionic Liquid Series

In this section, the focus is on, changes in the bulk microstructures of long-chain ILs that have both anionic and cationic alkyl chains. For this purpose, the anion –

octylsulfate $[C_8SO_4]^-$ – having 8 carbons in the alkyl chain is paired with imidazolium-based cations – $[C_n\text{mim}]^+$ – where n is systematically varied, evenly, from 2 to 12. The objective of this study is to determine the effect of increasing alkyl chain length in the cation on the nonpolar domain formation, especially when the alkyl chain lengths from both the ions participate in defining such domains. For this purpose, MD simulations (using GROMACS 4.5.5) were conducted at 400 K and 1 bar conditions. This temperature was chosen to ensure liquid phase for all the ILs. The origin of rich diversity of structures obtained by introducing nonpolar content on both the ions is discussed. The results indicate that all the ILs form nonpolar domains, morphology of which gradually changes from globular, sponge-like to layer-like structure, which has a long-range order. In fact, $[C_{12}\text{mim}][C_8SO_4]$ IL contains nonpolar domains of varying lengths. Please note that ILs with $n \geq 6$ are new ILs that have not been studied experimentally before. Hence, validation of the results rationalized here, perhaps, still remains to be seen. This work was published in 2017 [199] and all the analyses discussed here is based on the published simulation protocols, which slightly differ from the protocols mentioned in section 3.3.1 in terms of simulation times. The importance of simulation protocols, when reproducing results, is included as an aside.

Structural properties of the IL systems are described in terms of structure factors, radial distribution functions, heterogeneity and orientational order parameter, Voronoi domain analysis and aggregate size distributions. All the properties were computed as described in section 3.3.4. The results below are provided in terms of the polar and nonpolar groups present in $[C_n\text{mim}][C_8SO_4]$ IL systems. The cation-polar head group contains the imidazolium ring as well as the methyl and methylene groups directly bonded to the ring. Similarly, the anion-polar head group represents sulfur and oxygen atoms, and the methylene group attached to oxygen in octylsulfate. The nonpolar regions in the cation and anion are indicated by the uncharged carbon groups

while the terms cation-tail and anion-tail denote the terminal carbon atom of the side chain in the cation and anion, respectively.

5.1.1 Morphological Transitions

The first hint of the morphological changes that might occur in these systems can be visualized by analyzing the snapshot of a well-equilibrated trajectory. In Figures 5.1 are shown the structural evolution due to progressive segregation of domains of varying polarity, designated as polar and nonpolar domain, along the homologous series. The rendering scheme is color-coded to reflect the polar and nonpolar components of both the ion moieties: cation-polar in red, anion-polar in yellow, cation-nonpolar in green and anion-nonpolar in blue. This coloring scheme is adapted from the works of Amith et al. [126] As expected, in order to maintain the constraint of electrical neutrality, the cation-polar, and anion-polar groups always stay close to each other in an alternating fashion. This is consistent with previous studies. [102–104, 123] Based on the domain count, *vide infra*, the polar domain is continuous that spans the entire box for all the ILs. However, the morphology of this domain is found to be dependent on the identity of the cation, which can be attributed to the fact that the necessity of accommodating nonpolar domains further constraints and perhaps changes the placement of cation- and anion-polar heads. For smaller cationic alkyl chains, $n = 2$ and 4, the polar domain percolates the entire box resulting in a sponge-like morphology (no preferred direction) which is due to strong aggregation of octyl chains present on the anion. Additionally, since the cationic alkyl chains are incapable of forming a continuous network, they appear as small globules or islands within the polar network. As the alkyl chain is further increased, the two domains demonstrate a tendency to align in a layer-like fashion. For $n = 8$ the presence of lamellae (layer-like) is consistent with the structure reported by Amith et al. [126] One interesting thing to note here is that as the amount of nonpolar content increases the polar network appears to be thinner;

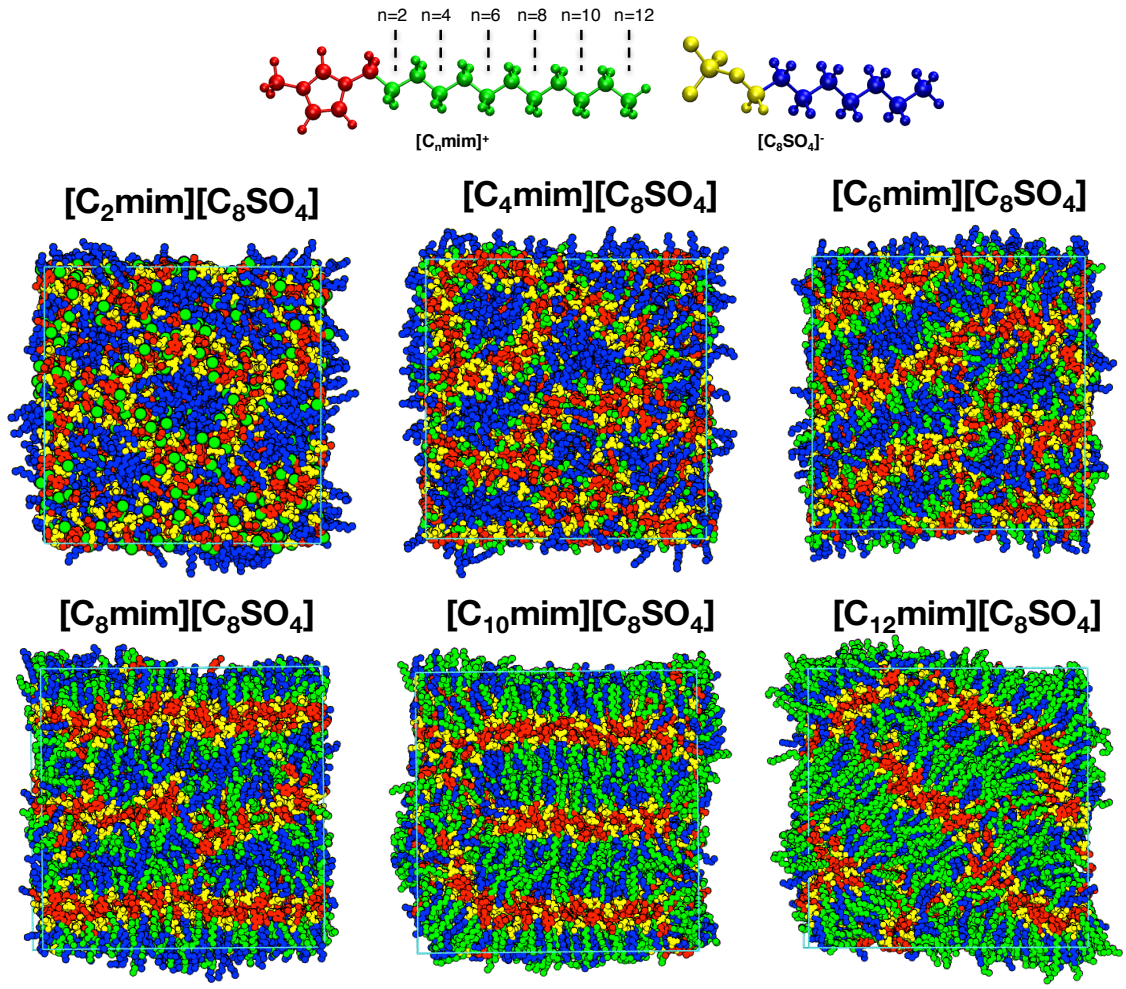

Figure 5.1: Instantaneous snapshot of the equilibrated system for $[C_n\text{mim}][C_8SO_4]$ IL homologous series. The snapshots are color-coded to reflect the polar and nonpolar components on both cation and anion. (Cation-polar: red, Anion-polar: yellow, Cation-nonpolar : green and Anion-nonpolar: blue)

this is probably due to the stretching of the polar domain trying to accommodate the nonpolar tails which need more polar heads for bridging to maintain the continuity. Furthermore, the layered arrangement of $n = 12$ IL appears to be less intermeshed since both cationic and anionic chains are capable for segregating two polar strands there are instances where either cationic, predominant, or anionic nonpolar domains interleave the polar strands, thus, giving rise to multiple structural features.

5.1.2 Structure Factors

In an effort to visualize the structural evolution and provide a quantitative metric, structure factors were calculated, as described in section 3.3.4. Figure 5.2 shows that

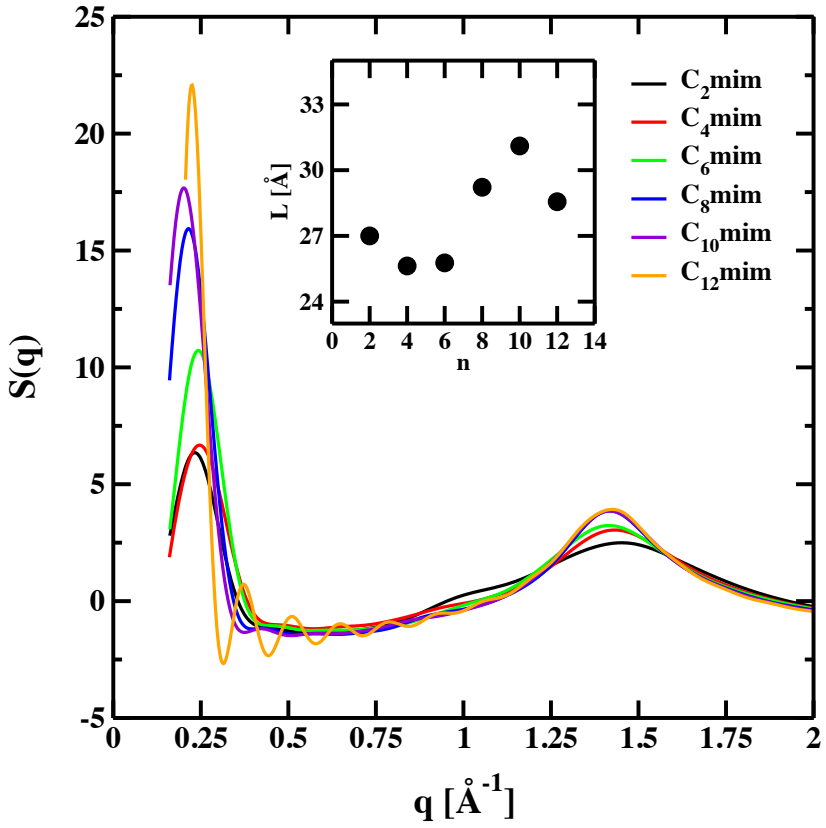

Figure 5.2: Structure factors, S(q), as a function of reciprocal space wavenumber, q [Å^{-1}] for [C$_n$mim][C$_8$SO$_4$] IL homologous series at 400 K. In the inset, the alkyl chain dependence of characteristic length of nonpolar domain, calculated as $\frac{2\pi}{q}$, is reported.

all the structure factors exhibit: (i) a well-defined pre-peak at about 0.23 Å^{-1} that is known to be associated with the alternating polar and nonpolar domains; (ii) an intermediate shoulder around 1 Å^{-1} corresponding to charge alternation within the polar network; and (iii) a peak at about 1.45 Å^{-1} arising due to intermolecular interactions of the juxtaposition of oppositely charged groups. This observation is similar to what has been reported previously for a range of ILs [102–104, 106–108, 110, 117, 123, 126]. In addition to these peaks, the [C$_{12}$mim][C$_8$SO$_4$] IL system displays peaks between

the pre-peak and intermediate-q regimes, the origin of which will be discussed below. The structure factor reported in this work for $[C_2mim][C_8SO_4]$, $[C_4mim][C_8SO_4]$ and $[C_8mim][C_8SO_4]$ can be compared to those reported earlier. [86, 94, 126] The features are similar although the present simulations were conducted at different temperature.

The pre-peak is present in all the systems indicating that all the systems have nano-segregated polar and nonpolar domains. The location of the pre-peak, however, exhibits a complex behavior such that the pre-peak shifts toward larger q values in going from $n = 2$ to $n = 4$, an observation consistent with the experiments. [94] In fact, even for $n = 6$ the location of pre-peak occurs at q values larger than that for $n = 2$. However, it should be noted that pre-peak monotonically shifts towards lower-q values in going from $n = 4$ to $n = 10$. Computing the real space distances, using Bragg's law, (shown in inset figure) shows that these distances do not follow a linear relationship with the length of the cation alkyl chain, in contrast to other IL systems where the $[C_nmim]^+$ combined with small anions such as Cl^-, $[PF_6]^-$, $[BF_4]^-$ and $[NTf_2]^-$ show linear relationship. [85, 86] Although the size of the nonpolar domain is a nonlinear function of the alkyl chain length, the length of the nonpolar domain increases by ∼1.1 Å per CH_2 unit from n = 4 to n = 10. Russina and Triolo reported a similar increment in the length of the nonpolar domain for an additional –CH2 group for the homologous series of $[C_nmim][PF_6]$ crystals. [94]

The structure factor of $[C_{12}mim][C_8SO_4]$ IL is characterized by additional peaks between the pre-peak and intermediate-q peaks with the corresponding real spaces distances of 16.9 Å, 12.3 Å, and 9.7 Å respectively, indicating that the nanoscale structural heterogeneity is present over multiple length scales for this IL. These conclusions are invariant regardless of the system size, initial configurations, and simulation time; and are not the artifact of finite size. To our knowledge, the occurrence of multiple

peaks between the charge alternation peak and the pre-peak has been observed for the first time in the IL literature. The presence of multiple peaks in this IL can be attributed to liquid crystalline nature of the system in which planes with different Miller indices contribute to the observed X-ray scattering intensities located between the pre-peak and the intermediate-q peak.

Start Aside

At this point, it is worth mentioning that, unexpectedly, the qualitative inferences may depend on the GROMACS software version employed to study these systems. It has been mentioned earlier, in this work, that the simulation scales mentioned in this dissertation are slightly different from that published elsewhere. [199] For ensuring the reliability of the results obtained, the simulation of $[C_{12}mim][C_8SO_4]$ IL was extended for another 1μs in the NPT production ensemble for thorough equilibration. Since we started using GROMACS 2018 (newer version) for other projects, initially the extension of the trajectory was started in this version. The density of the system was well reproduced as with the case of GROMACS 4.5.5 when using Berendsen thermostats and barostats (while trying to make the system reach equilibrium. However, as the production run is started with the Nosé-Hoover thermostat and Parrinello-Rahman barostat, to reproduce the NPT ensemble in a right way, Figure 5.3 shows that the density of the system reduces significantly within the first 200 ps for GROMACS 2018, and then stays at that average value for the entire simulation. Whereas, if the extension was done in GROMACS 4.5.5, the results of which were published, the density stays equilibrated for the entire μs. The change in density between the two versions is more than 5 %. Direct comparison of the simulation snapshots using both the versions, shown in Figure 5.3, indicates that the qualitative inferences are somewhat different. The polar domain is layer-like when using 4.5.5 version, while a complete lamellar phase is reached when using the 2018 version. In fact, former shows that the

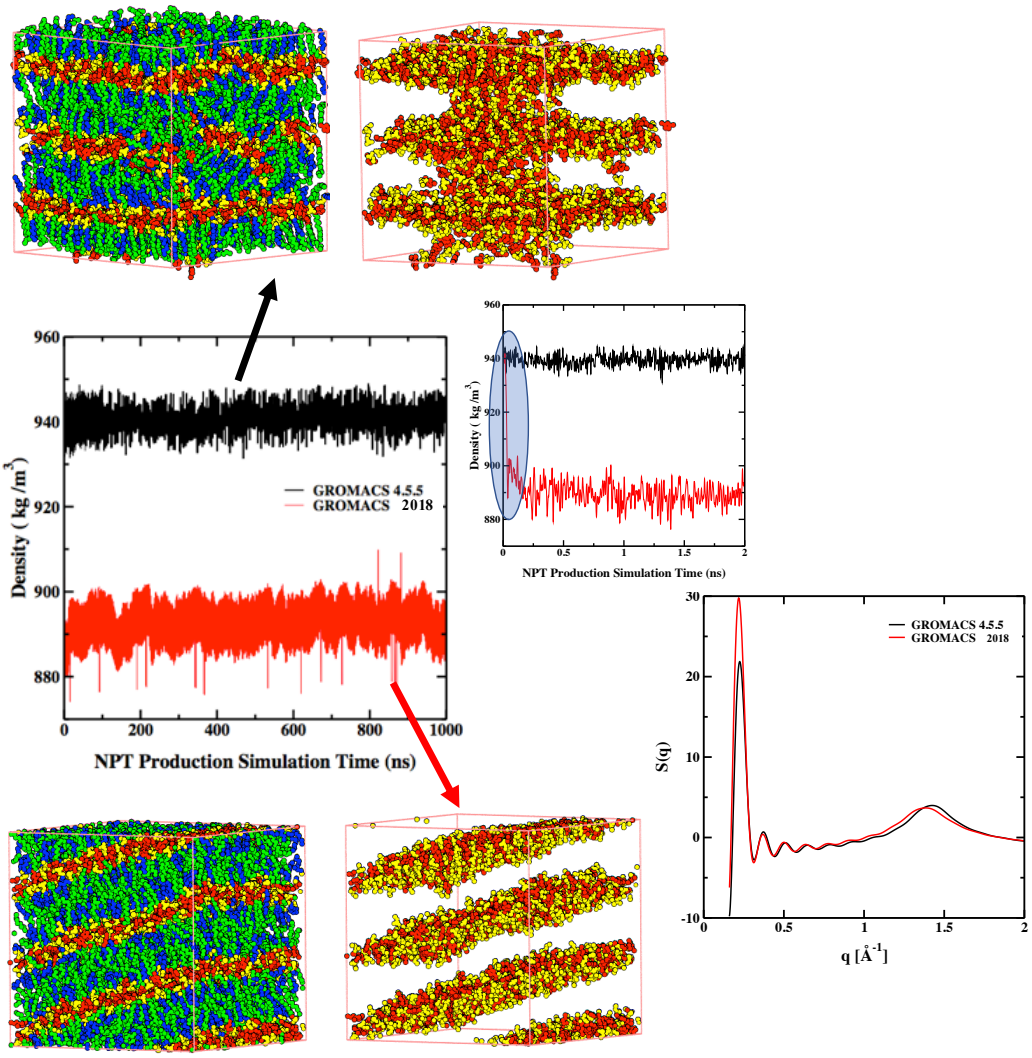

Figure 5.3: Dependence of structural morphology on GROMACS software versions. $[C_{12}mim][C_8SO_4]$ IL is shown as an example.

directions of the chains have slightly different directions while the latter display almost unidirectional arrangement. Nevertheless, the X-ray structure factors computed using both the trajectories have strikingly similar features. In addition, preliminary results (not shown here) for the extension of all other IL systems, of this section, show that the density is reduced for $n = 6$, 8, and 10 within the first 200 ps, giving qualitative snapshot slightly variant of the snapshots shown in Figure 5.1, whereas for $n = 2$ and 4 such reductions in density or changes in the morphology are not observed.

Thus, some take away points are:

- When trying to reproduce the previous results, it is a good practice to use simulation protocols as close as possible to the original work.
- Two qualitatively different morphologies can still give similar structural feature such as X-ray structure factor.
- Since such long-chain ILs are very sluggish systems, it is really important to equilibrate these systems long enough. Probably 0.5-1 μs should suffice. Also, note that the density or the total potential energy of the system might equilibrate within the first 50 ns. However, based on personal experience, long simulation times are required in order to allow molecules to diffuse to a more realistic trajectory position.

What is going wrong with the system, is out of the scope of this dissertation. To guide the readers, one can look at the works of Shirts et al. looking at equipartition energy or kinetic energy checks to make sure which GROMACS version is not able to reproduce NPT ensemble correctly.

End Aside

The shoulder at intermediate-q values is a signature associated with the charge alternation in the polar network of ILs. As evident from Figure 5.2, the shoulder shifts towards lower-q values indicating that the characteristic lengths between the same charged species increase as a consequence of swelling and stretching of the polar network in order to accommodate increasing nonpolar content. In order to dissect the origin of the shoulder in this region, the total structure factors were decomposed into partial structure factors due to cation-cation ($S(q)^{\text{C-C}}$), anion-anion ($S(q)^{\text{A-A}}$) and cation-anion ($S(q)^{\text{C-A}} + S(q)^{\text{A-C}}$) correlations as shown in Figure 5.4. It is clearly

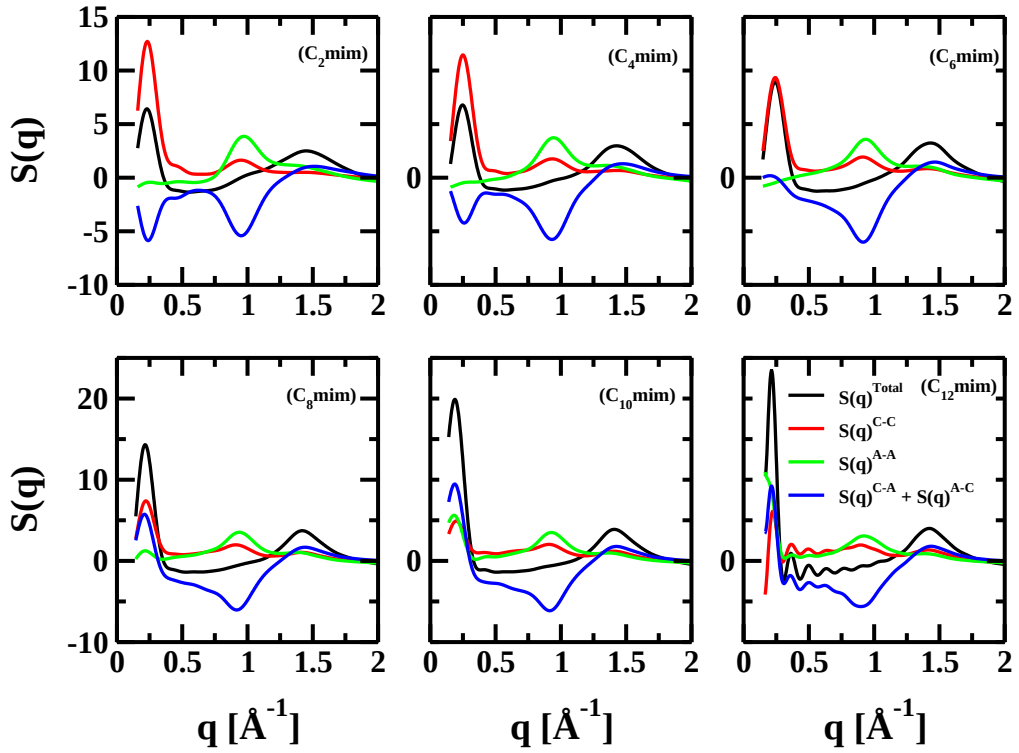

Figure 5.4: Total S(q) along with its subcomponents, partial structure factors, defined via ionic partitioning for $[C_n\text{mim}][C_8SO_4]$ IL homologous series at 400 K.

evident that the appearance of only a shoulder at q around 1 Å^{-1} is due to the cancellation of $S(q)^{\text{C-C}}$ and $S(q)^{\text{A-A}}$ peaks (like-like interactions) with counterion cross-correlations anti-peak of $S(q)^{\text{C-A}} + S(q)^{\text{A-C}}$. For $n \geq 8$ even cross-correlations display a pre-peak, suggesting formation of a biphasic system, intimately mixed alkyl chains belonging to both cations and anions into nonpolar domains. In other words, both cation and anion are treated as same-type species segregating polar and nonpolar network.

The peaks associated with large reciprocal space distances arise as a result of multiple intramolecular and intermolecular correlations and are typically attributed to the adjacent arrangement of oppositely charged species. For $n = 2$ through 6, the

elongation of alkyl chain causes the peak to shift towards lower-q values while the peak movements are rather insensitive to further increase in the alkyl chain length. Such behavior suggests a subtle rearrangement of oppositely charged ions in the first solvation shell of a given ion that helps maintain the connectivity of the network.

The intermediate and large-q peaks discussed above can also be analyzed in direct space using the cation-cation, cation-anion, and anion-anion RDFs. The results presented in Figure 5.5 also provides evidence for continuity and charge alternation within the polar network. RDFs between the polar-head groups based on center-of-masses (COMs), i.e., cation-polar COM and anion-polar COM, clearly indicates the presence of phase-shift in RDFs demonstrating medium-range periodical ordering that

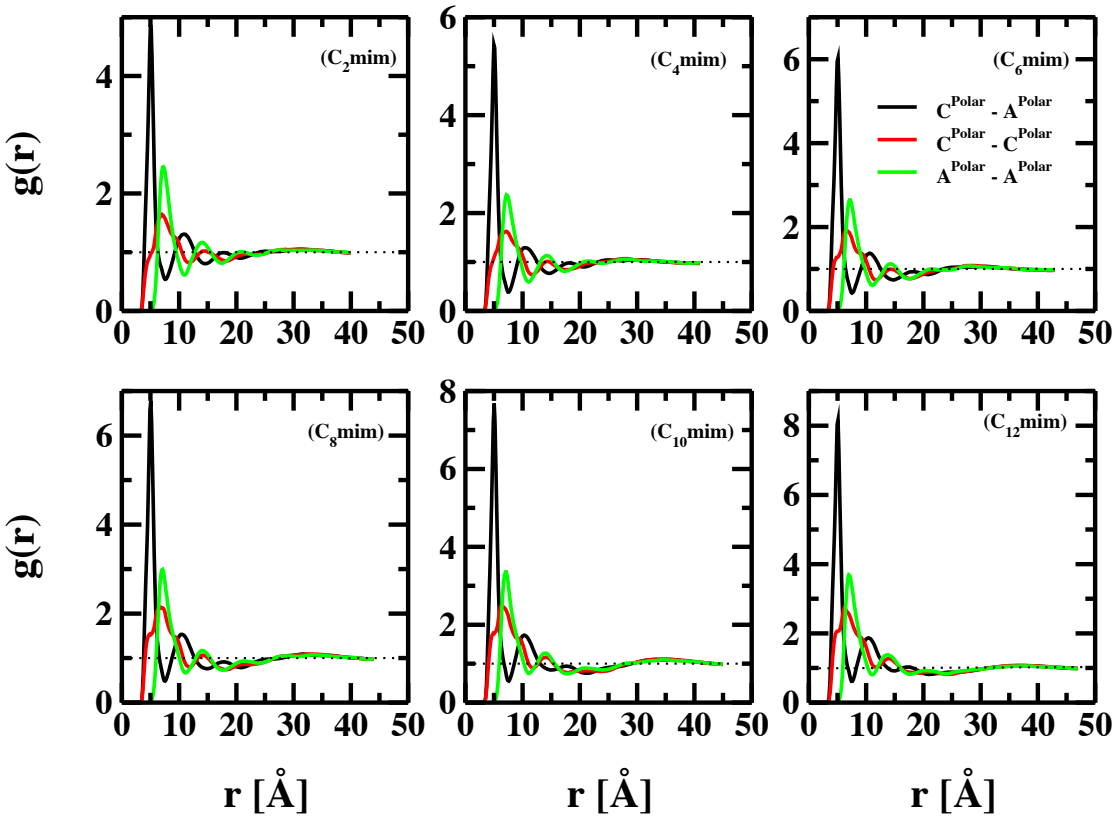

Figure 5.5: RDFs for cation-cation, cation-anion, and anion-anion polar head components for $[C_n\text{mim}][C_8SO_4]$ IL homologous series at 400 K, showcasing alternation of cations and anions.

contributes as peaks and anti-peaks in the partial structure factors. Such cation-anion RDF peak opposition-of-phase character with respect to the cation-cation and anion-anion interactions, is a signature of ILs and has been reported earlier for a range of ILs. [117] Such alternate phase behavior exists even at longer distances suggesting the presence of long-range ordering in these ILs. The number of surrounding shells almost remains the same along the homologous series as both polar and nonpolar domains have continuous subphase for all the IL systems under study. Interestingly, the direct space distances associated with the intermediate shoulder location can be taken as one full period of the alternating shell and the characteristic direct space wavelength of periodicity increases with an increase in the alkyl chain length. This is in consensus with the downshift of intermediate shoulder peaks indicating the presence of stretched polar network due to its need to accommodate the increasing nonpolar domains.

Thus, these results show that a simple strategy of selecting appropriate nonpolar content in both the cation and anion leads to not only tuning of the nonpolar domain length but also the formation of nanodomains spanning multiple length scales in the same IL.

5.1.3 Aggregate Analysis

Polar-nonpolar microstructure connectivity was further probed using an aggregate analysis based on the Voronoi tessellation as described by Brehm et al. [227] For this analysis, each of the IL systems is characterized in terms of four unique domains: (a) polar domain composed of the cation- and anion-polar head groups; (b) cation-nonpolar; (c) anion-nonpolar and (d) total nonpolar containing the nonpolar subunits from both the ions. The nonpolar groups are treated separately so that the origin for the change in the morphology can be identified.

Figure 5.6 (a) provides the number of domains based on this classification as a function of cationic alkyl chain length. For the entire homologous series, the domain count of polar domains is 1, indicating its continuity. On the other hand, various trends are apparent regarding the connectivity of nonpolar domains. For $n = 2$ and 4, the cation-nonpolar domain counts are significantly higher than 1, demonstrating that the nonpolar domains contributed by the cation-nonpolar subunits are dispersed in these systems. However, the anion-nonpolar groups aggregate to form one continuous domain. Furthermore, the domain count for the total nonpolar domain, irrespective of the chain source, is also greater than 1. This implies that although anion-nonpolar groups are connected, they must be isolated from the cation-nonpolar groups otherwise the total nonpolar domain count would be 1. This holds true for $n \geq 6$ beyond which total nonpolar domain count is 1. Thus, there is a transition from dispersed nonpolar phase to a continuous sub-phase with elongation of the cationic alkyl chain length. It is also interesting to note that, although the alkyl chain length is identical in both the ions in $n = 8$, the domain count for cation-nonpolar is greater than that for the anion-nonpolar group, indicating a stronger aggregation propensity of the anionic chains. In fact, the anion-nonpolar group exists as a single domain even for $n = 10$, although the length of the anionic alkyl chain is smaller than that in the cation. It is only for the $n = 12$ IL that there are multiple anion-nonpolar domains. Such behavior clearly demonstrates that an optimum combination of alkyl chain on cation and anion can be effectively employed as a strategy to tune the aggregation behavior of IL systems.

As inferred from the simulation snapshots, the shape of the morphology is changing from sponge-like to layer-like. In order to quantify such change of shapes, an average ratio of the volume vs. area of a given domain is calculated, denoted as Q^{peri} (section 3.3.4). By definition, the shape parameter assumes a value of 1 for a perfectly

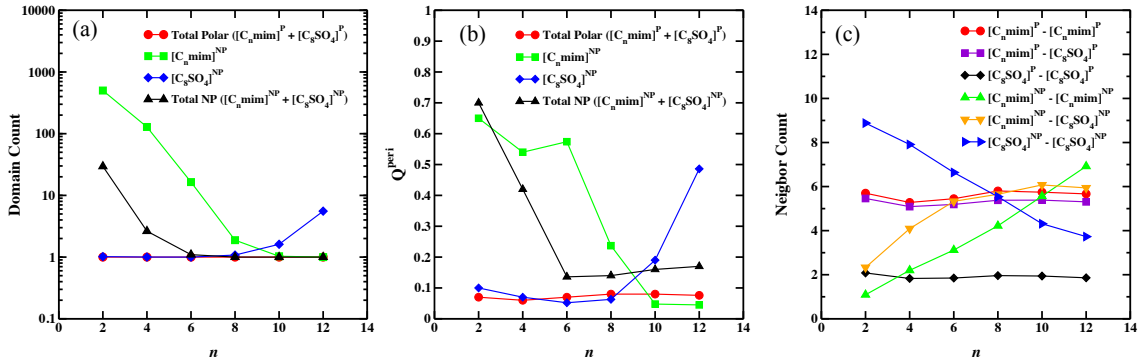

Figure 5.6: (a) Connectivity and (b) Shapes of aggregates; and (c) Number of neighbors around a given molecule in an aggregate probed via Voronoi tessellation domain analysis for the $[C_n\text{mim}][C_8SO_4]$ IL series. The aggregates are partitioned based on the respective polar and nonpolar components.

spherical shape while any deviations from sphericity lead to the values lower than 1. [227] From Figure 5.6 (b) it is clear that the shape of the polar network differs greatly from sphericity. On the other hand, the shape of the nonpolar domain constituted by both the cation- and anion-nonpolar subunit changes considerably along the series. For $n = 2$ and 4, due to the dispersed cation-nonpolar domain, the cationic-nonpolar domain assumes shape close to a sphere. On the contrary, the continuity of anionic octyl chains leads to an isoperimetric quotient of ~ 0.1, suggesting a shape dissimilar to a sphere. However, due to the presence of dispersed cation-nonpolar domain, the total nonpolar domain have the shape close to a sphere. Similar observation holds for $[C_4\text{mim}][C_8SO_4]$ IL. Very interesting observations are made for $n = 6$. The shape of the anion-nonpolar domain is furthest from sphericity while the cation-nonpolar domain, although long enough to form a continuous network, assumes behavior similar to a dispersed phase (domain count > 20), like that for $n = 2$ and 4. Interestingly, probably due to the onset of bi-continuity, the overall nonpolar domain also display the shape away from a sphere. As seen from the domain count the cation-nonpolar domain forms a continuous network only beyond $n = 10$, the isoperimetric quotient for the cation-nonpolar domain shows a sharp decline which coincides with the transformation of dispersed cation-nonpolar nanodomains into a continuous

domain. Further, an increase in the alkyl chain length on the cation results into a steady increase in the isoperimetric value for the total-nonpolar domains. Due to the appearance of segregated anion-nonpolar domains that are spherical ($Q^{peri} \sim 0.5$) the total-nonpolar domain in n =12 possesses a higher degree of sphericity as compared to that of the lower homologues.

Figure 5.6 (c) the number of first neighbors around a given subunit, that helps provide information on the molecular arrangement of molecules within the polar-nonpolar network. For interpretation, a neighbor count of ∼2 suggests a side-by-side arrangement over an interconnected network, while contact in two dimensions can give up to six neighbor count, similar to a hexagonal packing. Such hexagonal-type arrangement is seen for the polar network. Although the neighbor count remains almost invariant with the alkyl chain length, certain trends are apparent. A slight decrease in the number of neighbor contacts in going from $n = 2$ to 4 suggests the stretching of the polar network. However, from $n = 4$ to 10 the neighbor contacts increase slightly reaching similar number as those for $n = 2$, which indicates densification of the polar groups. The neighbor count between cation-nonpolar subunits increases monotonically along the homologous series. A neighbor count of ∼2 for ILs with small cationic alkyl chain ($n = 2,\ 4$) suggests that cation-nonpolar subunits favor side-by-side arrangement. This is consistent with the high domain count. As the cation-nonpolar subunits become larger, the side-by-side orientation is increased in more than one dimension, due to the formation of double ionic sublayers giving more than 6 neighbor contacts. On the contrary, an exact opposite trend is observed for anion-nonpolar subunits. With the increase in cationic alkyl chain length, the anion-nonpolar subunits orientation tends to shift from multi-dimension to side-by-side. The number of such contacts is always larger for the anion-nonpolar subunit than that for the cation-nonpolar group as long as the alkyl chain length of the cation is shorter or equal to the anion chain

length. While the neighbor counts for the cation-nonpolar exceed the corresponding anion-nonpolar counts indicating the dominance of these contacts for $n > 8$. The neighbor count between the cation-nonpolar and anion-nonpolar group increases up to $n = 8$ and reaches a plateau with further increase in the alkyl chain length on the cation. It is worth noting that the neighbor count is greater for the cation-nonpolar group with anion-polar group than the self-interaction contact up to $n = 8$. This observation is consistent with domain count (total nonpolar vs. cationic nonpolar). A neighbor count of ~ 2 for anion-polar subunits throughout the series suggests the anion-polar heads favor side-by-side arrangement over a globular network. Moreover, for $[C_{12}mim][C_8SO_4]$ IL system the anion as a whole favors side-by-side orientation, which probably leads to dispersion or sometimes isolation of the anionic chains.

Strong aggregation of alkyl chains can be further confirmed by computing RDFs between the respective terminal carbon atoms. The right panel of Figure 5.7 shows a strong aggregation behavior of cation-cation, cation-anion, and anion-anion chains as evidenced from first peak height greater than 1, which increases with the increase in the cationic alkyl chain. Interestingly, the cation-tail RDF approaches unity only for the $n = 2$, 4 and 6 ILs while the RDFs for the ILs with longer cationic alkyl chain exhibit oscillations suggesting that isotropic distribution of cation-tails at long distances cannot be observed for the large system sizes simulated in the study. The RDFs between the anionic terminal carbon atoms display a decrease in the intensity of the first peak as the cationic chain becomes bulkier indicating that the localization of the terminal carbon atom in the anion becomes progressively weaker due to the enhancement in the cation-tail aggregation. The reduction in the peak heights for the anion-tail RDFs, however, is less pronounced than the corresponding increase in the peak heights of the cation-tail RDFs. Unlike cation-tail RDFs, the long-range behavior of the anion-tail RDFs is periodic for all the systems. The RDFs between

the cross-interaction of cation-anion terminal carbons show complex behavior. Based on the observations, it can be inferred that the interactions between the cation-tail and anion-tail strengthen from $n = 2$ to 10 and diminish for $n = 12$. Overall there is a continuous increase in the cation-cation interaction and a corresponding decrease in the anion-anion interactions. The cation-anion interactions are, however, more complex which play a major role in defining the structural morphology.

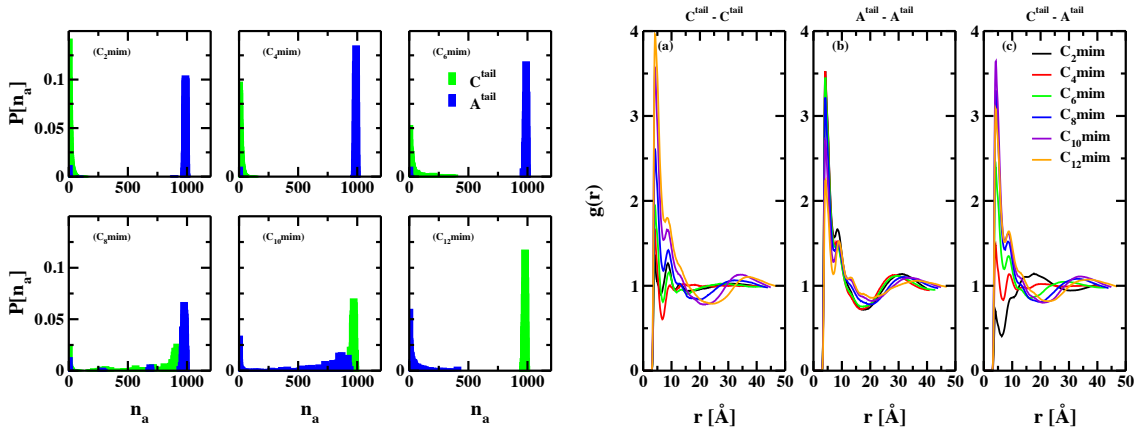

Figure 5.7: On the left: Discrete probability distribution of terminal carbon aggregate sizes, P(n_a), as a function of aggregate size number, n_a for the [$C_n$mim][C_8SO_4] IL series. On the right: Radial distribution function of terminal carbons, cation-cation, cation-anion, anion-anion; that also help define the aggregate criterion.

The connectivity of the nonpolar domain formed by either cationic or anionic chains was further probed by computing the probability distribution, $P(n_a)$, of observing aggregate size of n_a. This analysis provides information on the number of molecules that can be found in a given aggregate. Two chains are considered a part of the same aggregate if they were found within the first coordination shell of each other, defined by the minimum of the respective RDF. For $n = 2$, the cation aggregates are mostly isolated with very few aggregates of sizes exceeding 10% of the maximum possible aggregate size. On the other hand, the aggregate size distribution for the anion is skewed towards the largest aggregate size indicating that the anions percolate throughout the simulation box with a few isolated pairs. In the case of $n = 4$, the

probability of finding isolated cations decreases, while that for observing large anion aggregates increases. For n =6, the fraction of isolated cations in the system is significantly reduced, and the distribution extends to include large aggregates containing nearly half the maximum possible cations. As expected, based on analyses presented above, the aggregation probability distributions for the cationic and anionic alkyl chains are markedly different for $n = 8$ despite the presence of symmetry; the cation aggregates show a wide range of distributions assuming all possible aggregate sizes, while the aggregate size distribution continues to be centered around the maximum possible aggregate size suggesting that the anion is a dominant species in the nonpolar domain formation. For $n = 10$ the trend is reversed of what is observed for $n = 8$ pointing to the importance of the longer alkyl chain length in maintaining the connectivity of the nonpolar domain. Similarly, the aggregate probability distribution features for $n = 12$ are opposite to those of the $n = 6$ IL system suggesting that the cation aggregates are connected throughout the box. Further, a range of aggregate size distribution is observed for the anions from being isolated to a large aggregate containing more than 450 anions. It is believed that these aggregates can potentially separate polar domains giving rise to multiple length scale peaks in the structure factors.

5.1.4 Orientational Order

The analysis of the structures presented above suggests that the polar and nonpolar domains become spatially heterogeneous as the alkyl chain length increases. In order to dissect if such increase in heterogeneity is present for all the groups, heterogeneous order parameters (HOPs) were computed, as defined in eq. 3.40. The HOP values, shown in Figure 5.8 (a), suggests that for all the groups except anion-tail the HOP value increases with the alkyl chain length hinting that the heterogeneity of the anion-tail decreases while that for the other group increases. For all the systems, in general,

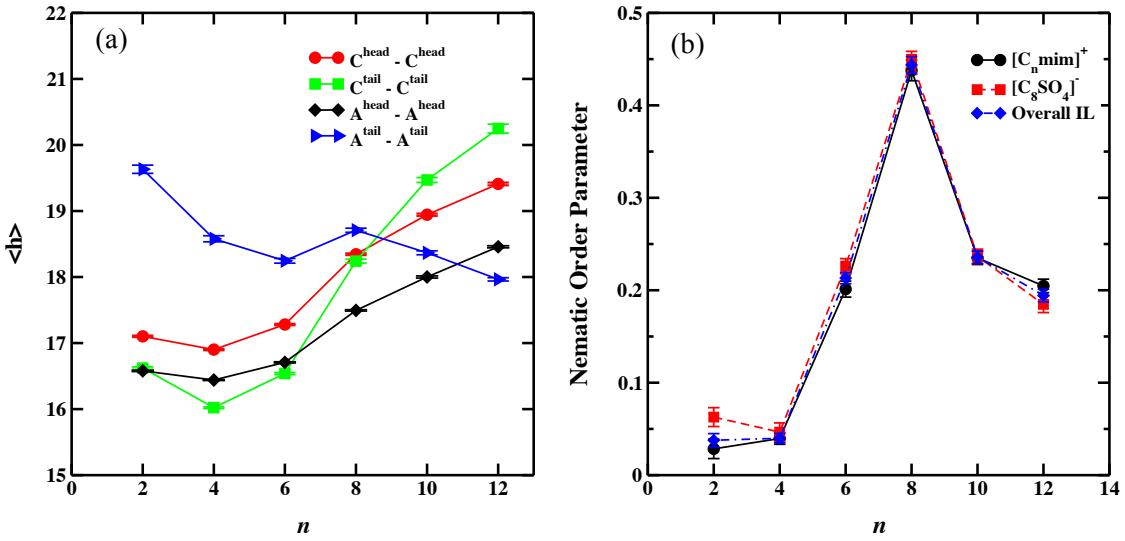

Figure 5.8: (a) Average heterogenous order parameters (HOP's) for various atomic groups in IL systems with different cationic chain lengths. Here head refers to center-of-mass of polar heads and tail refers to terminal carbons on side chains for both cation and anion. (b) Orientational order parameter for systems decomposed into cations and anions comprising the IL for the $[C_n mim][C_8SO_4]$ IL series. Please note that the lines joining the points are guide to the eye.

the average HOP values for either the cation- or anion-nonpolar tail groups are greater than those of the corresponding polar-head groups. The HOP values for cation- and anion-polar heads mirror each other which can be expected as they always interact head-to-head in order to maintain the electrical neutrality. The HOP values also exhibit an increasing trend with increase in the alkyl chain length suggesting that the distributions of the polar region becomes more heterogeneous. Thus, it is clear that the IL systems studied here are marked by structural heterogeneity at two levels: the distribution of polar and nonpolar domains and the elements within the two domains.

The degree of orientational order can be characterized using the nematic order parameter, which was computed as described in eq. 3.38. In this work, the order parameter has been analyzed considering each moiety, i.e., the IL cation and anion, along with the overall order parameter for the IL system. For all the IL systems, the order parameters for both the cation and anion and the overall system are nearly identical

which indicates high ordering among the cationic and anionic nonpolar chains due to the alternating placement of cations and anions. For $n = 2$ and 4, rather low values for the nematic order parameter is indicative of the fact that there exists no preferred alignment direction for the cations and anions as can also be observed in the simulation snapshot. However, going from $n = 4$ to 6, the nematic order parameter increases by four folds, from ~ 0.05 to 0.2, suggesting that the chains start to align in a particular direction. Nonetheless, this value suggests that order is not in the limit of liquid crystalline behavior range. Similarly, for $n = 8$ a more than two-fold increase, from $\sim$0.2 to 0.45, further advocates the increase in the long-range order. The value as high as 0.45 suggests that this IL is on the verge of displaying liquid-crystal like behavior. With further increase in the cationic alkyl chain length, the ordering starts to decrease. It is further important to mention at this point, that the order parameter is likely to depend on the simulation trajectories. As will be shown in the following section, the order parameter computed for $[C_{12}mim][C_8SO_4]$ IL increases up to 0.71 (cation), 0.65 (anion) and 0.68 (overall IL), depicting liquid-crystalline behavior, if trajectories obtained from GROMACS 2018 are used instead of 4.5.5 version. Nevertheless, this analysis shows the presence of long-range ordering in the systems studied in this work which gives rise to different structural morphology.

Thus, the results presented in this section demonstrate that the variation in the alkyl chain length on both the ions in an IL is an effective strategy to obtain different morphologies and induce nonpolar nanoscale heterogeneity not observed previously, adding to the already rich diversity of IL structures reported in the literature. Since very interesting results are observed for $[C_{12}mim][C_8SO_4]$ IL, nonpolar domains at multiple length scales, the following sections of this chapter will focus on controlling the structural morphology of this particular IL.

5.2 Influencing the Self-Assembly of 1-n-Dodecyl-3-Methylimidazolium Octylsulfate IL Using Binary Ionic Liquid Mixtures

As seen in chapter 4, mixtures of ILs can be employed as a strategy to influence the structures which can potentially fine-tune or enhance the functionality. In this section, the focus is on two binary IL mixtures, where we mix $[C_{12}mim][C_8SO_4]$ IL, a bi-amphiphilic system, with ILs containing alkyl chain on either cation or anion. For this purpose, $[C_{12}mim][MeSO_4]$ and $[C_1mim][C_8SO_4]$ ILs were chosen, that will generate IL mixtures containing either common cation or common anion. The objective of this work is determining morphological changes with the changing concentration of either $[C_{12}mim]^+$ or $[C_8SO_4]^-$ alkyl chain lengths.

MD simulations for (i) $[C_{12}mim]$ $[C_8SO_4]_x$ $[MeSO_4]_{1-x}$ (ii) $[C_{12}mim]_x$ $[C_1mim]_{1-x}[C_8SO_4]$ IL mixtures were carried out at a temperature of 400 K and pressure of 1 bar using GROMACS 2018 package. [196, 197] Simulations for a total of five molar ratios (10:90, 25:75, 50:50, 75:25, 90:10) obtained by varying the concentrations of the respective cations or anions along with the pure IL systems were performed. Since pure $[C_{12}mim][C_8SO_4]$ IL was also simulated in GROMACS 2018, the structural features are slightly different from that reported in the previous section. Please see the aside mentioned in the previous section regarding the probable reasons. The simulations were well equilibrated for at least 0.5 μs (including equilibration and production runs) containing 1000 ion pairs. More details on the simulation protocols can be found in the section 3.3.1.

The results indicate that concentration of less amphiphilic IL as low as 10 % is able to disrupt the connectivity of the polar domain of $[C_{12}mim][C_8SO_4]$ IL, while the connectivity of the overall nonpolar domain connectivity remains nearly unaltered at all concentrations with few instances of temporary breaking of small clusters. To

our knowledge, the discontinuity of the polar domain is reported for the first time in the IL literature, an observation that remains to be validated. Furthermore, on the other hand, the orientational order of morphology of $[C_{12}mim][C_8SO_4]$ IL is influenced only at higher concentrations of the other, less amphiphilic, IL (75 mol % for $[C_{12}mim][MeSO_4]$ IL and 50 mol % for $[C_1mim][C_8SO_4]$ and beyond). Such a study also points to the fact that the concentration at which significant changes in the ordering of the morphology is observed can potentially be shifted, and is influenced when aggregation behavior of longer-chain bearing ion moiety is affected. As, in this study, the structural features have high concentration dependence when the connectivity of $[C_{12}mim]^+$ alkyl chains is changed whereas changes in the aggregation of $[C_8SO_4]^-$ chains have a weak concentration dependence.

All the mixtures have been extensively characterized structurally using techniques of structure factors, nematic order parameters, Voronoi tessellation domain analysis, RDFs and aggregate size distributions; the descriptions of which are included in section 3.3.4. The results below are provided in terms of the polar and non-polar groups present in $[C_{12}mim]^+$, $[C_8SO_4]^-$, $[MeSO_4]^-$ and $[C_1mim]^+$. The polar and nonpolar groups of $[C_{12}mim]^+$ and $[C_8SO_4]^-$ are same as that described in section 5.1. While the cation – $[C_1mim]^+$ and anion – $[MeSO_4]^-$ are entirely polar. The overall polar and nonpolar domains are constituted by taking together the respective polar and nonpolar parts of all the cation and anion present in a given mixture system.

5.2.1 Structure Factors

The structure factors, based on X-ray atomic factors, obtained from MD simulation results for varying concentrations of binary IL mixtures of (i) $[C_{12}mim][C_8SO_4]$ and $[C_{12}mim][MeSO_4]$; and (ii) $[C_{12}mim][C_8SO_4]$ and $[C_1mim][C_8SO_4]$ are reported and compared in Figures 5.9. For both the mixture systems three distinct regions are

present. The pre-peak in the low-q region ($0.2 < q < 0.25$ Å^{-1}) associated with the presence of bi-continuous mesoscopic phase of alternating polar and nonpolar domains; a large-q or adjacency peak around q ~ 1.5 Å^{-1} due to the juxtaposition of cations and anions; and an intermediate-q shoulder ($0.5 < q < 1$ Å^{-1}) due to charge alternation. The pre-peak is present for all the pure ILs presented in this work, i.e., $[C_{12}mim][C_8SO_4]$, $[C_{12}mim][MeSO_4]$ and $[C_1mim][C_8SO_4]$, which can be expected as they all have alkyl chain lengths above the percolation threshold limit, $n = 6$, [19] capable of segregating polar and nonpolar domains.

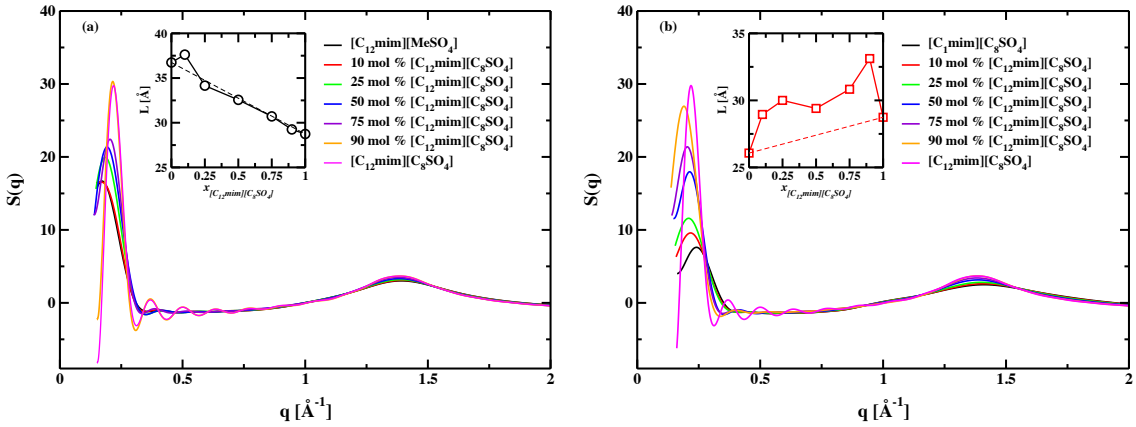

Figure 5.9: Structure factors, S(q), as a function of reciprocal space wavenumber, q [Å^{-1}] for (a) $[C_{12}mim]$ $[C_8SO_4]_x$ $[MeSO_4]_{1-x}$ and (b) $[C_{12}mim]_x$ $[C_1mim]_{1-x}$ $[C_8SO_4]$ IL mixtures as a function of concentration at 400 K. In the inset, the alkyl chain dependence of characteristic length of nonpolar domain, calculated as $\frac{2\pi}{q}$, is reported. Please note that solid lines are just guide to the eye while dotted lines are ideal mixing predictions.

Although not readily discernible, due to intensity scale of $S(q)$, a closer inspection of the adjacency peak shows a contrasting behavior when both the mixture systems are directly compared. For $[C_{12}mim][C_8SO_4]_x[MeSO_4]_{1-x}$ IL mixtures, no change in the adjacency peak location is observed pointing to the lack of presence of any re-organization of ion moieties within the polar network for the entire composition range. This suggests that the aggregation of tails in $[C_8SO_4]^-$ anion has less effect

on the way polar heads of the ions interact. This is possibly attributable to the fact that $[C_8SO_4]^-$ tails are always dispersed and the dispersion increases with the decreasing concentration of $[C_{12}mim][C_8SO_4]$, advocated by the aggregate size distributions and domain count always greater than 1 (see below), suggesting that the tails are not able to aggregate strongly enough to influence the interactions of the polar heads. This behavior may not be that surprising as the hydrogen bond acceptor ability of $[C_8SO_4]^-$ and $[MeSO_4]^-$ are comparable, for a given cation. For instance, for $[C_4mim]^+$ the values are 0.77 and 0.85, respectively, and should decrease linearly with an increase in the alkyl chain on the cation. [41, 42] Thus, cation-anion head interactions are least affected and can be seen as a simple exchange of anions. On the other hand, $[C_{12}mim]_x$ $[C_1mim]_{1-x}[C_8SO_4]$ mixture system shows that with the decreasing concentration of $[C_{12}mim][C_8SO_4]$ the intensities not only reduce in the intensity but also shifts to larger-q values (corresponding to smaller distances in real space) which indicates the presence of subtle re-organization of the ions within the polar network. This is consistent with the fact that hydrogen bond basicity of the anion with respect to the two cations differ considerably. Therefore, the presence of non-native interactions can be expected in this case. (Please refer to chapter 4 for more details on native vs. non-native interactions.)

Similarly, no such shifts or changes in intensities are seen for the intermediate-q shoulders of $[C_{12}mim][C_8SO_4]_x[MeSO_4]_{1-x}$ IL mixtures, whereas shifting of the charge alternation peak to lower-q values with the increasing concentration of $[C_{12}mim][C_8SO_4]$ IL is observed for the $[C_{12}mim]_x$ $[C_1mim]_{1-x}[C_8SO_4]$ mixture system, which suggests significant stretching of the polar network trying to accommodate the nonpolar domains. Further, as the mixtures become richer in $[C_{12}mim][C_8SO_4]$, the intensity of the pre-peak continuously increases for both the mixture systems due to higher nonpolar content in the mixture system. The location of the pre-peak, however, exhibits the

most noticeable trend. Computing the real space distances, using Bragg's law, (shown in inset figures) shows that these distances follow an ideal mixing linear relationship for the mixture of $[C_{12}mim][C_8SO_4]_x[MeSO_4]_{1-x}$ and increases linearly with the decreasing $[C_{12}mim][C_8SO_4]$ mole fraction. Contrastingly, the nonpolar domain length spacing for $[C_{12}mim]_x$ $[C_1mim]_{1-x}[C_8SO_4]$ mixtures not only follow a non-linear trend but, in fact, the lengths observed for all the mixture compositions are higher than those obtained for the pure ILs. Such nonideal behavior between pure ILs and their mixtures was already observed by Russina et al. in an experimental study involving $[C_n mim]Cl$ (n = 6,8 and 6,10) ILs and their mixtures [94] and computational study by Shimizu et al. for $[C_n mim][NTf_2]$ (n = 2,6) and $[C_n mim][PF_6]$ (n = 3,12). [103,124]

This shows that a simple strategy of mixing two ILs can potentially enhance the nonpolar domain lengths.

5.2.2 Instantaneous Simulation Snapshots

One of the important strengths that a computational investigation offers is the ability to visualize the positions of the molecules which can impart knowledge about the factors that might be responsible for the observed properties. Static snapshots of the well-equilibrated configurations obtained at the end of MD simulation are presented in Figures 5.10 and 5.11 to show the influence of varying concentrations on the morphology of both the binary IL mixture systems. The representatives of the rendering scheme employed for the mixture systems are included as part of the figure. As expected, the cation- and anion-polar heads are found close to one another. However, for both the mixture systems, the smallest addition of either $[C_{12}mim][MeSO_4]$ or $[C_1mim][C_8SO_4]$ IL (10 mol %) in $[C_{12}mim][C_8SO_4]$ completely isolates the layers of polar domain giving rise to ∼3 polar domains, based on the domain count and aggregate size distributions shown below. Moreover, more than one polar domain is also

seen for 75 mol % of $[C_{12}mim][MeSO_4]$ in $[C_{12}mim][C_8SO_4]$. For all the other compositions studied in this work, the polar domains are continuous. In fact, nanosegregated polar-nonpolar domains are clearly visible, which emerge as distinct pre-peaks in the structure factors.

For higher concentrations of $[C_{12}mim][C_8SO_4]$ at least up to 50 mol %, the layer-like morphology of alternating polar-nonpolar domains remains intact for both the mixture systems. Similar orientational order parameters also corroborate this, *vide infra*. However, as the concentration of $[C_{12}mim][C_8SO_4]$ become less than the other IL with which it is mixed, the morphological changes progressing towards sponge-like behavior starts to emerge. It is important to mention that the concentration at which such transition occurs is dependent on the IL mixture under study. For $[C_{12}mim][C_8SO_4]_x[MeSO_4]_{1-x}$ IL mixtures, sponge-like morphology is observed only at 10 mol % concentration. Since octyl chains of $[C_8SO_4]^-$ anion are almost always dispersed, and the dodecyl chains of $[C_{12}mim]^+$ cation itself can effectively sepa-

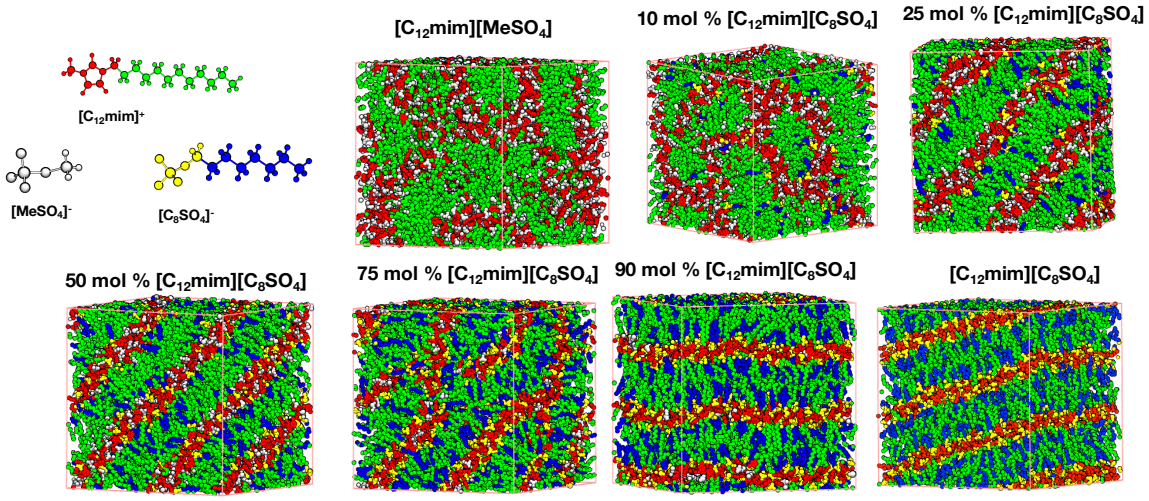

Figure 5.10: Instantaneous snapshots of the equilibrated system for $[C_{12}mim][C_8SO_4]_x$ $[MeSO_4]_{1-x}$ IL mixtures at varying concentrations. The snapshots are color-coded to reflect the polar and nonpolar components on both cation and anion. ($[C_{12}mim]^+$-polar: red, $[C_8SO_4]^-$-polar: yellow, $[C_{12}mim]^+$-nonpolar : green and $[C_8SO_4]^-$-nonpolar: blue, $[MeSO_4]^-$-polar : silver)

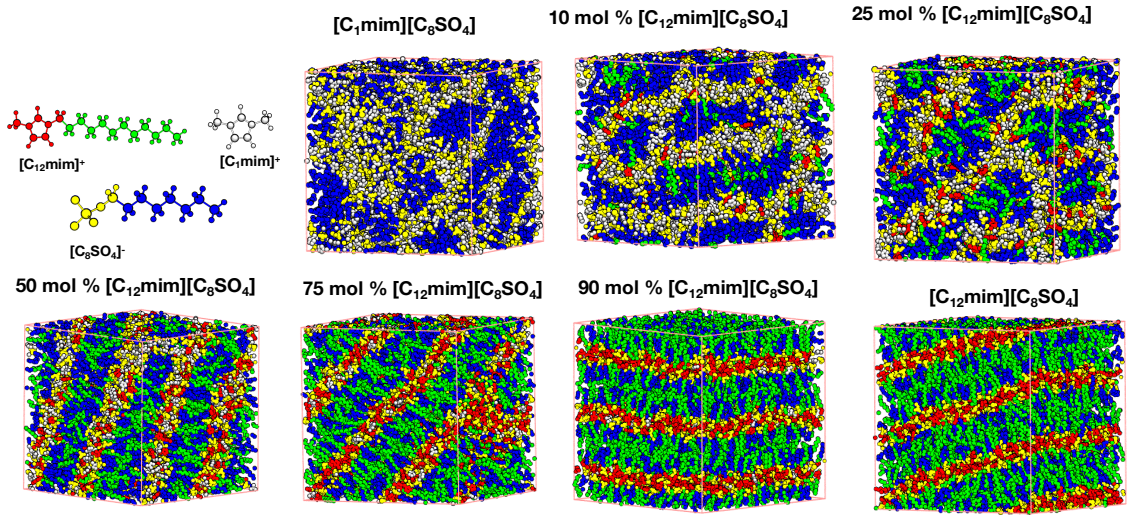

Figure 5.11: Instantaneous snapshots of the equilibrated system for $[C_{12}mim]_x[C_1mim]_{1-x}$ $[C_8SO_4]$ IL mixtures at varying concentrations. The snapshots are color-coded to reflect the polar and nonpolar components on both cation and anion. ($[C_{12}mim]^+$-polar: red, $[C_8SO_4]^-$-polar: yellow, $[C_{12}mim]^+$-nonpolar : green and $[C_8SO_4]^-$-nonpolar: blue, $[C_1mim]^+$-polar : silver)

rate the polar strands, the concentration dependence of their aggregation behavior and hence, the structural change is very weak. Moreover, such a weak concentration dependence of the cation-cation, cation-anion, and anion-anion tail aggregations is clearly visible in their respective RDFs, as shown in Figures 5.12.

Contrastingly, for $[C_{12}mim]_x$ $[C_1mim]_{1-x}[C_8SO_4]$ mixtures, RDFs shows strong concentration dependence. The cation-cation interactions strengthen by nearly two folds, from $\sim$ 3 to 6, while oppositely the cation-anion interactions weaken by more than 1.5 folds, from $\sim$ 3.5 to 2. This suggests that as $[C_{12}mim]^+$ chain is introduced, it has the ability to strongly aggregate. However, interestingly, the aggregation of cation chains is not able to alter the sponge-like mesoscopic morphology of $[C_1mim][C_8SO_4]$ at concentrations lower than the equimolar. This is probably attributable to the fact that the anion can aggregate strongly than the cation, eventhough its alkyl chain length is greater than 4 –CH2 groups. This becomes more evident from the aggregate size distribution, such that the aggregate size as big as the system size – all chains

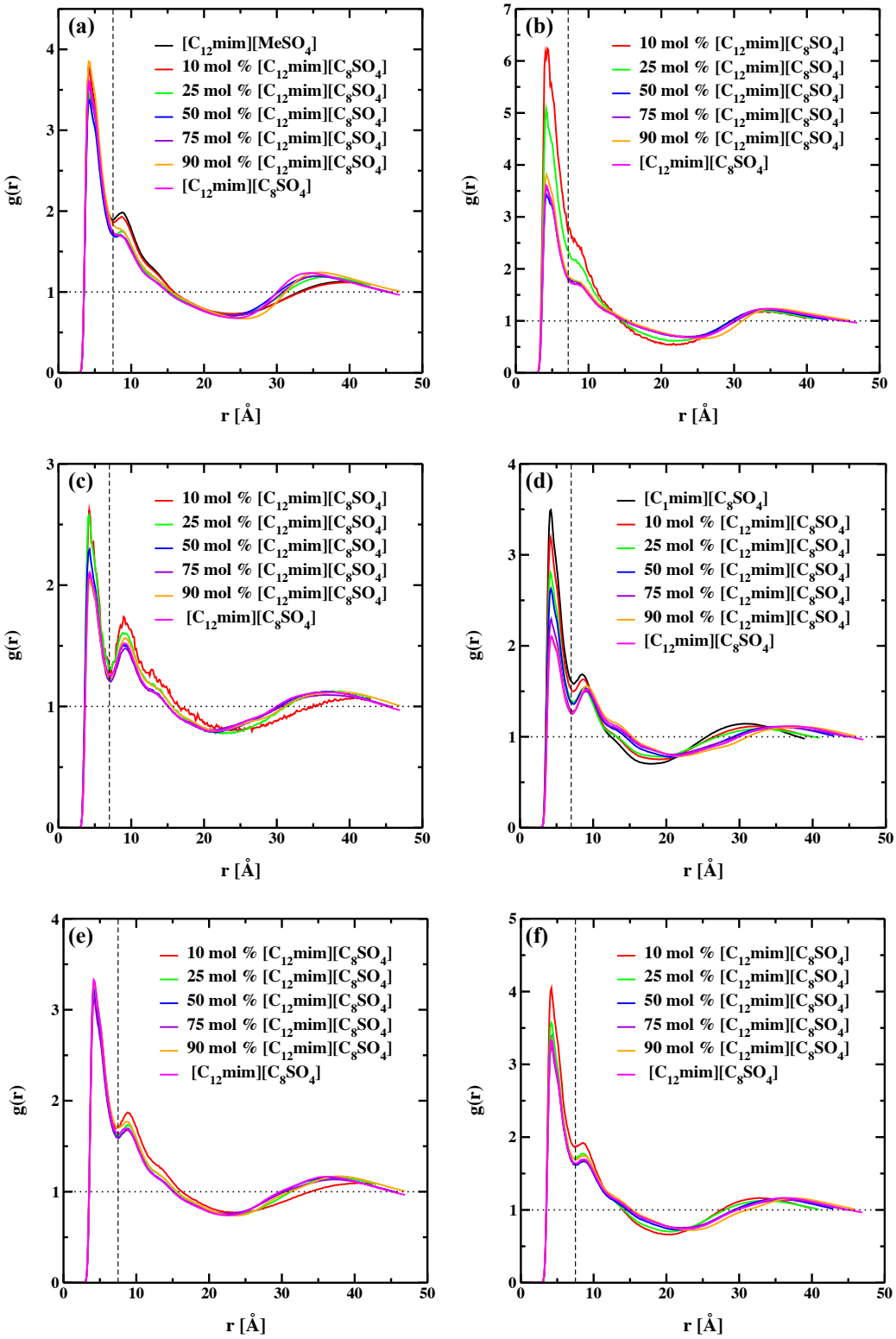

Figure 5.12: Radial distribution function of terminal carbons, (a) and (b) – cation-cation, (c) and (d) – cation-anion, (e) and (f) – anion-anion for both $[C_{12}mim][C_8SO_4]_x$ $[MeSO_4]_{1-x}$ and $[C_{12}mim]_x$ $[C_1mim]_{1-x}$ $[C_8SO_4]$ IL mixtures as a function of concentration at 400 K; that also help define the aggregate criterion.

connected – is not seen at any of the mixture compositions. In fact, in the previous sections it was observed that for the same alkyl chain length on both the cation and anion ($[C_8mim][C_8SO_4]$), the anion has a stronger aggregation tendency. Thus, from another standpoint, $[C_1mim][C_8SO_4]$ IL in concentrations greater than 50 mol % is able to disrupt the layer-like morphology of $[C_{12}mim][C_8SO_4]$ IL giving rise to a sponge-like behavior.

These results show that the minimum concentration at which significant changes in the morphology are observed can potentially be shifted, and disruption can be achieved much quickly when the aggregation behavior of the longer-chain bearing ion moiety is affected; as the structural features have high concentration dependence when aggregation behavior of $[C_{12}mim]^+$ is changed whereas changes in aggregation of $[C_8SO_4]^-$ has weak concentration dependence.

5.2.3 Orientational Order

The presence of long-range order can be quantified by computing the nematic order parameters. Figures 5.13 show order parameters for both the systems studied in this section. The order parameters have also been dissected into each moiety to pinpoint the source of the high ordering. Among the pure IL systems the order parameter follows the trend: $[C_{12}mim][C_8SO_4] > [C_{12}mim][MeSO_4] > [C_1mim][C_8SO_4]$; which is not surprising and can be expected, as we showed earlier that the presence of simultaneous chains on the cation and anion increases the ordering. Also, the alkyl chain lengths of $n = 12$ have been shown to possess smectic phases. [103] In fact, for $[C_{12}mim][C_8SO_4]$ IL the overall nematic order parameter of ~ 0.69, between 0.3-0.8, suggests that this IL is likely to exhibit a liquid-crystalline behavior. [232, 234] However, at this point, it is really important to mention that this order parameter value of 0.69 is very different from the value reported in the previous section, which is due

to qualitative differences obtained using two different versions of GROMACS (4.5.5 vs. 2018).

Comparison of the overall nematic orders with the ordering of each moiety suggests that the overall ordering is dependent on the size of the ion. Both the bigger cation, $[C_{12}mim]^+$, and the bigger anion, $[C_8SO_4]^-$, mirror each other and give rise to the trend observed for the overall order parameters, while the smaller ions have no preferred orientation. It is interesting to note that in comparison to pure $[C_{12}mim][C_8SO_4]$ IL, the overall ordering for the mixtures does not decrease for the concentration $\geq$ 50 mol % of $[C_{12}mim][C_8SO_4]$, and remain in the liquid-crystalline range. Strikingly, a steep drop in the ordering is observed at 10 mol % and 25 mol % concentration of $[C_{12}mim][C_8SO_4]$ in $[C_{12}mim][C_8SO_4]_x$ $[MeSO_4]_{1-x}$ and $[C_{12}mim]_x$ $[C_1mim]_{1-x}$ $[C_8SO_4]$ IL mixtures respectively. These observations are remarkably consistent with the inferences made after visualizing MD simulation snapshots. It

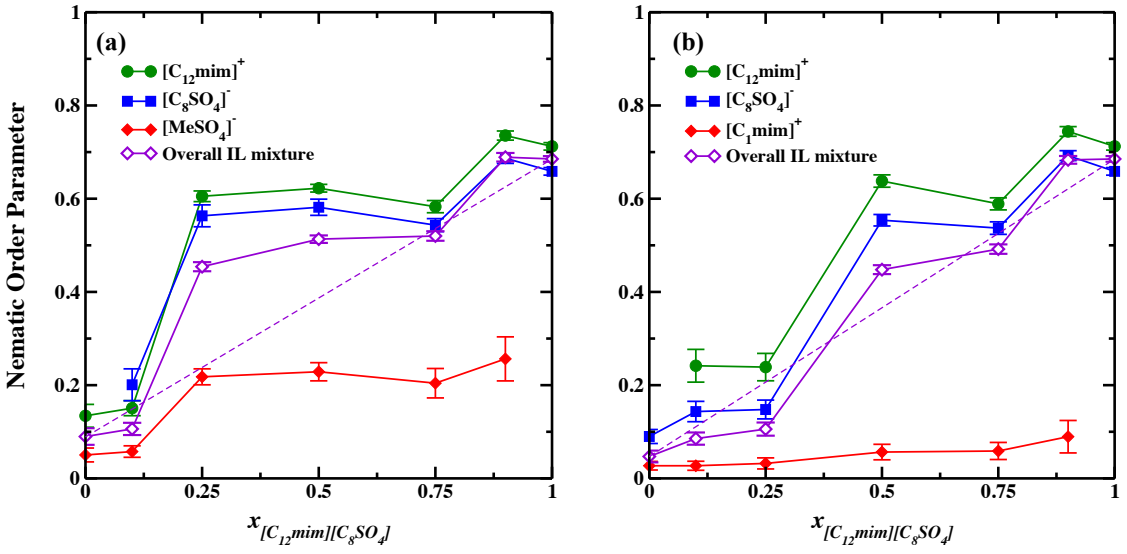

Figure 5.13: Orientational order parameters for systems decomposed into cations and anions comprising the IL for (a) $[C_{12}mim]$ $[C_8SO_4]_x$ $[MeSO_4]_{1-x}$ and (b) $[C_{12}mim]_x$ $[C_1mim]_{1-x}$ $[C_8SO_4]$ IL mixtures as a function of concentration at 400 K. Please note that the solid lines joining the points are guide to the eye while dotted line shows ideal mixing behavior.

is also important to mention that it is only at these respective concentrations, the multiple peaks between pre-peak and intermediate-q shoulder of the structure factors vanishes.

5.2.4 Aggregate Analysis

In order to provide a quantitative metric to the aggregation pattern that emerges due to the varying concentration of $[C_{12}mim][MeSO_4]$ and $[C_1mim][C_8SO_4]$ in $[C_{12}mim][C_8SO_4]$ the connectivity of the nanosegregated polar-nonpolar structure was examined using a Voronoi tessellation technique based domain analysis and the aggregate size distributions. Each of the binary IL mixture systems is characterized in terms of four unique domains: (a) total polar domain composed of the polar head groups of both the cations and the anions; (b) $[C_{12}mim]^+$-nonpolar; (c) $[C_8SO_4]^-$-nonpolar and (d) total nonpolar containing the nonpolar subunits from both $[C_{12}mim]^+$ and $[C_8SO_4]^-$. The uncharged alkyl chain of the cations is considered uniquely in order to identify the origin of the structural changes at various concentrations.

Figure 5.14 (a) and (b) provides the number of domains based on this classification as a function of the $[C_{12}mim][C_8SO_4]$ concentration for both the mixture systems. The polar domain count values for all the binary IL systems, are 1 except for 90:10 and 25:75 mixture compositions of $[C_{12}mim][C_8SO_4]_x[MeSO_4]_{1-x}$ and 90:10 of $[C_{12}mim]_x[C_1mim]_{1-x}[C_8SO_4]$. The domain count greater than 1 suggests a loss in the connectivity. This, to our knowledge, is the first time that discontinuous polar domains have been observed. It is worth mentioning that this result has been reproduced by conducting another additional independent simulation. The overall nonpolar domains, although, appears to show continuity for all the IL mixtures, including pure ILs, the value of domain count is not exactly 1 and is slightly greater than 1 for all the systems studied in this work. This is not readily discernible due to the logarithmic

scale. However, the value is not significant enough to confidently suggest the presence of a discontinuity. Thus, the overall nonpolar domain can be considered continuous with instances of temporary detachment of the small ion clusters. Further, the differences in the composition dependence of $[C_{12}mim]^+$ and $[C_8SO_4]^-$-nonpolar chains for both the IL mixtures can be easily visualized. For $[C_{12}mim][C_8SO_4]_x[MeSO_4]_{1-x}$ the $[C_{12}mim]^+$-nonpolar chains are connected, with the possibility of the existence of small clusters that temporarily lose their connectivity, for the entire composition

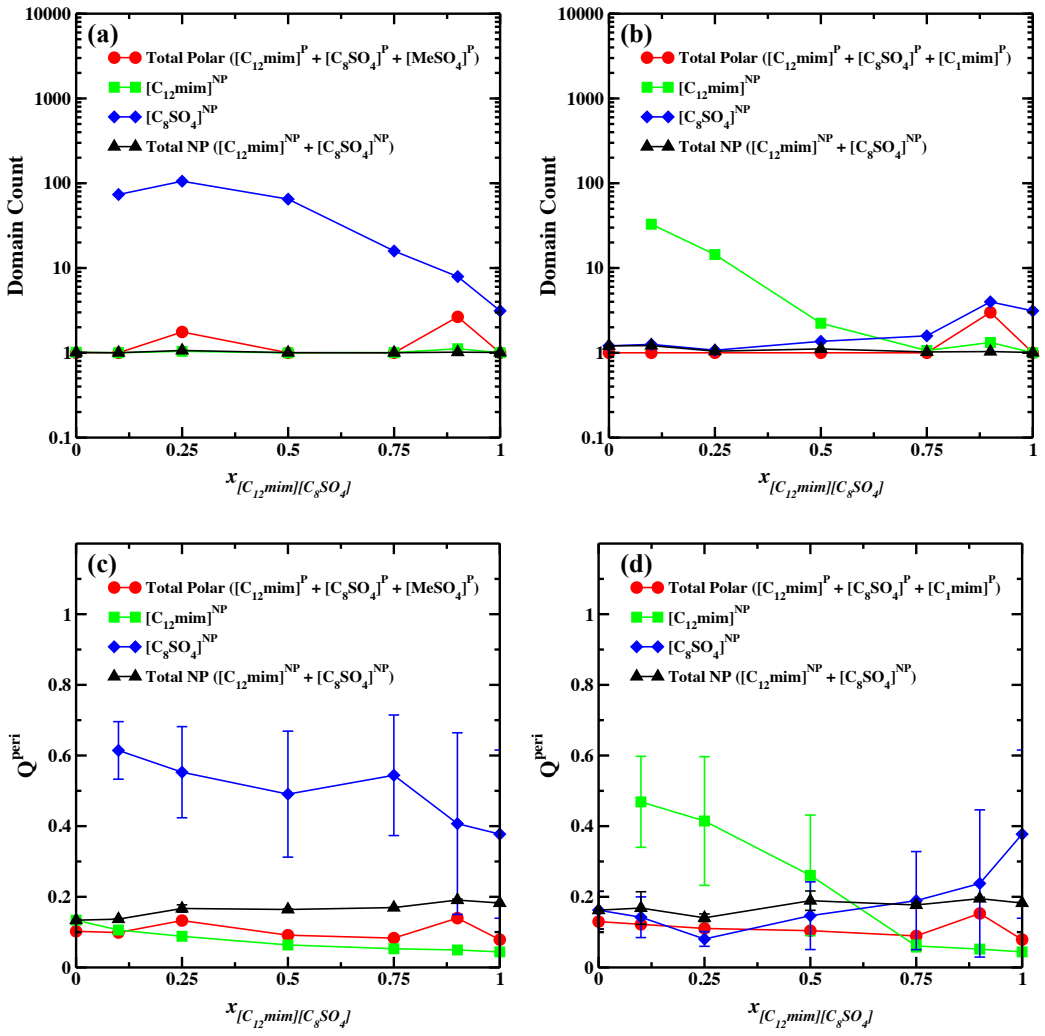

Figure 5.14: (a) and (b) Connectivity; and (c) and (d) Shapes of aggregates; for $[C_{12}mim]$ $[C_8SO_4]_x$ $[MeSO_4]_{1-x}$ and $[C_{12}mim]_x$ $[C_1mim]_{1-x}$ $[C_8SO_4]$ IL mixtures as a function of concentration at 400 K probed via Voronoi tessellation domain analysis. The aggregates are partitioned based on the respective polar and nonpolar components.

range, while $[C_8SO_4]^-$-nonpolar chains are always discontinuous. The dispersed phase increases with the decrease in $[C_{12}mim][C_8SO_4]$ concentration. On the other hand, for $[C_{12}mim]_x[C_1mim]_{1-x}[C_8SO_4]$ systems, as the concentration of $[C_{12}mim][C_8SO_4]$ increases, the transition from continuous subphase to dispersed phase and vice-versa is observed for both $[C_8SO_4]^-$- and $[C_{12}mim]^+$-nonpolar chains respectively. The transition appears to happen even when $[C_{12}mim][C_8SO_4]$ is in excess concentration with respect to $[C_1mim][C_8SO_4]$. Nonetheless, this does not have an impact on the overall morphology or ordering of the mixture systems.

The shape of the polar-nonpolar domains are assessed by computing average isoperimetric quotients, which by definition assumes a value of 1 for a perfectly spherical shape while any deviations from sphericity lead to the values lower than 1. [227] The change in isoperimetric quotient, as a function the $[C_{12}mim][C_8SO_4]$ concentration is shown in Figure 5.14(c) and (d) for both the mixture systems. From the figure, it is clear that this quotient for both the polar and overall nonpolar domains show a negligible dependence on the concentration of $[C_{12}mim][C_8SO_4]$ and always less than 0.2, which implies that the overall shapes are far from a sphere, which is consistent with simulation snapshots. Similar to the domain count analysis, significant trends become apparent when the cationic and anionic chains are treated separately. For $[C_{12}mim][C_8SO_4]_x[MeSO_4]_{1-x}$ mixture system, since $[C_{12}mim]^+$ chains are connected, the single aggregate assumes a shape that differs from sphericity, whereas the dispersion of $[C_8SO_4]^-$ chains allows the formation of aggregates of different sizes that demonstrates sphere-like morphology. However, these sphere-like aggregates do not alter the overall nonpolar domain shape. Further, within the statistical uncertainty, the shapes formed by both the cationic and anionic chains, separately, have weak concentration dependence. Unlike this mixture system, the mixture of $[C_{12}mim]_x[C_1mim]_{1-x}[C_8SO_4]$ ILs shows a strong composition dependence of shapes.

As the chains move from more dispersed phase to a continuous subphase the sphere-like shape of their aggregates is not retained, and vice-versa. However, again, such changes in the shape of the aggregates have a negligible impact on the overall shape of the nonpolar domain. Thus, the IL mixtures considered in this section does not alter the shape of the mesoscale aggregates significant enough, but slightly changes the orientational order.

Since the domain, connectivity and shapes, of the respective $[C_8SO_4]^-$- and $[C_{12}mim]^+$-nonpolar chains are very different, analysis of aggregate size distribution was performed that allows us to pinpoint the connectivity as well as the size of the various aggregates that both the chains are capable of forming. Figures 5.15 and 5.16 show the corresponding aggregate size probability distribution functions. Two molecules were considered to be a part of the same aggregate if the terminal carbon atoms present on the chain are located within the first coordination shell of each other. The distance corresponding to the first minimum in the radial distribution functions (RDFs) was used to define the coordination sphere (Figure 5.12).

For pure $[C_{12}mim][C_8SO_4]$ IL, the nonpolar aggregates formed by $[C_8SO_4]^-$ chains

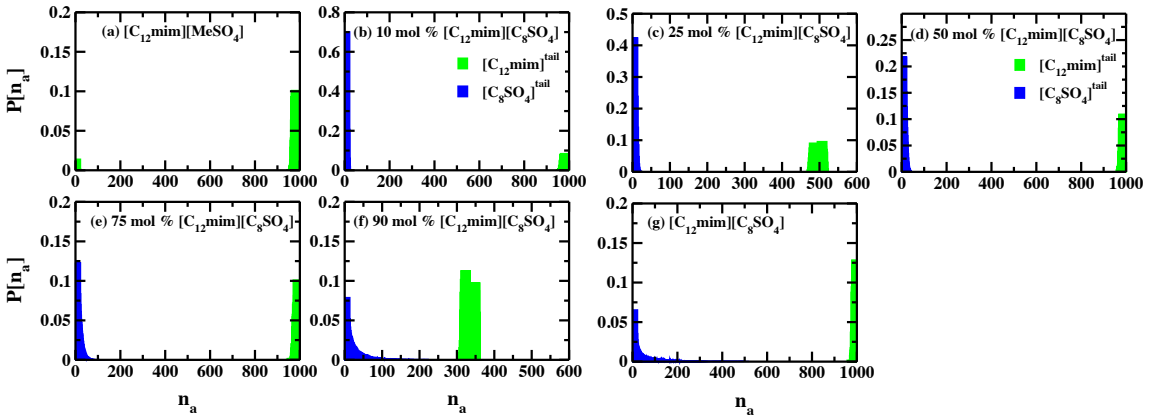

Figure 5.15: Discrete probability distribution of terminal carbon aggregate sizes, $P(n_a)$, as a function of aggregate size number, n_a for $[C_{12}mim]\ [C_8SO_4]_x\ [MeSO_4]_{1-x}$ IL mixtures at varying concentrations.

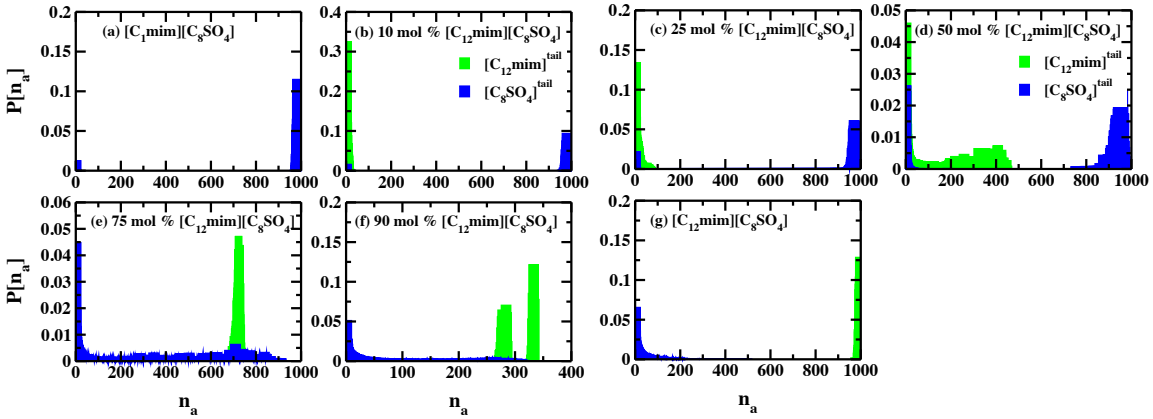

Figure 5.16: Discrete probability distribution of terminal carbon aggregate sizes, $P(n_a)$, as a function of aggregate size number, n_a for $[C_{12}mim]_x[C_1mim]_{1-x}$ $[C_8SO_4]$ IL mixtures at varying concentrations.

have some tendency to be isolated, as evidenced by non-zero probability, in addition to a larger size aggregate containing up to 400 anions. However, this analysis clearly shows that a complete percolation of anions is not achieved. This is in contrast to the pure IL system of $[C_1mim][C_8SO_4]$ that shows a higher propensity of large size aggregate connecting all the $[C_8SO_4]^-$ molecules. Similarly, for the pure $[C_{12}mim]MeSO_4]$ IL as well the aggregate size distribution is completely skewed towards the largest aggregate size with a larger probability suggesting that the $[C_{12}mim]^+$-nonpolar chain aggregates are always connected. In $[C_{12}mim][C_8SO_4]_x[MeSO_4]_{1-x}$ mixture system, with the decreasing concentration of $[C_{12}mim][C_8SO_4]$ IL the probability of finding isolated $[C_8SO_4]^-$ tails increase considerably, consistent with the increasing domain count. At 90:10 and 25:75 compositions, the maximum aggregate size of $[C_{12}mim]^+$ tails is nearly 300 and 500, respectively, suggesting multiple domains, as the total number of molecules is 1000.

For $[C_{12}mim]_x[C_1mim]_{1-x}[C_8SO_4]$ mixture system, with the increase in $[C_{12}mim][C_8SO_4]$ IL concentration, the $[C_8SO_4]^-$ become progressively isolated, while $[C_{12}mim]^+$ tails start to form larger aggregates. However, it is evident that for all the mixture com-

positions, $[C_{12}mim]^+$ tails is not able to completely connect and always form multiple domains. It is only for 90:10 composition where both $[C_8SO_4]^-$- and $[C_{12}mim]^+$-nonpolar chains form smaller size aggregates, probably leading to breakage of the polar domain.

Therefore, based on the structural analyses presented above it can be concluded that an increasing concentration of less amphiphilic IL can have multiple impacts on the self-assembly of a bi-amphiphilic IL. For concentrations as low as 10 % of less amphiphilic IL, the connectivity of polar domain can be disrupted while keeping the nonpolar domain nearly continuous. Although the morphological shape does not have a strong composition dependence, the orientational order of the morphology can be fine-tuned. Furthermore, this study points to the fact that the concentration at which the transition of morphology into various shapes occur is dependent on the IL mixture under investigation.

5.3 Importance of Controlling the Self-Assembly to Enhance the Function: An Example of Mixtures of 1-*n*-Octyl-3-Methylimidazolium Tetrafluoroborate and 1-Ethyl-3-Methylimidazolium Tetrafluoroborate Ionic Liquids

Very recently, an experimental group lead by Dr. Joshua Sangaro at the University of Tennessee, Knoxville approached us for studying binary IL mixtures of $[C_8mim]$ $[BF_4]$ and $[C_2mim]$ $[BF_4]$ as the authors observed a nearly 100 % increase in static dielectric constants, physicochemical property, as shown in Figure 5.17. The authors hypothesized that dilution with $[C_2mim]$ $[BF_4]$ drives a shift in the mesoscale organization of $[C_8mim]$ $[BF_4]$ from the bicontinuous morphology to more isolated spheroidal aggregates. We conducted simulations to provide insight/evidence into the morphologies, trying to validate their hypothesis behind the observed behavior.

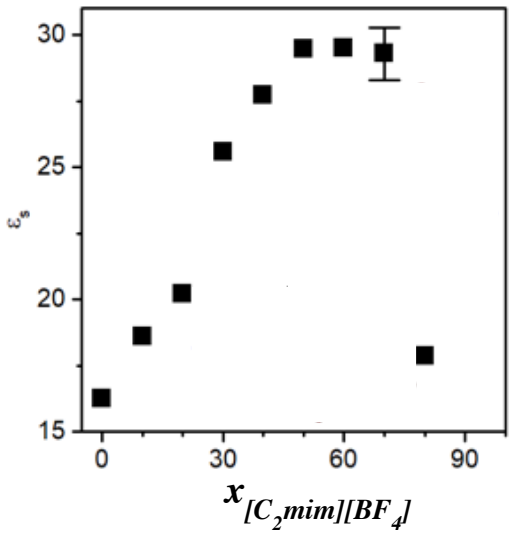

Figure 5.17: Concentration dependence of static dielectric permittivity for the binary IL mixtures of $[C_8mim]$ $[BF_4]$ and $[C_2mim]$ $[BF_4]$.

MD simulations for binary IL mixtures of $[C_8mim]$ $[BF_4]$ and $[C_2mim]$ $[BF_4]$ were carried out at a temperature of 298 K and pressure of 1 bar, ambient conditions, using GROMACS 2018 package. [196, 197] Simulations for a total of three molar ratios (30:70, 50:50, and 70:30) obtained by varying the concentrations of the respective cations along with pure IL systems were performed. Simulations were conducted in a cubic box containing 2000 ion pairs with periodic boundary conditions enforced in three dimensions. The systems were well equilibrated for 1 μs in the NPT ensemble. The trajectories obtained from the final 40 ns were used for the structural analysis. Structural properties of the IL systems are described in terms of X-ray structure factors, Voronoi domain analysis, and aggregate size distribution. The results below are provided in terms of the polar and non-polar groups present in binary IL mixture systems of $[C_8mim][BF_4]$ and $[C_2mim][BF_4]$. The polar group of the cation contains the imidazolium ring as well as the methyl and methylene groups directly bonded to the ring, for both $[C_8mim]^+$ and $[C_2mim]^+$, while anion is completely polar. The polar group of the cation and anion together constitute the overall polar domain. The

nonpolar regions in the two cations are indicated by the respective uncharged carbon groups.

5.3.1 Structure Factors

The structure factors obtained from MD simulation results for varying concentrations of binary IL mixtures of $[C_8mim][BF_4]$ and $[C_2mim[BF_4]$ are reported in Figure 5.18(a) and are compared to the corresponding experimental X-ray diffraction results. Although the intensity scale of $S(q)$ obtained from MD simulations and experimental diffraction data is different, the overall features are strikingly similar. In both the plots, the $[C_8mim][BF_4]$ spectra exhibit two well-defined peaks (i) a pre-peak in the low-q region ($0.2 < q < 0.3$ Å^{-1}) associated with the presence of bicontinuous mesoscopic phase of alternating polar and non-polar domains and (ii) a large-q or adjacency peak around q ~ 1.5 Å^{-1} due to the juxtaposition of cations and anions. It is interesting to note that intermediate-q peak ($0.5 < q < 1$ Å^{-1}) is completely absent for this system, unlike many other ILs. [117, 237] However, it is worth mentioning

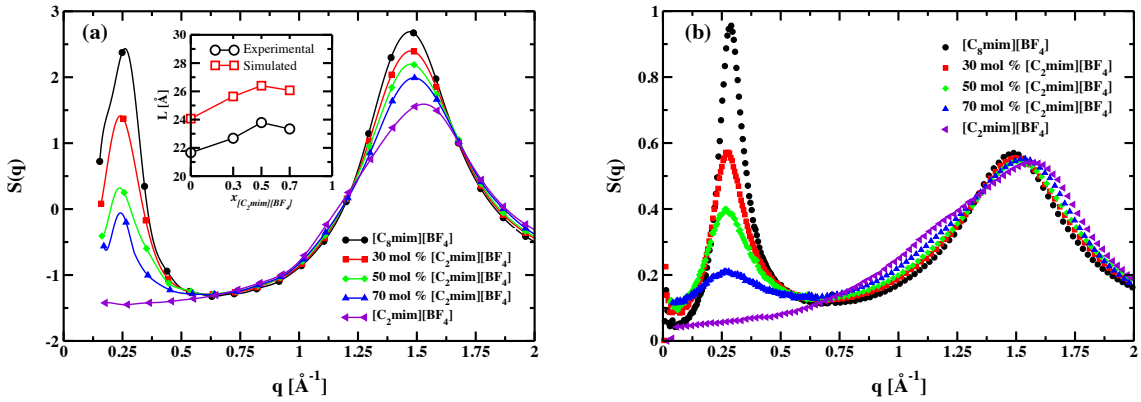

Figure 5.18: Structure factors, S(q), as a function of reciprocal space wavenumber, q [Å^{-1}] (a) computed from MD trajectories, and (b) representation based on experimental X-ray data; for the binary mixtures of $[C_8mim][BF_4]$ and $[C_2mim][BF_4]$ ILs at 298 K. In the inset of (a), concentration dependence of characteristic length of the real space distance is reported and comparison of simulation predicted vs. experimentally obtained values is shown.

that the absence of this charge alternation peak does not imply that the symmetry is absent; instead it denotes complete cancellations of same-type (cation-cation and anion-anion) and opposite-type (cation-anion) interactions. Similar observations have been reported previously by Margulis and co-workers [117] for $[C_8mim][BF_4]$ at 270 K.

It is clearly evident that as $[C_2mim][BF_4]$ is mixed with $[C_8mim][BF_4]$, with an increasing concentration the intensities of the two peaks shift in a regular fashion, both for MD and X-ray data. The shift of the adjacency peak to larger-q values (corresponding to smaller distances in real space) as the concentration of $[C_2mim][BF_4]$ is increased suggests a subtle re-organization of ions within the polar network.

The most conspicuous trend is observed for the pre-peaks. This peak is not present for $[C_2mim][BF_4]$. However, even at the lowest $[C_8mim][BF_4]$ concentration considered here ($[C_2mim][BF_4]$: $[C_8mim][BF_4]$ :: 70 : 30), there is an emergence of the pre-peak indicative of the presence of nano-segregated polar and nonpolar domains. As the mixtures become richer in $[C_8mim][BF_4]$, the intensity of the pre-peak continuously increases due to higher non-polar content in the mixture system. The location of the pre-peak, however, exhibits complex behavior. For all the mixture compositions considered, the location of pre-peak is slightly shifted towards smaller q-values (larger distances in real space). The inset in Figure 5.18 (a) presents the comparison of real space distance corresponding to this pre-peak obtained using both MD and X-ray data. Although MD simulations slightly overpredict the non-polar lengths as compared to the X-ray diffraction data, the non-monotonic dependence of the non-polar domain length on the mixture composition is well-produced. It must also be stressed that these lengths increase in a non-linear fashion. For example, there is a slight decrease in the non-polar domain length as the concentration is changed from $[C_2mim][BF_4]$: $[C_8mim][BF_4]$ :: 50 : 50 to 70 : 30, which coincides with the

drop in the static dielectric permittivity Similar non-linear trend in the size of nano-segregated domains was observed for $[C_{12}mim][C_8SO_4]$- $[C_1mim][C_8SO_4]$, as shown in the previous section, has been reported for the mixtures of $[C_6mim]Cl$ - $[C_8mim]Cl$ and $[C_6mim]Cl$-$[C_{10}mim]Cl$, [94] and $[C_2mim][NTf_2]$-$[C_6mim][NTf_2]$. [124]

5.3.2 MD Simulation Snapshots

In an effort to understand and visualize the influence of varying concentrations on the morphology of the binary IL mixture system of $[C_8mim][BF_4]$ and $[C_2mim][BF_4]$ ILs, static snapshots of the well-equilibrated configurations obtained at the end of MD simulation are provided in Figure 5.19. The rendering scheme employed is cation-polar head in blue, anion in yellow, $[C_8mim]$-nonpolar in silver, and $[C_2mim]$-nonpolar in pink (representatives also included as part of the figure). As expected, the cation-polar heads and the anions always are found close to one another, consistent with previous studies. [102–104, 123] Based on the domain count, *vide infra*, the polar domain remains continuous across the entire composition range. However, the morphology of the nonpolar domain system is found to be dependent on the concentration. It appears that the pure IL system of $[C_2mim][BF_4]$ has a globular morphology where the nonpolar methyl carbon groups present on the cation are observed as small islands

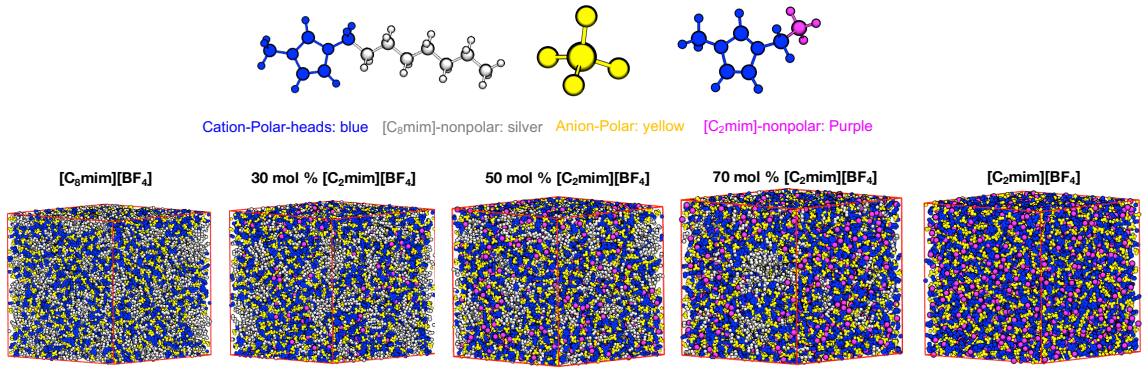

Figure 5.19: Instantaneous snapshot of the equilibrated system for the binary mixtures of $[C_8mim][BF_4]$ and $[C_2mim][BF_4]$ ILs. The snapshots are color-coded to reflect the polar and nonpolar components on both cation and anion. (Cation-polars: blue, Anion: yellow, $[C_8mim]$-nonpolar: silver, and $[C_2mim]$-nonpolar: pink).

interspersed in the polar network, whereas sponge-like morphology is observed for the pure $[C_8mim][BF_4]$ with both the polar and non-polar domains percolate throughout the system and exhibit a bicontinuous morphology. These results are consistent with the structures obtained for other $[C_nmim]^+$-based ILs. [96, 101–104, 123] With the increase in $[C_2mim][BF_4]$ concentration, it is clear that interconnectivity between the nonpolar tails of $[C_8mim]^+$ is highly disrupted, with many tails isolated and surrounded by non-polar methyl carbon of $[C_2mim]^+$. Nevertheless, even at the highest concentration of $[C_2mim][BF_4]$ (70 mol %) considered here, the aggregation of $[C_8mim]^+$ is clearly visible. We believe that such aggregation is responsible for segregating polar and nonpolar domains which is visible as pre-peak in the structure factors.

5.3.3 Aggregate Analysis

In this section we will use the statistical tools, same as used in the above sections, to analyze and provide a quantitative metric to the aggregation pattern that emerges due to varying concentration of $[C_2mim][BF_4]$ in $[C_8mim][BF_4]$. The connectivity of the nano-segregated polar–non-polar structure was examined using a Voronoi tessellation technique based domain analysis. For our purposes, each of the binary IL mixture system is characterized in terms of four unique domains: (a) total polar domain composed of the polar head groups of both the cations and the anion; (b) $[C_8mim]^+$-nonpolar; (c) $[C_2mim]^+$-nonpolar and (d) total nonpolar containing the nonpolar subunits from both the cation.

Figure 5.20 (a) provides the number of domains based on this classification as a function of the $[C_2mim][BF_4]$ concentration. As expected, a domain count of 1 is observed for the polar domain indicating its three-dimensional connectivity for all the ILs mixtures studied here. This observation is in line with previous simulation studies

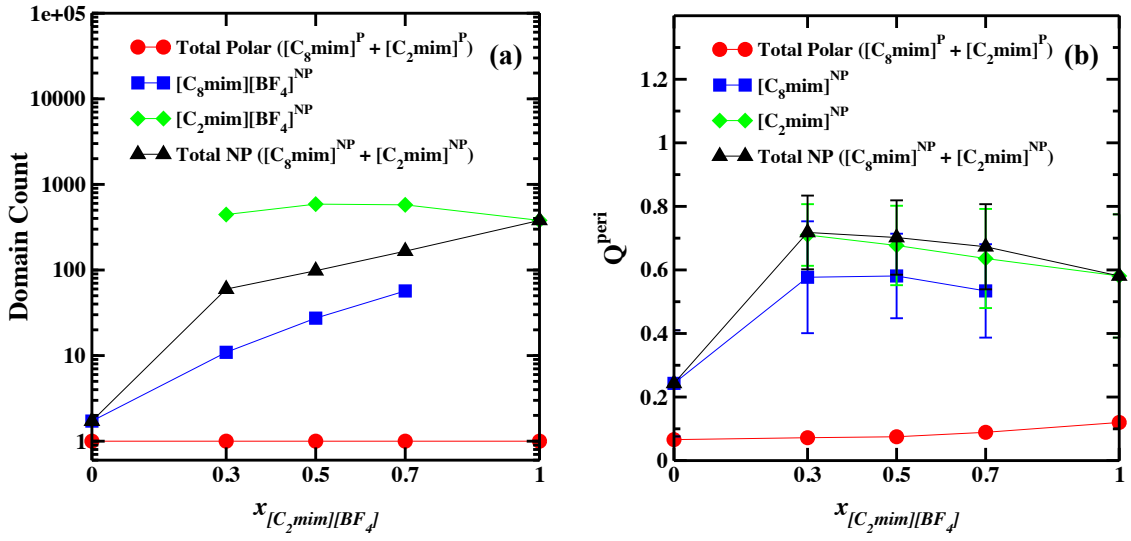

Figure 5.20: (a) Average domain count and (b) Average isoperimetric quotient, Q^{peri} of the respective cation/anion polar and nonpolar domains present in the simulation box plotted against the concentration of $[C_2mim][BF_4]$ in binary mixtures of $[C_8mim][BF_4]$ and $[C_2mim][BF_4]$ ILs. Please note that average numerical value and standard deviations were computed by dividing the trajectory into three blocks. However, the standard deviations are smaller than the symbol size.

involving a wide range of pure ILs. [19, 102–104, 123, 227, 231] For pure $[C_2mim][BF_4]$ IL, the domain counts are significantly higher than 1 ($\sim$ 380) indicating that the cation-nonpolar carbons are dispersed in the system. On the other hand, the domain count for the nonpolar tails in the pure $[C_8mim][BF_4]$ IL is between 1 and 2, indicating that there may be an occurrence of isolated $[C_8mim][BF_4]$ nonpolar chains. The addition of 30 mol% $[C_2mim][BF_4]$ results into a significant disruption of the non-polar connectivity as the large single continuous domain is broken into as many as ten separate domains, and the number reaches a high as 57 at the highest $[C_2mim][BF_4]$ concentration. This results corroborates the inferences derived from the qualitative snapshots that there is a transition from a continuous phase to a dispersed phase. Furthermore, it is interesting to note that the concentration dependence of the domain count of $[C_2mim]^+$-nonpolar methyl carbon is non-linear. It increases from 30 mol % to 50 mol % but then starts to decrease with further increase in the concentration, while the domain counts for $[C_8mim]^+$-nonpolar and total-nonpolar domain

increases monotonically with the increase in the $[C_2mim][BF_4]$ concentration. The breaking of the continuous non-polar phase of $[C_8mim][BF_4]$ into smaller aggregates appears to lead to a jump in the static dielectric permittivity at low $[C_2mim][BF_4]$ concentrations. Above 50 mol% of $[C_2mim][BF_4]$, the static dielectric permittivity shows a weak dependence with the concentration which correlates with almost negligible change in the number of non-polar domains of $[C_2mim][BF_4]$. Therefore, it is believed that the dispersed subphase of $[C_2mim]^+$-nonpolar methyl carbon modulates the overall non-polar domain connectivity and morphology in a way that gives rise to the variation in static dielectric permittivity as a function of $[C_2mim][BF_4]$ concentration.

The change in isoperimetric quotient, shape parameter, observed as the ratio of volume over area for an aggregate, as a function the $[C_2mim][BF_4]$ concentration is shown in Figure 5.20(b). From the figure, it is clear that Q^{peri} for the polar domain shows a negligible dependence on the concentration of $[C_2mim][BF_4]$ and is always less than 0.1, which implies that the shape of the polar network differs greatly from sphericity. Further, the non-polar domain present in pure $[C_8mim][BF_4]$ IL has the Q^{peri} value less than 0.25 suggesting a network whose shape is far removed from a sphere. However, even with 30 mol % introduction of $[C_2mim][BF_4]$ in $[C_8mim][BF_4]$ IL, the Q^{peri} value nearly doubles assuming a value of ~ 0.58 suggesting that a transition in the morphology of the domains which now more closely resemble a sphere in comparison to that in the pure $[C_8mim][BF_4]$. The observation is even more dramatic when the total nonpolar domain of the mixture is considered with values approaching as high as 0.7 at 30 mol% $[C_2mim][BF_4]$. An abrupt increase in the static dielectric permittivity at this concentration probably originates from such a morphological transition. With further increase in the concentration, the isoperimetric quotient is only marginally affected implying that the nonpolar domain continues to retain sphere-like morphology

which is reflected as the plateau in the static dielectric permittivity at these concentrations. Although the nonpolar domain in $[C_2mim][BF_4]$ assume a sphere-like shape ($Q_{peri} \sim 0.6$, the drop in the static dielectric permittivity is probably related to a large number of such domains present in the system (Figure 5.20(a)). Thus, it is believed that change in the shape of the mesoscale aggregates from rod-like (less spherical) to more sphere-like shapes gives rise to enhanced static dielectric permittivity.

The connectivity of the nonpolar domain formed only by $[C_8mim]^+$ cation was further probed by computing the probability distribution $P(n_a)$ of observing an aggregate size of n_a for each of the IL mixtures. Two $[C_8mim]^+$ cation molecules were considered to be a part of the same aggregate if the terminal carbon atoms in the octyl chain are located within the first coordination sphere of each other. The distance corresponding to the first minimum in the radial distribution functions (RDFs) was used to define the coordination sphere. Figures 5.21 (right panel) show RDFs of the terminal carbons of $[C_8mim]^+$ alkyl chain. In all the RDFs, the first minimum occurs at 7 Å, which was taken to be distance criteria for computing the aggregate size distribution.

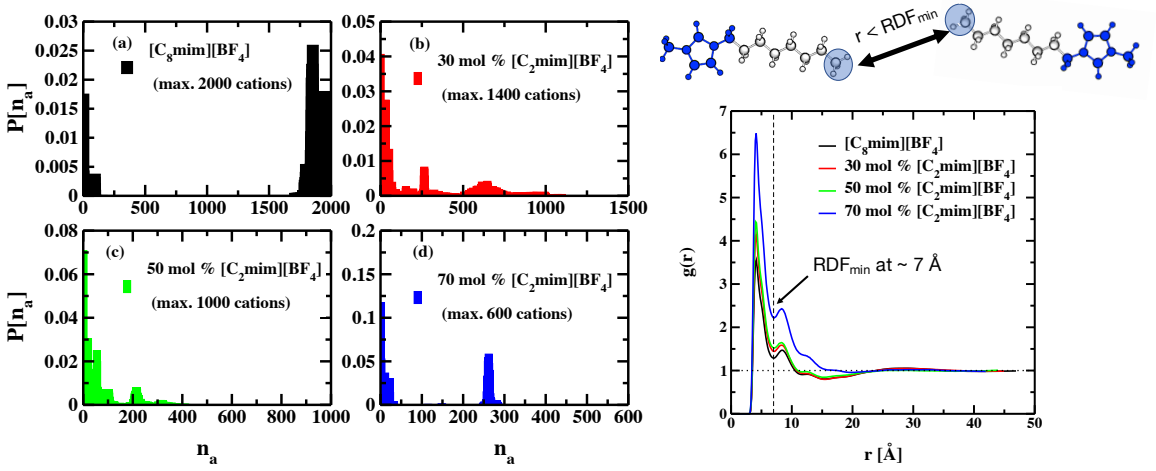

Figure 5.21: On the left: Discrete probability distribution of $[C_8mim]^+$ terminal carbon aggregate sizes, $P(n_a)$, as a function of aggregate size number, n_a, for all the binary IL mixtures studied in this work. On the right: Radial distribution function of $[C_8mim]^+$ terminal carbons at different concentrations of $[C_2mim][BF_4]$ to help define the aggregate criterion.

The increase in the intensity of the RDFs as a function of $[C_2mim][BF_4]$ concentration indicates that the association between the terminal carbon atoms becomes stronger.

Results of the probability distribution $P(n_a)$ of observing the aggregate size of n_a for $[C_8mim]^+$ is depicted in the left panel of Figure 5.21. For pure $[C_8mim][BF_4]$, the nonpolar aggregates have a small tendency to be isolated as evidenced by non-zero probability. On the other hand, the aggregate size distribution is also skewed towards the largest aggregate size with the larger probability and wider distribution than isolated pairs indicating that, on an average, the $[C_8mim]^+$-nonpolar tails percolate throughout the simulation box. The presence of smaller aggregates is also consistent with the domain count being slightly greater than 1. With the increase in the $[C_2mim][BF_4]$ concentration, the probability of finding isolated tails increase, while that for observing large aggregates decrease. In fact, none of the mixture systems, considered here, possess the largest possible aggregate (equivalent to the total number of $[C_8mim]^+$ cations) indicating that the IL mixtures are no longer in a bicontinuous phase. These results are consistent with the domain counts obtained from the Voronoi tessellation analysis which suggested a loss in the domain connectivity.

Therefore, based on the structural analyses presented above it can be concluded that increasing concentration of $[C_2mim][BF_4]$ IL in $[C_8mim][BF_4]$ IL results into a disruption of the non-polar continuity established in the pure $[C_8mim][BF_4]$ IL. These aggregates assume more sphere-like morphology, which is responsible for an enhanced static dielectric permittivity. These results highlight the potential of the mesoscale organization as a route to enhanced physicochemical properties of ILs.

5.4 Aggregation Behavior of 1-n-Dodecyl-3-Methylimidazolium Octylsulfate Ionic Liquid in Dilute Aqueous Solutions

Properties of ILs such as polarity, viscosity, conductivity, reactivity and solvating ability can be significantly affected by the presence of water. For different ILs, the role of water is different. The presence of water has been shown to play an essential role in capturing CO_2 from flue gas. [289] High concentrations of water in ILs can have a significant impact on the solubility of cellulose. [290] Mixture of hydrophobic ILs with water have been employed in extraction processes [291–293] while hydrophilic IL/water mixtures producing aqueous biphasic systems have shown potential for purification of biomolecules. [294, 295] Previous sections have demonstrated that the simultaneous presence of nonpolar moieties on both the ions ($[C_n mim][C_8SO_4]$) can transform the nanostructure of ILs from globular sponge-like to layer-like. Interestingly, when the cationic alkyl chain length is n-dodecyl ($n = 12$), nanoscale structuring (polar-nonpolar-polar) is observed at multiple length scales.

Bahadur and co-workers [172] have studied aqueous solution characteristics of $[C_n mim][C_8SO_4]$ (n = 4, 6, 8 and 10) and showed that at near critical micellar concentration, $n = 4$ and 6 form sphere-like or ellipsoidal micelles while $n = 8$ and 10 form vesicles. The same authors investigated the effect of these ILs on non-ionic surfactant, Triton X-100, and showed the formation of mixed micelles, that has surface charge and can potentially be used as a substitute in protein-surfactant colloidal solutions. Kumar and co-workers [170,171] showed that $[C_n mim][C_8SO_4]$ ($n = 4$, 6 and 8) could be used for synthesizing gold nanoparticles and microplates using photoreduction methodology, the size, and morphology of which can be controlled effectively. The reported critical micellar concentrations (CMC) for n = 4, 6, 8 are 34.9, 14.2 and 4.1 mmol/kg. The same authors also studied aggregation behavior of $[C_8mim][C_{12}SO_4]$ IL in aqueous solutions, CMC = 0.4 mmol/kg, and reported formation of vesicles, that stabilized

bovine serum albumin as well as cellulase against its aggregation and suggested its potential use as replacement for mixed micelles for enzyme stabilization in detergent industries. [169] All these studies have rationalized the thermodynamics based on scattering measurements but failed to provide a molecular-level picture. Further, to our knowledge, no simulation study is available that analyzed the structural changes.

Shimizu et al. [124] commented that in long-chain ILs, the morphology of the polar-nonpolar domains is independent of the source of the alkyl chain, irrespective of cation or anion. Assuming this holds, the aggregation behavior of $[C_{12}mim][C_8SO_4]$ IL in the aqueous solution should have a very similar morphology with respect to the aggregation behavior of $[C_8mim][C_{12}SO_4]$ IL reported by Kumar and co-workers [171].

Thus, this section focuses on the aggregation behavior of $[C_{12}mim][C_8SO_4]$ IL in a high water concentration range. MD simulations at 298 K and 1 bar were conducted at 6 water mole fractions, x_{water} = 0.857, 0.923, 0.962, 0.98, 0.99, 0.995, giving IL concentrations of 1.76, 1.47, 1.09, 0.74, 0.44 and 0.25 mol/kg, at the respective water mole fraction. Comparing with CMC of 0.4 mmol/kg for $[C_8mim][C_{12}SO_4]$ IL [171], even the lowest IL concentration studied in this work is much larger than the critical concentration. Please see section 3.3.1 for simulation protocols and system sizes used. The objective of this work is to reflect the structural modifications occurring in the solution as the dilution proceeds.

5.4.1 Spontaneous Vesicle-like Formation

Figures 5.22 show several snapshots illustrating the progression of the aggregation process over the course of the simulation. At the lowest IL concentration studied in this work (x_{water} = 0.995), starting from a random solution, a rapid local clustering into a micelle within 20 ns was observed. Although not shown here, analysis of the

initial trajectory shows the formation of a small vesicle-like structure that moves close to each other and forms one unilamellar vesicle within the first 20 ns. Comparison of the snapshots at 20 ns and 500 ns shows that changes in the morphology are virtually absent, which attest for the stability of that the unilamellar vesicle. The same spontaneity is observed even at a slightly higher IL concentration (x_{water} = 0.962), although the morphology changes from a unilamellar sphere-like vesicle to contain a bilayer-like vesicle mediated by the unilamellar vesicle. It can be easily seen that at both the concentrations the interface between the water and the vesicle has the distribution of the cationic and anionic polar heads. On the contrary, the cationic and anionic alkyl chains bury themselves inside the layers and are distributed far from the polar solvent.

To understand and visualize the influence of varying water concentrations on the aggregation behavior of [C_{12}mim][C_8SO_4] IL, static snapshots of the well-equilibrated

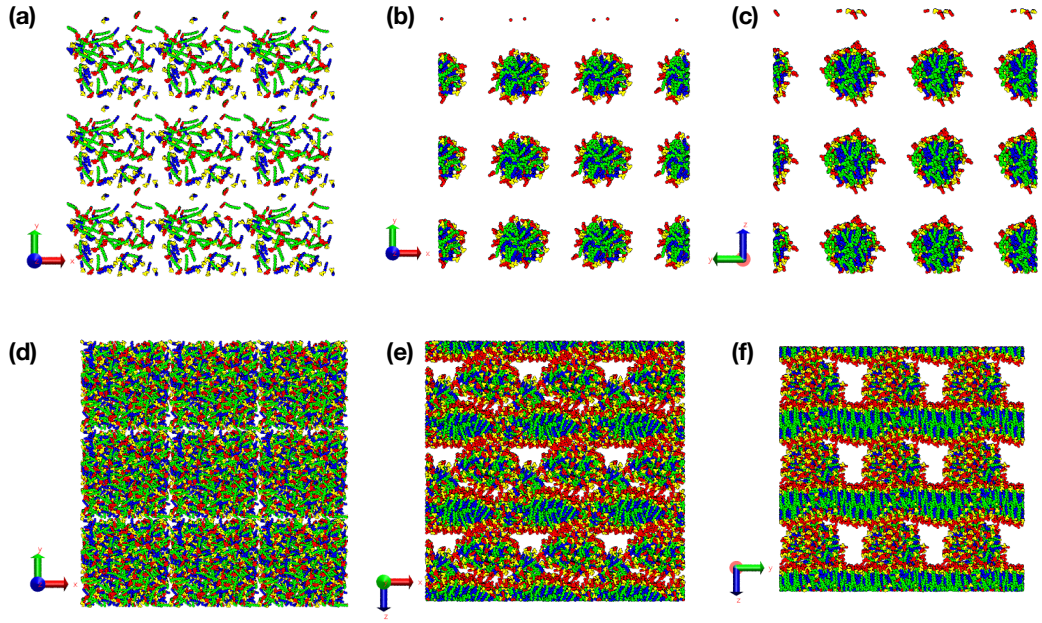

Figure 5.22: Snapshots showing spontaneous aggregation of [C_{12}mim][C_8SO_4] at 2 water concentrations x_{water} = 0.995 (a)-(c) and x_{water}= 0.962 (d)-(f), replicated in three dimensions. Snapshots in (a) and (c) are initial configurations, (b) and (d) are at 20 ns and (c) and (f) are at 500 ns. Water is not shown for clarity.

configurations, replicated in three dimensions, obtained at the end of 500 ns MD simulation are provided in Figure 5.23. The axis is also shown to recognize differences in top-view vs. side-view. The color rendering scheme employed for IL is the same as that used in previous sections, while the water is shown in purple. The representatives also included as part of the figure. Although we have also studied the effect of water, with $x_{water} = 0.75$, on the self-assembly of $[C_{12}mim][C_8SO_4]$ earlier, [200] it is important to note that the structures obtained in this work are not to be directly compared with that study, as the previous study was done at 400 K while this aggregation behavior is studied at the ambient conditions, and it has been well established that the IL-water interactions are temperature dependent. [162]

From Figures 5.23 it is easily discernible that water in high concentrations has a drastic effect on the aggregation behavior of $[C_{12}mim][C_8SO_4]$ bi-amphiphilic IL. It must be stressed that although the structural features presented here do not fully represent all the structural modifications that happen in these solutions for the entire concentration range, this work was able to identify distinct structural regimes. As expected, the cation-polar and anion-polar heads are always found close to each other. However, for $0.99 < x_{water}$, isolated ions or small ion clusters showing a unilamellar vesicle structure can be anticipated, suggesting that with an increase in the water concentration the polar network of IL breaks. As the IL concentration is slightly increased, for $0.98 < x_{water} < 0.99$, multiple isolated sphere-like aggregates start to connect that forms a bi-continuous system displaying a bilayer-like morphology. In $0.97 < x_{water} < 0.98$ although the continuous bilayer-like structures emerge, the complete layers are still isolated and are only mediated by the water molecules. With further increase in the IL concentration, for $0.96 < x_{water} < 0.97$ the bicontinuous layers starts to connect via unilamellar vesicles, and in $0.92 < x_{water} < 0.96$ continuous chain-like aggregates start to percolate the system. Nonetheless, they are still

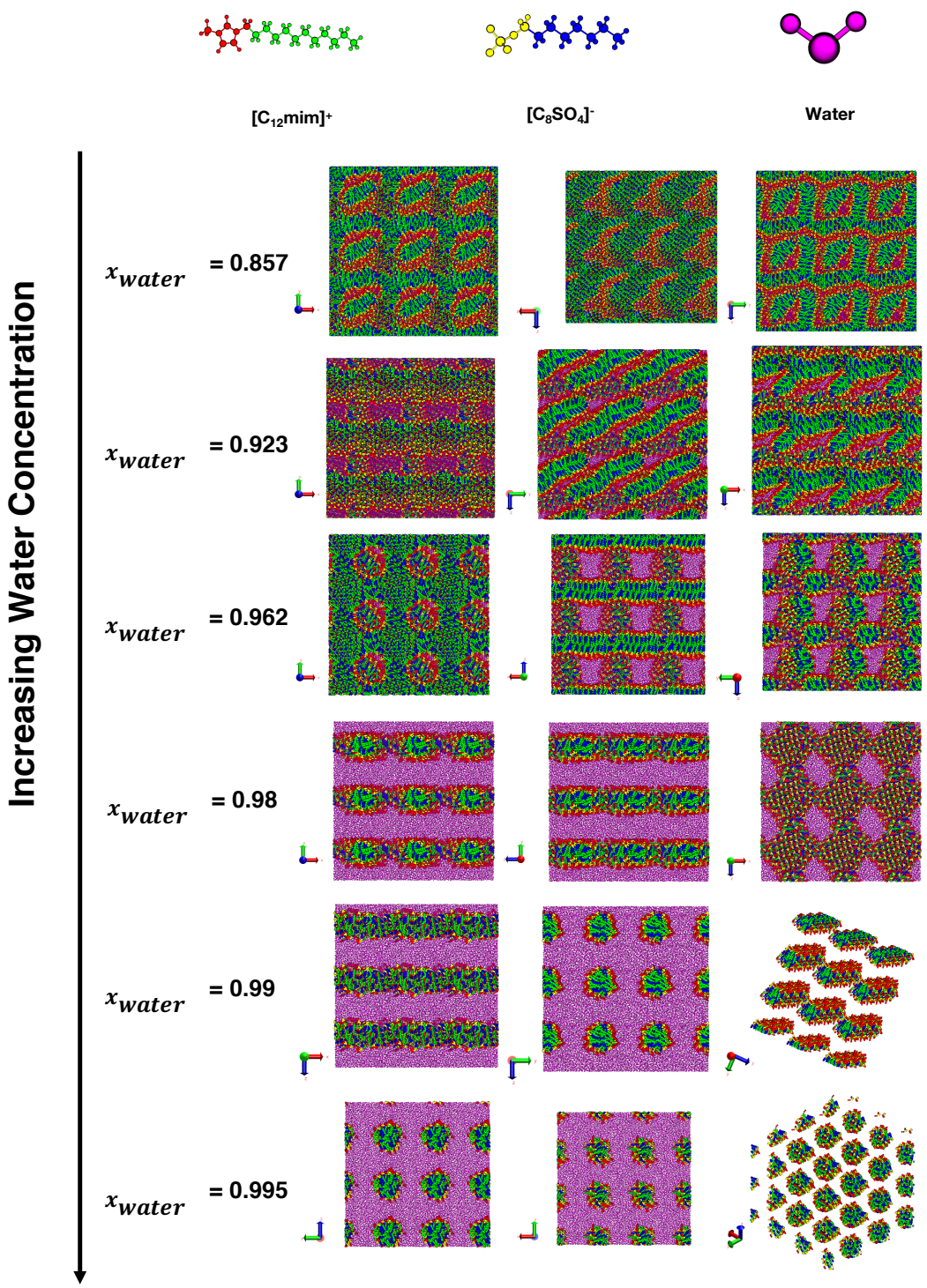

Figure 5.23: Simulation snapshots, replicated in three dimensions, show casing mesoscopic structure of pure $[C_{12}mim][C_8SO_4]$ IL and the structural changes that occur with an increasing water content

not completely continuous (see domain count). A complete percolation of such multi-dimensional vesicle structure is reached only beyond $x_{water} < 0.92$. Furthermore, in the snapshots shown for $x_{water} < 0.92$, the presence of multi-dimensional ordering and the multiple length bilayer connectivity can be observed.

5.4.2 Aggregate Analysis

The structure of $[C_{12}mim][C_8SO_4]$ aqueous solutions was analyzed using different statistical tools. While the water molecule is completely polar, the IL system is characterized in unique polar and nonpolar domains, as described in previous sections of this chapter. Further, for water, the analyses are based on its center of mass (COM).

Figure 5.24 shows the distribution of water with respect to the IL polar and nonpolar parts, in the form of RDFs. It is worth mentioning that the all the RDFs are generated based on the COM of the respective moiety and do not necessarily entail the hydrogen bond interaction present between IL-water and water-water. Comparison of Figure 5.24 (a)-(d) suggests that water likes to interact with the polar head groups of both the cation and anion. All the RDFs do not strictly follow the isotropic distribution, even for longer distances, signifying the presence of spatial heterogeneity within the polar network. The first peak of these RDFs systematically decrease with the increasing dilution with water. However, this doesn't necessarily indicate that as the solution becomes more diluted the interactions between water and ions become weaker. In fact, we believe that the observed intensity changes are dependent on the concentration. Based on the snapshots for IL rich systems (see Figure 5.23), water molecules are usually accumulated near the polar network of the IL giving rise to very high first RDF peak. The accumulation of water near the polar network is also corroborated by the RDFs of water with the nonpolar subunits of ILs, which suggests that the nonpolar domain is nearly free from water. However, as the dilution advances

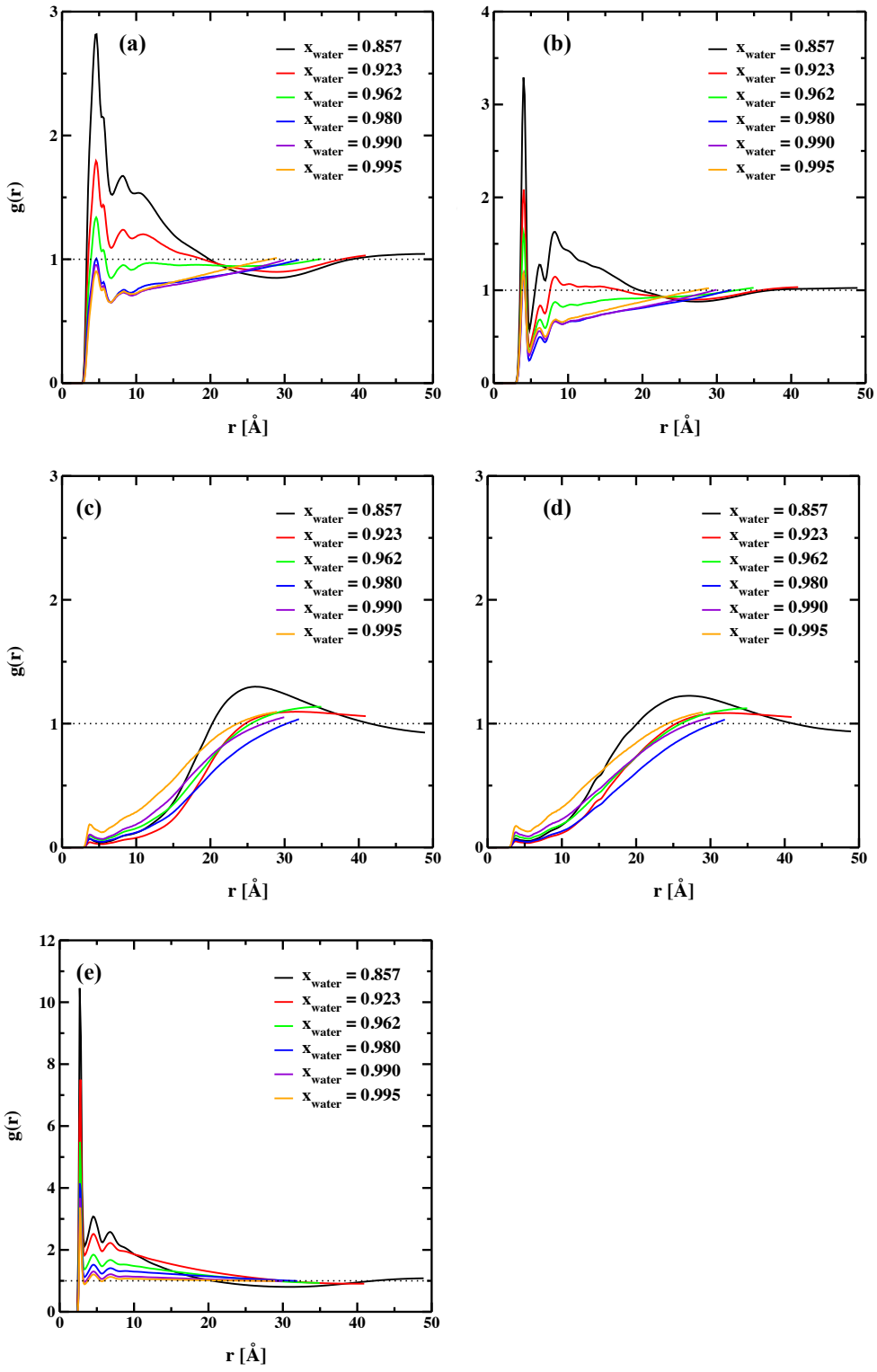

Figure 5.24: RDFs between (a) cation-polar head (COM) - water (COM) (b) anion-polar head (COM) - water (COM) (c) cationic chain terminal carbon - water (COM) (d) anionic chain terminal carbon - water (COM) and (e) water (COM) - water (COM); for different mole fractions of water

the homogenous distribution of water starts to increase, thus probably contributing to the progressively less-intense first peaks. It is also important to note that unlike anion-polar head, interaction of water with cation-polar head group display a split first peak suggesting the presence of more than one interaction site.

In case of RDFs between the polar-nonpolar groups of the IL (Figure 5.25), the change in intensity of the first peak with the increasing dilution has an opposite trend, as the intensity increases with an increase in water mole fraction. For less diluted systems the polar-head groups have relatively more homogeneous distribution than in very diluted systems. The changes in the first RDF peak intensity are more prominent for $x_{water} \geq 0.98$, where the polar network of IL starts to collapse, and the water aggregates start to resemble structural features similar to those of pure water (see below domain count and aggregate size distribution analyses). It is further important to mention that the RDF peak for cation-cation polar head groups progressively shifts towards larger distances while the first coordination shell for cation-anion polar head groups becomes progressively larger. The direct comparison of RDFs between IL-IL polar subunits with the IL polar subunits and water clearly shows an alternating shift suggesting that the polar network of IL increasingly accommodates water molecules until it breaks at very dilute conditions. Additionally, it is worthwhile to note that RDFs of the anion-anion tail groups change from split first-peak to a single high-intensity peak with an increasing dilution demonstrating that changes in the polar network also changes the interactions in the nonpolar domain.

Polar-nonpolar microstructure connectivity was probed using the aggregate analysis based on the Voronoi tessellation technique. For the analysis, the IL system was characterized into different subunits: cation-heads and anion-heads together comprising the polar domain of IL, cationic and anionic alkyl chain separately as a different

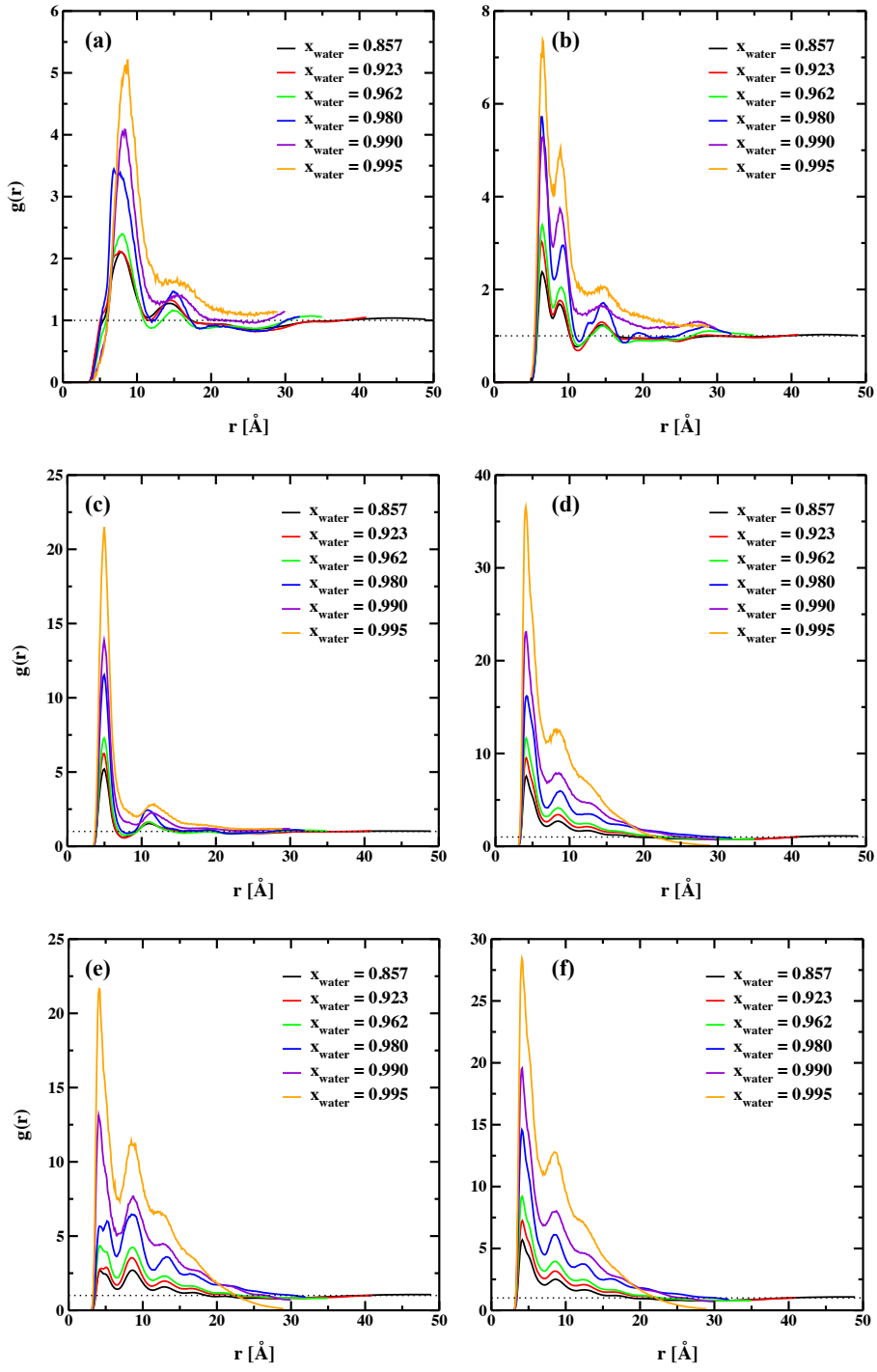

Figure 5.25: RDFs between (a) cation-polar head (COM) - cation-polar head (COM) (b) anion-polar head (COM) - anion-polar head (COM) (c) cation-polar head (COM) - anion-polar head (COM) (d) cationic chain terminal carbon - cationic chain terminal carbon (e) anionic chain terminal carbon - anionic chain terminal carbon and (f) cationic chain terminal carbon - anionic chain terminal carbon; for different mole fractions of water

source of nonpolar domain formation. Further, water is considered completely polar. Therefore, the overall polar domain comprises of all polar IL constituents and water. Figure 5.26 (a) provides the domain count based on the mentioned classification as a function of water mole fraction. For IL-rich system, at the minimum water concentration studied in this work, the IL system shows a bi-continuous phase as both the overall polar and nonpolar domains are connected (domain count = 1). Contrastingly, the domain count for water is very high signifying that there is an occurrence of isolated water clusters but are mediated by their interaction with IL polar domain. Similarly, anion-nonpolar chains may also be isolated but are probably found near cationic chains as the cationic and overall nonpolar domain count is one. As the dilution with water increases, although the overall polar domain remains connected, the individual polar subunits of IL vs. water display a contrasting behavior. Water clusters start to feel full connectivity and become continuous for $x_{water} \geq 0.98$, whereas polar network of IL increasingly become discontinuous. For $x_{water} \geq 0.923$, the presence of more than one domain count for the polar domain of IL suggests that that polar network start to break beyond this water concentration.

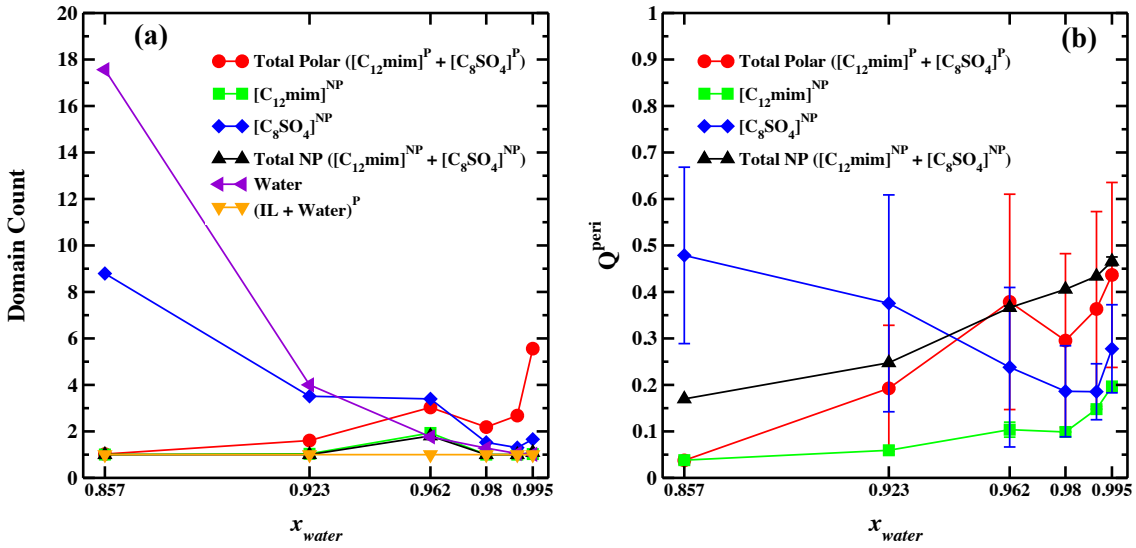

Figure 5.26: (a) Connectivity and (b) Shapes of aggregates of $[C_{12}mim][C_8SO_4]$ IL probed via Voronoi tessellation domain analysis for different mole fractions of water.

This result corroborates the inferences derived from the qualitative snapshots. It is interesting to note that for very dilute systems, $x_{water} \geq 0.98$, the anion-nonpolar domain almost becomes continuous, with a minimal occurrence of isolated pairs. This is clearly seen from the unilamellar vesicle morphology, as the chains are completely subsumed within the vesicle. Furthermore, at $x_{water} = 0.962$, where the structural transition from a continuous bilayer-like vesicle to the presence of bilayer mediated by unilamellar vesicles is observed, all the polar-nonpolar subunits are discontinuous except the overall polar domain. Thus, $0.923 < x_{water} < 0.98$ can be considered as the concentration range where the morphology of the IL vesicles is continuously changing.

The changes in the shape of the morphology of IL can be quantitatively analyzed by computing the isoperimetric quotient, that assumes a value of 1 for a perfect sphere. The change in the isoperimetric quotient as a function of water concentration is shown in Figure 5.26(b). From the figure, it is clear that as the concentration of water is increased, the shape of the aggregates of both the overall polar and nonpolar domains of the IL transitions from less sphere-like to a more sphere-like morphology. The average value of the shape parameter of the overall polar domain increases more than 10 folds, $\sim$0.04 to 0.45, while the value for the overall nonpolar domain changes nearly 3 folds, $\sim$0.17 to 0.47, as the mole fraction of water increases from 0.857 to 0.995, demonstrating significant structural changes that are more dominant for the polar domain. Similarly, considering the two extreme water concentrations studied in this work, x_{water} of 0.853 vs. 0.995, the cation-nonpolar domains also tend to assume a sphere-like vesicular morphology as the water concentration is increased. On the contrary, considering the statistical uncertainty, the shape of the nonpolar domain of the anion is not altered significantly and assumes a morphology that is more sphere-like, at all the water concentrations studied in this work.

IL and water clustering were also investigated by computing the distribution of various aggregate sizes. Similar to the Voronoi domain analysis, IL was divided into different subunits. The first minimum of the respective RDFs shown in Figure 5.25 was chosen as the distance criterion to consider two molecules part of the same aggregate. The size distribution of the IL aggregates as a function of water composition is reported in Figures 5.27. Please note that the maximum aggregate size is dependent on the system size. For IL-rich system, $x_{water} = 0.853$, both the overall polar and nonpolar domains are connected, as the probability of finding a single large aggregate is highest. Further, although the anion-tail aggregates have a wide distribution, with the probability of isolated pairs is nearly negligible, the overall nonpolar chain is connected via the cation-nonpolar chains. As the mole fraction of water is increased

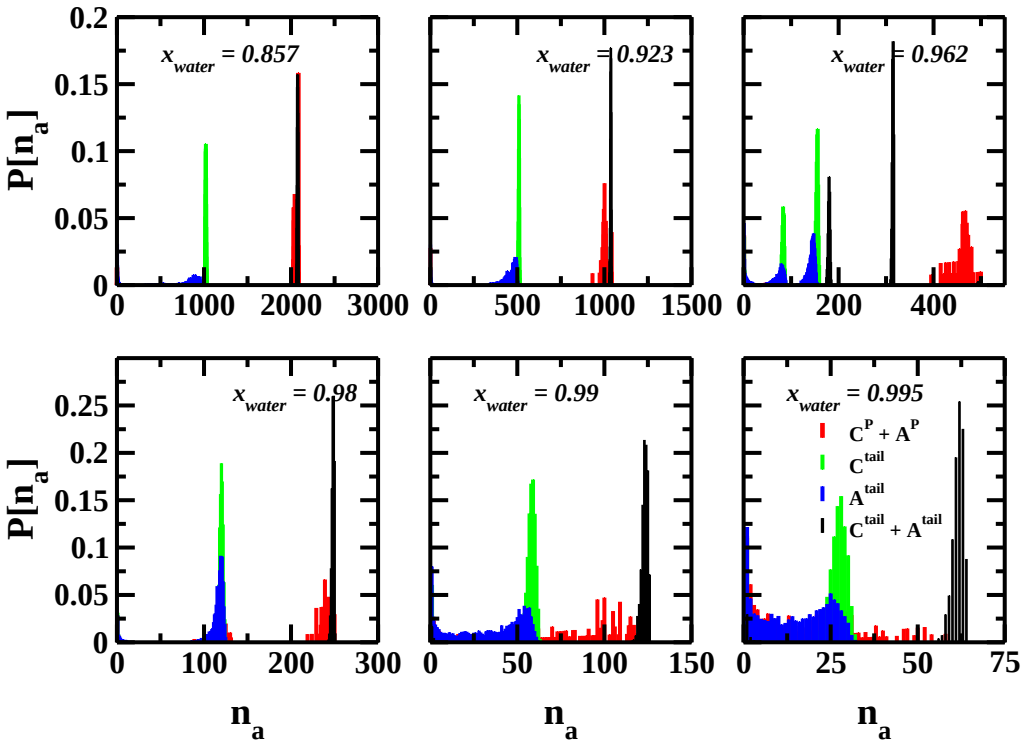

Figure 5.27: Discrete probability distribution of polar and nonpolar components of $[C_{12}mim][C_8SO_4]$ IL aggregate sizes, $P(n_a)$, as a function of aggregate size number, n_a, as a function of increasing water content.

to 0.923, the distribution of cationic-nonpolar, anionic-nonpolar and overall-nonpolar domains are very similar to that found for $x_{water} = 0.857$. Although the overall IL polar domain has a maximum probability for the largest size aggregate, a slightly wider distribution suggests the possibility of the existence of ionic clusters that, at least temporarily, lose their connectivity from the polar network. At $x_{water} = 0.962$, where a drastic morphological transition is observed, the nonpolar domain has a bimodal distribution. This can be attributed to the fact that the IL morphology contains bilayer-like vesicle mediate by a sphere-like vesicle. Thus, probably, the larger size distribution corresponds to the bilayer-like structure while smaller distribution denotes the distribution that of the sphere-like vesicle. Further, occurrences of the isolated nonpolar chains also increase. The wider distribution of IL polar domain suggests breaking of the polar network of IL. In fact, the largest size aggregate contains $\sim$ 500 molecules, with the lowest probability, suggesting that there may be few instances where the whole polar network is completely connected, but on an average, the polar domain of IL is broken. As the dilution is further increased, except the overall nonpolar domain that appears to be connected, all other subunits start to show a very wide range of aggregate size distribution ranging from an isolated molecule to a large size aggregate. The inferences drawn are consistent with the Voronoi domain analysis.

Similarly, Figure 5.28 shows the probability of finding a water molecule in an aggregate of size n_a, as a function of water composition. Please note that the distribution was split into two graphs for better clarity. From the figure, it is clear that there are three distinct tendencies: (i) for $x_{water} < 0.92$, the molecules have the tendency of being isolated or being in a cluster size of 20 or less, in addition to the large size aggregates; (ii) $0.92 < x_{water} < 0.98$, the tendency of isolated pairs decreases while the probability of spanning large size aggregates increase, therefore, this is probably the range where water is near the percolation limit; and (iii) $x_{water} > 0.98$, almost

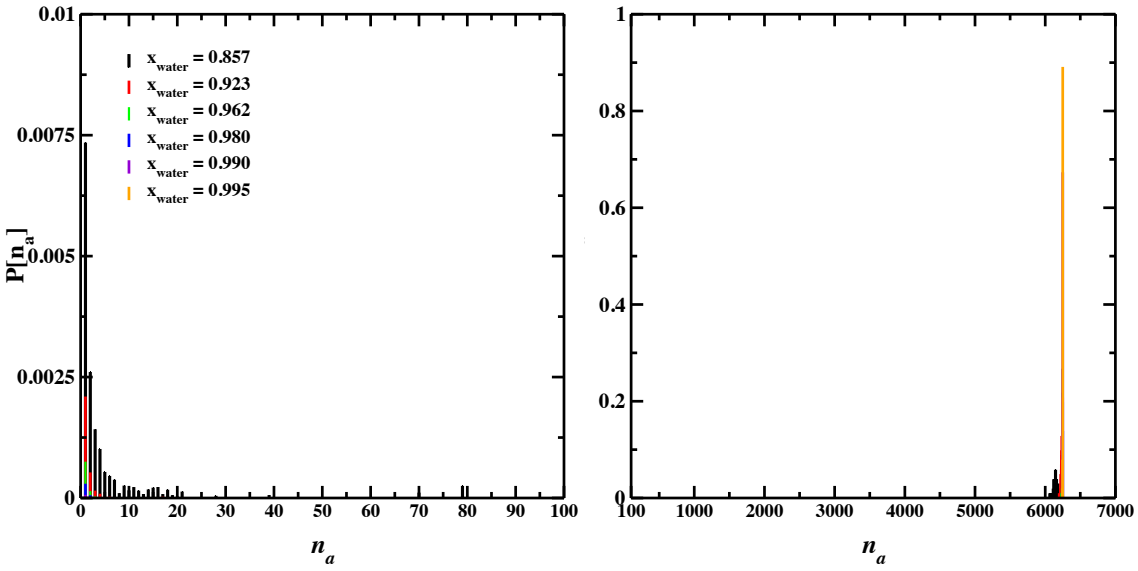

Figure 5.28: Discrete probability distribution of water aggregate sizes, $P(n_a)$, as a function of aggregate size number, n_a, broken into two graphs showing different range of data, as a function of increasing water content.

all the molecules belong to a single large size aggregate that spans the entire box and effectively forms a second continuous phase. However, it must be stressed that there are a few isolated pairs that may temporarily detach from the continuous polar network.

The connectivity of the aggregates is also analyzed based on the number of first shell neighbors within the cluster. Figure 5.29 shows the coordination number for the different polar and nonpolar subunits. As the concentration of water is increased, the average number of water neighbors increases from $\sim$ 3.5 to 5. It is known that for pure water the coordination number lies between 4 to 5. [149] Figure shows that only when $x_{water} \geq 0.962$ does each water molecule start to have more than 4 neighbors, which suggests that beyond this concentration the water aggregates start to show structural features resembling those of pure water. For IL, at highest water content, the average number of IL polar subunits is less than 2. This suggests that at this water concentration the polar network is stretched and has no branching nature that

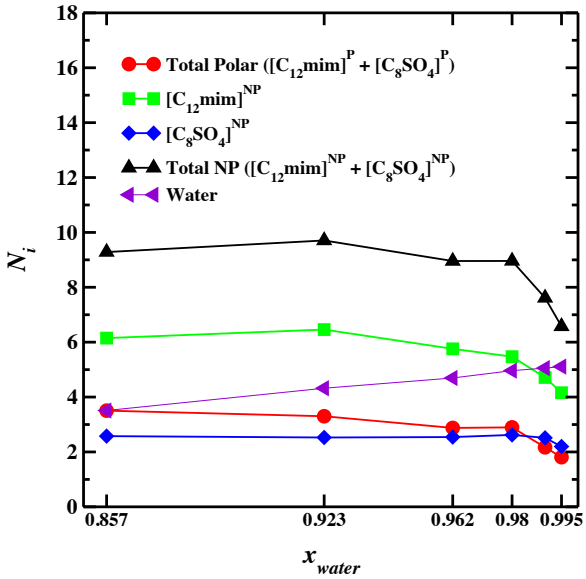

Figure 5.29: Number of neighbors in around a given molecule in an aggregate. The aggregates are partitioned based on the respective polar and nonpolar components.

forms alternating cation- and anion-head network. However, as the mole fraction of water is decreased, the number of IL polar neighbor increases eventually reaching a plateau for $x_{water} < 0.98$ indicating that the branching of the polar network is restored and the number of neighbors becomes approximately independent of the cluster size. Similar transitions are observed for the nonpolar subunits as well, which, however, have more number of average neighbors. In fact, even at the highest water concentration, the average number of neighbors is greater than 6 suggesting that the nonpolar domain neighbors probably have a two-dimensional hexagonal-like network.

Thus, the results reported in this subsection suggest that the structure of $[C_{12}mim][C_8SO_4]$ IL in aqueous solutions changes with the concentration in the following way: (i) for $x_{water} \geq 0.995$, IL assumes a unilamellar vesicle-like morphology where the IL polar network breaks apart, whereas continuous and highly branched water network resembling structural properties close to that of pure water remains; (ii) $0.98 < x_{water} < 0.995$, the presence of multiple sphere-like unilamellar vesicles starts to connect and

forms a bilayer-like vesicle but remains isolated and is only mediated by the water molecules; (iii) $\sim 0.96 < x_{water} < 0.98$, IL assumes a mixed morphology containing bilayer-like vesicles mediated not only by water molecules but also by sphere-like unilamellar vesicles. Additionally, water molecules almost remain connected. This is the range where, potentially, biphasic structure composed by continuous networks, one of IL and other of water, is observed; (iv) $0.92 < x_{water} < \sim 0.96$, the IL structure slowly transitions to assume bilayer-like morphology trying to reach the percolation limit for the polar network of IL while the branching of the water molecules is reduced giving rise to multiple clusters of varying sizes; and (v) $x_{water} < 0.923$, percolation of IL polar and nonpolar network is reached for the entire system.

Thus, at very dilute concentrations, the formation of spherical unilamellar vesicles is consistent with the experimental study of $[C_8mim][C_{12}SO_4]$ [171] where the chain length between the ions are swapped, and similar morphologies are expected in comparison to the system studied in this work. [124] This study further extends the understanding and provide useful molecular-level insights characterizing the morphological transitions. We believe that the concentration range of $0.962 < x_{water} < 0.98$ where a mixed morphology of bilayer-like vesicle mediated by spherical vesicles is observed and has continuous network of both water and IL, has the potential to be exploited for various applications such as a substitute for mixed surfactant or as an ingredient in pharmaceutical industries for stabilizing the proteins.

5.5 Summary

To summarize:

- Sponge-like morphology, with no preferred orientation, is observed for ILs containing long alkyl chains on either cation or anion.

- Aggregation behavior and self-assembled morphology of long chain ILs can be modulated effectively from sponge-like to layer-like by judiciously choosing an optimum combination of alkyl chains on both the cation and anion simultaneously: bi-amphiphilic ILs. In this study, it was shown that the bi-amphiphilic IL - $[C_{12}mim][C_8SO_4]$ - can potentially show nanoscale heterogeneity spanning over multiple length scales, an observation that remains to be validated.

- Mixing of ILs differing widely in the amphiphilicity can potentially possess extraordinary features. Mixtures of $[C_{12}mim][C_8SO_4]$ IL with a less amphiphilic IL showed changes in ordering and morphology such that discontinuity in the overall polar network was observed. This is the first time multiple polar domains are observed, an observation that remains to be validated. Furthermore, an example of $[C_8mim][BF_4]$-$[C_2mim][BF_4]$ shows that changing concentration leads to the formation of isolated mesoscale aggregates that show 100 % enhancement in the static dielectric permittivity, a physicochemical property. This demonstrates the importance of structures at mesoscale and the use of IL mixtures to fine-tune and potentially enhance the property behavior.

- Aggregation behavior of $[C_{12}mim][C_8SO_4]$ IL in aqueous solutions, at high water concentration shows unique structural regimes: (i) For $x_{water} \geq 0.98$ a spontaneous formation of isolated unilamellar vesicles of IL was observed; (ii) For $x_{water} < \sim 0.92$, IL formed bilayer-like vesicles that are mediated by small clusters of water; and (iii) In the region of $\sim 0.92 < x_{water} < 0.98$, IL assumes a mixed morphology containing bilayer-like vesicles mediated by sphere-like unilamellar vesicles.

- It was shown that different versions of the GROMACS package could give slightly different results. Hence, caution must be taken while reproducing any results. It is suggested to follow the simulation protocols as closely as possible.

CHAPTER 6

CONCLUSIONS AND RECOMMENDATIONS

6.1 Conclusions

The research reported in this dissertation explains the procedures, results, and analyses of molecular simulations that have been carried out on ionic liquids (ILs) and their binary mixtures. The work has demonstrated the applicability of simulations as a predictive tool to calculate thermophysical, structural, and phase equilibria properties. This dissertation focused on fundamentally understanding the molecular interactions responsible for the observed property behavior. The work can be divided into two parts.

The first part of the dissertation focused on initiating an understanding of the structure-property relationship for *a priori* predicting the presence of nonideality in the binary IL mixtures, which can be applied for tuning and perhaps enhancing the CO_2 absorption capability. Initially, 13 binary IL mixtures were chosen to showcase (i) anion effect and (ii) cationic alkyl chain dependence on the thermophysical properties. The IL mixtures contained a common cation paired with two different anions, where the anions were chosen based on their differences in size / molar volume and hydrogen bonding acceptor abilities. Isothermal-isobaric molecular dynamics simulations were performed to compute thermophysical properties such as density, molar volume, self-diffusion coefficients, and ionic conductivity as functions of the IL composition at a given temperature and pressure. The thermophysical property data for pure ILs was compared against the available literature data. The agreement between the predicted

values and the literature data for thermodynamic properties was excellent, within 1 %. Although the transport properties were slightly underpredicted, given the sluggishness of ILs and the range in which they display the dynamics, they were considered in reasonable agreement with the experimental data. The results presented also endorse the concept that the inclusion of non-integer charges on the constituting ions, that takes into account the polarization effect, improves the prediction of dynamic behavior using molecular simulations. Further, the composition dependent trends of the thermophysical properties were discussed. The deviation of actual values from the ideal mixing linear rule, mole fraction weighted arithmetic average, were computed to demonstrate the presence of nonideality. To rationalize the property behavior, local structure of the fluid was examined in terms radial distribution functions, spatial distribution functions, angular distribution functions, and coordination numbers.

The structural analyses revealed that for the anions having large differences in size / molar volume and hydrogen bond acceptor ability, the association of the anion with the cation has a strong composition dependence. The increasing concentration of strongly coordinating anion is able to displace the weakly coordinating anion from the equatorial position of the imidazolium-ring to the take positions above and below the ring-plane, losing its ability to coordinate at the most-acidic site vectorially. Due to this the π-π stacking interaction of the two cations is slightly disrupted, which leads to an increase in the distance between the two cations. This probably makes available free volume that is seen as a positive deviation from the ideal mixing molar volumes. The top-and-bottom arrangement of the larger anion also aids the formation of anion-π interaction. Such concentration-dependent structural transitions are termed "non-native" with respect to the pure IL analogues, which give rise to a nonlinear thermophysical property behavior. On the other hand, for the anions with similar hydrogen bond acceptor ability and sizes, such structural transitions are vir-

tually absent; leading to an ideal mixing behavior, which suggests that their property behavior can be easily estimated using pure IL data.

Two ILs, one with ideal and another with nonideal (non-native) structures, were chosen to assess the implications of such structures on the CO_2 solubility. CO_2 solubility in terms of Henry's constants was evaluated, where lower Henry's constants indicate a higher solubility. Henry's constants were calculated by computing excess chemical potentials using the BAR method. As expected, it was found that interactions of CO_2 molecules with the anions govern the degree of solubility in imidazolium-based ILs while the interactions with the cations plays a secondary role, and the CO_2 solubility was higher for ILs with a fluorinated anion. Binary IL mixtures that showed non-native structures also showed a non-linear dependence of Henry's constants, where Henry's constants were underpredicted from the ideal mixing rule, suggesting the presence of excess CO_2 solubilities whereas the mixture with ideal structures gave ideal mixing phase behavior. MD simulations with and without CO_2 molecules at 10 bar pressure were conducted. By interpreting the structures, it was found that CO_2 molecules do not alter the underlying structure of the ILs. However, CO_2 molecules position themselves above and below the cation ring-plane. The structural transition of the, larger size, weakly coordinating fluorinated anion above and below the ring-plane, with the increasing concentration of strongly coordinating anion, not only frees up the volume that aids in CO_2 molecule accommodation but also allows enhancement of the interaction between the CO_2 molecules and fluorinated anions, which gives rise to higher CO_2 solubilities. In this study, it was also shown that although the Henry's constants display non-linear behavior, they can still be estimated on the basis of pure IL data when mole fraction weighted harmonic mean instead of arithmetic mean is used, which suggests that in Henry's law regime the assumption of ideal CO_2 absorption still appears to remain valid. In other words, when assessing

the ideal-nonideal behavior of solubilities, it is the mole fraction of the solute that is linearly related rather than Henry's constants. Thus, it was shown that although the solubilities are apparently ideal the molecular origins of the non-linear behavior is entirely different.

Since Henry's constants only describe the system at the saturation limit, absorption isotherms for the pressure range of 1-100 bar were computed using Gibbs ensemble Monte Carlo method, for an IL mixture of $[C_4mim]$ Cl_x $[NTf_2]_{1-x}$ that displays non-native structures. Given the difficulty in sampling at higher pressures, the absorption isotherm for pure ILs was in excellent agreement with the literature. It was validated that at low-pressures, in Henry's law regime, the absorption of CO_2 follows ideal mixing behavior. However, for pressures beyond 20 bar deviations in the absorption data emerge. Large deviations were seen at the IL mixture concentrations that possess non-native structures. Further, this nonideal IL mixture was examined for the gas separation of the mixture of CO_2 and CH_4. For this, the mixed gas absorption isotherm at a higher pressure of 100 bar was computed, and the selectivity was compared with the selectivity calculated using pure gas absorption data. Non-linear behavior, indicating an enhanced CO_2 separation, was seen for the gaseous mixture containing CO_2 and CH_4 in the ratio of 5:95. Thus, the inferences drawn from the aforementioned studies above suggested that binary IL mixtures can be used as an avenue for finely tailoring the property behavior, and the presence of non-native structures can lead to an enhanced CO_2 solubility.

For long-term effects it is important to recognize which cation-anion combinations have the potential of forming non-native interactions (structures). Thus, a systematic study was performed where much of the focus was on the binary IL mixtures where one anion contained fluorine atoms while the other, strongly coordinating, an-

ion was nonfluorinated. This was done to find IL mixtures that can be exploited for better absorption of CO_2. Sixteen binary IL mixtures were structurally characterized to pinpoint a qualitative range of differences in size / molar volume and hydrogen bond acceptor ability of the anions that can lead to structures non-native to the pure IL analogues. It was found that if the two anions are chosen such that differences in the molar volume and the hydrogen bond acceptor ability is greater than 60 cm^3/mol and 0.4, simultaneously, then non-native structures can be anticipated.

The second part of the dissertation deals with long-chain containing ILs that can self-assemble. The focus was to fundamentally understand the self-assembly itself rather than its implications on a property behavior. For this purpose, the nanoscale structure of ILs containing cation and anion both having long alkyl chains were investigated at 400 K using MD simulations. The alkyl chain on the imidazolium-based cation was systematically increased while the alkylsulfate-based anion containing eight carbon atoms (octyl chain) was chosen. It was found that presence of alkyl chains on both the ion constituents can have profound impact on the morphology of the IL. For smaller cationic chains the morphology was sponge-like, but as the alkyl chain on the cation was increased the morphology was transformed to layer-like. A sluggish glass-like or liquid crystal-like behavior with a long-range order was found to be the characteristic of these materials. Despite carrying out very long simulations, up to 1 μs, the qualitative morphologies were found to be dependent on the versions of the GROMACS used to conduct the simulations. This was due to differences in the well equilibrated densities of around 5 %. However, the overall conclusions remain intact. Thus, it is advised that when attempting to reproduce results special care must be taken regarding the simulation protocols. To our knowledge, for the first time, nanoscale heterogeneities spanning over multiple length scales were observed for the system of $[C_{12}mim][C_8SO_4]$ IL, an observation that remains to be validated.

This observation was reproduced irrespective of the initial configuration and system size.

Due to the uniqueness of $[C_{12}mim][C_8SO_4]$ IL, the focus of the further study revolved around influencing its morphology and studying its aggregation behavior in aqueous mediums. In line with the first half of the work presented in this dissertation, binary IL mixtures were used to modulate the morphology, as it was shown earlier that different local structures could impart different property behavior. Specifically, two IL mixtures were chosen for this task: one with common cation $[C_{12}mim]$ $[C_8SO_4]_x$ $[MeSO_4]_{1-x}$ and one with common anion $[C_{12}mim]_x$ $[C_1mim]_{1-x}$ $[C_8SO_4]$. It was found that the presence of long-range ordering in $[C_{12}mim][C_8SO_4]$ IL can be influenced by changing the concentration of the other IL, as the morphology was changed from layer-like to sponge-like at low concentrations of $[C_{12}mim][C_8SO_4]$ IL. For the first time, to our knowledge, a discontinuous polar domain was observed at three concentrations – $x = 90$ mol% and 75 mol% for $[C_{12}mim]$ $[C_8SO_4]_x$ $[MeSO_4]_{1-x}$, and $x = 90$ mol% for $[C_{12}mim]_x$ $[C_1mim]_{1-x}$ $[C_8SO_4]$ – an observation that still remains to be validated. Although the morphology was less affected, the ordering could be fine-tuned and that could potentially possess enhanced nonpolar domain lengths in comparison to both pure IL counterparts. Additionally, an example of binary mixtures of $[C_8mim][BF_4]$ with $[C_2mim][BF_4]$ was included to show that the change in morphology from sponge-like to isolated spherical aggregates can translate into 100% enhancement in a physicochemical property such as static dielectric permittivity.

The ILs containing long-chains (≥ 8) on both the cation and anion have been shown, experimentally, to form vesicle-like structure at high water concentrations, which can find use as a protein stabilizing ingredient in pharmaceutical industries, for synthesis of nanoparticles or a potential substitute for the mixed surfactant systems. Aggre-

gation behavior of $[C_{12}mim][C_8SO_4]$ IL at high water concentrations was studied at 298 K using MD simulations. The spontaneous formation of vesicle-like structures was observed. Two major structural changes occur: (i) when the percolation limit of water was reached, in very dilute conditions ($x_{water} > 0.98$), water starts to show properties similar to pure water, whereas the polar network of IL although mediated by water molecules starts to break into smaller aggregates and loses its continuity; and (ii) for $x_{water} < \sim 0.92$ the percolation limit of IL was reached. The branched and continuous polar and nonpolar network of IL emerged and was mediated by small clusters of water. Unique and interesting observations were made in the water concentration range of $0.92 < x_{water} < 0.98$, where biphasic continuity in both IL and water was achieved simultaneously (at least temporarily). Furthermore, in this concentration range the IL showed mixed morphology containing both bilayer-like vesicle mediated by unilamellar sphere-like vesicle. We believe that this concentration range has a great potential to be exploited for pharmaceutical systems as well as material synthesis, as it provides one-phase continuous medium with the ability of solvating both the polar and nonpolar species simultaneously.

6.2 Recommendations for Future Work

In the study concerning chapter 4, binary IL mixtures have been employed for better/enhanced CO_2 absorption. Recently, it has been reported that confinement of pure ILs and in very few cases mixtures of ILs can also potentially increase the CO_2 absorption. Molecular simulation methods may be applied to study the behavior of nonideal mixtures in confinement for providing molecular origins and assessing the suitability. Henry's constants can be computed as a first step. Once the speculated enhancement, if any, is observed full isotherm calculations may be performed to determine the amount of IL mixture required for a set target removal.

Very recently, our research group also studied the phase equilibria of SO_2 in pure ILs containing the same cation $[C_4mim]^+$ and different anions namely Cl^-, $[MeSO_4]^-$, $[NTf_2]^-$ and $[DCA]^-$. [296] It was observed that the influence of anion on SO_2 solubility is not predominant as much as CO_2 solubility, although for a given IL, SO_2 or NH_3 solubility is two to three orders of magnitude higher than that of CO_2. Further, simultaneous capturing of CO_2 and SO_2 at high pressures is known to be of great industrial interest. Thus, nonideal binary ILs, that have shown potential of enhanced CO_2 solubility, can be employed for tuning the simultaneous capture of CO_2 and SO_2. Henry's constant of SO_2 in binary IL mixtures may be computed as the first step, before performing mixed gas isotherm calculations. Such calculation will also provide insight on selectivities rather than making ideal assumptions and the estimating it based on the Henry's constants.

On the other hand, the study concerning chapter 5 has provided many unique observations that can be exploited for multiple applications. Presence of an optimum combination of cationic and anionic alkyl chain has shown to possess nanoscale heterogeneities over multiple length scales. Also, it has been reported that the presence of fluorinated chains with carbon length ≥ 4 can also segregate in a separate domain, a third domain different from the polar and nonpolar domain. Therefore, we believe a molecular simulation study on 1-n-dodecyl-3-n-alkylfluoryl-imidazolium $[C_{12}C_mF_{2m+1}im][C_8SO_4]$ where m may be systematically increased from 4 to 12 can provide useful insights into the aggregation behavior. It would be really interesting to see how the third domain of fluorinated chains emerge within the polar-nonpolar domain that spans over multiple length scales.

Mixtures of $[C_{12}mim][C_8SO_4]$ have potentially shown discontinuity in polar domain, however, with a high long-range order. Moreover, even the nonpolar domain may have

existence of temporary detachment of small cluster of nonpolar aggregates. This suggests that the overall morphology is stable due to weak dispersion interactions. One of our early study has shown that long-chain alkanes such as n-octane, although have poor solubility, can reside in the nonpolar domain of this IL. [200] This provides a unique opportunity to study phase equilibria of long hydrocarbons in such mixtures of $[C_{12}mim][C_8SO_4]$ IL and study its effect on the connectivity of polar and nonpolar domain.

Molecular simulation study of very dilute aqueous solutions of $[C_{12}mim][C_8SO_4]$ IL has provided molecular level insights on the origin of the formation of different vesicular structures. A concentration range was identified where near percolation of both IL and water co-occurred. Experimentally, use of $[C_8mim][C_{12}SO_4]$ IL has been reported as mixed surfactant systems in detergent industry, stabilization of cellulase at various concentrations, and synthesis of gold nanoparticles. Due to the lack of any computational study, a direct attempt can be made to conduct a molecular simulation study and provide molecular-level insights into the interactions responsible for the observed behavior.

REFERENCES

[1] F. Endres, S. Zein El Abedin, Air and water stable ionic liquids in physical chemistry, Phys. Chem. Chem. Phys. 8 (18) (2006) 2101–16.

[2] M. Galiński, A. Lewandowski, I. Stepniak, Ionic Liquids as Electrolytes, Electrochim. Acta 51 (26) (2006) 5567–5580.

[3] R. Lin, P.-L. Taberna, S. Fantini, V. Presser, C. R. Pérez, F. Malbosc, N. L. Rupesinghe, K. B. K. Teo, Y. Gogotsi, P. Simon, Capacitive Energy Storage from –50 to 100 degree C Using an Ionic Liquid Electrolyte, J. Phys. Chem. Lett. 2 (19) (2011) 2396–2401.

[4] D. R. MacFarlane, N. Tachikawa, M. Forsyth, J. M. Pringle, P. C. Howlett, G. D. Elliott, J. H. Davis, M. Watanabe, P. Simon, C. A. Angell, Energy Applications of Ionic Liquids, Energy Environ. Sci. 7 (1) (2014) 232–250.

[5] P. Wasserscheid, W. Keim, Ionic Liquids-New "Solutions" for Transition Metal Catalysis, Angew. Chem. Int. Ed. (2000) 3772–3789.

[6] A. Riisagera, R. Fehrmanna, M. Haumannb, P. Wasserscheidb, Supported Ionic Liquids: Versatile Reaction and Separation Media, Top Catal 40 (1-4) (2006) 91–102.

[7] G. H. Lane, P. M. Bayley, B. R. Clare, A. S. Best, D. R. MacFarlane, M. Forsyth, A. F. Hollenkamp, Ionic Liquid Electrolyte for Lithium Metal Batteries: Physical, Electrochemical, and Interfacial Studies of N-Methyl- N-butylmorpholinium Bis(fluorosulfonyl)imide, J. Phys. Chem. C 114 (49) (2010) 21775–21785.

[8] L. T. Costa, B. Sun, F. Jeschull, D. Brandell, Polymer-Ionic Liquid Ternary Systems For Li-Battery Electrolytes: Molecular Dynamics Studies of LiTFSI in a EMIM-TFSI and PEO Blend, J. Chem. Phys. 143 (2) (2015) 024904–10.

[9] A. Basile, H. Yoon, D. R. MacFarlane, M. Forsyth, P. C. Howlett, Investigating Non-Fluorinated Anions For Sodium Battery Electrolytes Based on Ionic Liquids, Electrochem. Commun. 71 (C) (2016) 48–51.

[10] J. Szymczak, S. Legeai, S. Michel, S. Diliberto, N. Stein, C. Boulanger, Electrodeposition of Stoichiometric Bismuth Telluride Bi_2Te_3 Using a Piperidinium Ionic Liquid Binary Mixture, Electrochim. Acta 137 (2014) 586–594.

[11] Z. Liu, T. Cui, T. Lu, M. Shapouri Ghazvini, F. Endres, Anion Effects on the Solid/Ionic Liquid Interface and the Electrodeposition of Zinc, J. Phys. Chem. C 120 (36) (2016) 20224–20231.

[12] P. Wang, S. M. Zakeeruddin, J.-E. Moser, M. Grätzel, A New Ionic Liquid Electrolyte Enhances the Conversion Efficiency of Dye-Sensitized Solar Cells, J. Phys. Chem. B 107 (48) (2003) 13280–13285.

[13] C. Pinilla, M. G. Del Pópolo, R. M. Lynden-Bell, J. Kohanoff, Structure and Dynamics of a Confined Ionic Liquid. Topics of Relevance to Dye-Sensitized Solar Cells, J. Phys. Chem. B 109 (38) (2005) 17922–17927.

[14] M. Bidikoudi, T. Stergiopoulos, V. Likodimos, G. E. Romanos, M. Francisco, B. Iliev, G. Adamová, T. J. S. Schubert, P. Falaras, Ionic Liquid Redox Electrolytes Based on Binary Mixtures of 1-Alkyl-Methylimidazolium Tricyanomethanide with 1-Methyl-3-Propylimidazolium Iodide and Implication In Dye-Sensitized Solar Cells, J. Mater. Chem. A 1 (35) (2013) 10474–13.

[15] J. L. Anthony, E. J. Maginn, J. F. Brennecke, Solubilities and Thermodynamic Properties of Gases in the Ionic Liquid 1-n-Butyl-3-methylimidazolium Hexafluorophosphate, J. Phys. Chem. B 106 (29) (2002) 7315–7320.

[16] J. E. Bara, T. K. Carlisle, C. J. Gabriel, D. Camper, A. Finotello, D. L. Gin, R. D. Noble, Guide to CO_2 Separations in Imidazolium-Based Room-Temperature Ionic Liquids, Ind. Eng. Chem. Res. 48 (6) (2009) 2739–2751.

[17] D. Almantariotis, S. Stevanovic, O. Fandiño, A. S. Pensado, A. A. H. Pádua, J. Y. Coxam, M. F. Costa Gomes, Absorption of Carbon Dioxide, Nitrous Oxide, Ethane and Nitrogen by 1-Alkyl-3-methylimidazolium ($C_n$mim, n= 2,4,6) Tris(pentafluoroethyl)trifluorophosphate Ionic Liquids (eFAP), J. Phys. Chem. B 116 (26) (2012) 7728–7738.

[18] Z. Lei, C. Dai, B. Chen, Gas Solubility in Ionic Liquids, Chem. Rev. 114 (2) (2013) 1289–1326.

[19] R. Hayes, G. G. Warr, R. Atkin, Structure and Nanostructure in Ionic Liquids, Chem. Rev. 115 (13) (2015) 6357–6426.

[20] A. Stark, K. R. Seddon, Ionic Liquids, 5th ed., Seidel, A. (Ed.), Kirk-Othmer Encyclopedia of Chemical Technology, vol. 26, Wiley, Hoboken, 2007.

[21] J. S. Wilkes, M. J. Zaworotko, Air and Water Stable 1-Ethyl-3-Methylimidazolium Based Ionic Liquids, J. Chem. Soc., Chem. Commun. 13 (1992) 965–967.

[22] Chem.info/news/2016/10/chevron-and-honeywell-switch-revolutionary-alkylation-technology.

[23] M. Abai, M. P. Atkins, A. Hassan, J. D. Holbrey, Y. Kuah, P. Nockemann, A. A. Oliferenko, N. V. Plechkova, S. Rafeen, A. A. Rahman, R. Ramli, S. M. Shariff,

K. R. Seddon, G. Srinivasan, Y. Zou, An Ionic Liquid Process For Mercury Removal From Natural Gas, Dalton Trans. 44 (18) (2015) 8617–8624.

[24] L. M. Sidisky, M. D. Buchanan, Supelco Patented Ionic Liquid GC Phase Technology, Supelco Reporter 26 (2008) 3–4.

[25] C. M. White, B. R. Strazisar, E. J. Granite, J. S. Hoffman, H. W. Pennline, Separation and Capture of CO_2 from Large Stationary Sources and Sequestration in Geological Formations—Coalbeds and Deep Saline Aquifers, J. Air Waste Manage. Assoc. 53 (6) (2003) 645–715.

[26] C. Cadena, J. L. Anthony, J. K. Shah, T. I. Morrow, J. F. Brennecke, E. J. Maginn, Why is CO_2 So Soluble in Imidazolium-Based Ionic Liquids?, J. Am. Chem. Soc. 126 (16) (2004) 5300–5308.

[27] J. L. Anderson, J. K. Dixon, J. F. Brennecke, Solubility of CO_2, CH_4, C_2H_6, C_2H_4, O_2, and N_2 in 1-Hexyl-3-methylpyridinium Bis(trifluoromethylsulfonyl)imide: Comparison to Other Ionic Liquids, Acc. Chem. Res. 40 (11) (2007) 1208–1216.

[28] M. J. Muldoon, S. N. V. K. Aki, J. L. Anderson, J. K. Dixon, J. F. Brennecke, Improving Carbon Dioxide Solubility in Ionic Liquids, J. Phys. Chem. B 111 (30) (2007) 9001–9009.

[29] I. Khan, K. A. Kurnia, F. Mutelet, S. P. Pinho, J. A. P. Coutinho, Probing the interactions between ionic liquids and water: Experimental and quantum chemical approach, J. Phys. Chem. B 118 (7) (2014) 1848–1860.

[30] I. Khan, M. Taha, P. Ribeiro-Claro, S. P. Pinho, J. A. P. Coutinho, Effect of the cation on the interactions between alkyl methyl imidazolium chloride ionic liquids and water, J. Phys. Chem. B 118 (35) (2014) 10503–10514.

[31] A. Stoppa, R. Buchner, G. Hefter, How Ideal are Binary Mixtures of Room-Temperature Ionic Liquids?, J. Mol. Liq. 153 (1) (2010) 46–51.

[32] A. M. Pinto, H. Rodríguez, Y. J. Colón, A. Arce Jr., A. Arce, A. Soto, Absorption of Carbon Dioxide in Two Binary Mixtures of Ionic Liquids, Ind. Eng. Chem. Res. 52 (17) (2013) 5975–5984.

[33] A. M. Pinto, H. Rodríguez, A. Arce, A. Soto, Carbon dioxide absorption in the ionic liquid 1-ethylpyridinium ethylsulfate and in its mixtures with another ionic liquid, Int. J. Greenhouse Gas Control 18 (2013) 296–304.

[34] A. M. Pinto, H. Rodríguez, A. Arce, A. Soto, Combined physical and chemical absorption of carbon dioxide in a mixture of ionic liquids, J. Chem. Thermodyn. 77 (C) (2014) 197–205.

[35] M. T. Clough, C. R. Crick, J. Gräsvik, P. A. Hunt, H. Niedermeyer, T. Welton, O. P. Whitaker, A Physicochemical Investigation of Ionic Liquid Mixtures, Chem. Sci. 00 (2) (2014) 1–14.

[36] P. Navia, J. Troncoso, L. Romaní, Excess Magnitudes for Ionic Liquid Binary Mixtures with a Common Ion, J. Chem. Eng. Data 52 (4) (2007) 1369–1374.

[37] H. Niedermeyer, J. P. Hallett, I. J. Villar-Garcia, P. A. Hunt, T. Welton, Mixtures of Ionic Liquids, Chem. Soc. Rev. 41 (23) (2012) 7780–23.

[38] G. Chatel, J. F. B. Pereira, V. Debbeti, H. Wang, R. D. Rogers, Mixing Ionic Liquids – "Simple Mixtures" or "Double Salts"?, Green Chem. 16 (4) (2014) 2051–33.

[39] R. W. Taft, M. J. Kamlet, The Solvatochromic Comparison Method. 2. The .Alpha.-Scale of Solvent Hydrogen-Bond Donor (HBD) Acidities, J. Am. Chem. Soc. 98 (10) (1976) 2886–2894.

[40] M. J. Kamlet, R. W. Taft, The Solvatochromic Comparison Method. I. The .Beta.-Scale of Solvent Hydrogen-Bond Acceptor (HBA) Basicities, J. Am. Chem. Soc. 98 (2) (1976) 377–383.

[41] R. Lungwitz, S. Spange, A Hydrogen Bond Accepting (HBA) Scale For Anions, Including Room Temperature Ionic Liquids, New J. Chem. 32 (3) (2008) 392–3.

[42] R. Lungwitz, V. Strehmel, S. Spange, The Dipolarity/Polarisability of 1-Alkyl-3-Methylimidazolium Ionic Liquids as Function of Anion Structure and The Alkyl Chain Length, New J. Chem. 34 (6) (2010) 1135–6.

[43] M. A. Ab Rani, A. Brant, L. Crowhurst, A. Dolan, M. Lui, N. H. Hassan, J. P. Hallett, P. A. Hunt, H. Niedermeyer, J. M. Perez-Arlandis, M. Schrems, T. Welton, R. Wilding, Understanding The Polarity of Ionic Liquids, Phys. Chem. Chem. Phys. 13 (37) (2011) 16831–10.

[44] H. Niedermeyer, C. Ashworth, A. Brandt, T. Welton, P. A. Hunt, A Step Towards The *a priori* Design of Ionic Liquids, Phys. Chem. Chem. Phys. 15 (27) (2013) 11566–13.

[45] R. P. Matthews, I. J. Villar-Garcia, C. C. Weber, J. Griffith, F. Cameron, J. P. Hallett, P. A. Hunt, T. Welton, A Structural Investigation of Ionic Liquid Mixtures, Phys. Chem. Chem. Phys. 18 (12) (2016) 8608–8624.

[46] H. Wang, S. P. Kelley, J. W. Brantley III, G. Chatel, J. Shamshina, J. F. B. Pereira, V. Debbeti, A. S. Myerson, R. D. Rogers, Ionic Fluids Containing Both Strongly and Weakly Interacting Ions of the Same Charge Have Unique Ionic and Chemical Environments as a Function of Ion Concentration, Chem. Phys. Chem. 16 (5) (2015) 993–1002.

[47] H. Passos, T. B. V. Dinis, A. F. M. Cláudio, M. G. Freire, J. A. P. Coutinho, Hydrogen Bond Basicity of Ionic Liquids and Molar Entropy of Hydration of

Salts as Major Descriptors In The Formation of Aqueous Biphasic Systems, Phys. Chem. Chem. Phys. 20 (20) (2018) 14234–14241.

[48] J. N. Canongia Lopes, T. C. Cordeiro, J. M. S. S. Esperança, H. J. R. Guedes, S. Huq, L. P. N. Rebelo, K. R. Seddon, Deviations from Ideality in Mixtures of Two Ionic Liquids Containing a Common Ion, J. Phys. Chem. B 109 (8) (2005) 3519–3525.

[49] E. T. Fox, J. E. F. Weaver, W. A. Henderson, Tuning Binary Ionic Liquid Mixtures: Linking Alkyl Chain Length to Phase Behavior and Ionic Conductivity, J. Phys. Chem. C 116 (8) (2012) 5270–5274.

[50] H. F. D. Almeida, J. N. Canongia Lopes, L. P. N. Rebelo, J. A. P. Coutinho, M. G. Freire, I. M. Marrucho, Densities and Viscosities of Mixtures of Two Ionic Liquids Containing a Common Cation, J. Chem. Eng. Data 61 (8) (2016) 2828–2843.

[51] M. Larriba, S. García, P. Navarro, J. García, F. Rodríguez, Physical Properties of N-Butylpyridinium Tetrafluoroborate and N-Butylpyridinium Bis(trifluoromethylsulfonyl)imide Binary Ionic Liquid Mixtures, J. Chem. Eng. Data 57 (4) (2012) 1318–1325.

[52] S. Aparicio, M. Atilhan, Mixed Ionic Liquids: The Case of Pyridinium-Based Fluids, J. Phys. Chem. B 116 (8) (2012) 2526–2537.

[53] G. García, M. Atilhan, S. Aparicio, Interfacial Properties of Double Salt Ionic Liquids: A Molecular Dynamics Study, J. Phys. Chem. C 119 (51) (2015) 28405–28416.

[54] R. S. Payal, S. Balasubramanian, Homogenous mixing of ionic liquids: molecular dynamics simulations, Phys. Chem. Chem. Phys. 15 (48) (2013) 21077–7.

[55] K. Shimizu, M. Tariq, L. P. N. Rebelo, J. N. C. Lopes, Binary mixtures of ionic liquids with a common ion revisited: A molecular dynamics simulation study, J. Mol. Liq. 153 (1) (2010) 52–56.

[56] D. Xiao, J. R. Rajian, S. Li, R. A. Bartsch, E. L. Quitevis, Additivity in the Optical Kerr Effect Spectra of Binary Ionic Liquid Mixtures: Implications for Nanostructural Organization, J. Phys. Chem. B 110 (33) (2006) 16174–16178.

[57] M. Ramdin, T. W. de Loos, T. J. H. Vlugt, State-of-the-Art of CO_2 Capture with Ionic Liquids, Ind. Eng. Chem. Res. 51 (24) (2012) 8149–8177.

[58] S. Zeng, X. Zhang, L. Bai, X. Zhang, H. Wang, J. Wang, D. Bao, M. Li, X. Liu, S. Zhang, Ionic-Liquid-Based CO_2 Capture Systems: Structure, Interaction and Process, Chem. Rev. 117 (14) (2017) 9625–9673.

[59] J. L. Anderson, J. K. Dixon, J. F. Brennecke, Solubility of CO_2, CH_4, C_2H_6, C_2H_4, O_2, and N_2 in 1-Hexyl-3-methylpyridinium Bis(trifluoromethylsulfonyl)imide: Comparison to Other Ionic Liquids, Acc. Chem. Res. 40 (11) (2007) 1208–1216.

[60] J. Palomar, M. Gonzalez-Miquel, A. Polo, F. Rodríguez, Understanding the Physical Absorption of CO 2in Ionic Liquids Using the COSMO-RS Method, Ind. Eng. Chem. Res. 50 (6) (2011) 3452–3463.

[61] Z. Lei, J. Yuan, J. Zhu, Solubility of CO_2 in Propanone, 1-Ethyl-3-methylimidazolium Tetrafluoroborate, and Their Mixtures †, J. Chem. Eng. Data 55 (10) (2010) 4190–4194.

[62] T. K. Carlisle, J. E. Bara, C. J. Gabriel, R. D. Noble, D. L. Gin, Interpretation of CO_2 Solubility and Selectivity in Nitrile-Functionalized Room-Temperature Ionic Liquids Using a Group Contribution Approach, Ind. Eng. Chem. Res. 47 (18) (2008) 7005–7012.

[63] R. E. Baltus, B. H. Culbertson, S. Dai, H. Luo, D. W. DePaoli, Low-Pressure Solubility of Carbon Dioxide in Room-Temperature Ionic Liquids Measured with a Quartz Crystal Microbalance, J. Phys. Chem. B 108 (2) (2004) 721–727.

[64] Z. Lei, J. Han, B. Zhang, Q. Li, J. Zhu, B. Chen, Solubility of CO_2 in Binary Mixtures of Room-Temperature Ionic Liquids at High Pressures, J. Chem. Eng. Data 57 (8) (2012) 2153–2159.

[65] M. B. Shiflett, A. Yokozeki, Phase Behavior of Carbon Dioxide in Ionic Liquids: [emim][Acetate], [emim][Trifluoroacetate], and [emim][Acetate] + [emim][Trifluoroacetate] Mixtures, J. Chem. Eng. Data 54 (1) (2009) 108–114.

[66] D. G. Hert, J. L. Anderson, S. N. V. K. Aki, J. F. Brennecke, Enhancement of Oxygen and Methane Solubility in 1-Hexyl-3-Methylimidazolium Bis(Trifluoromethylsulfonyl) Imide Using Carbon Dioxide, Chem. Commun. 39 (20) (2005) 2603–3.

[67] M. B. Shiflett, A. M. S. Niehaus, A. Yokozeki, Separation of N_2O and CO_2 Using Room-Temperature Ionic Liquid [bmim][BF_4], J. Phys. Chem. B 115 (13) (2011) 3478–3487.

[68] M. B. Shiflett, A. M. S. Niehaus, A. Yokozeki, Separation of CO_2 and H_2S Using Room-Temperature Ionic Liquid [bmim][$MeSO_4$], J. Chem. Eng. Data 55 (11) (2010) 4785–4793.

[69] M. Solinas, A. Pfaltz, P. G. Cozzi, W. Leitner, Enantioselective Hydrogenation of Imines in Ionic Liquid/Carbon Dioxide Media, J. Am. Chem. Soc. 126 (49) (2004) 16142–16147.

[70] A. Yokozeki, M. B. Shiflett, Vapor–Liquid Equilibria of Ammonia + Ionic Liquid Mixtures, Appl. Energy 84 (12) (2007) 1258–1273.

[71] V. A. Toussaint, E. Kühne, A. Shariati, C. J. Peters, Solubility Measurements of Hydrogen In 1-Butyl-3-Methylimidazolium Tetrafluoroborate and The Effect of Carbon Dioxide and A Selected Catalyst On The Hydrogen Solubility in The Ionic Liquid, J. Chem. Thermodyn. 59 (C) (2013) 239–242.

[72] W. Shi, E. J. Maginn, Molecular Simulation and Regular Solution Theory Modeling of Pure and Mixed Gas Absorption in the Ionic Liquid 1-n-Hexyl-3-methylimidazolium Bis(Trifluoromethylsulfonyl)amide ([hmim][Tf_2N]), J. Phys. Chem. B 112 (51) (2008) 16710–16720.

[73] S. Budhathoki, J. K. Shah, E. J. Maginn, Molecular Simulation Study of the Solubility, Diffusivity and Permselectivity of Pure and Binary Mixtures of CO_2 and CH_4 in the Ionic Liquid 1-n-Butyl-3-methylimidazolium bis(trifluoromethylsulfonyl)imide, Ind. Eng. Chem. Res. 54 (35) (2015) 8821–8828.

[74] S. Budhathoki, J. K. Shah, E. J. Maginn, Molecular Simulation Study of the Performance of Supported Ionic Liquid Phase Materials for the Separation of Carbon Dioxide from Methane and Hydrogen, Ind. Eng. Chem. Res. 56 (23) (2017) 6775–6784.

[75] A. Finotello, J. E. Bara, S. Narayan, D. Camper, R. D. Noble, Ideal Gas Solubilities and Solubility Selectivities in a Binary Mixture of Room-Temperature Ionic Liquids, J. Phys. Chem. B 112 (8) (2008) 2335–2339.

[76] L. C. Tomé, D. J. S. Patinha, C. S. R. Freire, L. P. N. Rebelo, I. M. Marrucho, CO_2 Separation Applying Ionic Liquid Mixtures: The Effect of Mixing Different Anions on Gas Permeation Through Supported Ionic Liquid Membranes, RSC Advances 3 (30) (2013) 12220–10.

[77] L. C. Tomé, C. Florindo, C. S. R. Freire, L. P. N. Rebelo, I. M. Marrucho, Playing with Ionic Liquid Mixtures To Design Engineered CO_2 Separation Membranes, Phys. Chem. Chem. Phys. 16 (32) (2014) 17172–11.

[78] M. Kanakubo, T. Makino, T. Umecky, CO_2 Solubility In And Physical Properties For Ionic Liquid Mixtures of 1-Butyl-3-Methylimidazolium Acetate and 1-Butyl-3-Methylimidazolium Bis(Trifluoromethanesulfonyl)Amide, J. Mol. Liq. 217 (C) (2016) 112–119.

[79] A. M. Pinto, H. Rodríguez, A. Arce, A. Soto, Combined Physical and Chemical Absorption of Carbon Dioxide in A Mixture of Ionic Liquids, J. Chem. Thermodyn. 77 (C) (2014) 197–205.

[80] M. B. Shiflett, A. Yokozeki, Phase Behavior of Carbon Dioxide in Ionic Liquids: [emim][Acetate], [emim][Trifluoroacetate], and [emim][Acetate] + [emim][Trifluoroacetate] Mixtures, J. Chem. Eng. Data 54 (1) (2009) 108–114.

[81] T. L. Greaves, C. J. Drummond, Solvent Nanostructure, The Solvophobic Effect And Amphiphile Self-Assembly In Ionic Liquids, Chem. Soc. Rev. 42 (3) (2013) 1096–1120.

[82] U. Schröder, J. D. Wadhawan, R. G. Compton, F. Marken, P. A. Z. Suarez, C. S. Consorti, R. F. de Souza, J. Dupont, Water-Induced Accelerated Ion Diffusion: Voltammetric Studies In 1-Methyl-3-[2,6-(S)-Dimethylocten-2-Yl]Imidazolium Tetrafluoroborate, 1-Butyl-3-Methylimidazolium Tetrafluoroborate and Hexafluorophosphate Ionic Liquids, New J. Chem. 24 (12) (2000) 1009–1015.

[83] C. M. Gordon, J. D. Holbrey, A. R. Kennedy, K. R. Seddon, Ionic Liq. Cryst.: Hexafluorophosphate Salts, J. Mater. Chem. 8 (12) (1998) 2627–2636.

[84] J. D. Holbrey, K. R. Seddon, The Phase Behaviour of 1-Alkyl-3-methylimidazolium Tetrafluoroborates; Ionic Liquids and Ionic Liq. Cryst., J. Chem. Soc., Dalton Trans. 13 (1999) 2133–2140.

[85] A. Triolo, O. Russina, H.-J. Bleif, E. Di Cola, Nanoscale Segregation in Room Temperature Ionic Liquids †, J. Phys. Chem. B 111 (18) (2007) 4641–4644.

[86] O. Russina, L. Gontrani, B. Fazio, D. Lombardo, A. Triolo, R. Caminiti, Selected Chemical–Physical Properties and Structural Heterogeneities in 1-Ethyl-3-methylimidazolium Alkyl-Sulfate Room Temperature Ionic Liquids, Chem. Phys. Lett. 493 (4-6) (2010) 259–262.

[87] E. Bodo, M. Chiricotto, R. Caminiti, Structure of Geminal Imidazolium Bis(trifluoromethylsulfonyl)imide Dicationic Ionic Liquids: A Theoretical Study of the Liquid Phase, J. Phys. Chem. B 115 (49) (2011) 14341–14347.

[88] B. Aoun, A. Goldbach, M. A. González, S. Kohara, D. L. Price, M.-L. Saboungi, Nanoscale Heterogeneity in Alkyl-Methylimidazolium Bromide Ionic Liquids, J. Chem. Phys. 134 (10) (2011) 104509–8.

[89] C. S. Santos, N. S. Murthy, G. A. Baker, E. W. Castner, Communication: X-Ray Scattering from Ionic Liquids with Pyrrolidinium Cations, J. Chem. Phys. 134 (12) (2011) 121101–5.

[90] C. S. Santos, H. V. R. Annapureddy, N. S. Murthy, H. K. Kashyap, E. W. Castner, C. J. Margulis, Temperature-Dependent Structure of Methyltributylammonium Bis(Trifluoromethylsulfonyl)Amide: X Ray Scattering and Simulations, J. Chem. Phys. 134 (6) (2011) 064501–11.

[91] O. Russina, A. Triolo, L. Gontrani, R. Caminiti, Mesoscopic Structural Heterogeneities in Room-Temperature Ionic Liquids, J. Phys. Chem. Lett. 3 (1) (2012) 27–33.

[92] M. Macchiagodena, F. Ramondo, A. Triolo, L. Gontrani, R. Caminiti, Liquid Structure of 1-Ethyl-3-methylimidazolium Alkyl Sulfates by X-ray Scattering and Molecular Dynamics, J. Phys. Chem. B 116 (45) (2012) 13448–13458.

[93] A. Triolo, O. Russina, R. Caminiti, H. Shirota, H. Y. Lee, C. S. Santos, N. S. Murthy, E. W. Castner Jr, Comparing Intermediate Range Order for Alkyl- Vs. Ether-Substituted Cations in Ionic Liquids, Chem. Commun. 48 (41) (2012) 4959–4.

[94] O. Russina, A. Triolo, New Experimental Evidence Supporting the Mesoscopic Segregation Model in Room Temperature Ionic Liquids, Faraday Discuss. 154 (2012) 97–109.

[95] C. Hardacre, J. D. Holbrey, C. L. Mullan, T. G. A. Youngs, D. T. Bowron, Small Angle Neutron Scattering from 1-Alkyl-3-methylimidazolium Hexafluorophosphate Ionic Liquids ([CnMim][Pf6], n=4, 6, And 8), J. Chem. Phys. 133 (7) (2010) 074510–8.

[96] M. Macchiagodena, L. Gontrani, F. Ramondo, A. Triolo, R. Caminiti, Liquid Structure of 1-Alkyl-3-methylimidazolium-Hexafluorophosphates by Wide Angle X-Ray and Neutron Scattering and Molecular Dynamics, J. Chem. Phys. 134 (11) (2011) 114521–16.

[97] R. Hayes, S. Imberti, G. G. Warr, R. Atkin, Pronounced Sponge-Like Nanostructure in Propylammonium Nitrate, PCCP 13 (30) (2011) 13544–8.

[98] K. Fujii, R. Kanzaki, T. Takamuku, Y. Kameda, S. Kohara, M. Kanakubo, M. Shibayama, S.-i. Ishiguro, Y. Umebayashi, Experimental Evidences for Molecular Origin of Low-Q Peak in Neutron/X-Ray Scattering of 1-Alkyl-3-methylimidazolium Bis(Trifluoromethanesulfonyl)Amide Ionic Liquids, J. Chem. Phys. 135 (24) (2011) 244502–12.

[99] M. Kofu, M. Nagao, T. Ueki, Y. Kitazawa, Y. Nakamura, S. Sawamura, M. Watanabe, O. Yamamuro, Heterogeneous Slow Dynamics of Imidazolium-Based Ionic Liquids Studied by Neutron Spin Echo, J. Phys. Chem. B 117 (9) (2013) 2773–2781.

[100] T. Burankova, R. Hempelmann, A. Wildes, J. P. Embs, Collective Ion Diffusion and Localized Single Particle Dynamics in Pyridinium-Based Ionic Liquids, J. Phys. Chem. B 118 (49) (2014) 14452–14460.

[101] H. V. R. Annapureddy, H. K. Kashyap, P. M. De Biase, C. J. Margulis, What is the Origin of the Prepeak in the X-ray Scattering of Imidazolium-Based Room-Temperature Ionic Liquids?, J. Phys. Chem. B 114 (50) (2010) 16838–16846.

[102] K. Shimizu, C. E. S. Bernardes, J. N. Canongia Lopes, Structure and Aggregation in the 1-Alkyl-3-Methylimidazolium Bis(trifluoromethylsulfonyl)imide Ionic Liquid Homologous Series, J. Phys. Chem. B 118 (2) (2014) 567–576.

[103] K. Shimizu, J. N. C. Lopes, Probing the Structural Features of the 1-Alkyl-3-methylimidazolium Hexafluorophosphate Ionic Liquid Series Using Molecular Dynamics Simulations, J. Mol. Liq. 210 (PB) (2015) 257–263.

[104] K. Shimizu, A. A. Freitas, J. N. C. Lopes, Structural Characterization of the [CnC1im][C4F9SO3] Ionic Liquid Series: Alkyl Versus Perfluoroalkyl Side Chains, J. Mol. Liq. (2016) 1–7.

[105] Y. Ji, R. Shi, Y. Wang, G. Saielli, Effect of the Chain Length on the Structure of Ionic Liquids: from Spatial Heterogeneity to Ionic Liq. Cryst., J. Phys. Chem. B 117 (4) (2013) 1104–1109.

[106] H. K. Kashyap, J. J. Hettige, H. V. R. Annapureddy, C. J. Margulis, Saxs Anti-Peaks Reveal the Length-Scales of Dual Positive–Negative and Polar–Apolar

Ordering in Room-Temperature Ionic Liquids, Chem. Commun. 48 (42) (2012) 5103–4.

[107] H. K. Kashyap, C. S. Santos, N. S. Murthy, J. J. Hettige, K. Kerr, S. Ramati, J. Gwon, M. Gohdo, S. I. Lall-Ramnarine, J. F. Wishart, C. J. Margulis, E. W. Castner Jr, Structure of 1-Alkyl-1-methylpyrrolidinium Bis(trifluoromethylsulfonyl)amide Ionic Liquids with Linear, Branched, and Cyclic Alkyl Groups, J. Phys. Chem. B 117 (49) (2013) 15328–15337.

[108] K. Shimizu, A. A. H. Pádua, J. N. Canongia Lopes, Nanostructure of Trialkylmethylammonium Bistriflamide Ionic Liquids Studied by Molecular Dynamics, J. Phys. Chem. B 114 (47) (2010) 15635–15641.

[109] J. J. Hettige, H. K. Kashyap, H. V. R. Annapureddy, C. J. Margulis, Anions, the Reporters of Structure in Ionic Liquids, J. Phys. Chem. Lett. 4 (1) (2013) 105–110.

[110] H. K. Kashyap, C. S. Santos, H. V. R. Annapureddy, N. S. Murthy, C. J. Margulis, E. W. Castner Jr, Temperature-Dependent Structure of Ionic Liquids: X-Ray Scattering and Simulations, Faraday Discuss. 154 (2012) 133–143.

[111] J. J. Hettige, H. K. Kashyap, C. J. Margulis, Communication: Anomalous Temperature Dependence of the Intermediate Range Order in Phosphonium Ionic Liquids, J. Chem. Phys. 140 (11) (2014) 111102–5.

[112] M. Blesic, M. Swadźba-Kwaśny, J. D. Holbrey, J. N. Canongia Lopes, K. R. Seddon, L. P. N. Rebelo, New Catanionic Surfactants Based on 1-Alkyl-3-methylimidazolium Alkylsulfonates, $[C_nH_{2n+1}mim][C_mH_{2m+1}SO_3]$: Mesomorphism and Aggregation, Phys. Chem. Chem. Phys. 11 (21) (2009) 4260–9.

[113] A. J. L. Costa, J. M. S. S. Esperança, I. M. Marrucho, L. P. N. Rebelo, Densities and Viscosities of 1-Ethyl-3-methylimidazolium n-Alkyl Sulfates, J. Chem. Eng. Data 56 (8) (2011) 3433–3441.

[114] F. M. Gaciño, T. Regueira, L. Lugo, M. J. P. Comuñas, J. Fernández, Influence of Molecular Structure on Densities and Viscosities of Several Ionic Liquids, J. Chem. Eng. Data 56 (12) (2011) 4984–4999.

[115] M. Blesic, M. Swadźba-Kwaśny, T. Belhocine, H. Q. N. Gunaratne, J. N. C. Lopes, M. F. C. Gomes, A. A. H. Pádua, K. R. Seddon, L. P. N. Rebelo, 1-Alkyl-3-methylimidazolium Alkanesulfonate Ionic Liquids,$[C_nH_{2n+1}mim][C_kH_{2k+1}SO_3]$: Synthesis and Physicochemical Properties, Phys. Chem. Chem. Phys. 11 (39) (2009) 8939–10.

[116] M. J. Dávila, S. Aparicio, R. Alcalde, B. García, J. M. Leal, On the Properties of 1-Butyl-3-methylimidazolium Octylsulfate Ionic Liquid, Green Chem. 9 (3) (2007) 221–232.

[117] J. C. Araque, J. J. Hettige, C. J. Margulis, Modern Room Temperature Ionic Liquids, a Simple Guide to Understanding Their Structure and How It May Relate to Dynamics., J. Phys. Chem. B 119 (40) (2015) 12727–12740.

[118] Y. Wang, G. A. Voth, Unique Spatial Heterogeneity in Ionic Liquids, J. Am. Chem. Soc. 127 (35) (2005) 12192–12193.

[119] Y. Wang, G. A. Voth, Tail Aggregation and Domain Diffusion in Ionic Liquids, J. Phys. Chem. B 110 (37) (2006) 18601–18608.

[120] Y. Wang, W. Jiang, G. A. Voth, Spatial Heterogeneity in Ionic Liquids, J. Phys. Chem. B 110 (2006) 18601–18608.

[121] S. M. Urahata, M. C. C. Ribeiro, Structure of ionic liquids of 1-alkyl-3-methylimidazolium cations: A systematic computer simulation study, J. Chem. Phys. 120 (4) (2004) 1855–1863.

[122] J. N. A. Canongia Lopes, A. A. H. Pádua, Nanostructural Organization in Ionic Liquids, J. Phys. Chem. B 110 (7) (2006) 3330–3335.

[123] C. E. S. Bernardes, K. Shimizu, A. I. M. C. Lobo Ferreira, L. M. N. B. F. Santos, J. N. Canongia Lopes, Structure and Aggregation in the 1,3-Dialkylimidazolium Bis(trifluoromethylsulfonyl)imide Ionic Liquid Family: 2. From Single to Dou[C_{12}mim]$^+$ Long Alkyl Side Chains, J. Phys. Chem. B 118 (24) (2014) 6885–6895.

[124] K. Shimizu, M. F. C. Gomes, A. A. H. Pádua, L. P. N. Rebelo, J. N. C. Lopes, Three Commentaries on the Nano-Segregated Structure of Ionic Liquids, J. Mol. Struct.: Theochem. 946 (1-3) (2010) 70–76.

[125] J. D. Holbrey, W. M. Reichert, R. P. Swatloski, G. A. Broker, W. R. Pitner, K. R. Seddon, R. D. Rogers, Efficient, Halide Free Synthesis of New, Low Cost Ionic Liquids: 1,3-Dialkylimidazolium Salts Containing Methyl- and Ethyl-Sulfate Anions, Green Chem. 4 (5) (2002) 407–413.

[126] W. D. Amith, J. J. Hettige, E. W. Castner Jr., C. J. Margulis, Structures of Ionic Liquids Having Both Anionic and Cationic Octyl Tails: Lamellar Vacuum Interface vs Sponge-Like Bulk Order, J. Phys. Chem. Lett. 7 (19) (2016) 3785–3790.

[127] O. Russina, F. Lo Celso, N. V. Plechkova, A. Triolo, Emerging Evidences of Mesoscopic-Scale Complexity in Neat Ionic Liquids and Their Mixtures, J. Phys. Chem. Lett. (2017) 1197–1204.

[128] P. Lozano, J. M. Bernal, E. Garcia-Verdugo, G. Sanchez-Gomez, M. Vaultier, M. I. Burguete, S. V. Luis, Sponge-Like Ionic Liquids: A New Platform For Green Biocatalytic Chemical Processes, Green Chem. 17 (7) (2015) 3706–3717.

[129] P. Lozano, J. M. Bernal, R. Piamtongkam, D. Fetzer, M. Vaultier, One-Phase Ionic Liquid Reaction Medium for Biocatalytic Production of Biodiesel, Chem. Sus. Chem. 3 (12) (2010) 1359–1363.

[130] E. J. González, P. Navarro, M. Larriba, J. García, F. Rodríguez, A Comparative Study of Pure Ionic Liquids and Their Mixtures as Potential Mass Agents in The Separation of Hydrocarbons, J. Mol. Liq. 222 (C) (2016) 118–124.

[131] P. Navarro, M. Larriba, J. García, F. Rodríguez, Vapor–Liquid Equilibria for (n-Hexane, n-Octane, Cyclohexane, or 2,3-Dimethylpentane) + Toluene + [4empy][Tf 2N] (0.3) + [emim][DCA] (0.7) Mixed Ionic Liquids, J. Chem. Eng. Data 61 (7) (2016) 2440–2449.

[132] P. Navarro, M. Larriba, J. García, F. Rodríguez, Vapor-liquid equilibria for n-heptane + (benzene, toluene, p-xylene, or ethylbenzene) + [4empy][Tf2N] (0.3) + [emim][DCA] (0.7) binary ionic liquid mixture, Fluid Phase Equilib. 417 (C) (2016) 41–49.

[133] J. M. Crosthwaite, S. N. V. K. Aki, E. J. Maginn, J. F. Brennecke, Liquid Phase Behavior of Imidazolium-Based Ionic Liquids With Alcohols: Effect of Hydrogen Bonding and Non-Polar Interactions, Fluid Phase Equilib. 228-229 (2005) 303–309.

[134] M. G. Freire, P. J. Carvalho, R. L. Gardas, I. M. Marrucho, L. M. N. B. F. Santos, J. A. P. Coutinho, Mutual Solubilities of Water and the $[C_n\text{nmim}][Tf_2N]$ Hydrophobic Ionic Liquids, J. Phys. Chem. B 112 (6) (2008) 1604–1610.

[135] A. Chapeaux, L. D. Simoni, M. A. Stadtherr, J. F. Brennecke, Liquid Phase Behavior of Ionic Liquids with Water and 1-Octanol and Modeling of 1-Octanol/Water Partition Coefficients, J. Chem. Eng. Data 52 (6) (2007) 2462–2467.

[136] J. Anthony, E. Maginn, J. Brennecke, Solution Thermodynamics of Imidazolium-Based Ionic Liquids And Water, J. Phys. Chem. B 105 (44) (2001) 10942–10949.

[137] G. Raabe, J. Köhler, Thermodynamical And Structural Properties of Binary Mixtures of Imidazolium Chloride Ionic Liquids And Alcohols From Molecular Simulation, J. Chem. Phys. 129 (2008) 144503.

[138] S. Jahangiria, M. Taghikhanib, H. Behnejada, S. Ahmadib, Theoretical Investigation of Imidazolium Based Ionic Liquid/Alcohol Mixture: A Molecular Dynamic Simulation, Mol. Phys. 106 (8) (2008) 1015–1023.

[139] J. Carrete, T. Méndez-Morales, Ó. Cabeza, R. M. Lynden-Bell, L. J. Gallego, L. M. Varela, Investigation of the Local Structure of Mixtures of an Ionic Liquid with Polar Molecular Species through Molecular Dynamics: Cluster Formation and Angular Distributions, J. Phys. Chem. B 116 (20) (2012) 5941–5950.

[140] T. L. Greaves, D. F. Kennedy, N. Kirby, C. J. Drummond, Nanostructure Changes in Protic Ionic Liquids (PILs) Through Adding Solutes and Mixing PILs, Phys. Chem. Chem. Phys. 13 (30) (2011) 13501.

[141] O. Russina, A. Sferrazza, R. Caminiti, A. Triolo, Amphiphile Meets Amphiphile: Beyond the Polar–Apolar Dualism in Ionic Liquid/Alcohol Mixtures, J. Phys. Chem. Lett. (2014) 1738–1742.

[142] N. Sieffert, G. Wipff, Adsorption at The Liquid-Liquid Interface in The Biphasic Rhodium-Catalyzed Hydroformylation of 1-Hexene In Ionic Liquids: A Molecular Dynamics Study, J. Phys. Chem. C 112 (16) (2008) 6450–6461.

[143] L. Cammarata, S. Kazarian, P. Salter, T. Welton, Molecular States of Water In Room Temperature Ionic Liquids, Phys. Chem. Chem. Phys. 3 (23) (2001) 5192–5200.

[144] S. Saha, H. O. Hamaguchi, Effect of Water on The Molecular Structure and Arrangement of Nitrile-Functionalized Ionic Liquids, J. Phys. Chem. B 110 (6) (2006) 2777–2781.

[145] A.-L. Rollet, P. Porion, M. Vaultier, I. Billard, M. Deschamps, C. Bessada, L. Jouvensal, Anomalous Diffusion of Water in [BMIM][TFSI] Room-Temperature Ionic Liquid, J. Phys. Chem. B 111 (41) (2007) 11888–11891.

[146] Y. Xu, Y. Gao, L. Zhang, J. Yao, C. Wang, H. Li, Microscopic Structures of Ionic Liquids 1-Ethyl-3-Methylimidazolium Tetrafluoroborate in Water Probed by The Relative Chemical Shift, Sci. China, Ser. B 53 (7) (2010) 1561–1565.

[147] A. Stark, A. W. Zidell, M. M. Hoffmann, Is the Ionic Liquid 1-ethyl-3-methylimidazolium methanesulfonate [emim][$MeSO_3$] Capable of Rigidly Binding Water?, J. Mol. Liq. 160 (3) (2011) 166–179.

[148] U. Salma, N. V. Plechkova, R. Caminiti, L. Gontrani, The Opposite Effect of Water and N-Methyl-2-Pyrrolidone Cosolvents on the Nanostructural Organization of Ethylammonium Butanoate Ionic Liquid: A Small- and Wide-Angle X-Ray Scattering and Molecular Dynamics Simulations Study, J. Phys. Chem. B 121 (26) (2017) 6399–6407.

[149] C. E. S. Bernardes, M. E. Minas da Piedade, J. N. Canongia Lopes, The Structure of Aqueous Solutions of a Hydrophilic Ionic Liquid: The Full Concentration

Range of 1-Ethyl-3-methylimidazolium Ethylsulfate and Water, J. Phys. Chem. B 115 (9) (2011) 2067–2074.

[150] B. Bhargava, M. Klein, Initial stages of aggregation in aqueous solutions of ionic liquids: Molecular dynamics studies, J. Phys. Chem. B 113 (2009) 9499–9505.

[151] B. L. Bhargava, M. L. Klein, Formation of Interconnected Aggregates in Aqueous Dicationic Ionic Liquid Solutions, J. Chem. Theory Comput. 6 (3) (2010) 873–879.

[152] B. Bhargava, M. Klein, Aqueous Solutions of Imidazolium Ionic Liquids: Molecular Dynamics Studies, Soft Matter 5 (18) (2009) 3475–3480.

[153] C. E. S. Bernardes, K. Shimizu, J. N. Canongia Lopes, Solvent Effects on the Polar Network of Ionic Liquid Solutions, J. Phys.: Condens. Matter 27 (19) (2015) 194116–13.

[154] B. L. Bhargava, Y. Yasaka, M. L. Klein, Computational Studies of Room Temperature Ionic Liquid-Water Mixtures, Chem. Commun. 47 (22) (2011) 6228–6241.

[155] S. D. Nickerson, E. M. Nofen, H. Chen, M. Ngan, B. Shindel, H. Yu, L. L. Dai, A Combined Experimental and Molecular Dynamics Study of Iodide-Based Ionic Liquid and Water Mixtures., J. Phys. Chem. B 119 (28) (2015) 8764–8772.

[156] X. Zhong, Z. Fan, Z. Liu, D. Cao, Local Structure Evolution and its Connection to Thermodynamic and Transport Properties of 1-Butyl-3-methylimidazolium Tetrafluoroborate and Water Mixtures by Molecular Dynamics Simulations, J. Phys. Chem. B 116 (10) (2012) 3249–3263.

[157] S. Feng, G. A. Voth, Molecular Dynamics Simulations of Imidazolium-Based Ionic Liquid/Water Mixtures: Alkyl Side Chain Length and Anion Effects, Fluid Phase Equilib. 294 (1-2) (2010) 148–156.

[158] P. D'Angelo, A. Zitolo, G. Aquilanti, V. Migliorati, Using a Combined Theoretical and Experimental Approach to Understand the Structure and Dynamics of Imidazolium-Based Ionic Liquids/Water Mixtures. 2. EXAFS Spectroscopy, J. Phys. Chem. B 117 (41) (2013) 12516–12524.

[159] K. R. Ramya, P. Kumar, A. Kumar, A. Venkatnathan, Interplay of Phase Separation, Tail Aggregation, and Micelle Formation in the Nanostructured Organization of Hydrated Imidazolium Ionic Liquid, J. Phys. Chem. B 118 (29) (2014) 8839–8847.

[160] C. Jungnickel, J. Łuczak, J. Ranke, J. F. Fernández, A. Müller, J. Thöming, Micelle formation of imidazolium ionic liquids in aqueous solution, Colloids Surf. A-Physicochemical And Eng. Aspects 316 (1-3) (2008) 278–284.

[161] P. Yee, J. K. Shah, E. J. Maginn, State of Hydrophobic and Hydrophilic Ionic Liquids in Aqueous Solutions: Are the Ions Fully Dissociated?, J. Phys. Chem. B 117 (41) (2013) 12556–12566.

[162] A. P. Singh, R. L. Gardas, S. Senapati, How Water Manifests The Structural Regimes In Ionic Liquids, Soft Matter 13 (2017) 2348–2361.

[163] J. A. Widegren, J. W. Magee, Density, Viscosity, Speed of Sound, and Electrolytic Conductivity for the Ionic Liquid 1-Hexyl-3-methylimidazolium Bis(trifluoromethylsulfonyl)imide and Its Mixtures with Water †, J. Chem. Eng. Data 52 (6) (2007) 2331–2338.

[164] J. Widegren, E. Saurer, K. Marsh, J. Magee, Electrolytic conductivity of four imidazolium-based room-temperature ionic liquids and the effect of a water impurity, J. Chem. Thermodyn. 37 (6) (2005) 569–575.

[165] J. A. Widegren, A. Laesecke, J. W. Magee, The effect of dissolved water on the viscosities of hydrophobic room-temperature ionic liquids, Chem. Commun. 99 (12) (2005) 1610–1612.

[166] K. Seddon, A. Stark, M. Torres, Influence of Chloride, Water, and Organic Solvents on The Physical Properties of Ionic Liquids, in: Pure Appl. Chem., Queens Univ Belfast, QUILL Ctr, Belfast BT9 5AG, Antrim, North Ireland, 2000, pp. 2275–2287.

[167] R. Vashishat, R. Sanan, D. Ray, V. K. Aswal, R. K. Mahajan, Biamphiphilic Ionic Liquids-Drug Mixtures: Interactional and Morphological Aspects, Chem. Sel. 3 (25) (2018) 7089–7099.

[168] R. Sanan, T. S. Kang, R. K. Mahajan, Complexation, Dimerisation And Solubilisation of Methylene Blue In The Presence Of Biamphiphilic Ionic Liquids: A Detailed Spectroscopic And Electrochemical Study, Phys. Chem. Chem. Phys. 16 (12) (2014) 5667–11.

[169] P. Bharmoria, K. S. Rao, T. J. Trivedi, A. Kumar, Biamphiphilic Ionic Liquid Induced Folding Alterations in the Structure of Bovine Serum Albumin in Aqueous Medium, J. Phys. Chem. B 118 (1) (2013) 115–124.

[170] P. Bharmoria, M. J. Mehta, I. Pancha, A. Kumar, Structural and Functional Stability of Cellulase in Aqueous-Biamphiphilic Ionic Liquid Surfactant Solution, J. Phys. Chem. B 118 (33) (2014) 9890–9899.

[171] K. S. Rao, T. J. Trivedi, A. Kumar, Aqueous-Biamphiphilic Ionic Liquid Systems: Self-Assembly and Synthesis of Gold Nanocrystals/Microplates, J. Phys. Chem. B 116 (49) (2012) 14363–14374.

[172] K. Thakkar, B. Bharatiya, V. K. Aswal, P. Bahadur, Aggregation of 1-Alkyl-3-Methylimidazolium Octylsulphate Ionic Liquids and their Interaction with Triton X-100 Micelles, RSC Advances 6 (84) (2016) 80585–80594.

[173] J. N. Canongia Lopes, J. Deschamps, A. A. H. Pádua, Modeling Ionic Liquids Using a Systematic All-Atom Force Field, J. Phys. Chem. B 108 (30) (2004) 11250–11250.

[174] J. N. Canongia Lopes, A. A. H. Pádua, Molecular Force Field for Ionic Liquids Composed of Triflate or Bistriflylimide Anions, J. Phys. Chem. B 108 (43) (2004) 16893–16898.

[175] J. N. Canongia Lopes, A. A. H. Pádua, Molecular Force Field for Ionic Liquids III: Imidazolium, Pyridinium, and Phosphonium Cations; Chloride, Bromide, and Dicyanamide Anions, J. Phys. Chem. B 110 (39) (2006) 19586–19592.

[176] J. N. Canongia Lopes, A. A. H. Pádua, K. Shimizu, Molecular Force Field for Ionic Liquids IV: Trialkylimidazolium and Alkoxycarbonyl-Imidazolium Cations; Alkylsulfonate and Alkylsulfate Anions, J. Phys. Chem. B 112 (16) (2008) 5039–5046.

[177] S. V. Sambasivarao, O. Acevedo, Development of OPLS-AA Force Field Parameters for 68 Unique Ionic Liquids, J. Chem. Theory Comput. 5 (4) (2009) 1038–1050.

[178] B. Doherty, X. Zhong, S. Gathiaka, B. Li, O. Acevedo, Revisiting OPLS Force Field Parameters for Ionic Liquid Simulations, J. Chem. Theory Comput. 13 (12) (2017) 6131–6145.

[179] B. Doherty, X. Zhong, O. Acevedo, Virtual Site OPLS Force Field for Imidazolium-Based Ionic Liquids, J. Phys. Chem. B 122 (11) (2018) 2962–2974.

[180] T. Köddermann, D. Paschek, R. Ludwig, Molecular dynamic simulations of ionic liquids: a reliable description of structure, thermodynamics and dynamics, Chem. Phys. Chem. 8 (17) (2007) 2464–2470.

[181] J. Neumann, B. Golub, L.-M. Odebrecht, R. Ludwig, D. Paschek, Revisiting imidazolium based ionic liquids: Effect of the conformation bias of the [NTf 2] anion studied by molecular dynamics simulations, J. Chem. Phys. 148 (19) (2018) 193828–10.

[182] C. Cadena, E. Maginn, Molecular simulation study of some thermophysical and transport properties of triazolium-based ionic liquids, J. Phys. Chem. B 110 (36) (2006) 18026–18039.

[183] K. E. Gutowski, B. Gurkan, E. J. Maginn, Force Field For The Atomistic Simulation of The Properties of Hydrazine, Organic Hydrazine Derivatives, And Energetic Hydrazinium Ionic Liquids, Pure Appl. Chem. 81 (10) (2009) 1799–1828.

[184] H. Liu, E. Maginn, A molecular dynamics investigation of the structural and dynamic properties of the ionic liquid 1-n-butyl-3-methylimidazolium bis(trifluoromethanesulfonyl)imide, J. Chem. Phys. 135 (12) (2011) 124507.

[185] Y. Zhang, E. J. Maginn, A Simple AIMD Approach to Derive Atomic Charges for Condensed Phase Simulation of Ionic Liquids, J. Phys. Chem. B 116 (33) (2012) 10036–10048.

[186] Y. Zhang, E. J. Maginn, Direct Correlation between Ionic Liquid Transport Properties and Ion Pair Lifetimes: A Molecular Dynamics Study, The Journal of Physical Chemistry Letters 6 (4) (2015) 700–705.

[187] Z. Liu, S. Huang, W. Wang, A Refined Force Field for Molecular Simulation of Imidazolium-Based Ionic Liquids, J. Phys. Chem. B 108 (34) (2004) 12978–12989.

[188] Z. Liu, T. Chen, A. Bell, B. Smit, Improved United-Atom Force Field for 1-Alkyl-3-methylimidazolium Chloride, J. Phys. Chem. B 114 (13) (2010) 4572–4582.

[189] X. Zhong, Z. Liu, D. Cao, Improved Classical United-Atom Force Field for Imidazolium-Based Ionic Liquids: Tetrafluoroborate, Hexafluorophosphate, Methylsulfate, Trifluoromethylsulfonate, Acetate, Trifluoroacetate, and Bis(trifluoromethylsulfonyl)amide, J. Phys. Chem. B 115 (33) (2011) 10027–10040.

[190] F. Dommert, K. Wendler, R. Berger, L. Delle Site, C. Holm, Force Fields for Studying the Structure and Dynamics of Ionic Liquids: A Critical Review of Recent Developments, Chem. Phys. Chem. 13 (7) (2012) 1625–1637.

[191] H. J. C. Berendsen, J. R. Grigera, T. P. Straatsma, The Missing Term in Effective Pair Potentials, J. Phys. Chem. 91 (24) (1987) 6269–6271.

[192] A. K. Soper, F. Bruni, M. A. Ricci, Site–Site pair Correlation Functions of Water from 25 to 400Å^{o}C: Revised Analysis of New and Old Diffraction Data, J. Chem. Phys. 106 (1) (1997) 247–254.

[193] P. Mark, L. Nilsson, Structure and Dynamics of the TIP3P, SPC, and SPC/E Water Models at 298 K, J. Phys. Chem. A 105 (43) (2001) 9954–9960.

[194] J. J. Potoff, J. I. Siepmann, Vapor-Liquid Equilibria of Mixtures Containing Alkanes, Carbon Dioxide, and Nitrogen, AIChE Journal 47 (7) (2004) 1676–1682.

[195] W. Shi, E. J. Maginn, Atomistic Simulation of the Absorption of Carbon Dioxide and Water in the Ionic Liquid 1-n-Hexyl-3-methylimidazolium Bis(trifluoromethylsulfonyl)imide ([hmim][Tf_2N], J. Phys. Chem. B 112 (7) (2008) 2045–2055.

[196] M. J. Abraham, D. van der Spoel, E. Lindahl, B. Hess, , the GROMACS development team, GROMACS User Manual Version 5.1.4, www.gromacs.org, J. Mol. Model.

[197] E. Lindahl, B. Hess, D. van der Spoel, GROMACS 3.0: A Package for Molecular Simulation and Trajectory Analysis, Molec. Model. Ann. 7 (8) (2001) 306–317.

[198] L. Martínez, R. Andrade, E. G. Birgin, J. M. Martínez, PACKMOL: A Package for Building Initial Configurations for Molecular Dynamics Simulations, J. Comput. Chem. 30 (13) (2009) 2157–2164.

[199] U. Kapoor, J. K. Shah, Globular, Sponge-like to Layer-like Morphological Transition in 1-n-Alkyl-3-methylimidazolium Octylsulfate Ionic Liquid Homologous Series, J. Phys. Chem. B 122 (1) (2017) 213–228.

[200] U. Kapoor, J. K. Shah, Effect of Molecular Solvents of Varying Polarity on The Self-Assembly of 1-n-Dodecyl-3-Methylimidazolium Octylsulfate Ionic Liquid, J. Theor. Comput. Chem. 17 (03) (2018) 1840004–26.

[201] J. G. Kirkwood, Statistical Mechanics of Fluid Mixtures, J. Chem. Phys. 3 (5) (1935) 300–313.

[202] T. P. Straatsma, J. A. McCammon, Multiconfiguration thermodynamic integration, J. Chem. Phys. 95 (2) (1991) 1175–1188.

[203] M. R. Shirts, V. S. Pande, Comparison of efficiency and bias of free energies computed by exponential averaging, the Bennett acceptance ratio, and thermodynamic integration, J. Chem. Phys. 122 (14) (2005) 144107–17.

[204] C. H. Bennett, Efficient Estimation of Free Energy Differences from Monte Carlo Data, J. Comput. Phys. 22 (1976) 245–268.

[205] N. Lu, J. K. Singh, D. A. Kofke, Appropriate methods to combine forward and reverse free-energy perturbation averages, J. Chem. Phys. 118 (7) (2003) 2977–2984.

[206] N. Lu, D. A. Kofke, T. B. Woolf, Improving the efficiency and reliability of free energy perturbation calculations using overlap sampling methods, J. Comput. Chem. 25 (1) (2004) 28–40.

[207] J. P. Valleau, D. N. Card, Monte Carlo Estimation of the Free Energy by Multistage Sampling, J. Chem. Phys. 57 (12) (1972) 5457–5462.

[208] R. W. Zwanzig, High-Temperature Equation of State by a Perturbation Method. I. Nonpolar Gases, J. Chem. Phys. 22 (8) (1954) 1420–1426.

[209] G. M. Torrie, J. P. Valleau, Nonphysical sampling distributions in Monte Carlo free-energy estimation: Umbrella sampling, J. Computational Phys. 23 (2) (1976) 187–199.

[210] S. Kumar, J. M. Rosenberg, D. Bouzida, R. H. Swendsen, P. A. Kollman, Multidimensional free-energy calculations using the weighted histogram analysis method, J. Comput. Chem. 16 (11) (1995) 1339–1350.

[211] S. Kumar, J. M. Rosenberg, D. Bouzida, R. H. Swendsen, P. A. Kollman, The weighted histogram analysis method for free-energy calculations on biomolecules. i. the method, J. Comput. Chem. 13 (8) (1992) 1011–1021.

[212] C. Jarzynski, Equilibrium free-energy differences from nonequilibrium measurements: A master-equation approach, Phys. Rev. E 56 (1997) 5018–5035.

[213] C. Jarzynski, Nonequilibrium equality for free energy differences, Phys. Rev. Lett. 78 (1997) 2690–2693.

[214] G. E. Crooks, Path-ensemble averages in systems driven far from equilibrium, Phys. Rev. E 61 (2000) 2361–2366.

[215] H. Resat, M. Mezei, Studies on Free Energy Calculations. I. Thermodynamic Integration Using A Polynomial Path, J. Chem. Phys. 99 (8) (1993) 6052–6061.

[216] P. V. Klimovich, M. R. Shirts, D. L. Mobley, Guidelines For The Analysis of Free Energy Calculations, J. Comput. Aided Mol. Des. 29 (5) (2015) 397–411.

[217] M. Fasnacht, R. H. Swendsen, J. M. Rosenberg, Adaptive integration method for monte carlo simulations, Phys. Rev. E 69 (2004) 056704.

[218] T. Steinbrecher, D. L. Mobley, D. A. Case, Nonlinear Scaling Schemes For Lennard-Jones Interactions In Free Energy Calculations, J. Chem. Phys. 127 (21) (2007) 214108–14.

[219] H. Tokuda, K. Hayamizu, K. Ishii, H. Susan, M. Watanabe, Physicochemical Properties and Structures of Room Temperature Ionic Liquids. 2. Variation of Alkyl Chain Length in Imidazolium Cation, J. Phys. Chem. B 109 (13) (2005) 6103–6110.

[220] R. Shi, Y. Wang, Ion-Cage Interpretation for the Structural and Dynamic Changes of Ionic Liquids under an External Electric Field, J. Phys. Chem. B 117 (17) (2013) 5102–5112.

[221] K. R. Harris, Relations between the Fractional Stokes–Einstein and Nernst–Einstein Equations and Velocity Correlation Coefficients in Ionic Liquids and Molten Salts, J. Phys. Chem. B 114 (29) (2010) 9572–9577.

[222] C. Rey-Castro, L. F. Vega, Transport Properties of the Ionic Liquid 1-Ethyl-3-Methylimidazolium Chloride from Equilibrium Molecular Dynamics Simulation. The Effect of Temperature, J. Phys. Chem. B 110 (29) (2006) 14426–14435.

[223] J. P. Hansen, I. R. Mcdonald, Theory of Simple Liquids, Academic,New York, 1986.

[224] K. R. Harris, M. Kanakubo, N. Tsuchihashi, K. Ibuki, M. Ueno, Effect of Pressure on the Transport Properties of Ionic Liquids: 1-Alkyl-3-methylimidazolium Salts, J. Phys. Chem. B 112 (32) (2008) 9830–9840.

[225] K. E. Newman, Kirkwood–Buff Solution Theory: Derivation and Applications, Chem. Soc. Rev. 23 (1) (1994) 31–40.

[226] M. Brehm, B. Kirchner, TRAVIS - A Free Analyzer and Visualizer for Monte Carlo and Molecular Dynamics Trajectories, J. Chem. Inf. Model. 51 (8) (2011) 2007–2023.

[227] M. Brehm, H. Weber, M. Thomas, O. Hollóczki, B. Kirchner, Domain Analysis in Nanostructured Liquids: A Post-Molecular Dynamics Study at the Example of Ionic Liquids, Chem. Phys. Chem. 16 (15) (2015) 3271–3277.

[228] W. Humphrey, A. Dalke, K. Schulten, VMD: Visual Molecular Dynamics, J. Mol. Graph. 14 (1996) 33–38.

[229] P. J. Brown, A. G. Fox, E. N. Maslen, M. A. O?Keefe, T. M. Willis, International Tables for Crystallography, Prince, E., Ed. International Union of Crystallography: Dordrecht,The Netherlands C (2004) 554–595.

[230] E. Lorch, Neutron Diffraction by Germania, Silica and Radiation-Damaged Silica Glasses, J. Phys. C: Solid State Phys. 2 (8) (1969) 229–237.

[231] O. Hollóczki, M. Macchiagodena, H. Weber, M. Thomas, M. Brehm, A. Stark, O. Russina, A. Triolo, B. Kirchner, Triphilic Ionic-Liquid Mixtures: Fluorinated and Non-fluorinated Aprotic Ionic-Liquid Mixtures, Chem. Phys. Chem. 16 (15) (2015) 3325–3333.

[232] P. d. Gennes, J. Prost, The Physics of Liquid Crystals , Clarendon Press: Oxford, Clarendon Press: Oxford, 1995.

[233] Saupe, A., Recent Results in the Field of Liquid Crystals, Angew. Chem. Internat. Edit. 7 (2) (1968) 97–112.

[234] P. d. Gennes, Scaling Concepts in Polymer Physics , Cornell University Press: Oxford, Cornell University Press: Oxford, 1979.

[235] B. J. Lemaire, P. Panine, J. C. P. Gabriel, P. Davidson, The Measurement by SAXS of the Nematic Order Parameter of Laponite Gels, Europhys. Lett. 59 (1) (2002) 55–61.

[236] H. Guo, K. Kremer, Molecular Dynamics Simulation of the Phase Behavior of Lamellar Amphiphilic Model Systems, J. Chem. Phys. 119 (17) (2003) 9308–9320.

[237] J. J. Hettige, W. D. Amith, E. W. Castner Jr, C. J. Margulis, Ionic Liquids with Symmetric Diether Tails: Bulk and Vacuum-Liquid Interfacial Structures, J. Phys. Chem. B 121 (1) (2017) 174–179.

[238] R. T. McGibbon, K. A. Beauchamp, M. P. Harrigan, C. Klein, J. M. Swails, C. X. Hernández, C. R. Schwantes, L.-P. Wang, T. J. Lane, V. S. Pande, MDTraj: A Modern Open Library for the Analysis of Molecular Dynamics Trajectories, Biophysj 109 (8) (2015) 1528–1532.

[239] K. Wei, L. Deng, Y. Wang, Z.-C. Ou-Yang, G. Wang, Effect of Side-Chain Length on Structural and Dynamic Properties of Ionic Liquids with Hydroxyl Cationic Tails, J. Phys. Chem. B 118 (13) (2014) 3642–3649.

[240] L. Deng, Y. Wang, Z.-C. Ou-Yang, Concentration and Temperature Dependences of Polyglutamine Aggregation by Multiscale Coarse-Graining Molecular Dynamics Simulations, J. Phys. Chem. B 116 (34) (2012) 10135–10144.

[241] B. J. Gellatly, J. L. Finney, Calculation of protein volumes: An alternative to the Voronoi procedure, J. Molecular Biology 161 (2) (1982) 305–322.

[242] C. H. Rycroft, Voro++: A Three-Dimensional Voronoi Cell Library in C++, Chaos 19 (2009) 041111.

[243] C. E. S. Bernardes, AGGREGATES: Finding Structures in Simulation Results of Solutions, J. Comput. Chem. 38 (10) (2017) 753–765.

[244] N. Metropolis, A. W. Rosenbluth, M. N. Rosenbluth, A. H. Teller, E. Teller, Equation of State Calculations by Fast Computing Machines, J. Chem. Phys. 21 (6) (1953) 1087–1092.

[245] J. K. Shah, E. J. Maginn, A General And Efficient Monte Carlo Method For Sampling Intramolecular Degrees of Freedom of Branched and Cyclic Molecules, J. Chem. Phys. 135 (13) (2011) 134121–12.

[246] J. K. Shah, E. Marin-Rimoldi, R. G. Mullen, B. P. Keene, S. Khan, A. S. Paluch, N. Rai, L. L. Romanielo, T. W. Rosch, B. Yoo, E. J. Maginn, Cassandra: An Open Source Monte Carlo Package For Molecular Simulation, J. Comput. Chem. 38 (19) (2017) 1727–1739.

[247] S. Raeissi, C. J. Peters, High Pressure Phase Behaviour of Methane in 1-Butyl-3-Methylimidazolium Bis(Trifluoromethylsulfonyl)Imide, Fluid Phase Equilib. 294 (1-2) (2010) 67–71.

[248] N. V. Plechkova, K. R. Seddon, Applications of Ionic Liquids in the Chemical Industry, Chem. Soc. Rev. 37 (2008) 123–150.

[249] A. F. M. Cláudio, L. Swift, J. P. Hallett, T. Welton, J. A. P. Coutinho, M. G. Freire, Extended Scale for Hydrogen-Bond Basicity of Ionic Liquids, Phys. Chem. Chem. Phys. 16 (2014) 5975–5984.

[250] U. Kapoor, J. K. Shah, Preferential Ionic Interactions and Microscopic Structural Changes Drive Nonideality in Binary Ionic Liquid Mixtures as Revealed from Molecular Simulations, Ind. Eng. Chem. Res. 55 (51) (2016) 13132–13146.

[251] U. Kapoor, J. K. Shah, Thermophysical Properties of Imidazolium-Based Binary Ionic Liquid Mixtures Using Molecular Dynamics Simulations, J. Chem. Eng. Data 63 (7) (2018) 2512–2521.

[252] A. B. Pereiro, P. Verdía, E. Tojo, A. Rodríguez, Physical Properties of 1-Butyl-3-methylimidazolium Methyl Sulfate as a Function of Temperature, J. Chem. Eng. Data 52 (2) (2007) 377–380.

[253] W. Li, Z. Zhang, B. Han, S. Hu, Y. Xie, G. Yang, Effect of Water and Organic Solvents on the Ionic Dissociation of Ionic Liquids, J. Phys. Chem. B 111 (23) (2007) 6452–6456.

[254] R. L. Gardas, M. G. Freire, P. J. Carvalho, I. M. Marrucho, I. M. A. Fonseca, A. G. M. Ferreira, J. A. P. Coutinho, High-Pressure Densities and Derived Thermodynamic Properties of Imidazolium-Based Ionic Liquids, J. Chem. Eng. Data 52 (1) (2007) 80–88.

[255] E. Gómez, B. González, Á. Domínguez, E. Tojo, J. Tojo, Dynamic Viscosities of a Series of 1-Alkyl-3-methylimidazolium Chloride Ionic Liquids and Their Binary Mixtures with Water at Several Temperatures, J. Chem. Eng. Data 51 (2) (2006) 696–701.

[256] J. Jacquemin, P. HUSSON, V. Mayer, I. Cibulka, High-Pressure Volumetric Properties of Imidazolium-Based Ionic Liquids: Effect of the Anion, J. Chem. Eng. Data 52 (6) (2007) 2204–2211.

[257] R. D. Chirico, V. Diky, J. W. Magee, M. Frenkel, K. N. Marsh, Thermodynamic and thermophysical properties of the reference ionic liquid: 1-Hexyl-3-methylimidazolium bis[(trifluoromethyl)sulfonyl]amide (including mixtures). Part 2. Critical evaluation and recommended property values (IUPAC Technical Report), Pure Appl. Chem. 81 (5) (2009) 781–38.

[258] R. Kato, J. Gmehling, Systems with ionic liquids: Measurement of VLE and $\gamma\infty$ data and prediction of their thermodynamic behavior using original UNIFAC, mod. UNIFAC(Do) and COSMO-RS(Ol), J. Chem. Thermodyn. 37 (6) (2005) 603–619.

[259] J. F. Brennecke, personal Communications.

[260] Y. Hiraga, K. Koyama, Y. Sato, R. L. Smith Jr, High Pressure Densities For Mixed Ionic Liquids Having Different Functionalities: 1-Butyl-3-Methylimidazolium Chloride and 1-Butyl-3-Methylimidazolium Bis(Trifluoromethylsulfonyl)Imide, J. Chem. Thermodyn. 108 (2017) 7–17.

[261] H. Tokuda, K. Hayamizu, K. Ishii, M. A. B. H. Susan, M. Watanabe, Physicochemical properties and structures of room temperature ionic liquids. 1. variation of anionic species, J. Phys. Chem. B 108 (42) (2004) 16593–16600.

[262] S. Urahata, M. Ribeiro, Single Particle Dynamics in Ionic Liquids of 1-Alkyl-3-Methylimidazolium Cations, J. Chem. Phys. 122 (2) (2005) 024511.

[263] T. Umecky, M. Kanakubo, Y. Ikushima, Self-Diffusion Coefficients of 1-Butyl-3-Methylimidazolium Hexafluorophosphate with Pulsed-Field Gradient Spin-Echo NMR Technique, Fluid Phase Equilib. 228-229 (2005) 329–333.

[264] M. Kanakubo, K. R. Harris, N. Tsuchihashi, K. Ibuki, M. Ueno, Effect of Pressure on Transport Properties of the Ionic Liquid 1-Butyl-3-methylimidazolium Hexafluorophosphate, J. Phys. Chem. B 111 (8) (2007) 2062–2069.

[265] R. L. Gardas, J. A. P. Coutinho, A Group Contribution Method for Viscosity Estimation of Ionic Liquids, Fluid Phase Equili. 266 (1-2) (2008) 195–201.

[266] Triolo, A, Russina, O, Fazio, B, Triolo, R, Di Cola, E, Morphology of 1-Alkyl-3-methylimidazolium Hexafluorophosphate Room Temperature Ionic Liquids, Chem. Phys. Lett. 457 (4-6) (2008) 362–365.

[267] Russina, O, Triolo, A, Gontrani, L, Caminiti, R, Xiao, D, Hines Jr, LG, Bartsch, RA, Quitevis, EL, Pleckhova, N, Seddon, KR, Morphology and Intermolecular Dynamics of 1-Alkyl-3-Methylimidazolium Bis (Trifluoromethane) Sulfonyl Amide Ionic Liquids: Structural and Dynamic Evidence of Nanoscale Segregation, J. Phys.: Condens. Matter 21 (2009) 424121.

[268] Mbondo Tsamba, B E, Sarraute, S, Traïkia, M, Husson, P, Transport Properties and Ionic Association in Pure Imidazolium-Based Ionic Liquids as a Function of Temperature, J. Chem. Eng. Data 59 (6) (2014) 1747–1754.

[269] H. Tokuda, S. Tsuzuki, M. A. B. H. Susan, K. Hayamizu, M. Watanabe, How Ionic Are Room-Temperature Ionic Liquids? An Indicator of the Physicochemical Properties, J. Phys. Chem. B 110 (39) (2006) 19593–19600.

[270] H. Tokuda, K. Ishii, M. A. B. H. Susan, S. Tsuzuki, K. Hayamizu, M. Watanabe, Physicochemical Properties and Structures of Room-Temperature Ionic Liquids. 3. Variation of Cationic Structures, J. Phys. Chem. B 110 (6) (2006) 2833–2839.

[271] H. Weber, O. Hollóczki, A. S. Pensado, B. Kirchner, Side Chain Fluorination and Anion Effect on the Structure of 1-Butyl-3-Methylimidazolium Ionic Liquids, J. Chem. Phys. 139 (8) (2013) 084502.

[272] Y. Hiraga, K. Koyama, Y. Sato, R. L. Smith Jr., Measurement and Modeling of CO_2 Solubility in [Bmim]Cl – [Bmim][Tf_2N] Mixed-Ionic Liquids for Design of Versatile Reaction Solvents, J. Supercrit. Fluids. (2017) 1–9.

[273] U. Kapoor, J. K. Shah, Molecular Origins of the Apparent Ideal CO_2 Solubilities in Binary Ionic Liquid Mixtures, J. Phys. Chem. B 122 (42) (2018) 9763–9774.

[274] S. Raeissi, C. J. Peters, Carbon Dioxide Solubility in the Homologous 1-Alkyl-3-methylimidazolium Bis(trifluoromethylsulfonyl)imide Family, J. Chem. Eng. Data 54 (2) (2009) 382–386.

[275] J. Kumełan, Á. Pérez-Salado Kamps, D. Tuma, G. Maurer, Solubility of CO_2 in the Ionic Liquids [bmim][CH_3SO_4] and [bmim][PF_6], J. Chem. Eng. Data 51 (5) (2006) 1802–1807.

[276] R. Taguchi, Measurement and Calculation of High Pressure CO_2 Solubilities in Functional Ionic Liquids, M.S., Thesis, Graduate School of Environmental Studies, Tohoku University,.

[277] X. Huang, C. J. Margulis, Y. Li, B. J. Berne, Why is the Partial Molar Volume of CO_2 so Small When Dissolved in a Room Temperature Ionic Liquid? Structure and Dynamics of CO_2 Dissolved in $[bmim]^+$ $[PF_6]^-$, J. Am. Chem. Soc. 127 (50) (2005) 17842–17851.

[278] X. Zhang, F. Huo, Z. Liu, W. Wang, W. Shi, E. J. Maginn, Absorption of CO_2 in the Ionic Liquid 1-n-Hexyl-3-methylimidazolium Tris(pentafluoroethyl)trifluorophosphate ([hmim][FEP]): A Molecular View by Computer Simulations, J. Phys. Chem. B 113 (21) (2009) 7591–7598.

[279] L. A. Blanchard, J. F. Brennecke, Green Processing using Ionic Liquids and CO_2, Nature (1999) 1–2.

[280] A. Finotello, J. E. Bara, D. Camper, R. D. Noble, Room-Temperature Ionic Liquids: Temperature Dependence of Gas Solubility Selectivity, Ind. Eng. Chem. Res. 47 (10) (2008) 3453–3459.

[281] M. Ramdin, S. P. Balaji, J. M. Vicent-Luna, J. J. Gutiérrez-Sevillano, S. Calero, T. W. de Loos, T. J. H. Vlugt, Solubility of the Precombustion Gases CO_2, CH_4, CO, H_2, N_2, and H_2S in the Ionic Liquid [bmim][Tf_2N] from Monte Carlo Simulations, J. Phys. Chem. C 118 (41) (2014) 23599–23604.

[282] S. Jang, D.-W. Cho, T. Im, H. Kim, High-Pressure Phase Behavior of CO_2 + 1-Butyl-3-Methylimidazolium Chloride System, Fluid Phase Equilib. 299 (2) (2010) 216–221.

[283] P. J. Carvalho, V. H. Álvarez, I. M. Marrucho, M. Aznar, J. A. P. Coutinho, High Pressure Phase Behavior of Carbon Dioxide in 1-Butyl-3-Methylimidazolium Bis(Trifluoromethylsulfonyl)Imide and 1-Butyl-3-Methylimidazolium Dicyanamide Ionic Liquids, J. Supercrit. Fluids 50 (2) (2009) 105–111.

[284] M. Ramdin, A. Amplianitis, T. W. de Loos, T. J. H. Vlugt, Solubility of CO_2/CH_4 Gas Mixtures in Ionic Liquids, Fluid Phase Equilib. 375 (2014) 134–142.

[285] M. Petermann, T. Weissert, S. Kareth, H. W. Lösch, F. Dreisbach, New Instrument to Measure the Selective Sorption of Gas Mixtures Under High Pressures, J. Supercrit. Fluids 45 (2) (2008) 156–160.

[286] W. L. Jorgensen, D. S. Maxwell, J. Tirado-Rives, Development and Testing of the OPLS All-Atom Force Field on Conformational Energetics and Properties of Organic Liquids, J. Am. Chem. Soc. 118 (45) (1996) 11225–11236.

[287] A. A. Niazi, B. D. Rabideau, A. E. Ismail, Effects of Water Concentration on the Structural and Diffusion Properties of Imidazolium-Based Ionic Liquid–Water Mixtures, J. Phys. Chem. B 117 (5) (2013) 1378–1388.

[288] B. D. Rabideau, A. E. Ismail, Mechanisms of hydrogen bond formation between ionic liquids and cellulose and the influence of water content, Phys. Chem. Chem. Phys. 17 (8) (2015) 5767–5775.

[289] B. F. Goodrich, J. C. de la Fuente, B. E. Gurkan, Z. K. Lopez, E. A. Price, Y. Huang, J. F. Brennecke, Effect of Water and Temperature on Absorption of CO 2by Amine-Functionalized Anion-Tethered Ionic Liquids, J. Phys. Chem. B 115 (29) (2011) 9140–9150.

[290] R. P. Swatloski, S. K. Spear, J. D. Holbrey, R. D. Rogers, Dissolution of Cellose with Ionic Liquids, J. Am. Chem. Soc. 124 (18) (2002) 4974–4975.

[291] S. P. M. Ventura, S. G. Sousa, L. S. Serafim, Á. S. Lima, M. G. Freire, J. A. P. Coutinho, Ionic-Liquid-Based Aqueous Biphasic Systems with Controlled pH: The Ionic Liquid Anion Effect, J. Chem. Eng. Data 57 (2) (2011) 507–512.

[292] S. P. M. Ventura, S. G. Sousa, L. S. Serafim, Á. S. Lima, M. G. Freire, J. A. P. Coutinho, Ionic Liquid Based Aqueous Biphasic Systems with Controlled pH: The Ionic Liquid Cation Effect, J. Chem. Eng. Data 56 (11) (2011) 4253–4260.

[293] J. Han, Y. Wang, C.-l. Yu, Y.-s. Yan, X.-q. Xie, Extraction and determination of chloramphenicol in feed water, milk, and honey samples using an ionic liquid/sodium citrate aqueous two-phase system coupled with high-performance liquid chromatography, Anal Bioanal Chem 399 (3) (2010) 1295–1304.

[294] M. G. Freire, A. F. M. Cláudio, J. M. M. Araújo, J. A. P. Coutinho, I. M. Marrucho, J. N. C. Lopes, L. P. N. Rebelo, Aqueous biphasic systems: a boost brought about by using ionic liquids, Chem. Soc. Rev. 41 (14) (2012) 4966–30.

[295] E.-S. R. E. Hassan, F. Mutelet, S. Pontvianne, J.-C. Moïse, Studies on the Dissolution of Glucose in Ionic Liquids and Extraction Using the Antisolvent Method, Environ. Sci. Technol. 47 (6) (2013) 2809–2816.

[296] U. Kapoor, A. Banerjee, J. K. Shah, Evaluation of the Predictive Capability of Ionic Liquid Force Fields for CH_4, CO_2, NH_3, and SO_2 Phase Equilibria, Fluid Phase Equilb. (2018) submitted manuscript.

APPENDIX A

Thermophysical Property Data

Table A.1: Summary of the average densities: ρ (g/cm^3), and excess densities ρ^{ex} (g/cm^3) (deviation from linear mixing rule) as a function of molar composition at T = 353 K and P = 1 bar. AV: refers to average value and SD: refers to standard deviation computed using three independent molecular dynamics trials.

Binary IL Mixture	x	ρ		ρ^{ex}	
		AV	SD	AV	SD
$[C_4mim]Cl_x[OAC]_{1-x}$	0.00	1.027	0.000	0.000	0.000
	0.10	1.029	0.000	0.000	0.000
	0.25	1.033	0.000	-0.001	0.000
	0.50	1.039	0.000	-0.002	0.000
	0.75	1.047	0.000	-0.001	0.001
	0.90	1.052	0.001	-0.001	0.001
	1.00	1.055	0.001	0.000	0.000
$[C_4mim]Cl_x[TFA]_{1-x}$	0.00	1.181	0.000	0.000	0.000
	0.10	1.170	0.000	0.002	0.000
	0.25	1.154	0.000	0.005	0.000
	0.50	1.125	0.000	0.007	0.000
	0.75	1.092	0.000	0.006	0.001
	0.90	1.071	0.000	0.003	0.001
	1.00	1.055	0.001	0.000	0.000
$[C_4mim]Cl_x[TFS]_{1-x}$	0.00	1.281	0.000	0.000	0.000
	0.10	1.264	0.000	0.005	0.000
	0.25	1.236	0.000	0.012	0.000
	0.50	1.185	0.001	0.016	0.001
	0.75	1.126	0.000	0.014	0.000
	0.90	1.085	0.000	0.007	0.001
	1.00	1.055	0.001	0.000	0.000
$[C_4mim][OAC]_x[TFA]_{1-x}$	0.00	1.181	0.000	0.000	0.000
	0.10	1.167	0.000	0.002	0.000
	0.25	1.146	0.000	0.004	0.000
	0.50	1.109	0.000	0.005	0.000
	0.75	1.069	0.000	0.004	0.000
	0.90	1.044	0.000	0.002	0.000
	1.00	1.027	0.000	0.000	0.000
$[C_4mim][OAC]_x[TFS]_{1-x}$	0.00	1.281	0.000	0.000	0.000
	0.10	1.259	0.000	0.003	0.000
	0.25	1.225	0.000	0.008	0.000
	0.50	1.165	0.000	0.011	0.000

	0.75	1.098	0.000	0.008	0.001
	0.90	1.056	0.000	0.004	0.000
	1.00	1.027	0.000	0.000	0.000
	0.00	1.288	0.000	0.000	0.000
	0.10	1.277	0.000	0.004	0.000
	0.25	1.258	0.000	0.008	0.000
$[C_2mim]Cl_x[MeSO_4]_{1-x}$	0.50	1.223	0.000	0.012	0.000
	0.75	1.183	0.000	0.009	0.000
	0.90	1.155	0.001	0.005	0.001
	1.00	1.135	0.000	0.000	0.000
	0.00	1.142	0.000	0.000	0.000
	0.10	1.131	0.000	0.002	0.001
	0.25	1.113	0.001	0.005	0.001
$[C_6mim]Cl_x[MeSO_4]_{1-x}$	0.50	1.081	0.001	0.007	0.001
	0.75	1.046	0.001	0.006	0.001
	0.90	1.023	0.000	0.003	0.000
	1.00	1.006	0.000	0.000	0.000
	0.00	1.096	0.000	0.000	0.000
	0.10	1.085	0.000	0.002	0.001
	0.25	1.069	0.000	0.003	0.000
$[C_8mim]Cl_x[MeSO_4]_{1-x}$	0.50	1.042	0.000	0.006	0.000
	0.75	1.010	0.000	0.004	0.000
	0.90	0.990	0.000	0.002	0.000
	1.00	0.976	0.000	0.000	0.000
	0.00	1.474	0.000	0.000	0.000
	0.10	1.456	0.000	0.016	0.000
	0.25	1.425	0.000	0.036	0.000
$[C_2mim]Cl_x[NTf_2]_{1-x}$	0.50	1.361	0.000	0.056	0.000
	0.75	1.271	0.000	0.051	0.000
	0.90	1.197	0.001	0.027	0.001
	1.00	1.135	0.000	0.000	0.000
	0.00	1.326	0.000	0.000	0.000
	0.10	1.306	0.000	0.012	0.000
	0.25	1.273	0.000	0.027	0.000
$[C_6mim]Cl_x[NTf_2]_{1-x}$	0.50	1.205	0.000	0.039	0.000
	0.75	1.120	0.001	0.034	0.001
	0.90	1.055	0.001	0.017	0.001
	1.00	1.006	0.000	0.000	0.000
	0.00	1.274	0.000	0.000	0.000
	0.10	1.254	0.000	0.010	0.000
	0.25	1.221	0.000	0.021	0.000
$[C_8mim]Cl_x[NTf_2]_{1-x}$	0.50	1.156	0.000	0.031	0.000
	0.75	1.077	0.000	0.026	0.000
	0.90	1.019	0.000	0.013	0.000
	1.00	0.976	0.000	0.000	0.000

Table A.2: Summary of the average simulation box volume size (Å^3), molar volumes: V_m (cm^3/mol), and excess molar volumes: V_m^{ex} (cm^3/mol) as a function of molar composition at T = 353 K and P = 1 bar. AV: refers to average value and SD: refers to standard deviation computed using three independent molecular dynamics trials.

Binary IL Mixture	x	Volume		V_m		V_m^{ex}	
		AV	SD	AV	SD	AV	SD
$[C_4mim]Cl_x[OAC]_{1-x}$	0.00	82135.57	28.55	193.24	0.07	0.00	0.00
	0.10	79066.37	10.68	190.49	0.03	0.01	0.07
	0.25	79212.33	22.51	186.37	0.05	0.04	0.08
	0.50	76291.37	22.37	179.49	0.05	0.08	0.08
	0.75	73353.03	27.67	172.58	0.07	0.08	0.10
	0.90	69906.50	40.77	168.42	0.10	0.06	0.13
	1.00	70381.87	38.42	165.59	0.09	0.00	0.00
$[C_4mim]Cl_x[TFA]_{1-x}$	0.00	90847.17	7.85	213.74	0.02	0.00	0.00
	0.10	86749.70	10.32	209.00	0.02	0.07	0.03
	0.25	85791.33	16.97	201.84	0.04	0.14	0.05
	0.50	80683.53	13.46	189.83	0.03	0.16	0.06
	0.75	75541.67	26.10	177.73	0.06	0.10	0.09
	0.90	70768.00	32.05	170.49	0.08	0.09	0.11
	1.00	70381.87	38.42	165.59	0.09	0.00	0.00
$[C_4mim]Cl_x[TFS]_{1-x}$	0.00	95662.10	13.64	225.07	0.03	0.00	0.00
	0.10	90978.37	17.05	219.19	0.04	0.07	0.05
	0.25	89372.00	18.63	210.27	0.04	0.07	0.05
	0.50	83093.50	40.87	195.50	0.10	0.17	0.11
	0.75	76727.20	13.12	180.52	0.03	0.06	0.07
	0.90	71229.53	28.28	171.61	0.07	0.07	0.11
	1.00	70381.87	38.42	165.59	0.09	0.00	0.00
$[C_4mim][OAC]_x[TFA]_{1-x}$	0.00	90847.17	7.85	213.74	0.02	0.00	0.00
	0.10	87835.13	11.55	211.61	0.03	-0.08	0.03
	0.25	88589.77	18.74	208.43	0.04	-0.19	0.05
	0.50	86402.03	17.87	203.28	0.04	-0.21	0.05
	0.75	84231.17	13.35	198.17	0.03	-0.19	0.06
	0.90	81030.17	24.69	195.22	0.06	-0.07	0.08
	1.00	82135.57	28.55	193.24	0.07	0.00	0.00
$[C_4mim][OAC]_x[TFS]_{1-x}$	0.00	95662.10	13.64	225.07	0.03	0.00	0.00
	0.10	92086.77	9.54	221.86	0.02	-0.03	0.04
	0.25	92237.97	2.45	217.01	0.01	-0.10	0.03
	0.50	88834.30	8.31	209.00	0.02	-0.15	0.04
	0.75	85484.37	35.56	201.12	0.08	-0.08	0.10
	0.90	81500.87	4.74	196.35	0.01	-0.07	0.06
	1.00	82135.57	28.55	193.24	0.07	0.00	0.00
$[C_2mim]Cl_x[MeSO_4]_{1-x}$	0.00	73389.07	7.65	172.66	0.02	0.00	0.00
	0.10	69842.20	12.76	168.26	0.03	-0.06	0.03
	0.25	68740.93	11.50	161.73	0.03	-0.08	0.03
	0.50	64108.10	3.41	150.83	0.01	-0.12	0.02
	0.75	59517.53	4.06	140.03	0.01	-0.06	0.03

	0.90	55433.53	30.12	133.55	0.07	-0.02	0.08
	1.00	54925.33	16.14	129.22	0.04	0.00	0.00
$[C_6mim]Cl_x[MeSO_4]_{1-x}$	0.00	103637.33	27.14	243.83	0.06	0.00	0.00
	0.10	99452.63	41.75	239.60	0.10	-0.02	0.12
	0.25	99144.73	58.94	233.26	0.14	-0.04	0.15
	0.50	94649.43	78.43	222.68	0.18	-0.08	0.19
	0.75	90153.93	85.22	212.11	0.20	-0.13	0.20
	0.90	85416.87	19.98	205.79	0.05	-0.13	0.05
	1.00	85730.87	2.46	201.70	0.01	0.00	0.00
$[C_8mim]Cl_x[MeSO_4]_{1-x}$	0.00	118946.33	51.64	279.85	0.12	0.00	0.00
	0.10	114344.67	30.86	275.48	0.07	-0.04	0.13
	0.25	114415.33	27.68	269.19	0.07	0.15	0.11
	0.50	109663.33	44.61	258.01	0.10	-0.21	0.12
	0.75	105115.33	41.53	247.31	0.10	-0.10	0.10
	0.90	100010.10	47.88	240.94	0.12	0.02	0.12
	1.00	100563.00	6.24	236.60	0.01	0.00	0.00
$[C_2mim]Cl_x[NTf_2]_{1-x}$	0.00	112876.00	3.00	265.57	0.01	0.00	0.00
	0.10	104587.67	8.08	251.97	0.02	0.04	0.02
	0.25	98478.00	7.53	231.69	0.02	0.21	0.02
	0.50	84021.63	26.51	197.68	0.06	0.28	0.07
	0.75	69536.27	2.56	163.60	0.01	0.29	0.03
	0.90	59376.73	26.46	143.05	0.06	0.19	0.07
	1.00	54925.33	16.14	129.22	0.04	0.00	0.00
$[C_6mim]Cl_x[NTf_2]_{1-x}$	0.00	143448.00	19.67	337.50	0.05	0.00	0.00
	0.10	134467.00	18.52	323.96	0.04	0.04	0.06
	0.25	129053.00	22.11	303.63	0.05	0.08	0.06
	0.50	114692.33	9.07	269.84	0.02	0.24	0.03
	0.75	100205.00	47.51	235.76	0.11	0.11	0.11
	0.90	89424.30	78.86	215.44	0.19	0.16	0.19
	1.00	85730.87	2.46	201.70	0.01	0.00	0.00
$[C_8mim]Cl_x[NTf_2]_{1-x}$	0.00	158670.00	23.58	373.31	0.06	0.00	0.00
	0.10	149315.33	9.02	359.73	0.02	0.09	0.05
	0.25	144267.33	41.00	339.42	0.10	0.29	0.11
	0.50	129888.67	52.94	305.59	0.12	0.64	0.13
	0.75	115332.33	36.20	271.35	0.09	0.57	0.09
	0.90	104018.00	42.51	250.60	0.10	0.33	0.10
	1.00	100563.00	6.24	236.60	0.01	0.00	0.00

Table A.3: Summary of the self-diffusion coefficients, D, (10^{-7} cm^2/sec) for cation and anions, and their excess diffusivities, D^{ex} (deviation from linear mixing rule) as a function of molar composition at T = 353 K and P = 1 bar. AV: refers to average value and SD: refers to standard deviation computed using three independent molecular dynamics trials. (Please note $[C_4mim]Cl_x[OAC]_{1-x}$ is designated as [Cation] $[Anion1]_x$ $[Anion2]_{1-x}$)

BILM	x	D_{Cation}		D^{ex}_{Cation}		D_{Anion1}		D^{ex}_{Anion1}		D_{Anion2}		D^{ex}_{Anion2}	
		AV	SD	AV	SD	AV	SD	AV	SD	AV	SD	AV	SD
	0.00	4.49	0.27	0.00	0.00	-	-	-	-	4.14	0.36	0.00	0.00
	0.10	4.27	0.13	0.10	0.28	3.46	0.52	-0.37	0.61	3.84	0.26	0.01	0.42
	0.25	3.90	0.34	0.20	0.40	3.67	0.65	0.31	0.71	3.69	0.59	0.33	0.65
[C4]Cl-[OAC]	0.50	2.80	0.17	-0.10	0.25	2.45	0.23	-0.14	0.30	2.65	0.22	0.06	0.29
	0.75	1.96	0.11	-0.15	0.22	1.83	0.10	0.01	0.16	1.81	0.24	-0.01	0.28
	0.90	1.57	0.22	-0.06	0.30	1.48	0.08	0.12	0.14	1.58	0.09	0.22	0.15
	1.00	1.31	0.23	0.00	0.00	1.05	0.12	0.00	0.00	-	-	-	-
	0.00	19.50	0.40	0.00	0.00	-	-	-	-	16.74	0.33	0.00	0.00
	0.10	15.91	0.74	-1.77	0.83	11.06	2.79	-4.12	2.81	14.43	0.84	-0.74	0.89
	0.25	12.20	0.60	-2.76	0.67	8.71	1.07	-4.11	1.10	11.40	1.20	-1.42	1.23
[C4]Cl-[TFA]	0.50	6.53	0.43	-3.88	0.49	4.80	0.33	-4.10	0.38	6.68	0.81	-2.22	0.83
	0.75	2.91	0.43	-2.95	0.48	2.48	0.43	-2.49	0.45	3.60	0.60	-1.38	0.61
	0.90	1.65	0.19	-1.48	0.28	1.49	0.07	-1.13	0.14	1.67	0.02	-0.95	0.12
	1.00	1.31	0.23	0.00	0.00	1.05	0.12	0.00	0.00	-	-	-	-
	0.00	8.97	0.14	0.00	0.00	-	-	-	-	5.97	0.35	0.00	0.00
	0.10	7.95	0.63	-0.25	0.65	5.10	0.60	-0.38	0.67	5.55	0.49	0.07	0.58
	0.25	5.95	0.30	-1.11	0.32	4.11	0.17	-0.63	0.31	4.55	0.17	-0.19	0.31
[C4]Cl-[TFS]	0.50	3.56	0.24	-1.58	0.28	2.69	0.13	-0.82	0.23	3.11	0.30	-0.40	0.36
	0.75	2.35	0.09	-0.87	0.20	1.87	0.13	-0.41	0.18	2.07	0.31	-0.21	0.33
	0.90	1.62	0.07	-0.46	0.22	1.36	0.06	-0.19	0.13	1.46	0.16	-0.08	0.19
	1.00	1.31	0.23	0.00	0.00	1.05	0.12	0.00	0.00	-	-	-	-
	0.00	19.50	0.40	0.00	0.00	-	-	-	-	16.74	0.33	0.00	0.00
	0.10	17.06	1.39	-0.94	1.43	11.55	3.11	-3.93	3.13	14.55	0.31	-0.93	0.43
	0.25	13.77	0.94	-1.97	0.99	10.18	1.13	-3.41	1.16	12.91	0.71	-0.68	0.76
[OAC]-[TFA]	0.50	9.08	0.37	-2.92	0.44	7.75	0.40	-2.69	0.47	10.41	0.86	-0.03	0.89
	0.75	6.90	0.74	-1.34	0.78	6.30	0.14	-0.99	0.31	7.86	1.19	0.57	1.23
	0.90	5.83	0.15	-0.16	0.29	5.38	0.78	-0.02	0.85	6.93	0.94	1.53	0.99
	1.00	4.49	0.27	0.00	0.00	4.14	0.36	0.00	0.00	-	-	-	-
	0.00	8.97	0.14	0.00	0.00	-	-	-	-	5.97	0.35	0.00	0.00
	0.10	8.50	0.49	-0.02	0.51	6.37	1.77	0.58	1.79	6.20	0.11	0.41	0.33
	0.25	7.56	0.07	-0.28	0.14	4.90	0.50	-0.61	0.57	5.34	0.37	-0.17	0.46
[OAC]-[TFS]	0.50	6.35	0.14	-0.38	0.20	4.53	0.44	-0.53	0.50	5.22	0.54	0.16	0.60
	0.75	5.79	0.02	0.19	0.21	4.79	0.76	0.20	0.81	4.93	0.36	0.33	0.46
	0.90	4.93	0.27	-0.01	0.37	4.49	0.25	0.16	0.41	4.79	0.17	0.47	0.37
	1.00	4.49	0.27	0.00	0.00	4.14	0.36	0.00	0.00	-	-	-	-
	0.00	5.08	0.20	0.00	0.00	-	-	-	-	2.36	0.23	0.00	0.00
	0.10	5.48	0.32	0.61	0.37	3.01	0.87	0.68	0.89	2.25	0.06	-0.08	0.22

	0.25	4.86	0.36	0.30	0.39	2.80	0.19	0.52	0.26	2.24	0.24	-0.04	0.29
[C_2]Cl-[MeS]	0.50	3.95	0.35	-0.08	0.37	2.41	0.07	0.21	0.15	2.03	0.06	-0.17	0.14
	0.75	3.58	0.09	0.09	0.17	2.25	0.24	0.14	0.26	1.91	0.10	-0.20	0.15
	0.90	3.01	0.16	-0.17	0.22	2.03	0.15	-0.03	0.19	1.92	0.21	-0.14	0.24
	1.00	2.97	0.17	0.00	0.00	2.03	0.11	0.00	0.00	-	-	-	-
	0.00	1.55	0.10	0.00	0.00	-	-	-	-	1.28	0.14	0.00	0.00
	0.10	1.51	0.19	0.06	0.21	1.32	0.40	0.13	0.42	1.27	0.07	0.08	0.15
	0.25	1.46	0.11	0.16	0.13	1.33	0.16	0.27	0.19	1.19	0.06	0.13	0.12
[C_6]Cl-[MeS]	0.50	1.09	0.12	0.04	0.14	0.92	0.13	0.07	0.15	0.84	0.06	0.00	0.10
	0.75	0.84	0.05	0.05	0.09	0.71	0.02	0.08	0.07	0.75	0.04	0.13	0.08
	0.90	0.67	0.08	0.03	0.12	0.59	0.11	0.09	0.14	0.55	0.04	0.05	0.08
	1.00	0.54	0.09	0.00	0.00	0.41	0.08	0.00	0.00	-	-	-	-
	0.00	0.92	0.07	0.00	0.00	-	-	-	-	0.87	0.17	0.00	0.00
	0.10	0.80	0.05	-0.07	0.08	0.81	0.19	0.00	0.24	0.77	0.15	-0.04	0.21
	0.25	0.77	0.13	-0.02	0.14	0.71	0.03	-0.02	0.14	0.67	0.09	-0.06	0.16
[C_8]Cl-[MeS]	0.50	0.61	0.09	-0.04	0.11	0.57	0.11	-0.02	0.15	0.58	0.08	-0.02	0.14
	0.75	0.60	0.03	0.08	0.09	0.49	0.04	0.03	0.13	0.46	0.07	0.01	0.14
	0.90	0.44	0.06	0.00	0.12	0.39	0.03	0.01	0.14	0.38	0.07	0.00	0.15
	1.00	0.38	0.11	0.00	0.00	0.32	0.15	0.00	0.00	-	-	-	-
	0.00	17.33	0.11	0.00	0.00	-	-	-	-	10.04	0.30	0.00	0.00
	0.10	14.40	0.87	-1.49	0.88	6.69	0.94	-2.55	0.98	8.58	0.53	-0.66	0.59
	0.25	10.93	0.25	-2.81	0.27	5.41	0.60	-2.63	0.64	5.85	0.70	-2.19	0.74
[C_2]Cl-[NTf]	0.50	6.85	0.47	-3.30	0.48	3.98	0.37	-2.05	0.40	4.70	0.32	-1.33	0.36
	0.75	4.43	0.42	-2.13	0.44	2.73	0.31	-1.30	0.33	2.88	0.46	-1.15	0.48
	0.90	3.11	0.07	-1.29	0.17	2.06	0.20	-0.77	0.22	1.54	0.46	-1.29	0.47
	1.00	2.97	0.17	0.00	0.00	2.03	0.11	0.00	0.00	-	-	-	-
	0.00	9.73	1.17	0.00	0.00	-	-	-	-	7.64	0.49	0.00	0.00
	0.10	7.17	0.20	-1.65	1.07	3.81	0.61	-3.11	0.75	6.47	0.41	-0.45	0.60
	0.25	5.37	0.46	-2.06	0.99	3.39	0.60	-2.44	0.70	5.24	0.60	-0.60	0.71
[C_6]Cl-[NTf]	0.50	2.97	0.05	-2.17	0.59	2.00	0.05	-2.03	0.25	3.49	0.37	-0.53	0.45
	0.75	1.39	0.35	-1.45	0.46	1.06	0.28	-1.16	0.32	1.60	0.44	-0.61	0.46
	0.90	0.88	0.07	-0.58	0.16	0.73	0.07	-0.40	0.11	1.09	0.39	-0.04	0.40
	1.00	0.54	0.09	0.00	0.00	0.41	0.08	0.00	0.00	-	-	-	-
	0.00	6.13	0.27	0.00	0.00	-	-	-	-	6.06	0.75	0.00	0.00
	0.10	4.84	0.37	-0.72	0.44	2.59	0.27	-2.89	0.73	4.64	0.45	-0.85	0.81
	0.25	3.82	0.21	-0.87	0.29	2.47	0.31	-2.15	0.64	3.76	0.33	-0.87	0.65
[C_8]Cl-[NTf]	0.50	1.79	0.13	-1.46	0.19	1.21	0.13	-1.98	0.40	2.13	0.40	-1.06	0.55
	0.75	0.88	0.14	-0.94	0.18	0.67	0.06	-1.08	0.23	1.25	0.11	-0.50	0.24
	0.90	0.55	0.13	-0.41	0.17	0.40	0.13	-0.49	0.20	0.44	0.13	-0.45	0.20
	1.00	0.38	0.11	0.00	0.00	0.32	0.15	0.00	0.00	-	-	-	-

Table A.4: Summary of the ionic conductivities calculated using, both, Nernst-Einstein, σ_{NE} (S/m) and Einstein's relation, σ (S/m), and excess ionic conductivities σ^{ex}_{NE} & σ^{ex} (deviation from linear mixing rule), and ionicity (Y=$\frac{\sigma}{\sigma_{NE}}$) as a function of molar composition at T = 353 K and P = 1 bar. AV: refers to average value and SD: refers to standard deviation computed using three independent molecular dynamics trials.

Binary IL Mixture	x	σ_{NE}		σ^{ex}_{NE}		σ		σ^{ex}		Y
		AV	SD	AV	SD	AV	SD	AV	SD	AV
	0.00	0.91	0.05	0.00	0.00	0.29	0.00	0.00	0.00	0.32

	0.10	0.86	0.03	0.02	0.06	0.26	0.03	-0.02	0.03	0.30
	0.25	0.83	0.08	0.07	0.09	0.22	0.00	-0.05	0.01	0.27
$[C_4mim]Cl_x[OAC]_{1-x}$	0.50	0.61	0.04	0.01	0.08	0.27	0.03	0.03	0.04	0.44
	0.75	0.45	0.04	0.00	0.09	0.16	0.00	-0.05	0.03	0.37
	0.90	0.37	0.08	0.02	0.12	0.29	0.04	0.10	0.05	0.80
	1.00	0.29	0.11	0.00	0.00	0.19	0.04	0.00	0.00	0.64
	0.00	3.44	0.01	0.00	0.00	0.83	0.11	0.00	0.00	0.24
	0.10	2.91	0.04	-0.21	0.04	0.79	0.02	0.02	0.10	0.27
	0.25	2.31	0.05	-0.35	0.06	0.73	0.12	0.06	0.15	0.32
$[C_4mim]Cl_x[TFA]_{1-x}$	0.50	1.31	0.05	-0.55	0.07	0.41	0.06	-0.10	0.09	0.31
	0.75	0.65	0.10	-0.43	0.13	0.20	0.13	-0.14	0.14	0.31
	0.90	0.38	0.06	-0.23	0.12	0.18	0.02	-0.07	0.04	0.48
	1.00	0.29	0.11	0.00	0.00	0.19	0.04	0.00	0.00	0.64
	0.00	1.35	0.03	0.00	0.00	0.44	0.02	0.00	0.00	0.32
	0.10	1.25	0.06	0.00	0.06	0.39	0.03	-0.02	0.03	0.32
	0.25	1.00	0.03	-0.08	0.05	0.38	0.06	0.01	0.06	0.38
$[C_4mim]Cl_x[TFS]_{1-x}$	0.50	0.67	0.05	-0.15	0.07	0.27	0.06	-0.04	0.07	0.40
	0.75	0.48	0.04	-0.07	0.09	0.16	0.04	-0.09	0.05	0.33
	0.90	0.35	0.03	-0.04	0.10	0.13	0.02	-0.08	0.04	0.36
	1.00	0.29	0.11	0.00	0.00	0.19	0.04	0.00	0.00	0.64
	0.00	3.44	0.01	0.00	0.00	0.83	0.11	0.00	0.00	0.24
	0.10	3.00	0.05	-0.18	0.05	0.89	0.07	0.11	0.12	0.30
	0.25	2.53	0.04	-0.28	0.05	0.84	0.11	0.15	0.14	0.33
$[C_4mim][OAC]_x[TFA]_{1-x}$	0.50	1.81	0.03	-0.36	0.04	0.54	0.07	0.00	0.09	0.30
	0.75	1.39	0.06	-0.15	0.07	0.38	0.05	-0.01	0.05	0.27
	0.90	1.18	0.06	0.02	0.08	0.31	0.06	0.00	0.06	0.26
	1.00	0.91	0.05	0.00	0.00	0.25	0.00	0.00	0.00	0.27
	0.00	1.35	0.03	0.00	0.00	0.44	0.02	0.00	0.00	0.32
	0.10	1.35	0.04	0.04	0.04	0.41	0.01	0.00	0.03	0.31
	0.25	1.20	0.02	-0.04	0.03	0.36	0.03	-0.03	0.04	0.30
$[C_4mim][OAC]_x[TFS]_{1-x}$	0.50	1.09	0.03	-0.04	0.04	0.35	0.02	0.00	0.03	0.32
	0.75	1.07	0.05	0.06	0.07	0.29	0.04	0.00	0.04	0.27
	0.90	0.98	0.04	0.03	0.06	0.27	0.00	0.01	0.00	0.28
	1.00	0.91	0.05	0.00	0.00	0.25	0.00	0.00	0.00	0.27
	0.00	0.67	0.04	0.00	0.00	0.39	0.05	0.00	0.00	0.57
	0.10	0.71	0.04	0.06	0.06	0.34	0.02	-0.04	0.05	0.47
	0.25	0.68	0.06	0.04	0.06	0.41	0.11	0.04	0.12	0.60
$[C_2mim]Cl_x[MeSO_4]_{1-x}$	0.50	0.60	0.06	0.00	0.06	0.38	0.05	0.03	0.06	0.64
	0.75	0.58	0.04	0.02	0.05	0.37	0.03	0.03	0.03	0.64
	0.90	0.52	0.04	-0.02	0.06	0.36	0.05	0.04	0.05	0.70
	1.00	0.52	0.04	0.00	0.00	0.32	0.00	0.00	0.00	0.62
	0.00	0.26	0.06	0.00	0.00	0.09	0.02	0.00	0.00	0.34
	0.10	0.25	0.07	0.01	0.09	0.10	0.03	0.01	0.04	0.38
	0.25	0.25	0.05	0.03	0.07	0.09	0.02	0.02	0.03	0.37
$[C_6mim]Cl_x[MeSO_4]_{1-x}$	0.50	0.19	0.07	0.01	0.10	0.07	0.01	0.01	0.01	0.37
	0.75	0.16	0.03	0.02	0.10	0.07	0.00	0.02	0.01	0.44
	0.90	0.13	0.11	0.01	0.16	0.05	0.01	0.01	0.01	0.37

	1.00	0.10	0.13	0.00	0.00	0.04	0.00	0.00	0.00	0.36
$[C_8mim]Cl_x[MeSO_4]_{1-x}$	0.00	0.16	0.10	0.00	0.00	0.06	0.01	0.00	0.00	0.39
	0.10	0.14	0.09	-0.01	0.13	0.07	0.00	0.01	0.01	0.47
	0.25	0.14	0.10	0.00	0.14	0.06	0.01	0.00	0.01	0.43
	0.50	0.12	0.10	0.00	0.17	0.06	0.00	0.01	0.01	0.49
	0.75	0.11	0.04	0.01	0.20	0.05	0.01	0.00	0.01	0.41
	0.90	0.09	0.09	0.00	0.25	0.05	0.00	0.01	0.00	0.55
	1.00	0.07	0.26	0.00	0.00	0.04	0.00	0.00	0.00	0.47
$[C_2mim]Cl_x[NTf_2]_{1-x}$	0.00	2.47	0.01	0.00	0.00	0.67	0.01	0.00	0.00	0.27
	0.10	2.09	0.04	-0.19	0.05	0.62	0.14	-0.02	0.14	0.30
	0.25	1.56	0.04	-0.42	0.04	0.56	0.14	-0.02	0.14	0.36
	0.50	1.09	0.05	-0.41	0.05	0.40	0.04	-0.09	0.04	0.37
	0.75	0.73	0.07	-0.28	0.08	0.39	0.05	-0.02	0.05	0.54
	0.90	0.53	0.04	-0.19	0.05	0.32	0.02	-0.04	0.02	0.60
	1.00	0.52	0.04	0.00	0.00	0.32	0.00	0.00	0.00	0.62
$[C_6mim]Cl_x[NTf_2]_{1-x}$	0.00	1.57	0.07	0.00	0.00	0.31	0.05	0.00	0.00	0.20
	0.10	1.22	0.03	-0.20	0.07	0.24	0.05	-0.04	0.07	0.20
	0.25	0.95	0.07	-0.25	0.09	0.18	0.04	-0.06	0.06	0.19
	0.50	0.56	0.03	-0.28	0.08	0.14	0.02	-0.03	0.03	0.25
	0.75	0.26	0.16	-0.21	0.19	0.08	0.03	-0.02	0.03	0.30
	0.90	0.17	0.06	-0.08	0.13	0.08	0.03	0.02	0.03	0.50
	1.00	0.10	0.13	0.00	0.00	0.04	0.00	0.00	0.00	0.36
$[C_8mim]Cl_x[NTf_2]_{1-x}$	0.00	1.10	0.07	0.00	0.00	0.25	0.03	0.00	0.00	0.22
	0.10	0.85	0.06	-0.15	0.09	0.17	0.03	-0.05	0.04	0.20
	0.25	0.68	0.05	-0.16	0.09	0.19	0.06	0.00	0.07	0.29
	0.50	0.34	0.07	-0.25	0.15	0.11	0.01	-0.03	0.02	0.33
	0.75	0.17	0.09	-0.16	0.22	0.07	0.00	-0.02	0.01	0.40
	0.90	0.10	0.19	-0.08	0.30	0.05	0.01	0.00	0.01	0.55
	1.00	0.07	0.26	0.00	0.00	0.04	0.00	0.00	0.00	0.47

APPENDIX B

Lever Rule For Henry's Constants of Binary IL Mixtures

Consider two ionic liquids designated as A and B. Let n_A and n_B denote the corresponding moles of the two ionic liquids, respectively. If the ionic liquids are subjected to a low gas phase pressure P of CO_2, then it can be easily shown that the number moles of CO_2 in each of the ionic liquids is $(n_A P)/(x_A H_A)$ and $(n_B P)/(x_B H_B)$. x_A and x_B are the mole fractions of the ionic liquids when CO_2 is absorbed; H_A and H_B represent the Henry's Law constants of CO_2 in the ionic liquids A and B, respectively. Therefore,

$$x_A = 1 - \frac{P}{H_A} \tag{B.1}$$

$$x_B = 1 - \frac{P}{H_B} \tag{B.2}$$

Now consider the ionic liquid mixtures formed by mixing the two ionic liquids. The mole fractions of the two ionic liquids, in the mixture, on CO_2-free basis are then given by

$$x_A{}' = \frac{n_A}{n_A + n_B} \tag{B.3}$$

and

$$x_B{}' = \frac{n_B}{n_A + n_B} \tag{B.4}$$

If the ionic liquid mixture is subjected to a pressure P of CO_2, the mole fraction of CO_2 in the ionic liquid mixture is given by P/H_{mix} such that

$$\frac{P}{H_{mix}} = \frac{(n_A P)/(x_A H_A) + (n_B P)/(x_B H_B)}{n_A + n_B + (n_A P)/(x_A H_A) + (n_B P)/(x_B H_B)} \tag{B.5}$$

assuming that the dissolution of CO_2 is ideal so that the number of moles of CO_2 in the ionic liquid mixture can be obtained by adding the corresponding moles in the pure ionic liquids. Dividing the numerator and denominator by $n_A + n_B$ and substituting the definitions of x'_A and x'_B, eq. B.5 can be reduced to

$$\frac{1}{H_{mix}} = \frac{x'_A/(x_A H_A) + x'_B/(x_B H_B)}{1 + (x'_A P)/(x_A H_A) + (x'_B P)/(x_B H_B)} \tag{B.6}$$

For the applicability of the Henry's Law, we let $P \to 0$, such that $x_A \to 1$ and $x_B \to 1$. In this limit, eq. B.6 simplifies to

$$\frac{1}{H_{mix}} = \frac{x'_A}{H_A} + \frac{x'_B}{H_B} \tag{B.7}$$

demonstrating that the Henry's Law constant of CO_2 in an ionic liquid mixture can be computed as a Harmonic mean of the Henry's Law constants for the pure ionic liquids if the assumption of ideal absorption of CO_2 is made.

APPENDIX C

Structures of Binary Ionic Liquid Mixtures Discussed in Chapter 4 - Section 4.5

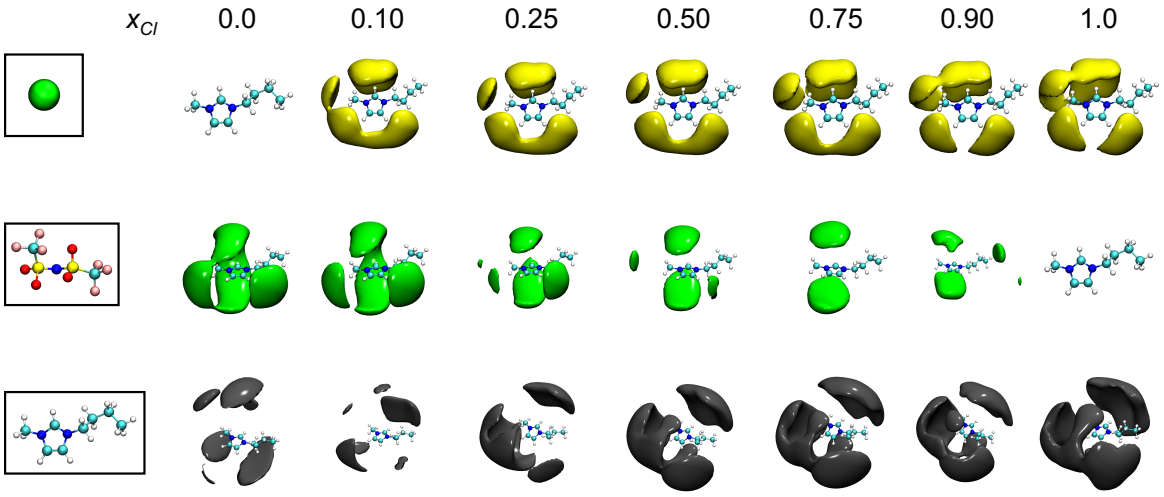

Figure C.1: SDFs of $[C_4mim]Cl_x[NTf_2]_{1-x}$ binary ionic liquid mixture (a) cation-Cl (COM-based), (b) cation-$[NTf_2]$ (COM-based), and (c) cation-cation (COR-based). Spatial densities of anions around cations - 2.5 times bulk density while spatial densities of cations around cations - 1.5 times bulk density.

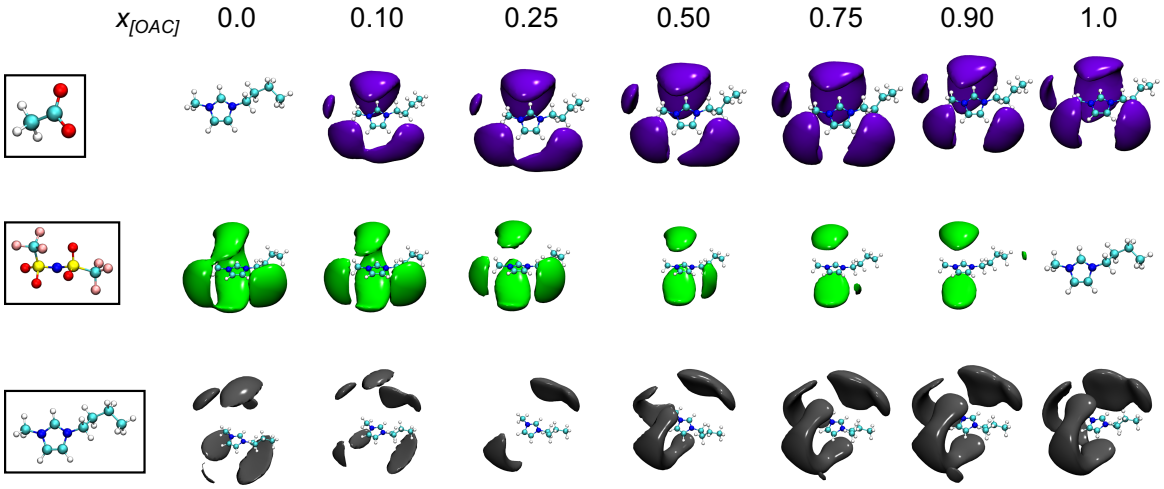

Figure C.2: SDFs of $[C_4mim][OAC]_x[NTf_2]_{1-x}$ binary ionic liquid mixture (a) cation-[OAC] (COM-based), (b) cation-$[NTf_2]$ (COM-based), and (c) cation-cation (COR-based). Spatial densities of anions around cations - 2.5 times bulk density while spatial densities of cations around cations - 1.5 times bulk density.

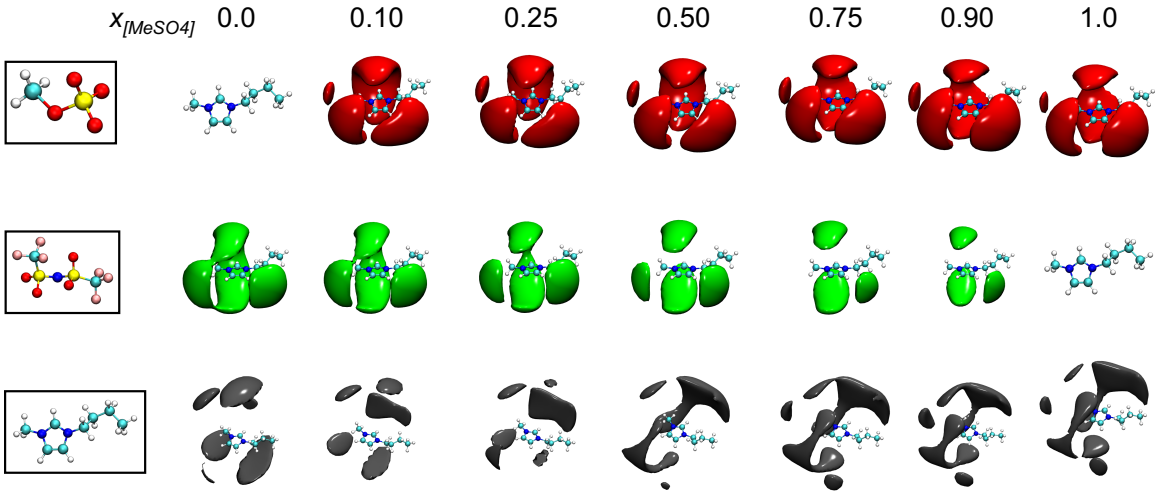

Figure C.3: SDFs of $[C_4mim][MeSO_4]_x[NTf_2]_{1-x}$ binary ionic liquid mixture (a) cation-$[MeSO_4]$ (COM-based), (b) cation-$[NTf_2]$ (COM-based), and (c) cation-cation (COR-based). Spatial densities of anions around cations - 2.5 times bulk density while spatial densities of cations around cations - 1.5 times bulk density.

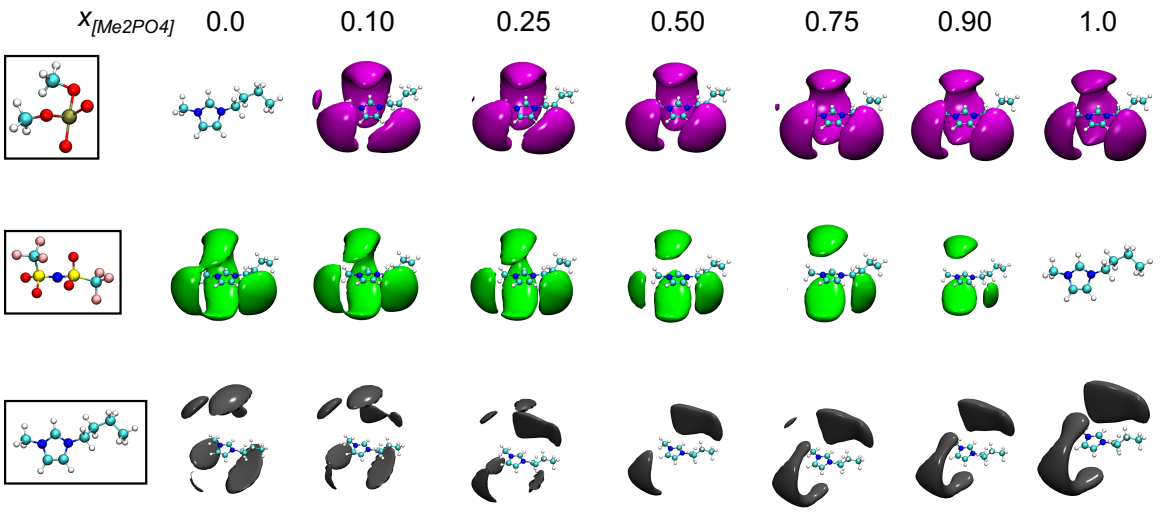

Figure C.4: SDFs of $[C_4mim][Me_2PO_4]_x[NTf_2]_{1-x}$ binary ionic liquid mixture (a) cation-$[Me_2PO_4]$ (COM-based), (b) cation-$[NTf_2]$ (COM-based), and (c) cation-cation (COR-based). Spatial densities of anions around cations - 2.5 times bulk density while spatial densities of cations around cations - 1.5 times bulk density.

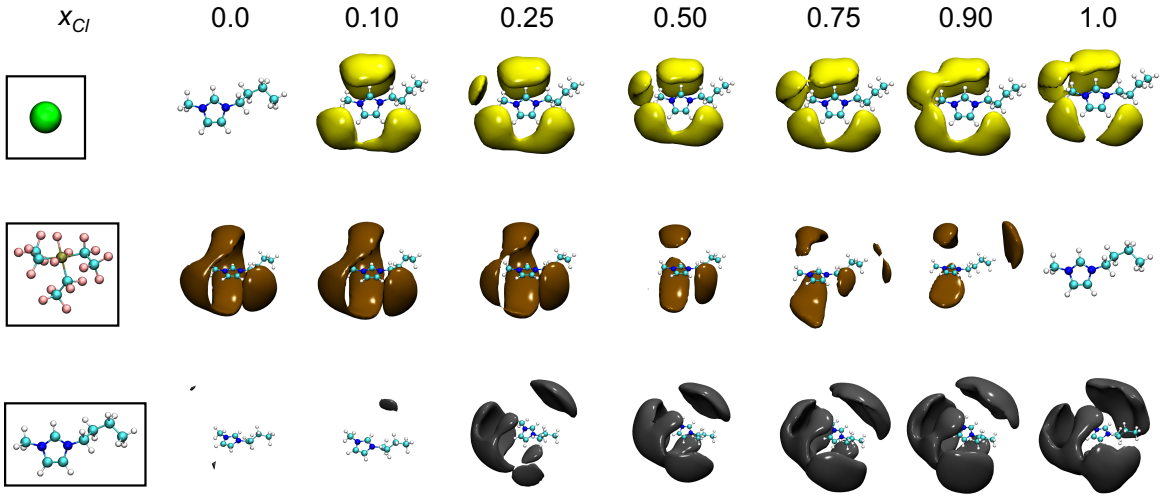

Figure C.5: SDFs of $[C_4mim]Cl_x[eFAP]_{1-x}$ binary ionic liquid mixture (a) cation-Cl (COM-based), (b) cation-[eFAP] (COM-based), and (c) cation-cation (COR-based). Spatial densities of anions around cations - 2.5 times bulk density while spatial densities of cations around cations - 1.5 times bulk density.

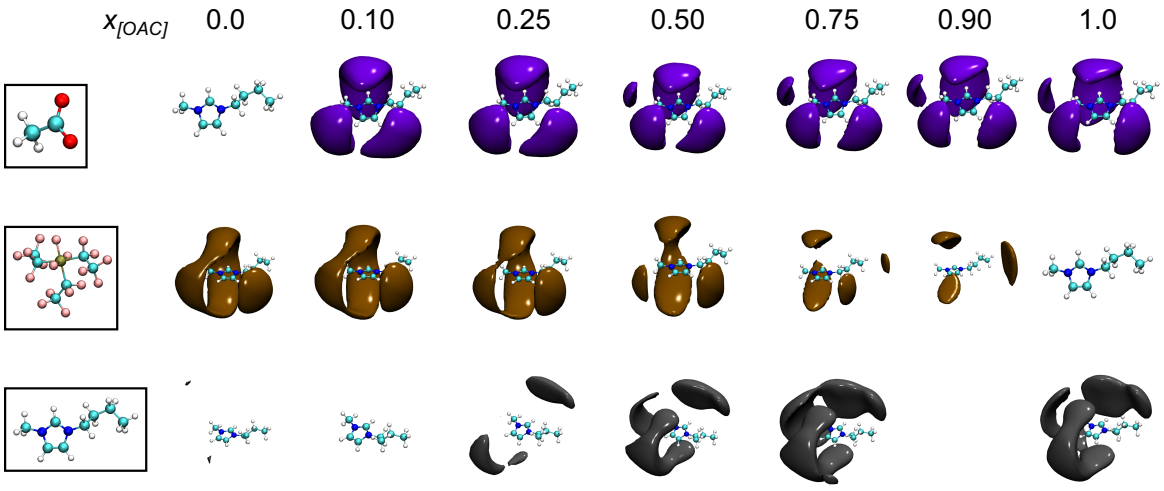

Figure C.6: SDFs of $[C_4mim][OAC]_x[eFAP]_{1-x}$ binary ionic liquid mixture (a) cation-[OAC] (COM-based), (b) cation-[eFAP] (COM-based), and (c) cation-cation (COR-based). Spatial densities of anions around cations - 2.5 times bulk density while spatial densities of cations around cations - 1.5 times bulk density.

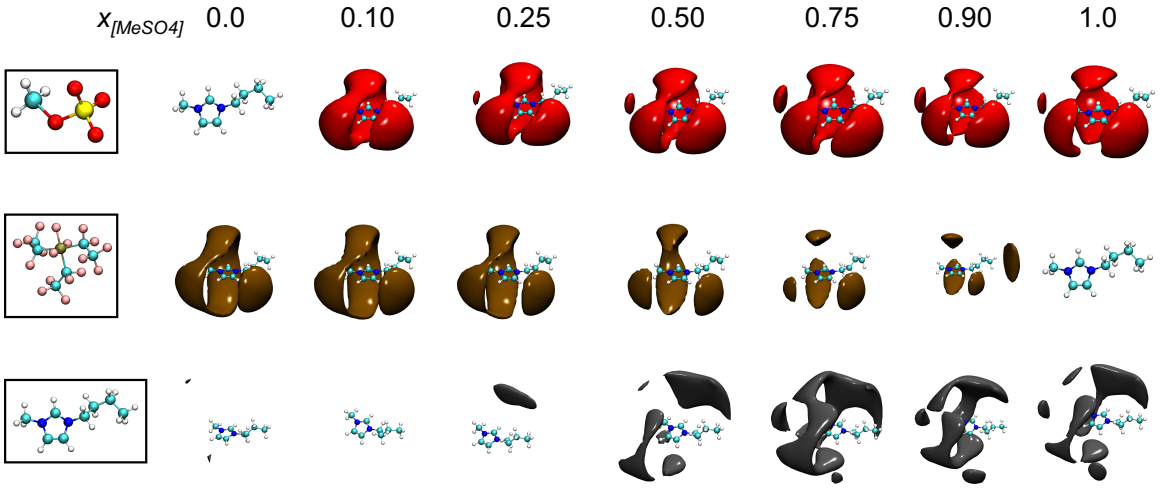

Figure C.7: SDFs of $[C_4mim][MeSO_4]_x[eFAP]_{1-x}$ binary ionic liquid mixture (a) cation-$[MeSO_4]$ (COM-based), (b) cation-[eFAP] (COM-based), and (c) cation-cation (COR-based). Spatial densities of anions around cations - 2.5 times bulk density while spatial densities of cations around cations - 1.5 times bulk density.

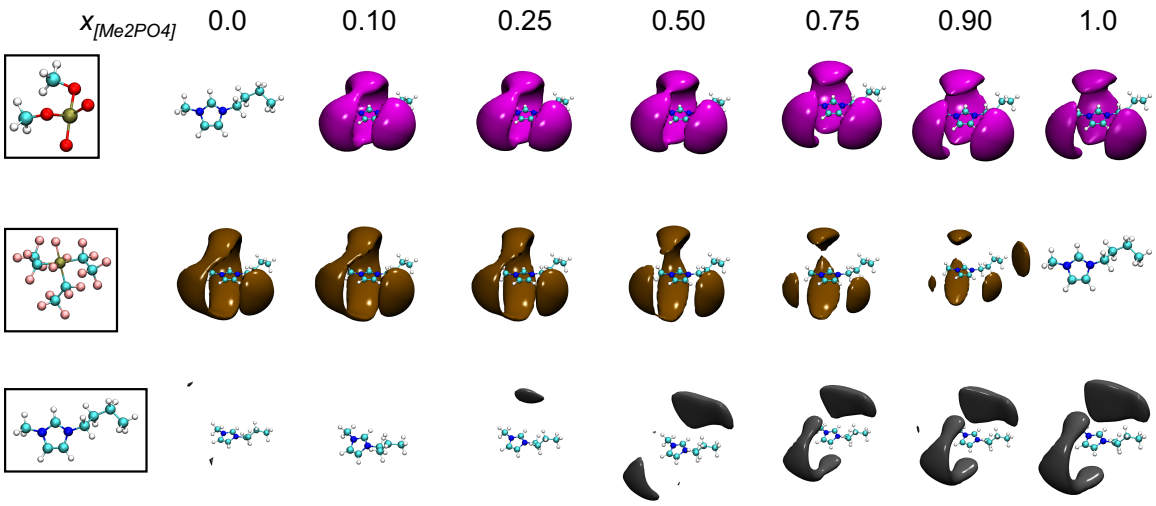

Figure C.8: SDFs of $[C_4mim][Me_2PO_4]_x[eFAP]_{1-x}$ binary ionic liquid mixture(a) cation-$[Me_2PO_4]$ (COM-based), (b) cation-[eFAP] (COM-based), and (c) cation-cation (COR-based). Spatial densities of anions around cations - 2.5 times bulk density while spatial densities of cations around cations - 1.5 times bulk density.

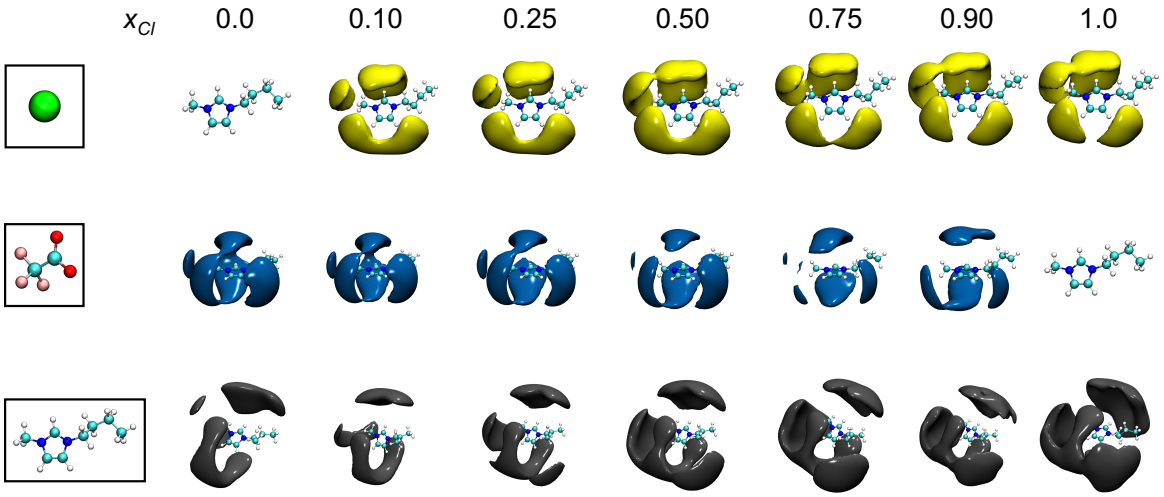

Figure C.9: SDFs of $[C_4mim]Cl_x[TFA]_{1-x}$ binary ionic liquid mixture (a) cation-Cl (COM-based), (b) cation-[TFA] (COM-based), and (c) cation-cation (COR-based). Spatial densities of anions around cations - 2.5 times bulk density while spatial densities of cations around cations - 1.5 times bulk density.

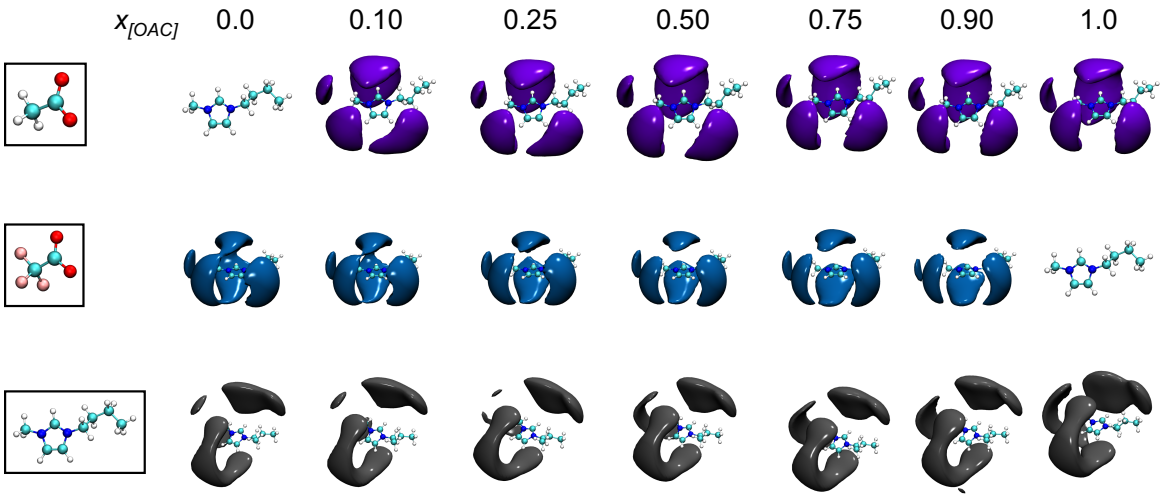

Figure C.10: SDFs of $[C_4mim][OAC]_x[TFA]_{1-x}$ binary ionic liquid mixture (a) cation-[OAC] (COM-based), (b) cation-[TFA] (COM-based), and (c) cation-cation (COR-based). Spatial densities of anions around cations - 2.5 times bulk density while spatial densities of cations around cations - 1.5 times bulk density.

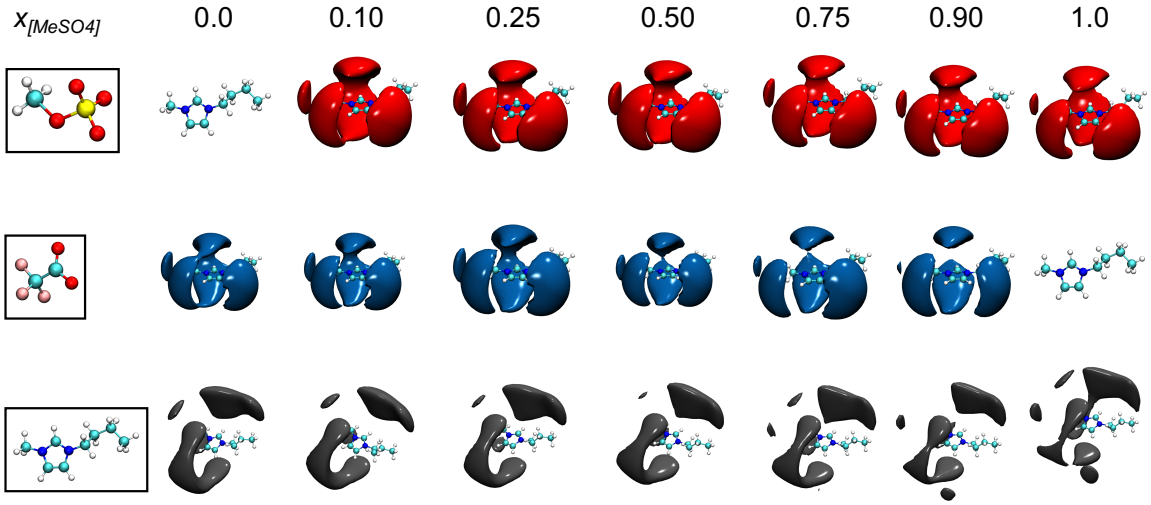

Figure C.11: SDFs of $[C_4mim][MeSO_4]_x[TFA]_{1-x}$ binary ionic liquid mixture (a) cation-$[MeSO_4]$ (COM-based), (b) cation-[TFA] (COM-based), and (c) cation-cation (COR-based). Spatial densities of anions around cations - 2.5 times bulk density while spatial densities of cations around cations - 1.5 times bulk density.

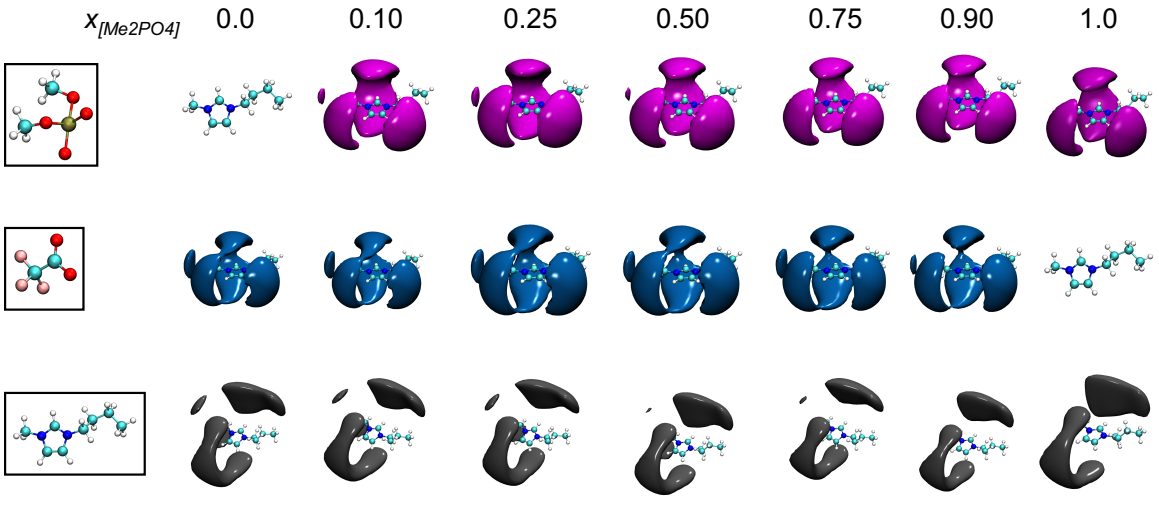

Figure C.12: SDFs of $[C_4mim][Me_2PO_4]_x[TFA]_{1-x}$ binary ionic liquid mixture (a) cation-$[Me_2PO_4]$ (COM-based), (b) cation-[TFA] (COM-based), and (c) cation-cation (COR-based). Spatial densities of anions around cations - 2.5 times bulk density while spatial densities of cations around cations - 1.5 times bulk density.

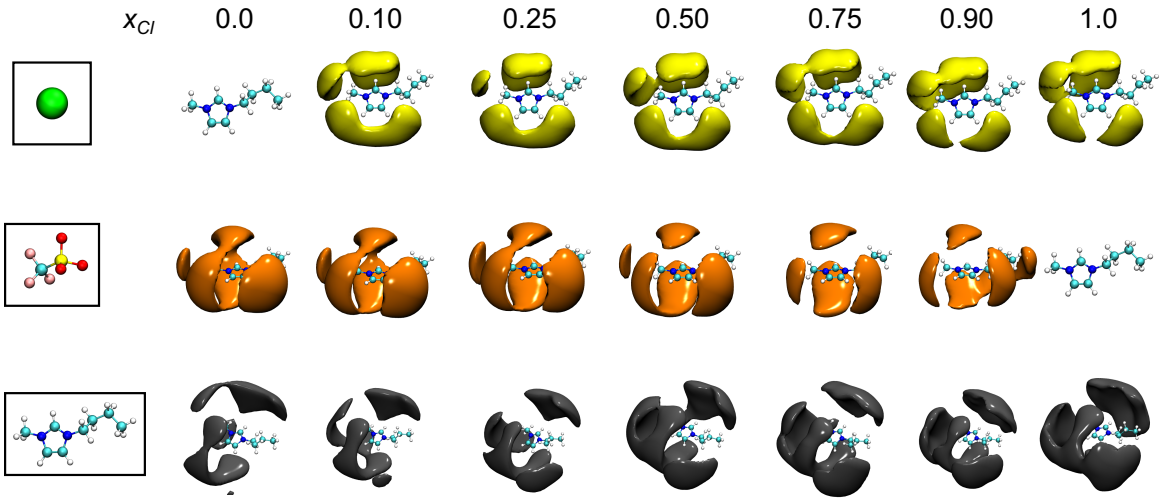

Figure C.13: SDFs of $[C_4mim]Cl_x[TFS]_{1-x}$ binary ionic liquid mixture (a) cation-Cl (COM-based), (b) cation-[TFS] (COM-based), and (c) cation-cation (COR-based). Spatial densities of anions around cations - 2.5 times bulk density while spatial densities of cations around cations - 1.5 times bulk density.

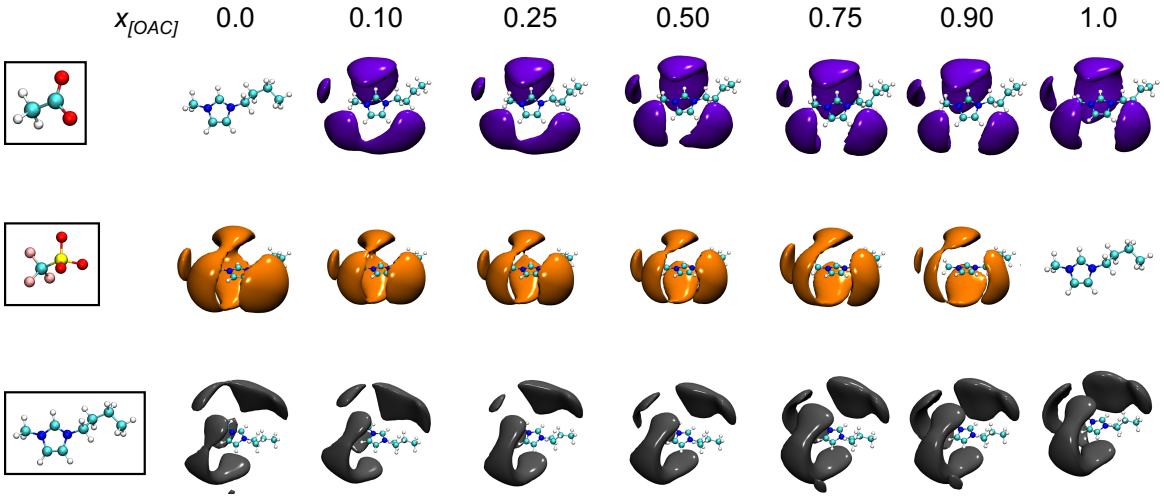

Figure C.14: SDFs of $[C_4mim][OAC]_x[TFS]_{1-x}$ binary ionic liquid mixture (a) cation-[OAC] (COM-based), (b) cation-[TFS] (COM-based), and (c) cation-cation (COR-based). Spatial densities of anions around cations - 2.5 times bulk density while spatial densities of cations around cations - 1.5 times bulk density.

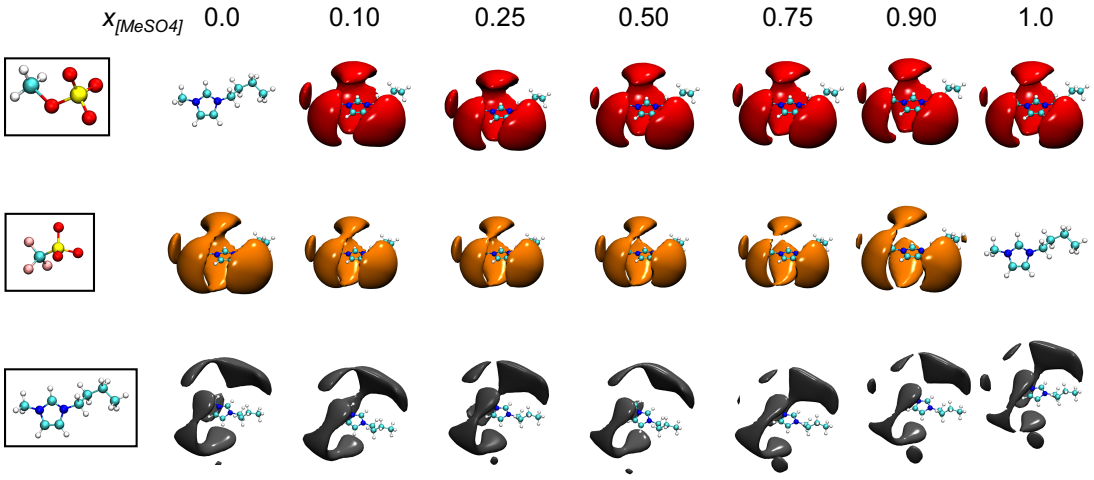

Figure C.15: SDFs of $[C_4mim][MeSO_4]_x[TFS]_{1-x}$ binary ionic liquid mixture (a) cation-$[MeSO_4]$ (COM-based), (b) cation-[TFS] (COM-based), and (c) cation-cation (COR-based). Spatial densities of anions around cations - 2.5 times bulk density while spatial densities of cations around cations - 1.5 times bulk density.

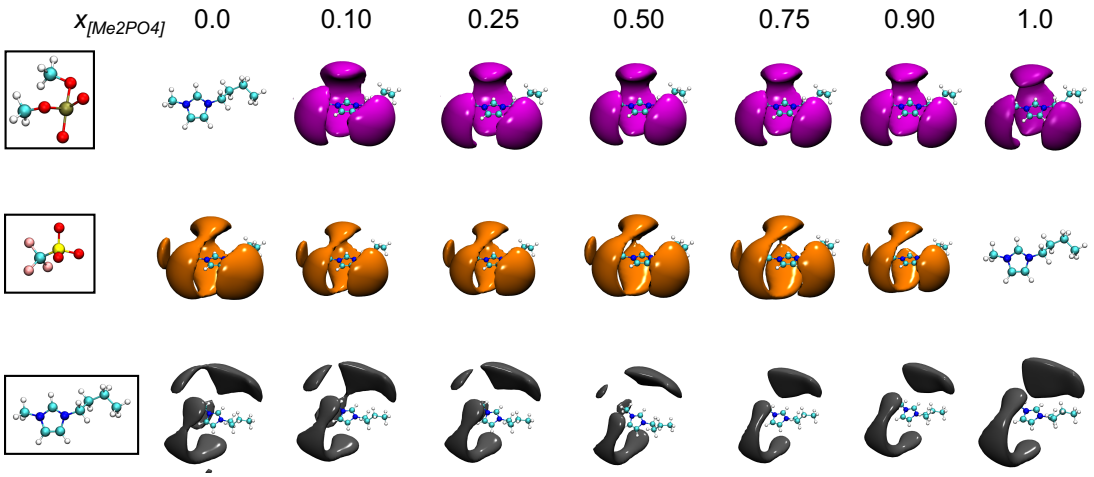

Figure C.16: SDFs of $[C_4mim][Me_2PO_4]_x[TFS]_{1-x}$ binary ionic liquid mixture (a) cation-$[Me_2PO_4]$ (COM-based), (b) cation-[TFS] (COM-based), and (c) cation-cation (COR-based). Spatial densities of anions around cations - 2.5 times bulk density while spatial densities of cations around cations - 1.5 times bulk density.

VITA

UTKARSH KAPOOR

Candidate for the Degree of

DOCTOR OF PHILOSOPHY

Thesis: IONIC LIQUIDS: THE IMPORTANCE OF LOCAL STRUCTURES AT MICRO- AND MESOSCALE AND DESCRIPTORS TO TUNE THEM

Major Field: CHEMICAL ENGINEERING

Biographical:

Education:

- Doctor of Philosophy in Chemical Engineering, at Oklahoma State University, Stillwater, Oklahoma, USA, December 2018
- Bachelor of Engineering (Hons.) in Chemical Engineering, at Birla Institute of Technology and Science – Pilani University, Rajasthan, India, December 2012

Publications:

- U. Kapoor and J. K. Shah; J. Phys. Chem. B, 2018, 122, 42, 9763–9774
- U. Kapoor and J. K. Shah; J. Theor. Comput. Chem. 2018, 17, 1840004-1–1840004-26
- U. Kapoor and J. K. Shah; J. Chem. Eng. Data, 2018, 63 (7), 2512–2521
- U. Kapoor and J. K. Shah; J. Phys. Chem. B, 2018, 122(1), 213–228
- U. Kapoor and J. K. Shah; Ind. Eng. Chem. Res., 2016, 55 (51), 13132–13146